Quantification of Lutetium-177 on a Cadmium Zinc Telluride Gamma Camera

A thesis submitted to The University of Manchester for the degree of

Doctor of Clinical Science in the Faculty of Biology, Medicine and Health

2023

Anna K Chilcott

School of Medical Sciences

CONTENTS

The final word count, including footnotes and endnotes: 40400

LIST OF FIGURES

LIST OF TABLES

LIST OF ABBREVIATIONS

AC: Attenuation correction

APDI: Analytical photon distribution interpolated

Bq: Becquerel

CFOV: Central field of view

cm: Centimetre

COR: Centre of rotation

cps: Counts per second

CQC: Care Quality Commission

CT: Computed tomography

CTAC: Computed tomography attenuation correction

CZT: Cadmium zinc telluride

DEW: Dual energy window

EANM: European Association of Nuclear Medicine

ESSE: Effective source scatter estimation

FOV: Field of view

FWHM: Full width at half the maximum height

g: Gram

^{67}Ga: Gallium-67

GATE: Geant4 application for tomographic emission

GBq: Gigabecquerel

GE: General Electric

GEP-NET: Gastroenteropancreatic neuroendocrine tumour

GI: Gastrointestinal

GI-NET: Gastrointestinal-neuroendocrine tumour

Gy: Gray

h: [factor used in CZT TEW SC, defined in Equation 27]

HEGP: High energy general purpose

^{177}Hf: Hafnium-177

HSST: Higher specialist scientist training

IAEA: International Atomic Energy Agency

IEC: International Electrotechnical Commission

^{123}I: Iodine-123

^{131}I: Iodine-131

it: Iteration

kBq: Kilobecquerel

kcps: Kilocounts per seconds

keV: Kiloelectronvolt

kV: Kilovolt

LEGP: Low energy general purpose

LEHR: Low energy high resolution

LEHS: Low energy high sensitivity

^{177}Lu: Lutetium-177

mA: Milliamps

MBq: Megabecquerel

MC: Monte Carlo

mCRPC: Metastatic castration-resistant prostate cancer

MEGP: Medium energy general purpose

MEHRS: Medium energy high resolution sensitivity

MIRD: Medical Internal Radiation Dose (Committee)

ml: Millilitre

mm: Millimetre

NaI: Sodium iodine

NaI(Tl): Thallium doped sodium iodide

NEMA: National Electrical Manufacturers Association

NET: Neuroendocrine tumour

NICE: National Institute for Health and Care Excellence

NM: Nuclear medicine

NSC: No scatter correction

OAR: Organ at risk

PET: Positron emission tomography

PHA: Pulse height analyser

PMT: Photomultiplier tube

PRRT: Peptide receptor radiotherapy

PSMA: Prostate specific membrane antigen

PVC: Partial volume correction

PVE: Partial volume effect

QC: Quality control

RC: Recovery coefficient

ROI: Region of interest

RR: Resolution recovery

RSCH: Royal Surrey County Hospital

s: Seconds

SC: Scatter correction

SPECT: Single photon emission computed tomography

ss: Subset

SSTR: Somatostatin receptor

SUV: Standardised uptake value

^{99m}Tc: Technetium-99m

TEW: Triple energy window

^{201}Tl: Thallium-201

UFOV: Useful field of view

VOI: Volume of interest

WEHR: Wide energy high resolution

ABSTRACT

Quantitative gamma camera imaging of Lutetium-177 (^{177}Lu) is a vital step in accurately calculating the radiation dose to a patient following ^{177}Lu-labelled radiopharmaceutical therapy. Post-therapy ^{177}Lu-labelled radiopharmaceutical imaging is routinely acquired using sodium iodide gamma cameras, however, there has been a development in solid-state gamma camera technology for general purpose imaging. The aim of this work was to investigate the accuracy of quantitative ^{177}Lu-labelled radiopharmaceutical gamma camera imaging on a cadmium zinc telluride (CZT) single photon emission computed tomography (SPECT) system.

A GE Discovery NM/CT 870 DR CZT system with wide energy high resolution (WEHR) collimators was used for this work. ^{177}Lu image uniformity was calibrated and verified for both 113 and 208 keV primary photopeaks and adjacent scatter windows using a fillable flood phantom. A scatter correction technique was derived for imaging ^{177}Lu on a CZT gamma camera, accounting for the hole tailing effects. A cylindrical phantom was filled with a known activity concentration of ^{177}Lu-labelled compounds and imaged to derive a sensitivity calibration. A range of different size spheres were imaged with a known activity concentration of ^{177}Lu-labelled compounds to optimise the SPECT reconstruction parameters and to calculate the partial volume correction. The gamma camera calibrations were validated by applying them to a 0.5 ml sphere imaged in a scatter material. A Monte Carlo model of the CZT SPECT system was developed to aid the validation process.

The optimal reconstruction was determined to be with OSEM iterative reconstruction with 5 iterations, 10 subsets, CT attenuation correction, triple energy window scatter correction adjusted to account for hole tailing and no resolution recovery. The sensitivity was calculated to be 7.84 ± 0.39 cps/MBq for the 113 keV photopeak and 10.61 ± 0.53 cps/MBq for the 208 keV photopeak. The accuracy of the calibrations was -40% (95% confidence interval -75% to 102%) for a 113 keV photopeak and was -36% (95% confidence interval -83% to 40%) for a 208 keV photopeak. There was septal penetration artefact observed on the 208 keV images. There was increased scatter on the 113 keV images, compared to 208 keV images. The Monte Carlo model was created successfully and was tested using a water-filled cylindrical phantom and a sphere in a scatter material.

Quantitative imaging of ^{177}Lu on a CZT gamma camera is possible and this work suggests some of the calibrations required. A new scatter correction technique was developed to account for the hole tailing effect within a CZT detector. Due to the septal penetration artefact at 208 keV, it may be optimal to use the 113 keV photopeak for imaging ^{177}Lu on a CZT gamma camera with WEHR collimators. Further work is required to fully validate the gamma camera calibrations and the Monte Carlo simulation.

DECLARATION

No portion of the work referred to in this thesis has been submitted in support of an application for another degree or qualification of this or any other university or other institute of learning.

COPYRIGHT

ACKNOWLEDGEMENTS

I am hugely grateful to everyone who has helped, supported and encouraged me through this work and the higher specialist scientist training (HSST) programme.

I would like to thank my supervisors, James Scuffham, Dave Cullen and Jill Tipping for providing me with invaluable guidance throughout this work. I am particularly grateful to James who has supported me throughout the whole process and has regularly provided me with helpful advice and encouragement.

I would also like to thank Sophia Pells, Alex Fish, Ben Pietras and Andrew Robinson who have provided me with assistance in the computing aspects of this work, particularly at the start of the project. They provided me with endless advice, support, and knowledge.

Thank you to everyone at the Nuclear Medicine and Nuclear Medicine Physics departments at Royal Surrey County Hospital for allowing me to carry out the work on their gamma camera and using their processing software. I am also grateful for the support and advice they have provided me throughout HSST.

Thank you to all my colleagues in the Imaging Physics and Nuclear Medicine teams at Southampton General Hospital for supporting me through this work and providing me with time to focus on finishing HSST, particularly Sofia Michopoulou and Matt Guy.

Finally, I would like to thank my partner, family and friends for continually encouraging me and supporting me through this process.

1 INTRODUCTION

1.1 Overview

Lutetium-177 (^{177}Lu) labelled radiopharmaceuticals can be used for the treatment of cancer, such as neuroendocrine tumours and metastatic prostate cancer. To optimise treatment outcomes for an individual patient, the distribution of ^{177}Lu-labelled radiopharmaceutical therapy can be imaged, using a gamma camera, for visual assessment and for quantitative analysis [1]. The quantitative analysis of the ^{177}Lu-labelled radiopharmaceutical images can be used to calculate the radiation dose the patient received from the therapy, which can include the dose to the target tumour and the healthy organs [1]–[3]. Quantitative gamma camera images can provide vital information about the ^{177}Lu-labelled radiopharmaceutical uptake within a patient, however there are many sources of uncertainty in quantitative gamma camera imaging, and it is dependent on the equipment, calibrations, image processing and geometry of the object being imaged [1], [4]. There are several studies that have investigated quantitative imaging using ^{177}Lu on sodium iodide (NaI) gamma cameras. However, for general purpose nuclear medicine imaging, a new solid-state technology has been introduced to the clinical environment with the introduction of cadmium zinc telluride (CZT) gamma cameras, which could lead to increased accuracy of quantitative imaging. This thesis investigates whether a CZT gamma camera can be used for imaging ^{177}Lu and the accuracy of the quantitative analysis from the images.

This thesis includes the background theory for gamma camera imaging, ^{177}Lu-labelled radiopharmaceutical therapy, various components of quantitative imaging and Monte Carlo simulations, summarised in chapter 2. A literature review investigating the research which has been carried out on quantitative ^{177}Lu imaging on NaI gamma cameras, how the CZT gamma camera differs from a NaI gamma camera and where the gaps in quantitative CZT ^{177}Lu imaging research currently lie, is presented in chapter 3. The primary focus of the practical work in this thesis is on the gamma camera calibrations for ^{177}Lu imaging on a CZT gamma camera, which include uniformity, scatter correction (SC), sensitivity, optimisation of reconstruction, partial volume correction and calculation of the accuracy of the calibrations, which is detailed in chapter 4. In addition, a Monte Carlo simulation was created for the CZT gamma camera to aid in the future validation process of the implementation of this new gamma camera technology, with methods and results presented in chapter 5. The thesis is summarised with conclusions and suggestions for further work in chapter 6.

1.2 Aims of Research Project

The overall objective of this research project was to assess the quantitative accuracy of imaging ^{177}Lu on a CZT gamma camera by using a range of gamma camera calibrations and Monte Carlo simulations. The aims of the research were further developed following the literature review to identify the specific research questions. The research aims were to:

- Perform a literature review to identify the methods used for quantitative NaI gamma camera imaging and analyse whether these techniques could be used for quantitative CZT gamma camera imaging.
- Develop a SC technique that can be used for imaging ^{177}Lu on a CZT gamma camera which is appropriate for routine clinical use.
- Calculate ^{177}Lu CZT gamma camera calibrations for uniformity, sensitivity and partial volume correction and determine the optimal parameters for single photon emission computed tomography (SPECT) reconstruction.
- Carry out a validation for the ^{177}Lu gamma camera calibrations calculated.
- Develop a Monte Carlo model of a CZT gamma camera which could be used to aid the validation of the gamma camera calibrations calculated.

There is currently limited published research into imaging ^{177}Lu on a CZT gamma camera or creating a Monte Carlo simulation for imaging ^{177}Lu on a CZT gamma camera. There is some research into suggested SC techniques for a CZT gamma camera, however using different radionuclides or complex techniques. Therefore, the research aims for this thesis have been developed to assess the quantification accuracy of ^{177}Lu on a CZT gamma camera which can be applied within a clinical environment.

2 BACKGROUND THEORY

2.1 Nuclear Medicine

Nuclear medicine involves administering radioactive pharmaceuticals, or radiopharmaceuticals, for diagnosis or therapy, covering a range of applications such as oncology, cardiology and neurology. The radiopharmaceutical is a radioactive tracer used to target a specific physiological system. Diagnostic nuclear medicine assesses the physiology of the patient by selecting a specific radiopharmaceutical to administer depending on the clinical question. The diagnostic radiopharmaceutical is usually a gamma-emitter, for example Technetium-99m (^{99m}Tc). The distribution of the radiopharmaceutical is often measured using a gamma camera, which is further described in section 2.3. For a gamma camera to effectively image a radionuclide, the physics interactions that the radiation undergo whilst travelling through matter must be considered, which are summarised in section 2.2. It is also possible to use radiopharmaceuticals to treat disease, known as molecular radiotherapy, which is described in section 2.4.

2.2 Radiation Interaction with Matter

2.2.1 Photon Radiation Interactions

Photons that are produced through radioactive decay interact with matter within the patient and within the gamma camera, before being detected. The probability of a photon undergoing an interaction is defined by the linear attenuation coefficient (μ), which is dependent on the composition of the attenuating material and the photon energy [5], [6]. For a mono-energetic beam of photons the intensity (I) at any point in the material is defined by Equation 1.

$$I = I_0 e^{-\mu x} \qquad \textbf{Equation 1}$$

Where I_0 is the initial intensity of the incident photons and x is the thickness of the material the photons have passed through [5], [6]. A photon can undergo three main interactions with electrons in a material: photoelectric effect, Compton scattering or pair production. The dominant type of interaction depends on the energy of the photons that are incident on the material. For low energy photons the dominant interaction is photoelectric effect, for medium energy photons the dominant interaction is Compton scattering and for high energy photons the dominant interaction is pair production [6], [7]. The energy ranges for each interaction depends on the properties of the matter the photon is travelling through. Photoelectric effect is where a photon is completely absorbed and the energy is transferred to an electron, causing the electron to be ejected from the atom [6], [7]. Compton scattering occurs when a photon interacts with a loosely bound electron of an atom, which will cause the photon to lose energy

and change direction [6], [7]. Pair production is not applicable to the nuclear medicine imaging discussed in this work.

2.2.2 Beta Radiation Interactions

When beta particles travel through matter, they lose energy and slow down as they pass atoms within the matter, which can cause an electron to be removed from the atom (causing ionisation), cause an electron to move to an excited state or it can interact with the nucleus causing bremsstrahlung radiation [6]. If the beta particle causes an ionisation, then the beta particle loses energy which can transferred to a secondary electron as kinetic energy, or it can lead to characteristic x-rays. If the beta particle causes an electron to move to an excited state, then there will be less energy loss than an ionisation event. If the beta particle interacts with the nucleus, the beta particle is deflected by the electrical force of the nucleus and causes rapid deceleration and energy loss. The energy is transferred to a bremsstrahlung photon which can be any energy up to the full energy of the incident particle, which is displayed for a range of isotopes in Figure 1 [6], [8].

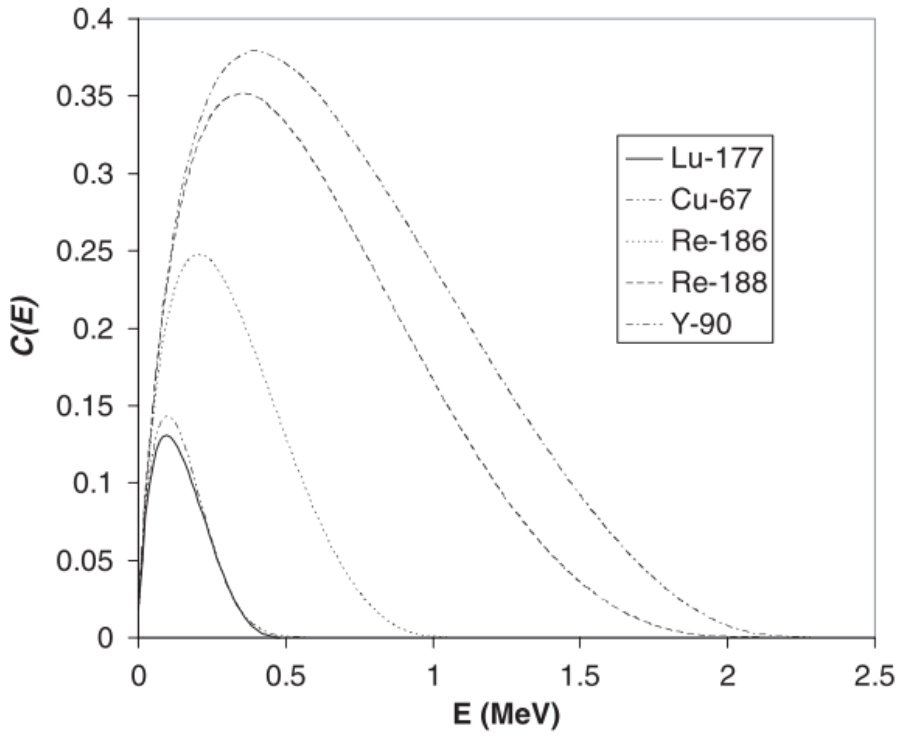

Figure 1: The beta energy spectrum for a range of radionuclides, where C(E) is the relative intensity of electrons and E is the energy at any point in the medium (taken from Syme et al 2004) [8]

2.3 Gamma Camera Technology

A gamma camera detects the radiation within a patient and provides an image of the radiopharmaceutical distribution within the patient. It is possible to acquire various types of images using a gamma camera, such as planar or static, dynamic, gated, whole-body or tomographic images. The type of imaging used depends on the clinical question and radiopharmaceutical used. For example, static scans can be used for thyroid uptake imaging prior to molecular radiotherapy, dynamic scans can be used for kidney function, gated scans can be used for cardiac imaging, whole-body scans can be used for bone imaging and tomographic imaging is used for three-dimensional imaging of a particular site of interest. Tomographic imaging is called single photon emission computed tomography (SPECT). Most gamma cameras which are used for SPECT imaging also include a computed tomography (CT) scanner, so the anatomical and physiological information can be collected in one imaging event, referred to as SPECT/CT. These hybrid systems can also derive an attenuation map, with the acquired CT of the patient, to enable attenuation correction to the SPECT image. More information about attenuation correction is given in section 2.6.3.

There are a few properties of a gamma camera detector which can identify how useful the detector will be for gamma camera imaging. The key properties are efficiency of detecting the photons, which depends on the density, effective atomic number and thickness of detector material, which all depend on the energy of the photons being imaged [9]. Other key properties include spatial resolution, energy resolution, uniformity, count-rate capability, mechanical robustness and cost [9]. A commonly used material for clinical gamma cameras is NaI, which is further described in section 2.3.1. Research into gamma camera technology was mostly following the same basic technology first used in a gamma camera when invented by Anger in the 1950s [9], which has underlying limitations (described in section 2.3.1), until recently. The CZT detector, which directly converts gamma radiation to an electrical signal, was developed to outperform the traditional Anger camera technology [10], which is further described in section 2.3.2.

2.3.1 Sodium Iodide Gamma Camera Technology

A NaI gamma camera detector consists of a collimator, scintillation crystal, light guide, photomultiplier tubes (PMT) and electronics, as shown in Figure 2 [9]. The gamma photons emitted from the patient will travel in all directions and therefore the collimator will filter out the gamma photons that are not travelling approximately perpendicular to the scintillation crystal. Collimators are further described in section 2.3.4.

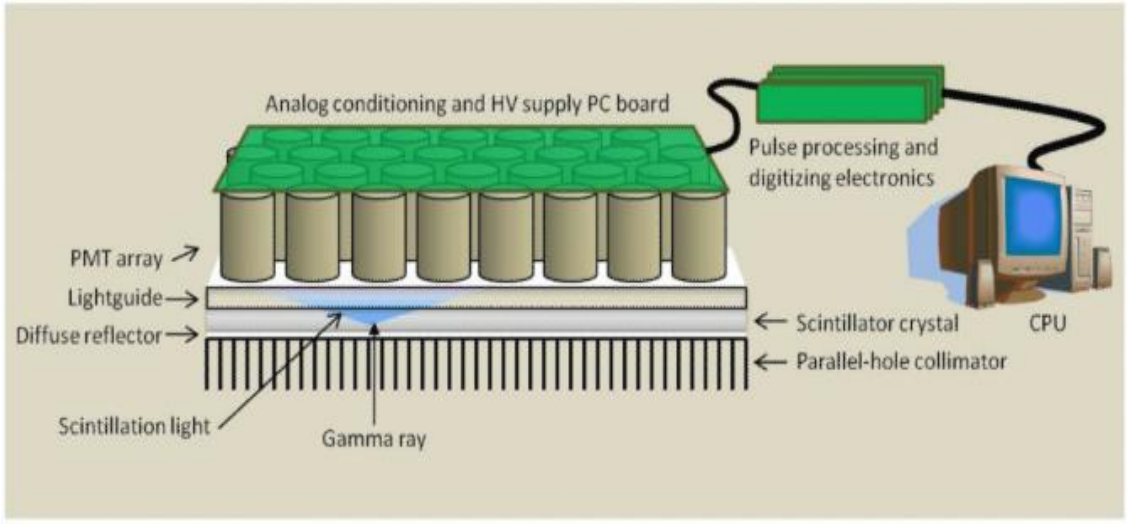

Figure 2: The basic structure of a sodium iodide gamma camera featuring a collimator, scintillation crystal, light guide, PMTs and electronics (taken from Peterson et al 2011) [9]

The scintillation crystal is a thallium doped sodium iodide (NaI(Tl)) crystal. The incident gamma photon will scintillate into light photons and travel through the crystal to the light guide. The light guide ensures the photons travel efficiently between the scintillation crystal and the PMTs. The light photon enters the PMT and reaches a photocathode and is converted to electrons [11]. The PMT consists of multiple dynodes which increase the number of electrons, until they reach the anode at the opposite end of the PMT [11]. The electrons are then converted to an electronic signal, which is then processed to give the energy, location and number of counts in the signal [11].

The amplitude of the voltage pulse is proportional to the amount of energy deposited in the detector from the incident photon [6]. The amplitudes of the pulses are assessed to determine the energy of the detected radiation event. It is possible to use a pulse height analyser (PHA) to select which pulses should be included. Therefore, during an acquisition the energy spectrum is used to identify the photons with the correct energy that should be included in the image, as displayed in Figure 3 for ^{99m}Tc. The energy window is set depending on the radionuclide being imaged. For example, for ^{99m}Tc the energy window could be set for 140 keV ± 10%. This will help reduce the number of scattered photons that effect the image. However, some scattered radiation will fall within this energy window (as displayed in Figure 3), which can be corrected for as discussed in section 2.6.1. The energy window used will depend on the energy resolution of the detector. The energy resolution is a measurement of how wide the detected photopeak is and can be defined as the full width at half the maximum height (FWHM). It is usually expressed as a percentage of the photopeak energy [6].

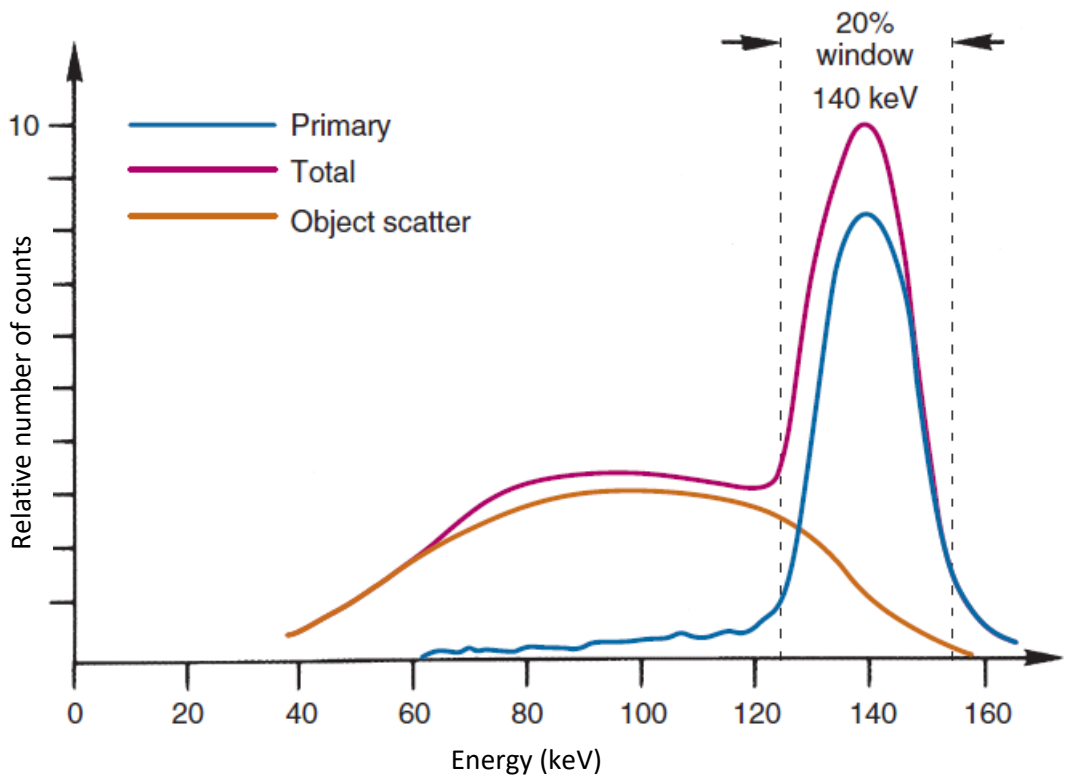

Figure 3: An energy spectrum for ^{99m}Tc for a NaI gamma camera, where the purple line is the total counts detected, the blue line represents the primary (unscattered) gamma radiation and the orange line represents the scattered gamma radiation (taken from Cherry et al 2012) [6]

For the detected photons to form an adequate energy spectrum and image, there are three main corrections that need to be applied which are energy, linearity, and uniformity. The corrections are applied as maps based on specific calibrations carried out. The energy map applies a correction to ensure the PHA is calibrated to display the appropriate energy being detected [12]. The linearity map applies a correction to ensure that a line source given to the gamma camera will provide a linear image. The non-linearities appear from the variation in sensitivity of the PMT across the surface, they are more sensitive in the middle of each PMT than towards the edges [12]. The uniformity map applies a correction to smooth any other non-uniformities in the image, such as variation in sensitivities between PMTs. A basic quality control test, which is regularly carried out, is a uniformity test, which involves imaging a uniform source from which the differential uniformity and integral uniformity can be calculated. The differential uniformity is the uniformity within a local region (5 adjacent pixels) and integral uniformity is the global uniformity across the field of view (FOV) [13]. The uniformity test is usually given as the results for useful FOV (UFOV) and central FOV (CFOV), where the CFOV is 75% of the size of the UFOV [6].

The NaI gamma camera has been in use for many years and is currently the most common material in clinical SPECT imaging, as it is readily available and cost effective [11]. The NaI scintillation crystal is typically about 6 to 12.5 mm thick and can be up to 60 by 40 cm for a rectangular detector [6]. Due to the number of steps involved in the NaI gamma camera the light yield is 38 photons/keV (displayed in the pulse height analyser) [9], which results in the uncertainty in the measured signal to be large. A number of PMTs are required (approximately 30 to 100 in a typical gamma camera, where each PMT is approximately 5 cm in diameter [6]) to resolve the location of the incident gamma photon, causing the camera head to be fairly large [11]. The PMTs require fine tuning to ensure they all give the same gain and therefore output for the same incident photon [11]. The gamma camera technology results in relatively poor spatial and energy resolution compared to other imaging modalities and there is a trade-off between detection efficiency and spatial resolution [14], which is due to the collimator design (described in section 2.3.4) and crystal thickness [6].

2.3.2 Cadmium Zinc Telluride Gamma Camera Technology

The CZT detector is a direct conversion semiconductor with a specific density of 5.82 $g.cm^{-3}$ [9], to effectively stop gamma radiation within the energy range used for most SPECT imaging [10]. When a gamma ray interacts with the CZT detector, one or more electrons are created, which lose energy and propagate through ionisation and phonon generation [9]. The ionisation creates electron-hole pairs, where the hole is a positively charged electron vacancy in the valence band and the electron moves to the conduction band [7], [9]. When a bias voltage is applied it creates an electric field causing the charge carriers to drift in opposite directions inducing a current on the electrodes. This current is detected by an electrical circuit, therefore providing a measurement of the CZT detector's response to the radiation interaction [9]. This process is visualised in Figure 4. Semiconductors are often doped with impurities to create an extra electron or hole to reduce the effective energy gap between the valence and conduction bands by creating a donor level [7]. The amount of energy absorbed is proportional to the size of the electrical signal, therefore the CZT detector is able to differentiate between different energy photons [6]. The CZT crystal is grown in a sealed container as a single large crystal, where it can then be cut into thin wafers and metal contacts added to readout the electrical signal, creating a small individual detector [10]. An example of a general purpose CZT gamma camera has individual detectors of 2.46 mm (for a GE Discovery 870 CZT) [15]. Two main advantages of a CZT detector over other semiconductors (e.g. silicon and germanium) is that it can be used at room temperature, without excessive noise, and it has a high atomic number, and therefore a relatively thin detector can have effective stopping efficiency for gamma radiation [6].

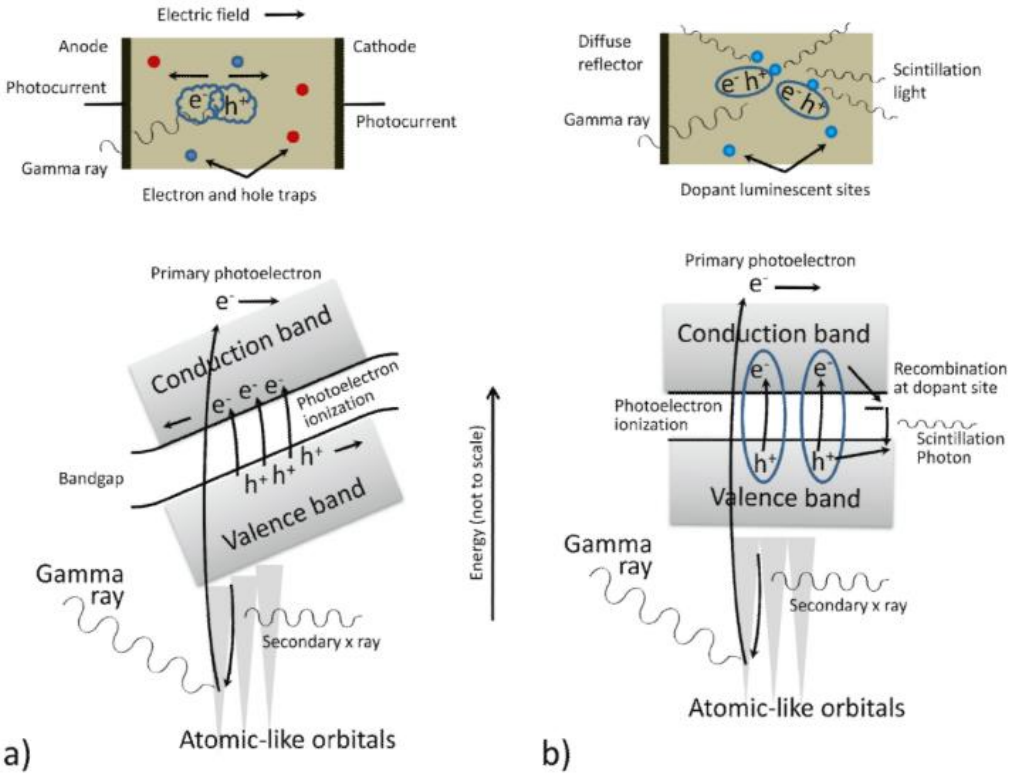

Figure 4: a) Representation of the photoelectric process in a direct-conversion material, where the excitation of electron-hole pairs drift in opposite directions due to the electric field, as used in a CZT detector. b) The photoelectric effect in a scintillator creates electron-hole pairs but without the electric field and therefore the pairs are loosely bound excitons, as used in a NaI detector. The excitons diffuse and recombine, emitting secondary scintillation photons that can be read out by a light sensor (taken from Peterson et al 2011) [9]

The CZT detector generally suffers from reduced hole transport, relative to electron, due to hole trapping, which occurs at the site of the crystalline defects (e.g. vacancies or impurities) [9]. Therefore the trapping has an effect on charge collection as one type of charge carrier will have a dominant trapping level and the traps will be uniformly distributed across the detector [9]. The number of the trapped charge carriers decreases exponentially over time, with a mean lifetime of τ [9]. The charge, *Q*, on the electrode is given by the Hecht relation [9], [16] in Equation 2:

$$Q = qN_0\left[\frac{\mu_h\tau_h E}{L}\left(1 - e^{-x/\mu_h\tau_h E}\right) + \frac{\mu_e\tau_e E}{L}\left(1 - e^{-(x-L)/\mu_e\tau_e E}\right)\right] \quad \textbf{Equation 2}$$

Where N_0 is the number of electron-hole pairs created by the radiation interaction, μ is the mobility of the charge in the material, E is the electric field, L is the detector thickness and x is the depth of the interaction. Equation 2 shows that the mobility-lifetime product controls the contribution of each charge-carrier type to the measured signal. There is a trade-off between

increasing the electric field through increasing the voltage which results in an improved charge collection, and the increase in leakage current increases the noise. The CZT detector has a relatively poor hole to electron mobility-lifetime product ($\mu\tau$) compared to other semiconductors (summarised in Table 1), which creates a depth dependence in signal generation that introduces a low-energy tail on the photopeak of the pulse height spectrum [9], as seen in Figure 5. A full amplitude signal is generated only when both the electrons and holes created are fully collected, however when the hole collection is incomplete there will be a deficiency in the detector signal [17]. The level of deficiency depends on the location of the carrier generator with respect to the electrodes (therefore, creating the depth dependence) [17].

Table 1: Mobility-lifetime product for different semiconductor materials [9]

Semiconductor	**Mobility-lifetime product (cm^2/V)**	
	Electron	**Hole**
Silicon	0.42	0.22
Germanium	0.72	0.84
CZT	0.003	0.00005

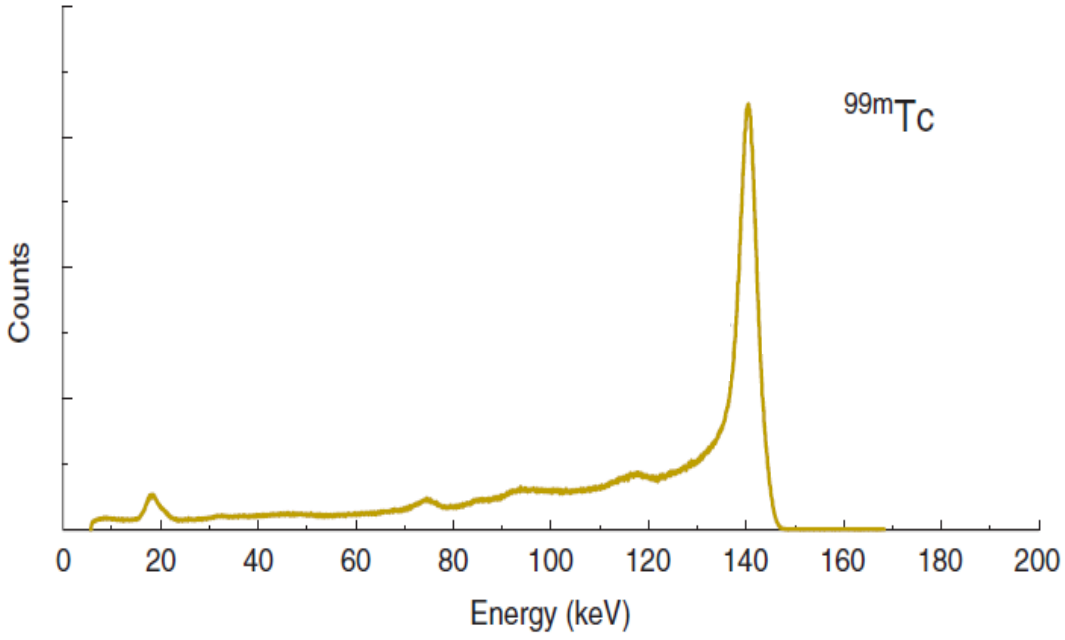

Figure 5: The ^{99m}Tc energy spectrum from a 5 x 5 x 5 mm CZT detector, where evidence of the low energy tail can be seen at around 130 to 140 keV (taken from Cherry et al 2012) [6]

When comparing the energy spectrum in Figure 5 for a CZT gamma camera to Figure 3 for a NaI gamma camera, it can be seen that the photopeak for the CZT gamma camera is more

asymmetrical than for the NaI gamma camera (due to the hole tailing), which will affect the SC technique required, which is further discussed in sections 2.6.1 and 3.

2.3.3 Comparison Between Sodium Iodide and Cadmium Zinc Telluride Gamma Cameras

There are various properties of a detector which indicate its usefulness in a particular application, for example, the efficiency, density, atomic number and thickness need to be considered [9]. However, there is often a compromise that needs to be made between characteristics such as detector efficiency and spatial resolution. Energy resolution is another consideration as this can affect SC, which is described in section 2.6.1. Comparing the CZT gamma camera to the NaI gamma camera, the CZT gamma camera is more efficient at converting the incident gamma photon to an electrical signal, which produces improved energy resolution [10], [18]. CZT detectors exceed the energy resolution that is expected from applying a Poisson model to the charge carrier generation due to the efficiency of converting the photon to an electrical signal [9]. Phonons are the primary opposing process that competes with the electron-hole pair formation as an energy loss mechanism of electrons, and the CZT can efficiently transfer energy to the phonons resulting in reduced energy loss [9]. There are other sources of noise in semiconductors, however this is less than experienced in NaI detectors [19]–[21]. For ^{99m}Tc the energy resolution for a NaI detector is 10% FWHM at 140 keV but can be less than 7% FWHM for CZT gamma cameras [9], [10].

Practically, CZT gamma cameras are lighter and smaller than NaI gamma cameras, as there are no PMTs and therefore less shielding required [9], [10]. There is dead space around the edge of the NaI camera as there is difficulty resolving incident gamma radiation at the edge of the PMTs, which is not a problem for the CZT gamma camera as it is made up of independent small detectors [10], as seen in Figure 6. Assessing the uniformity in NaI gamma cameras involves a UFOV and a CFOV where the uniformity is expected to be improved in the middle, however in CZT gamma cameras the uniformity should be the same across the whole detector [10].

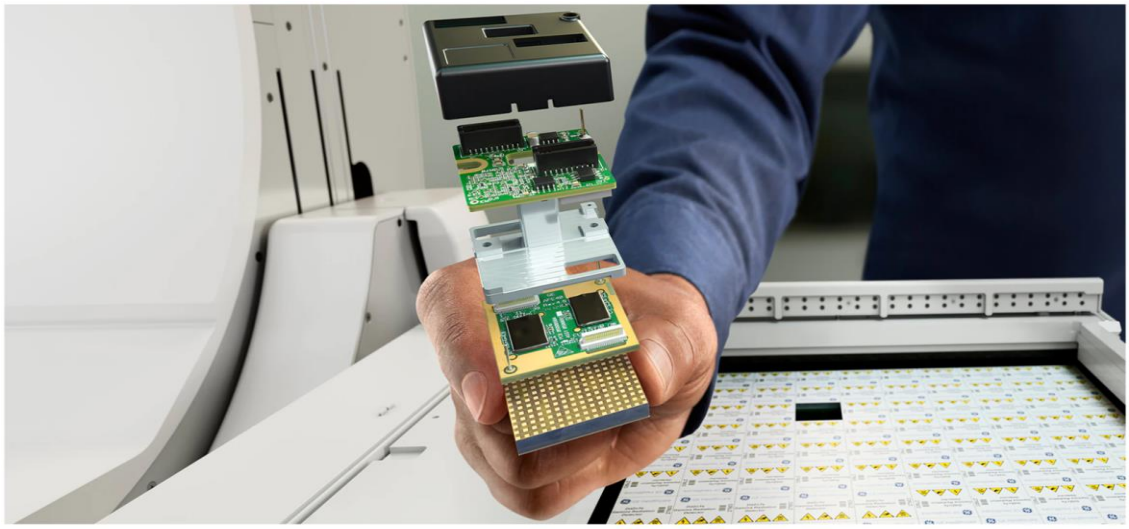

Figure 6: An example of the detector modules and technology used within the GE Discovery 870 DR CZT gamma camera (taken from GE Healthcare 2023) [22]

The spatial resolution of the GE Discovery 870 DR CZT gamma camera is approximately 2.5 mm, as opposed to 4 mm for a NaI gamma camera [10]. The photons in a NaI crystal will diffuse over a significant distance before they are detected causing inaccuracies in the position information about the photon [10]. Alternatively, in the CZT gamma camera a compact charge cloud is detected by an anode that is only millimetres away and the resolution can be further improved by making the anode pixels smaller [10]. Table 2 shows data for CZT gamma cameras and NaI gamma cameras as a comparison.

Table 2: Comparison between scintillation gamma cameras and solid-state gamma cameras

Parameter	**Solid-State Gamma Cameras (CZT)**	**Scintillation Gamma Cameras (NaI)**
Density of scintillator (g/cm^3) [9]	5.82	3.67
Attenuation at 140 keV (cm^{-1}) [9]	3.07	3.12
Energy resolution (for ^{99m}Tc) (%) [9], [10], [15], [23]	<7	~10
Spatial resolution (without water) (mm) [15], [23], [24]	1.73-3.48	3.7-12.63
Spatial resolution (with water) (mm) [15], [23], [24]	3.88-6.64	15.48-16.28

Uniformity FOV size [15], [23]	Full FOV (51 x 39 cm for GE Discovery 870 CZT)	It is improved in the CFOV compared to the UFOV
Collimators [15], [25]	Limited options available, generally only wide energy general purpose (WEHR) are readily available	Range available from low energy to high energy
Pixel size (mm) [15], [26], [27]	2.46 (Individual detector elements for GE Discovery 870 CZT)	Range, depending on matrix size used and size of detector (approximately 2 to 7 mm)
Intrinsic count rate (kilocounts per second (kcps)) [15], [23]	650 (maximum), 330 (in 20% window)	460 (maximum), 400 (in 20% window)

2.3.4 Collimator Design

There are different types of collimators available, which can be used for imaging different radionuclides and for different types of studies. A commonly used collimator consists of hexagonal parallel holes for the gamma photons to travel through, or for CZT gamma cameras the collimator holes can be square to align with the CZT detector elements. There are different collimators available with different septa thicknesses and lengths which are designed for use with different isotopes, as detailed in Table 3. For example, a high energy general purpose (HEGP) collimator has thick septa and is used for high energy isotopes, such as Iodine-131 (^{131}I) with a photopeak of 364 keV, whereas a low energy high sensitivity (LEHS) or low energy high resolution (LEHR) collimator has a thin septa and is used for low energy isotopes, such as ^{99m}Tc with a photopeak of 141 keV [28]. In addition, a medium energy general purpose (MEGP) or medium energy high resolution sensitivity (MEHRS) collimator can be used for isotopes such as Gallium-67 (^{67}Ga) with a photopeak at 185 keV or ^{177}Lu (described in section 2.4.1) [28].

Table 3: The collimator designs as described by Ito et al and GE Healthcare

Collimator	Type of hole	Hole length (mm)	Hole diameter (mm)	Septal thickness (mm)	Penetration (%)
WEHR [15]	Square	45	2.26	0.2	0.55 (^{99m}Tc)
MEHRS [29]	Hexagonal	40.25	2.8	0.9	0.3 (^{177}Lu)
LEHR [23]	Hexagonal	35	1.5	0.2	0.3 (^{99m}Tc)
LEHS [23]	Hexagonal	34	2.31	0.152	5 (^{99m}Tc)
MEGP [23]	Hexagonal	58	3.0	1.05	2.0 (^{67}Ga)

HEGP [23]	Hexagonal	66	4.0	1.8	2.0 (^{131}I)

If a high energy radionuclide is used it is possible to observe septal penetration artefacts within the image, which can affect the qualitative and quantitative analysis. Septal penetration artefact occurs when a high energy gamma photon penetrates the septa of the collimator and is then detected by the gamma camera, as displayed in Figure 7 [30]. In addition, there is a trade-off between sensitivity and resolution in collimator design, so a LEHS will have shorter septa and larger hole diameter than a LEHR collimator. The selection of collimator is a key step in gamma camera imaging optimisation.

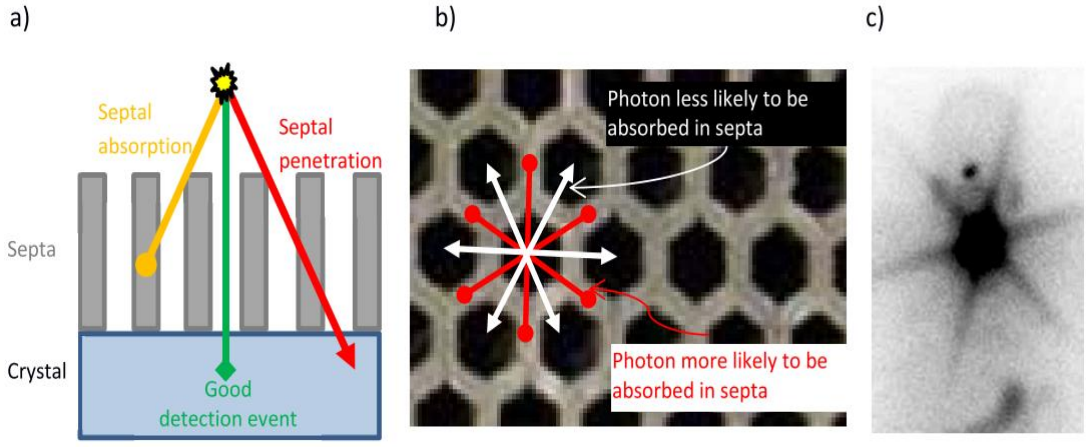

Figure 7: Schematic of septal penetration; a) a cross-sectional view of a collimator displaying photons that are detected by travelling through the collimator hole, absorbed in the septa and have penetrated the septa, b) an example of a hexagonal collimator which can produce a "star" artefact on patient images, as displayed in c). (Taken from Barrack et al 2018) [30]

2.4 Molecular Radiotherapy

Molecular radiotherapy (MRT) is a branch of nuclear medicine which aims to treat disease (often cancer) with radiopharmaceuticals. The radiopharmaceuticals used for therapies are labelled with beta- or alpha-emitting isotopes, however some of the isotopes used for MRT also have additional gamma emissions. The beta or alpha radiation aims to kill diseased cells in target organs or disease sites and the gamma radiation can be used to assess the distribution of the therapy, as for diagnostic nuclear medicine. The type of radiopharmaceutical used depends on the target disease. It is possible to use the same pharmaceutical for both diagnostic investigation and therapeutic effect, which can aid treatment planning or follow up [31]. There is a particular interest in ^{177}Lu-labelled radiopharmaceuticals due to the increase in MRT applications available, therefore this project focusses on quantification of ^{177}Lu imaging using a CZT gamma camera.

2.4.1 Lutetium-177

^{177}Lu decays to Hafnium-177 (^{177}Hf) and emits short range beta radiation (maximum tissue range of 2 mm) and low energy gamma radiation (photopeaks at 113 keV (6% relative abundance) and 208 keV (11% relative abundance)) with a half-life of 160 hours [32]–[36]. During the decay events, ^{177}Lu emits beta particles with a maximum energy of 497 keV (78.6 %), 384 keV (9.1 %) and 176 keV (12.2 %), where a simplified decay scheme is shown in Figure 8 [37]. The beta emission is used for therapy and the gamma emissions can be imaged using a gamma camera, which is used for treatment verification and response monitoring [33]. As there is beta radiation, the gamma camera energy spectrum for ^{177}Lu, includes bremsstrahlung radiation, as described in section 2.2.2 [7]. ^{177}Lu is often used as a treatment for neuroendocrine tumours (NET) or metastatic prostate cancer, described in more detail in sections 2.4.2 and 2.4.3, respectively.

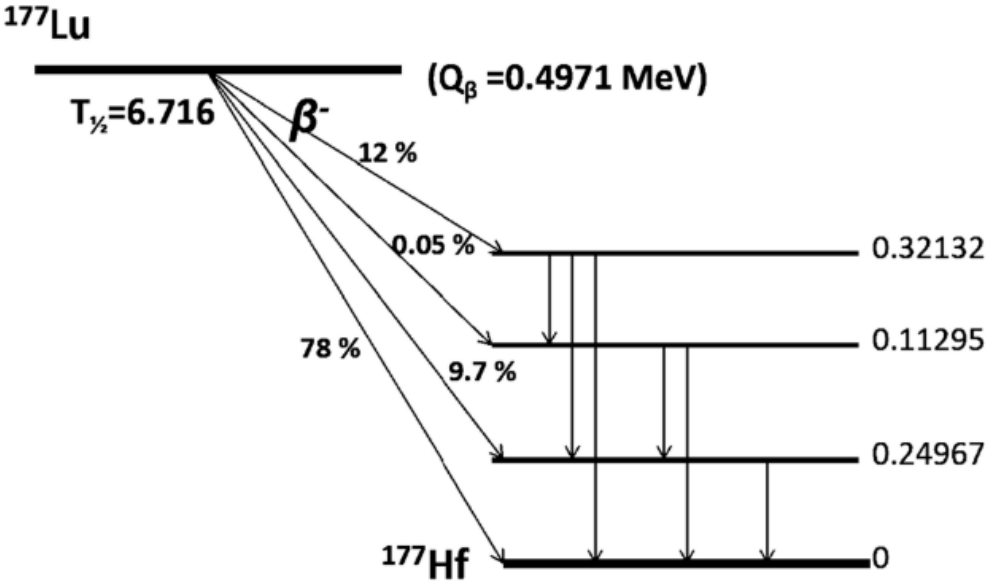

Figure 8: A simply decay scheme of ^{177}Lu (taken from Dash et al 2015) [37]

2.4.2 Lutetium-177-DOTA-TATE for Neuroendocrine Tumours

Somatostatin can regulate growth hormone, thyroid-stimulating hormone and cellular processes [38]. Somatostatin receptors (SSTR) are proteins which receive somatostatin, and SSTRs are overexpressed on NETs [34], [39]. NETs arise from neuroendocrine cells that are distributed in several areas of the body, such as gastro-intestinal (GI) and bronchopulmonary tracts [33]. The worldwide incidence of NETs has been increasing and, for example, NET of the midgut commonly metastasise and are frequently associated with carcinoid syndrome [34]. Carcinoid syndrome consists of flushing, bronchospasm and diarrhoea, and is due to the release of serotonin and other vasoactive substances [40], [41]. NETs of the midgut are the most

common type of malignant GI NETs and are associated with a 5-year survival of less than 50% where the disease has metastasised [34]. Somatostatin analogues can be used for diagnosis or treatment of NETs, which, therefore, provide a useful molecular radiotherapy tracer for patients with inoperable or metastatic NETs [34], [42].

[^{177}Lu]Lu-DOTA-TATE is a type of peptide receptor radionuclide therapy (PRRT), which is a type of MRT using a somatostatin analogue [43]. The [^{177}Lu]Lu-DOTA-TATE binds to SSTRs on NETs and cause a therapeutic effect from the beta-emitting ^{177}Lu. The treatment consists of administering approximately four cycles (three to five) of 7.4 Gigabecquerel (GBq) (5.55-7.4 GBq) [^{177}Lu]Lu-DOTA-TATE at approximately 8 week intervals (6 to 12 weeks) [35]. PRRT has shown considerable promise for the treatment of advanced, well-differentiated NET, a majority of which express high levels of SSTRs to which the somatostatin analogues bind [34]. The initial treatment of NETs includes surgery, for removal of the tumour, and somatostatin analogue therapy, for control of both hormonal secretion and tumour growth [34]. Patients with advanced midgut NET, who had disease progression during somatostatin analogue therapy, had limited therapeutic options with modest survival improvements. The introduction of PRRT improved patient care and outcomes for patients with NET, which involved the administration of a ^{177}Lu- or ^{90}Yttrium (^{90}Y)-labelled radiopharmaceutical as part of MRT [34].

A key milestone in the introduction of PRRT into the NET clinical pathway was the NETTER-1 clinical trial. NETTER-1 was a randomised controlled phase 3 clinical trial which investigated the efficacy and safety of [^{177}Lu]Lu-DOTA-TATE in patients with advanced, progressive, SSTR-positive midgut NET [34]. Patients were given 7.4 GBq [^{177}Lu]Lu-DOTA-TATE every 8 weeks with octreotide or octreotide alone [34]. Octreotide is a SSTR agonist and controls both symptomatic and asymptomatic NETs [35]. The primary end point was progression free survival and the secondary aims were objective response rate, overall survival, safety and side-effect profile [34]. NETTER-1 found that progression free survival at 20 months increased significantly from 10.8% without [^{177}Lu]Lu-DOTA-TATE to 65.2% with [^{177}Lu]Lu-DOTA-TATE, as displayed in Figure 9 [34]. Additionally, a preliminary study in Spain, compared biochemical response to the imaging response following [^{177}Lu]Lu-DOTA-TATE to show 60% of patients had normalised biochemical markers and imaging showed there was a partial response in 85.7% of patients and 14.3% of patients had stable disease [44].

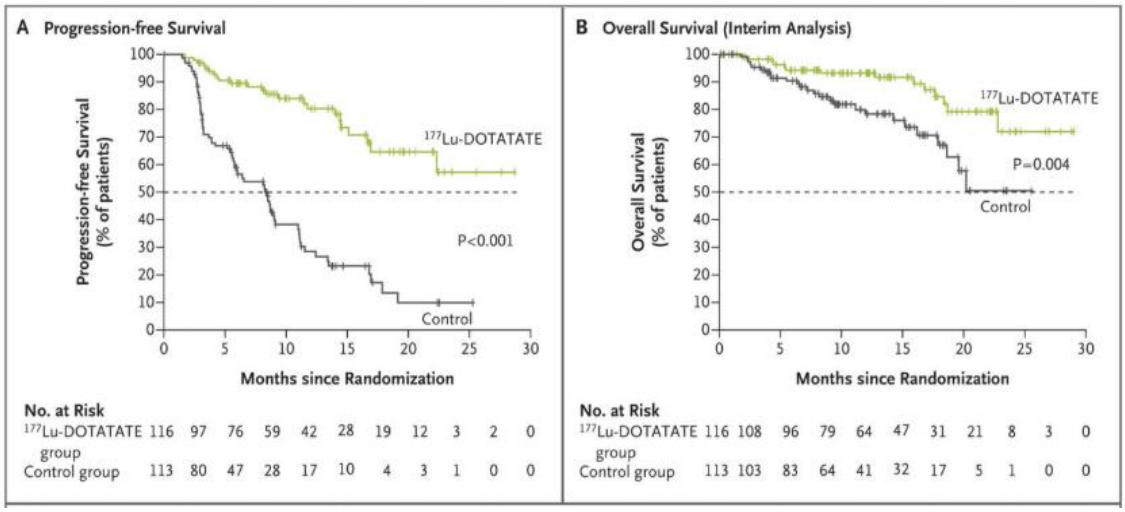

Figure 9: Kaplan-Meier analysis of progression-free survival (A) and overall survival (B) from the NETTER-1 clinical trial (taken from Strosberg et al 2017) [34]

In 2018, the National Institute for Health and Care Excellence (NICE) approved [^{177}Lu]Lu-DOTA-TATE for use in gastroenteropancreatic NET (GEP-NET) [45]. [^{177}Lu]Lu-DOTA-TATE has been shown to decrease tumour size, improve symptoms, improve survival and improve quality of life [33], [34], [40]. [^{177}Lu]Lu-DOTA-TATE requires the patient to have SSTR-positive NETs, and near-normal kidney and bone marrow function [33]. [^{177}Lu]Lu-DOTA-TATE has been shown to have a comparable efficacy and better haematological toxicity than [^{90}Y]Yttrium-DOTA-TOC [33].

The side effects of [^{177}Lu]Lu-DOTA-TATE include myelosuppression, due to the bone marrow being irradiated, haemotoxicity and renal damage [33], [35]. An infusion of lysine and arginine are administered prior to and during the treatment to reduce the renal side effects [33]. The kidneys can receive an absorbed radiation dose (per cycle) of 5.13 ± 2.12 Gy, the liver can receive 4.49 ± 2.49 Gy and the spleen can receive 14.44 ± 8.97 Gy, whereas the mean absorbed dose to the tumour lesion can be 31.43 ± 36.86 Gy [46].

2.4.3 Lutetium-177 PSMA for Metastatic Prostate Cancer

Prostate cancer is one of the most common cancers and it is one of the leading causes of mortality from cancer [2], [47], [48]. The first line treatment is surgery, followed by hormone treatments and radiotherapy [49]. If the prostate cancer becomes metastatic then [^{177}Lu]Lu-PSMA (prostate specific membrane antigen) MRT may be a treatment option. The PSMA pharmaceutical will target the spread of prostate cancer throughout the patient in order to treat metastatic disease (including soft tissue and bone metastases) as PSMA is highly expressed in metastatic castration-resistant prostate cancer (mCRPC) [50]. [^{177}Lu]Lu-PSMA MRT is indicated in patients with mCRPC who have exhausted or are ineligible for alternative options, and they

must have sufficient uptake of a diagnostic imaging PSMA radiopharmaceutical [51]. The treatment course consists of approximately 7.4 GBq (3.7-9.3 GBq) [^{177}Lu]Lu-PSMA administered over approximately 6 cycles (4 to 6 cycles), approximately 6 weeks apart (6 to 8 weeks) [51]. The administration technique involves a slow intravenous injection over approximately 2 minutes, or an infusion. The organs at risk (OAR) are the salivary glands, kidneys and bone marrow [2]. [^{177}Lu]Lu-PSMA is not currently approved for NHS patients by NICE and therefore is only available for private patients or in a research setting in the UK [52].

Reports of improvement in patient outcomes using [^{177}Lu]Lu-PSMA can be found in the literature, for example in the VISION trial. The VISION trial was an international phase 3 clinical trial to investigate the efficacy and safety of [^{177}Lu]Lu-PSMA-617 [50]. The results showed that there was overall improvement when [^{177}Lu]Lu-PSMA was administered with standard of care compared with standard of care alone; median progression-free survival was 8.7 versus 3.7 months and overall survival was 15.3 months versus 11.3 months, as shown in Figure 10 [50]. The side effects of [^{177}Lu]Lu-PSMA MRT include fatigue, dry mouth, nausea, and dry eyes.

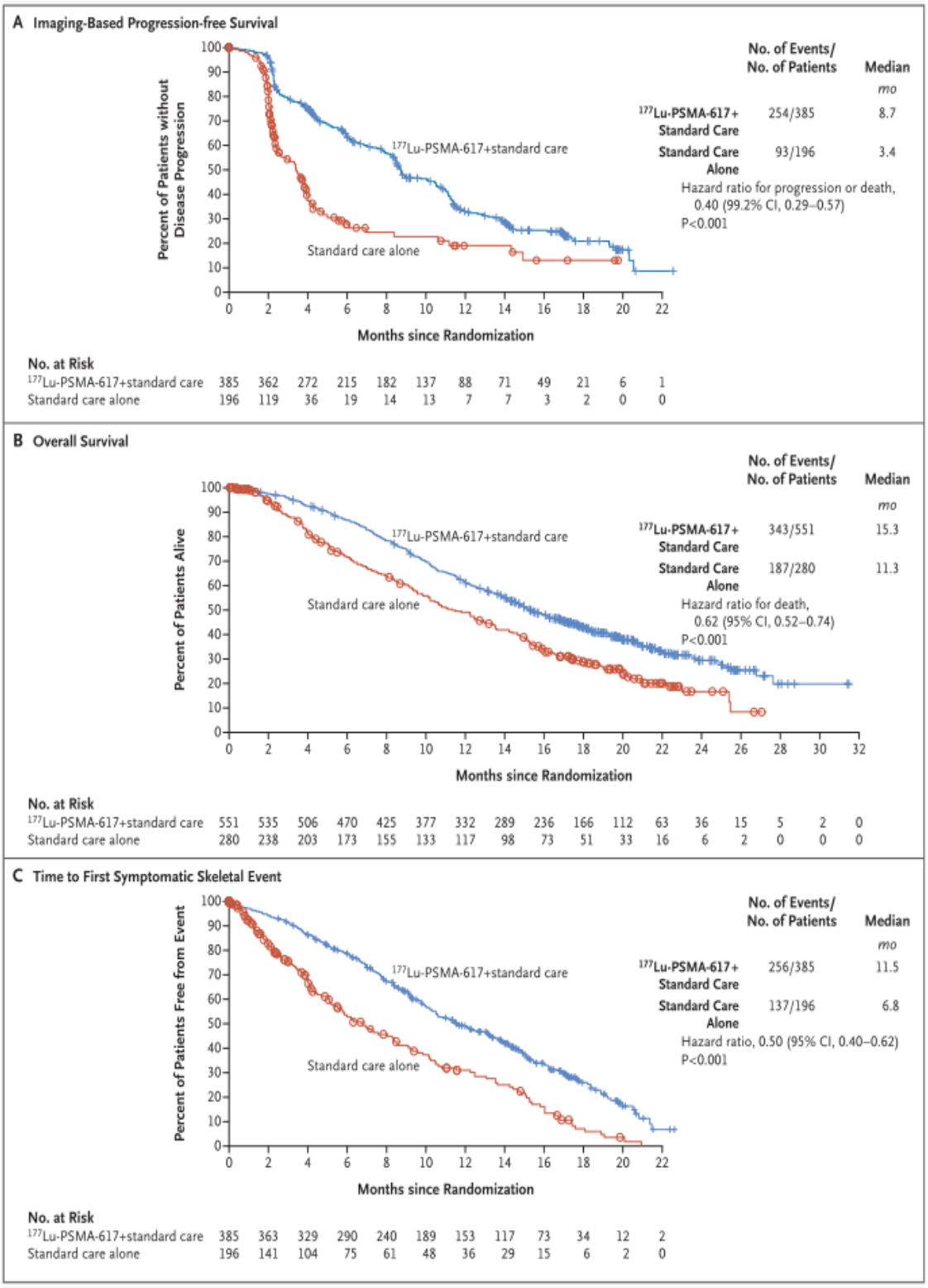

Figure 10: The Kaplan-Meier analysis for imaging-based progression free survival (A), overall survival (B) and time to first symptomatic skeletal event (C) for the VISION clinical trial (taken from Sartor et al 2021) [50]

2.5 Molecular Radiotherapy Dosimetry

Dosimetry involves calculating the radiation dose planned or administered to a patient. It can either be via whole body dosimetry or via organ and tumour specific dosimetry. The European Association of Nuclear Medicine (EANM) guidance for dosimetry specifies the level of dosimetry that should be used for each type of MRT, and states that dosimetry is optional for [^{177}Lu]Lu-DOTA-TATE and dosimetry is advisable for [^{177}Lu]Lu-PSMA [53]. The Ionising Radiation (Medical Exposure) Regulations 2017 (IRMER) requires radiotherapeutic exposures to be individually planned, and the distribution should be appropriately verified to ensure doses to non-target organs are as low as reasonably practicable, and the intended target should achieve the radiotherapeutic purpose of the exposure [54]. The Care Quality Commission (CQC) guidance states that routine therapies can be standardised and do not require individual patient plans, however non-standard molecular radiotherapy requires patient specific dosimetry calculations [55]. In practice this involves acquiring SPECT/CT scans at single or multiple time points following the patient's therapy administration [53]. This is particularly important for [^{177}Lu]Lu-PSMA which is a relatively new procedure and is yet to be widely available in the UK [55].

Radiopharmaceutical uptake and clearance differs between patients and therefore, patient-specific dosimetry of ^{177}Lu-labelled radiopharmaceuticals is important [56]. Dosimetry can be used to plan a patient's treatment in order to calculate the optimal activity to treat the tumours with a prescribed absorbed dose, whilst minimising the side effects caused by ^{177}Lu-labelled radiopharmaceuticals uptake in normal tissue, or OARs [57]. Verification dosimetry can be used to retrospectively calculate the absorbed dose received by the patient following MRT, which is able to assess the success of the therapy and aid with follow up [58], [59]. It is possible to carry out dosimetry through multiple time point dosimetry or single time point dosimetry, however the accuracy and cost-benefit analysis of each method varies [2].

This work will focus on verification dosimetry for ^{177}Lu-labelled radiopharmaceutical MRT, which involves post therapy uptake imaging of the patient. The images acquired can include a whole-body static image and a SPECT/CT image. Ideally, multiple time point imaging would be carried out to assess the full pharmacokinetics of the ^{177}Lu-labelled radiopharmaceuticals distribution for each individual patient [51]. However, this is often not possible, due to limited resources (gamma camera capacity, staffing time and funding) and the practicalities for the patient attending multiple hospital visits. Therefore, it can be more appropriate to use single time point dosimetry, which requires one imaging time point at a set time point after the therapy administration [2]. This approach has reduced accuracy over multiple time point dosimetry and

the most appropriate imaging time point can depend on the patient, therapy type and which organ or tumour is being targeted [2], [60].

A vital step in the dosimetry calculations involves accurate quantitative imaging, to provide minimal errors in the dose calculated [2], [47]. The images are used to outline regions of interest (ROI), which could include OARs and tumour. The counts within the ROI are extracted and converted to activity using a derived sensitivity factor for the gamma camera, isotope and image geometry. The cumulated activity is multiplied by an S-factor (described by the Medical Internal Radiation Dose (MIRD) Committee) to calculate the dose to that region [3], [61]–[64], as given in Equation 3:

$$\dot{\boldsymbol{D}}(\boldsymbol{r_T}, \boldsymbol{t}) = \sum_{\boldsymbol{r_S}} \boldsymbol{A}(\boldsymbol{r_S}, \boldsymbol{t})\, \boldsymbol{S}(\boldsymbol{r_T} \leftarrow \boldsymbol{r_S}, \boldsymbol{t}) \qquad \textbf{Equation 3}$$

Where $\dot{D}(r_T, t)$ is the time-dependent rate at which the absorbed dose is delivered to the target tissue r_T within a patient from a radioactive source distributed uniformly within a source tissue r_S at time t after the administration. $A(r_S,t)$ is the time-dependent activity of the radiopharmaceutical and $S(r_T \leftarrow r_S, t)$ is the radionuclide-specific quantity representing the mean absorbed dose rate to the target tissue at a time following the administration per unit activity in the source tissue [64]. For single time point dosimetry the images are processed as for the multiple time dosimetry, however they are then converted to absorbed dose through general population-based clearance curves [2]. For MRT with multiple cycles, it is possible to create patient-specific clearance curves using multiple time point dosimetry for the first cycle, then use those for single time point dosimetry for the following cycles, as a hybrid approach.

2.6 Quantitative Imaging

Quantitative imaging is a method of converting the counts measured in a gamma camera image to the activity within the object or patient being imaged [1], [65]–[67]. It is a key component to calculate accurate patient doses or to calculate other quantitative values such as standardised uptake value (SUV), which is commonly used in positron emission tomography (PET). To accurately quantify an image there are various corrections that need to be applied to recover the original image, including scatter, reconstruction technique, attenuation, and partial volume effect (PVE) [6]. SC can be applied to each gamma camera image created and is described in section 2.6.1. SPECT images need to be reconstructed from the individual projection images, which is described in section 2.6.2. The SPECT images should be corrected for the intensity loss due to attenuation that is associated with each photon being detected, which is described in section 2.6.3. Section 2.6.4 describes the partial volume effect and how it can be corrected. Dead

time is a characteristic of gamma camera detectors which needs to be considered and is described in section 2.6.5. In addition, each of the measurements have an associated uncertainty, which needs to be included in the results and is described in section 2.6.6.

2.6.1 Scatter

As described in section 2.2, when a gamma photon interacts with a material it can scatter, change direction and lose energy, as shown in Figure 11 [68]–[71]. Compton scatter will reduce the number of gamma photons that arrive with the full energy of the isotope being imaged and there will be several photons with a lower energy which will reduce the contrast and resolution of the image. Generally, the scattered photons can make up 30-40% of the photons detected in the photopeak energy window [71]. The collimator will help to reduce the number of gamma photons detected which are not travelling perpendicular to the crystal, but it cannot reduce the photons that travel perpendicular to the crystal after being scattered.

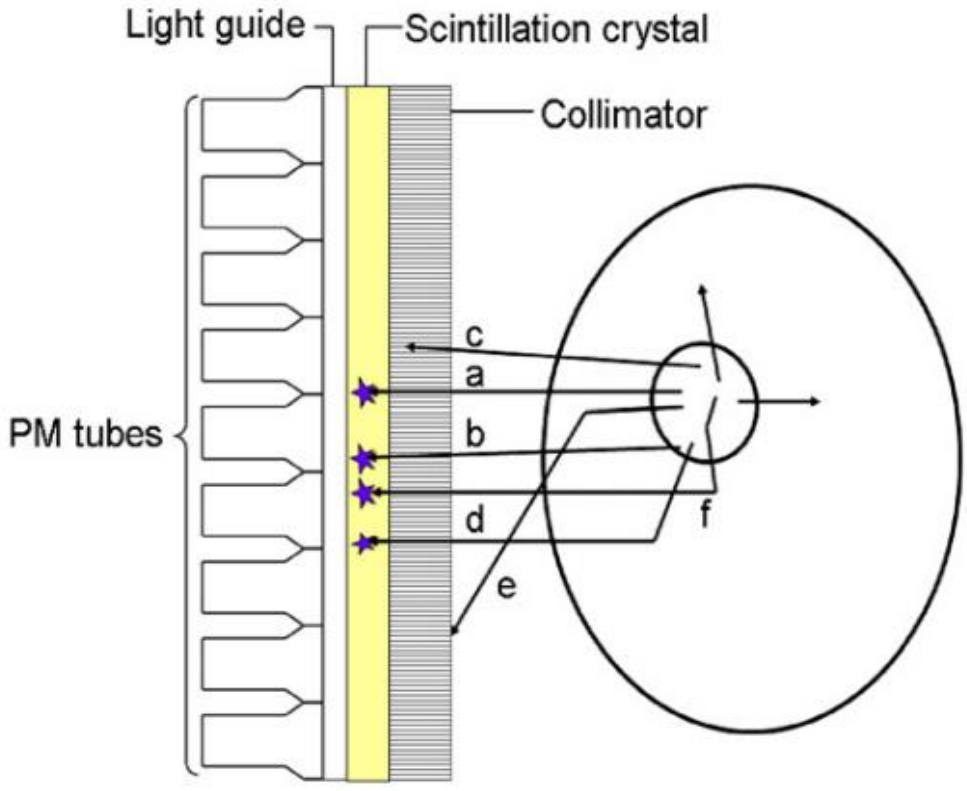

Figure 11: An example of different types of scattered photons that occur from a gamma-emitting source within a patient; (a) shows a photon that travels directly through the collimator hole, (b) goes through the collimator septa but is detected by the gamma camera, (c) is absorbed in the collimator, (d) is scattered once and then is detected, (e) is scattered but not detected and (f) undergoes multiple scatter events before being detected (taken from Hutton et al 2011) [71]

As discussed in section 2.3, the energy spectrum is used to identify the photons with the correct energy that should be included in the image, and it will help reduce the number of scattered photons that effect the image. However, some scattered radiation will fall within this energy window. This is particularly important for ^{177}Lu as there are two main gamma emissions that can be imaged and therefore the energy window can be focussed around 113 keV or 208 keV. The lower photopeak is generally more affected by scattered photons due to the scatter from the higher (208 keV) photopeak falling within the energy window for the lower photopeak. Therefore, SC can be used to estimate how much scatter is in the photopeak energy window used for imaging.

There are different methods of SC, including using a single scatter window below the photopeak (dual energy window (DEW) SC) or using two scatter windows where one is above the photopeak, and one is below the photopeak (triple energy window (TEW) SC) [72]. For DEW SC, the scatter energy window is applied to the photopeak energy window using a scatter fraction [73]. For TEW SC the true counts in the primary energy window (C_{prim}) are calculated using Equation 4 [72]:

$$\boldsymbol{C_{prim} = C_{pm} - \left(\left(\frac{C_l}{W_l} + \frac{C_u}{W_u} \right) \times \frac{W_p}{2} \right)} \qquad \textbf{Equation 4}$$

Where C_{pm} is the counts measured in photopeak, C_l and C_u are the counts in lower and upper scatter windows, w_l and w_u are the window widths of lower and upper scatter window (keV) and w_p is the window width of photopeak (keV), which is visualised in Figure 12. It is not possible to fully account for the lost gamma photons which have been scattered, and the SC applied can be dependent on the amount of scatter within the material used. SC methods are further discussed in the literature review in chapter 3.

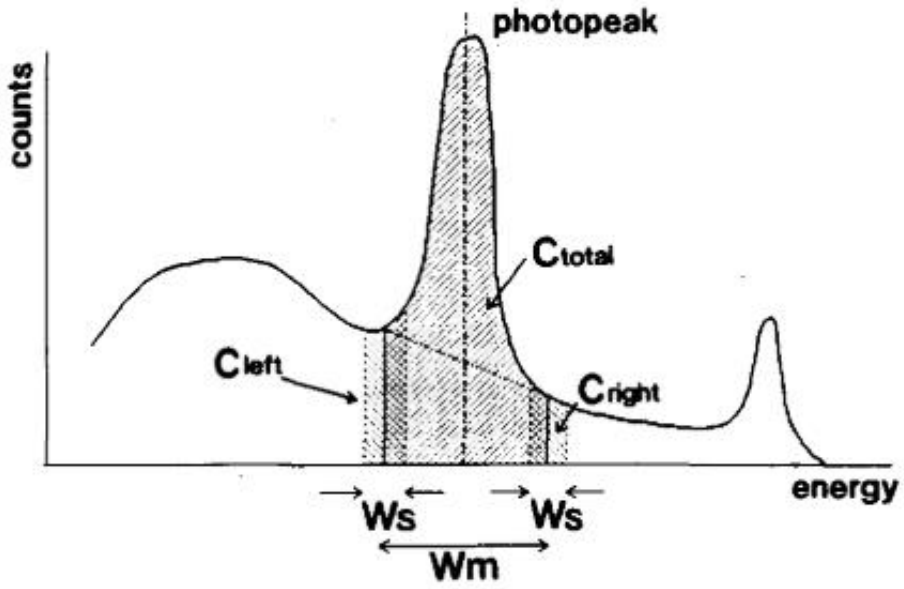

Figure 12: The location and width of the energy windows used for TEW SC. The scatter windows can be referenced as "lower" or "left" and as "upper" or "right". The window widths may be the same or different for each scatter window. The window width of the photopeak is referenced as Wm. (Taken from Ogawa et al 1991) [72]

For a CZT gamma camera, the gamma photons detected in the low energy scatter window will be a combination of the scattered gamma photons (Compton scatter) and the gamma photons that are released as part of the hole trapping in the CZT material (as described in section 2.3.2) [9], [74]. Therefore, this can cause issues when applying a conventional method of SC. The photopeak is generally narrower for a CZT gamma camera compared to a NaI gamma camera (as seen by comparing Figure 3 and Figure 5), due to the improvement in energy resolution (as highlighted in Table 2), therefore it may be possible to use a narrower energy window to reduce the number of Compton-scattered photons detected, however this may significantly compromise the detection efficiency as over 60% of interactions may be subject to hole-tailing effects [9], [74]. SC techniques are further discussed in chapter 3.

2.6.2 Reconstruction

There are various methods to reconstruct a SPECT image, however the most commonly used method is iterative reconstruction, and is recommended for quantitative SPECT imaging [65]. The set of projections from the SPECT is used to create a sinogram, which is visualised for a point source in Figure 13. A sinogram is a two-dimensional representation of the count profiles (*r*) for projections at a range of angles (ϕ) around the object [6].

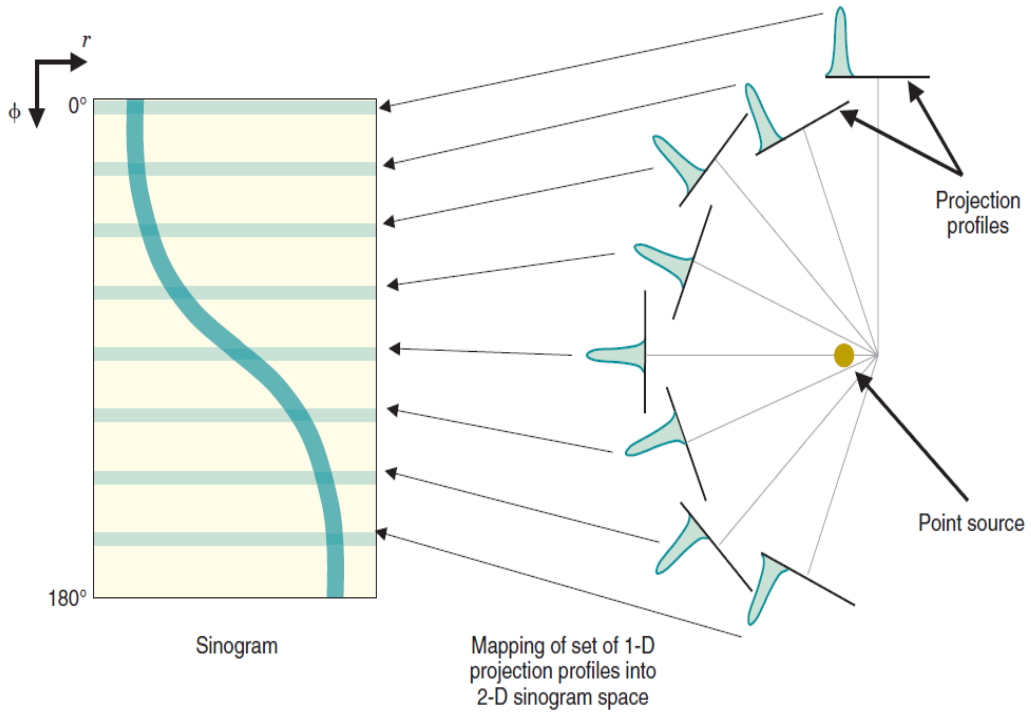

Figure 13: A two-dimensional representation of the intensity profile at each projection angle, to produce a sinogram for a point source in air (taken from Cherry et al 2012) [6]

Iterative reconstruction is the process of using the sinogram to forward project to an estimated image, the estimated image is iteratively updated, where each new predicted sinogram is compared to the true sinogram acquired, as displayed in Figure 14. The more iterations completed the closer the reconstructed image is to the true image of the object. However, increasing the iterations too high can cause increased image noise. The number of iterations must be optimised to identify the ideal reconstruction for the type of object being imaged, however this will be different depending on various factors, such as size of the object, the amount of scatter material around the radioactive object and whether the image will be assessed qualitatively or quantitatively. The algorithm for iterative reconstruction can include some prior information, such as SC, attenuation correction or system geometry, which will increase the computation time for the reconstruction [6].

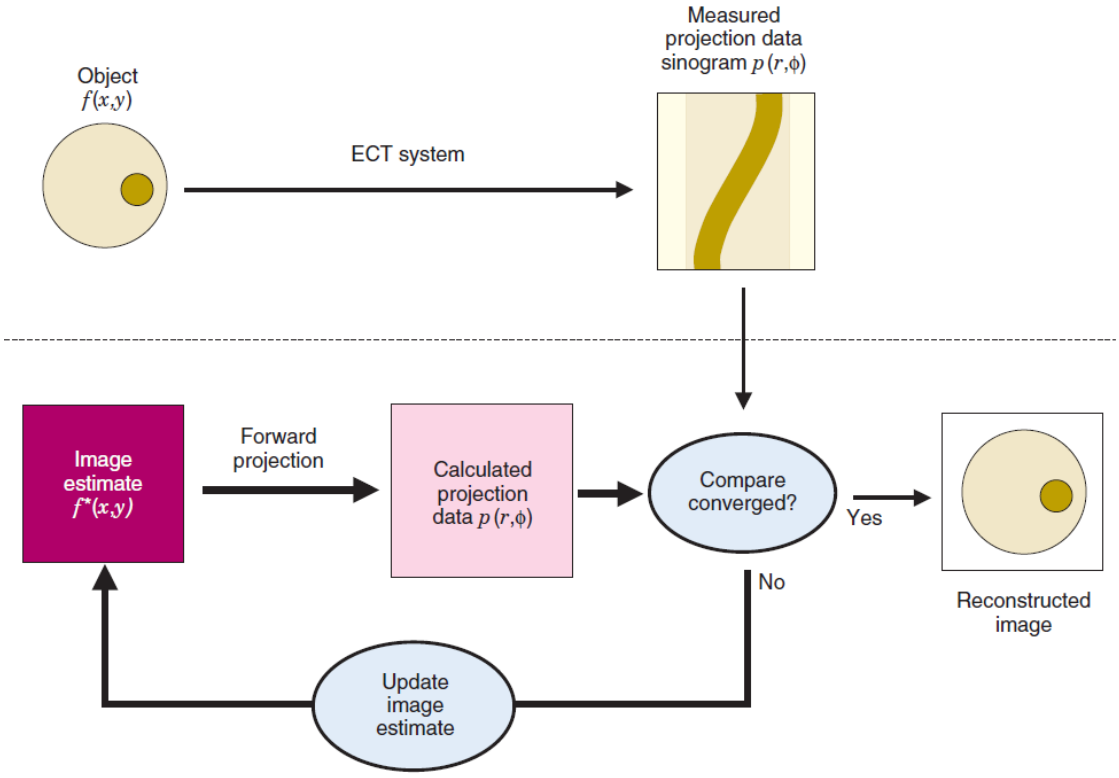

Figure 14: An illustration of the iterative reconstruction process. The initial image estimate is used to create an estimate of the sinogram, which is compared to the true sinogram of the object being imaged. The estimated image and resulting sinogram are updated until the estimated sinogram has converged with the true sinogram. ECT is the emission computed tomography. (Taken from Cherry et al) [6]

Optimisation of reconstruction parameters should be carried out using phantom measurements, ensuring that there is not an excessive level of noise and artefacts are not introduced, for example Gibbs artefacts creates a reduction in counts at higher activity levels. An example of this optimisation process using a National Electrical Manufacturers Association (NEMA) International Electrotechnical Commission (IEC) image quality phantom is displayed in Figure 15 [65]. A common reconstruction technique is maximum-likelihood expectation-maximisation (MLEM) which incorporates Poisson statistics to estimate the most likely source distribution that could have created the observed sinogram [6], [75]. It is possible to group the iterations (it) into subsets (ss) to speed up the reconstruction process in a method called ordered subset expectation maximisation (OSEM) [75], [76]. To optimise SPECT image reconstruction the number of iterations and subsets must be altered until the optimal reconstruction is determined.

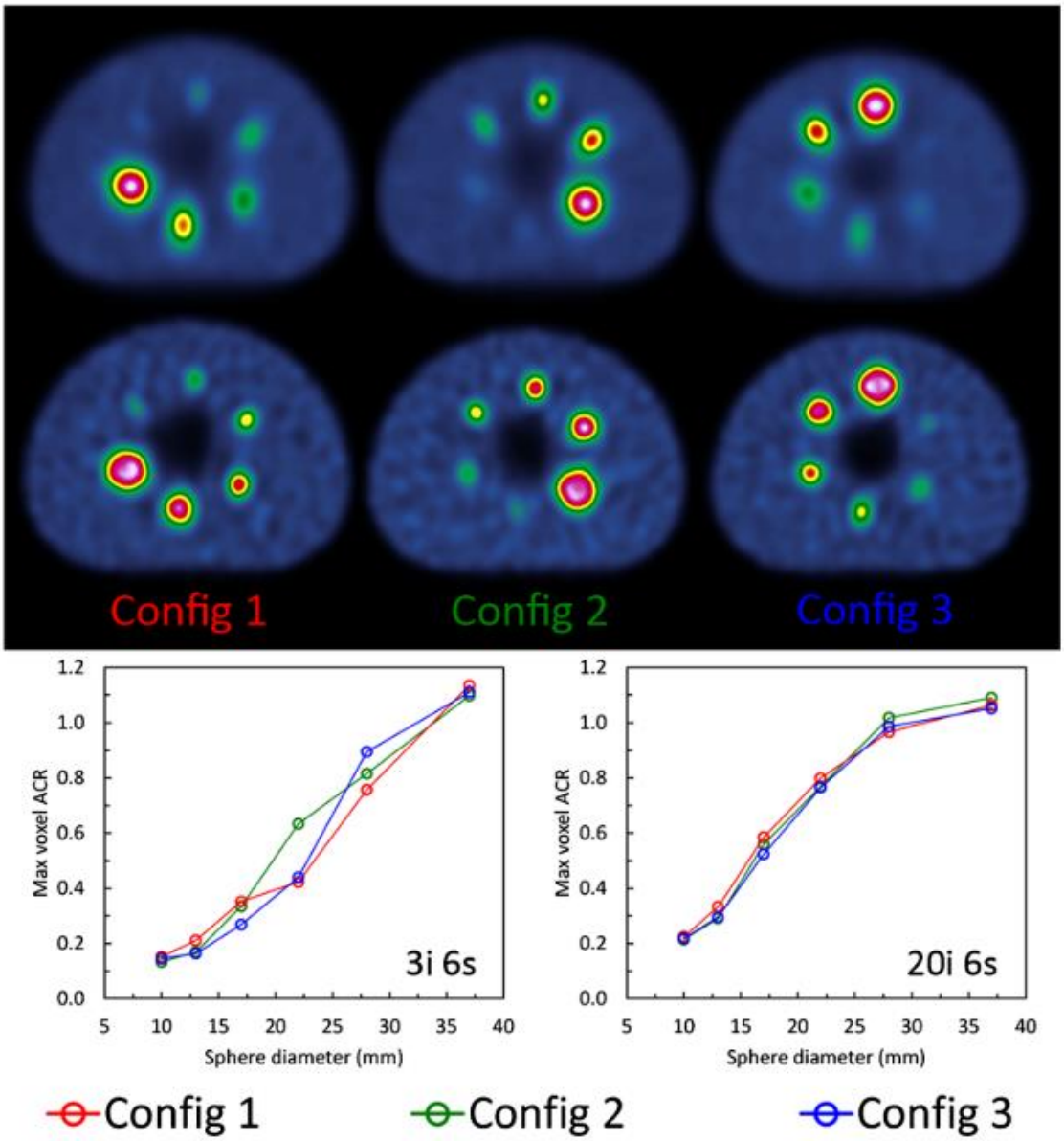

Figure 15: An example of a NEMA IEC image quality phantom filled with ^{99m}Tc at 10:1 contrast in three different configurations, reconstructed with 3 iterations and 6 subsets (top row) and 20 iterations and 6 subsets (bottom row of images), with associated activity recovery curves displayed for each configuration and reconstruction (taken from Dickson et al 2022) [65]

A filter can then be applied to smooth the image, however this may not be accurate for quantitative purposes [65]. A filter can be useful for qualitative review of clinical images and therefore the use and type of filter can be dependent on the preferences of the image reviewer and will also require optimisation.

Resolution recovery (RR) or resolution modelling can be used as part of the reconstruction algorithm. RR introduces a depth dependent collimator response model in the projection

operation of the reconstruction algorithm to compensate for the limited spatial resolution due to the collimator and detector [6], [65], [77]. The technique can include various corrections, including the detector intrinsic response, collimator geometric response, septal penetration and scatter from the collimator [77].

2.6.3 Attenuation

Gamma photons emitted through radioactive decay will pass through the patient and interact with material inside the patient, before reaching the gamma camera, as described in section 2.2 [5]. If a gamma photon has further to travel through an object before reaching the gamma camera, then it will experience greater attenuation and less gamma photons will reach the gamma camera, which will make the signal appear less intense than gamma photons that travel a shorter distance, as displayed in Figure 16 [6], [78].

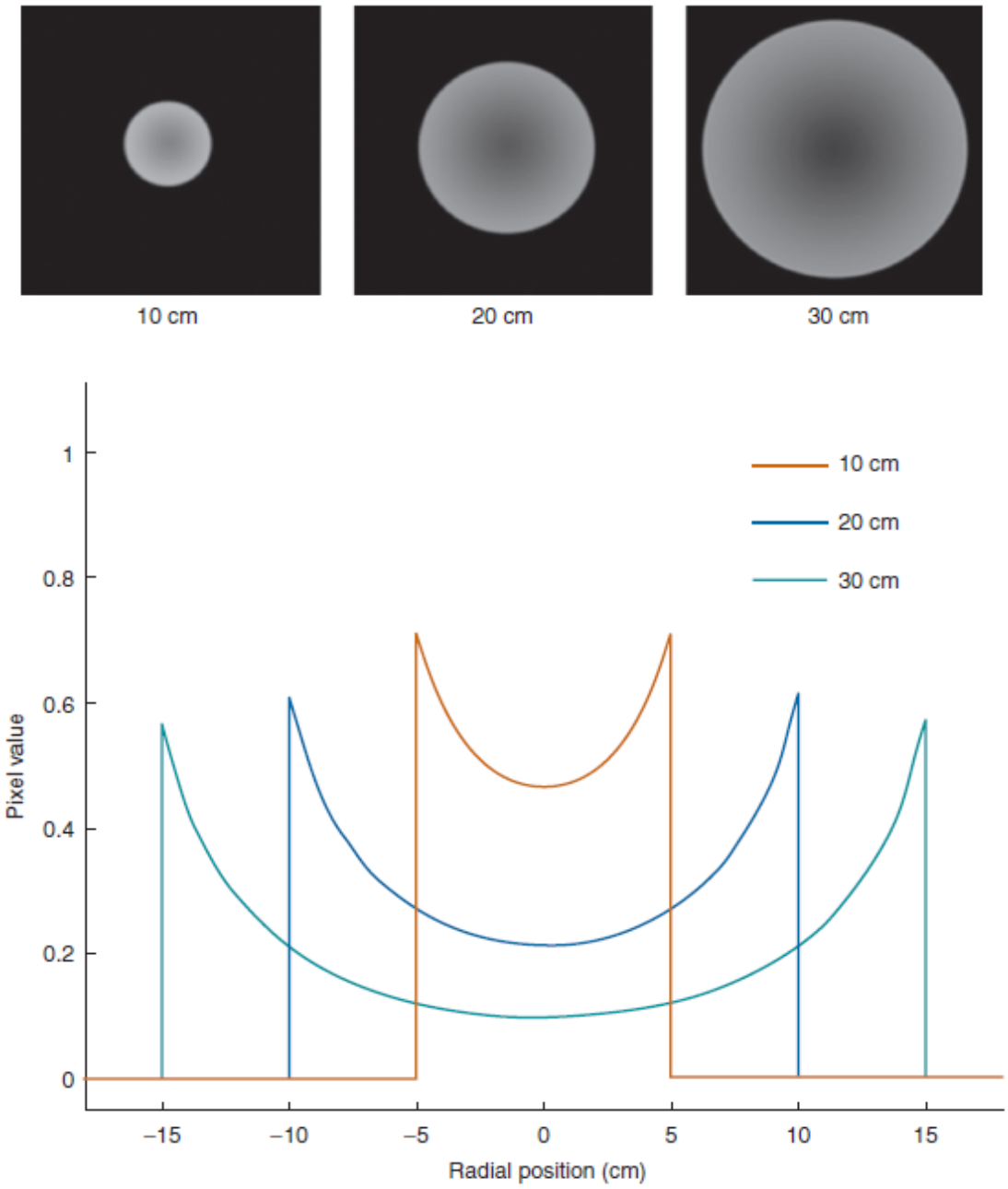

Figure 16: An example of the effect of attenuation on the images created and the count profiles within the image for ^{99m}Tc uniformly filled cylinders of different sizes (taken from Cherry et al 2012) [6]

Attenuation correction (AC) can be applied using the CT image, which is essentially a map of the densities within the object [65]. The CT image data is dependent on the beam energy and the density of tissue, and each pixel is given a Hounsfield unit (HU), which is described by Equation 5 [5].

$$HU = 1000 \times \left(\frac{\mu(E_{CT}) - \mu_w(E_{CT})}{\mu_w(E_{CT})}\right) \qquad \textbf{Equation 5}$$

Where μ is the linear attenuation coefficient, μ_w is the linear attenuation coefficient of water and E_{CT} is the effective energy of the CT [5]. The CT image can be used for AC by converting the HU into linear attenuation coefficients for a particular energy [79]. This technique is often referred to as CT attenuation correction (CTAC). An attenuation map is created from the CT image and applied to the SPECT image to correct for the attenuation differences in the image, and a different attenuation map is required for each energy. However, it is important to note that CT images can include artefacts, which may affect the CTAC that is applied to the SPECT image, which in turn causes artefacts in the reconstructed SPECT image [65].

2.6.4 Partial Volume Effect

The partial volume effect (PVE) is where the counts within a small object are not fully resolved, due to the limited spatial resolution of a gamma camera, as displayed in Figure 17 for radioactive objects imaged in a non-radioactive background as an ideal case [6], [65], [80]. The total counts within the object are distributed over a larger area and therefore the maximum counts within the centre of a small object may not reach the true level. However, the sum of all the counts that are associated with the object will reflect the activity within the object [6]. When applying this to clinical imaging it can lead to misdiagnosis or under reporting of small lesions, especially if the small object is adjacent to another larger object.

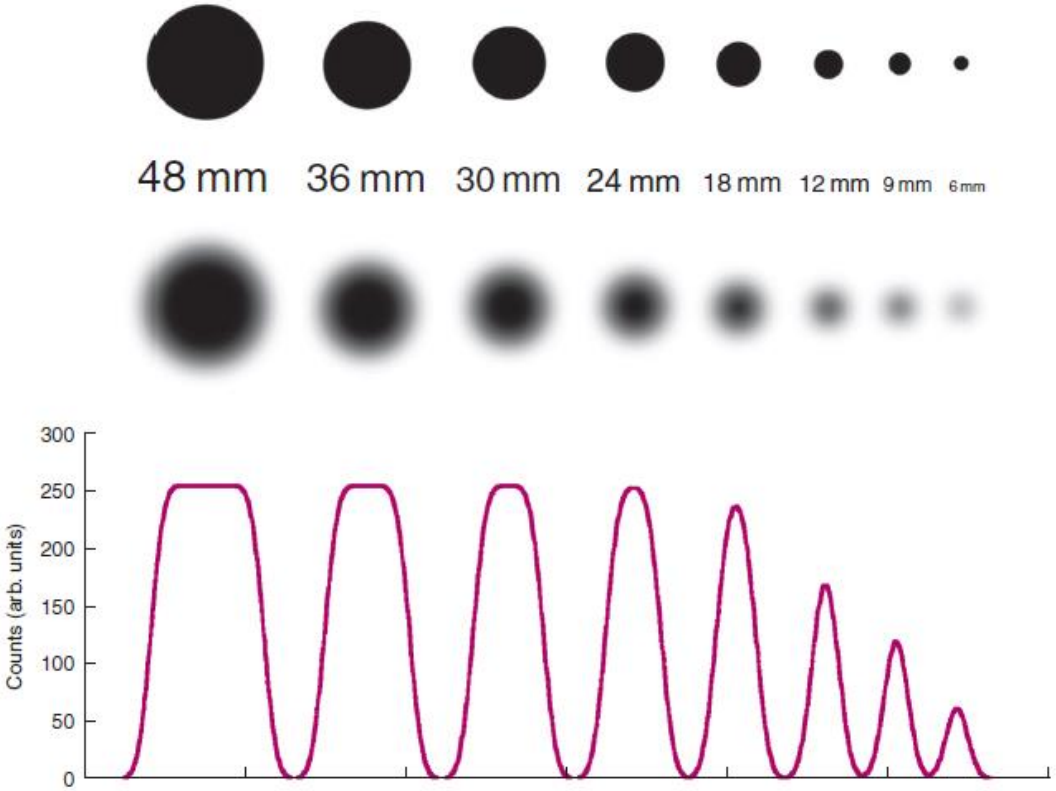

Figure 17: An example of partial volume effect for a radioactive object imaged in a non-radioactive background. The top row of different size cylinders illustrates the true activity within each object. The middle row displays the counts imaged in each cylinder for a SPECT system with a spatial resolution of 12 mm FWHM. The bottom row shows the count profiles for each cylinder. (Taken from Cherry et al 2012) [6]

It is possible to correct for PVE using partial volume correction (PVC), which can be applied post reconstruction. Creating a PVC involves imaging a range of different size spheres with a known activity and creating an activity recovery curve [62]. The recovery curve is created by calculating the recovery coefficient for each object, as described in Equation 6 [81]:

$$R = \frac{C}{C_{total}} \qquad \textbf{Equation 6}$$

Where R is the recovery coefficient, C is the observed count rate measured within a volume of interest (VOI) equal to the volume of the object and C_{total} is the total count rate from the phantom. The recovery curve can then be used to identify what recovery coefficient is required for a particular sized object. PVC is generally not commercially available and therefore there needs to be a department-based method derived, however any software used for clinical applications need to align with the appropriate medical device legislation [82]. It is possible to use RR software, which is commercially available, which can partially compensate for limited spatial resolution, however it is unlikely to fully recover the activity for small objects [65]. Often

the PVC is applied assuming there is a non-radioactive background, however, it is also important to consider the level of the background activity surrounding the VOI as this will cause PVE to change and the counts from the background region will be detected within the target VOI.

2.6.5 Dead time

Dead time occurs when the gamma camera becomes saturated, and it cannot record all the photons that are incident on the detector, therefore leading to a reduced measured count rate [6]. There are two types of dead time that can occur in detection systems: paralysable and non-paralysable, as displayed in Figure 18. For non-paralysable systems the loss of counts reduces until it plateaus with increasing input counts. For paralysable systems the loss of counts results in a saturation point, at which increasing the count rate reduces the observed count rate. Gamma cameras have paralysable dead time which therefore requires modelling and correcting for if the gamma camera will be used for measuring high count rates.

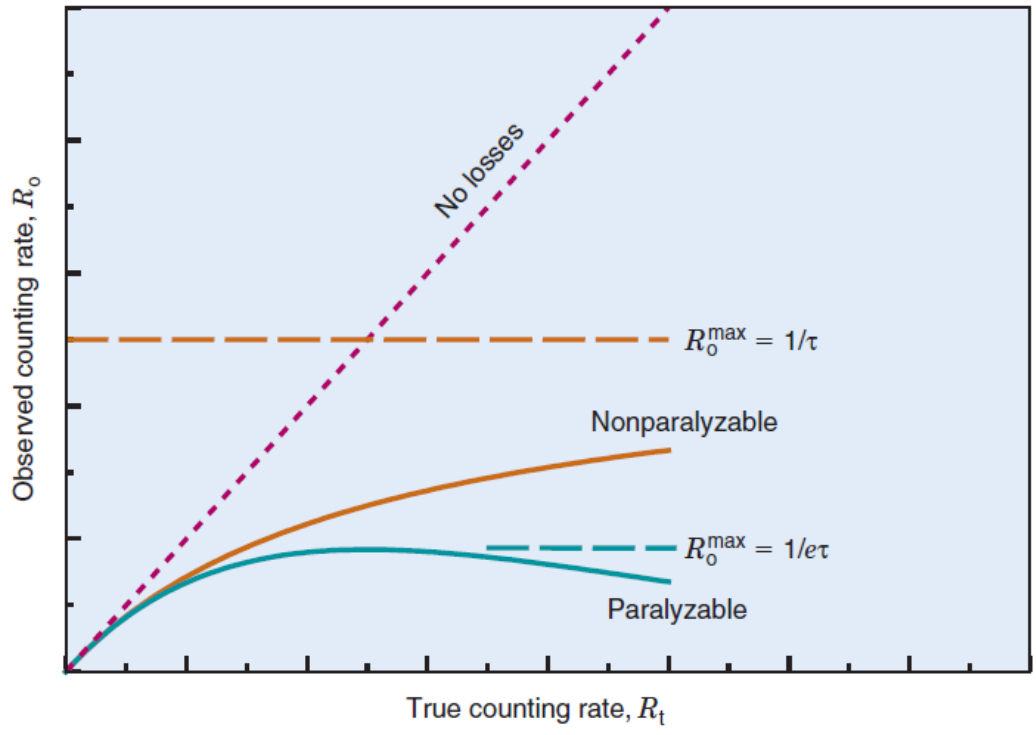

Figure 18: The observed count rate (R_O) against the true count rate (R_t) for systems with paralysable and non-paralysable dead time (τ) (taken from Cherry et al) [6]

Dead time is a particular issue when gamma camera imaging takes place soon after a therapy has been administered, which can be an important step in capturing the full time-activity curve required for MRT dosimetry. For ^{177}Lu imaging the dead time effects are small as there is a low

yield of gamma photons emitted [3]. This is discussed within chapter 3, however it has not been investigated within this work.

2.6.6 Uncertainty Analysis

All measurements have a level of uncertainty that should be considered in the reported results. For calculations which involve multiple measurements with associated uncertainties, the law of propagation of uncertainty must be used [81]. The EANM practical guidance on uncertainty analysis for MRT absorbed dose calculations [81] summarises the approach to use for quantitative imaging. This includes uncertainty for the volume from the VOI, count rate, activity, recovery coefficient and calibration factor.

There are a few factors which effect the VOI uncertainty for the volume definition. For every VOI that is drawn there is an intra- and inter-operator variability which needs to be accounted for. Ideally the VOI delineation should be repeated by various operators, or there should be a standard approach. When defining VOIs for phantom work it is possible to use a consistent approach to minimise variation. Another factor is the effect the digitised images have on the VOI definition and therefore the VOI is affected by the voxel size used, therefore the uncertainty is given by Equation 7 [81]:

$$\boldsymbol{u^2}_{\boldsymbol{vox}}(\boldsymbol{d}) = \boldsymbol{u^2}(\boldsymbol{P_i} - \boldsymbol{P_j}) = \frac{\boldsymbol{a^2}}{\boldsymbol{6}} \qquad \textbf{Equation 7}$$

Where d is the diameter, $P_{i,j}$ are points a distance is measured between and a is the width of one voxel. Often the VOIs can be defined using the CT images and copied to the registered SPECT dataset and therefore the SPECT voxel size will need to be used in Equation 7. Another consideration is the spatial resolution of the imaging system as the voxel size can be less than the spatial resolution and therefore only using Equation 7 would lead to an underestimate of uncertainty. The uncertainty in the spatial resolution is the standard deviation of the Gaussian point spread function with the FWHM equal to the spatial resolution, therefore the total uncertainty in the volume is described by the voxel uncertainty and the resolution uncertainty, as in Equation 8 [81]:

$$\boldsymbol{u^2}(\boldsymbol{d}) = \boldsymbol{u^2_{vox}}(\boldsymbol{d}) + \boldsymbol{u^2_{res}}(\boldsymbol{d}) = \frac{\boldsymbol{a^2}}{\boldsymbol{6}} + \frac{(\boldsymbol{FWHM})^2}{\boldsymbol{4ln2}} \qquad \textbf{Equation 8}$$

However, in practice the diameter is not normally measured, but the volume of the VOI is reported. The standard uncertainty in the volume ($u(v)$) can be calculated from the standard uncertainty in the diameter ($u(d)$). The volume is calculated as the mean diameter cubed,

multiplied by a constant, and therefore the uncertainty in volume can be defined by Equation 9 [81]:

$$\left[\frac{u(v)}{v}\right]^2 = \left[3\frac{u(d)}{d}\right]^2 = \left[3\frac{u_{vox}(d)}{d}\right]^2 + \left[3\frac{u_{res}(d)}{d}\right]^2 \quad \textbf{Equation 9}$$

Where *v* is the volume. The count rate measured from the VOI depends on the VOI delineation and therefore can be described as function of volume. The count rate density can normally be assumed to be uniformly distributed across the volume. The count rate uncertainty measured in the VOI can be calculated using Equation 10 [81]:

$$\frac{u(C)}{C} = \frac{\varphi}{2R}\frac{u(v)}{v} \quad \textbf{Equation 10}$$

Where *C* is the count rate, *R* is the recovery coefficient and *φ* is given by Equation 11 [81]:

$$\varphi = erf\left(\frac{2r}{\sigma\sqrt{2}}\right) - \frac{2\sigma}{r\sqrt{2\pi}}\left[1 - e^{-\left(\frac{2r^2}{\sigma^2}\right)}\right] \quad \textbf{Equation 11}$$

Where *r* is the radius of the source with a uniformly distributed spherical count rate and *σ* is the standard deviation of the measured Gaussian point spread function. The recovery coefficient uncertainty can be calculated through the law of propagation of uncertainty and is give in Equation 12:

$$\left[\frac{u(R)}{R}\right]^2 = \left[\frac{u(C)}{C}\right]^2 + \left[\frac{u(A)}{A}\right]^2 + \left[\frac{u(S)}{S}\right]^2 \quad \textbf{Equation 12}$$

Where *A* is the measured activity within the object and *S* is the sensitivity factor. The same theory can be applied to calculate the uncertainty for the sensitivity factor, as shown in Equation 13:

$$\left[\frac{u(S)}{S}\right]^2 = \left[\frac{u(C)}{C}\right]^2 + \left[\frac{u(A)}{A}\right]^2 + \left[\frac{u(t)}{t}\right]^2 \quad \textbf{Equation 13}$$

Where *t* is the time.

2.7 Monte Carlo Simulations

Monte Carlo (MC) simulations are a computer model used to simulate a random variable, in this case radioactive decay [83]. It uses repeated random events to predict an outcome. In this context, the MC simulation will simulate radioactive decay, how the radiation interacts with a material and how it will be detected by an imaging system [84], [85]. MC simulations are used

in nuclear medicine to assist in the design of a new imaging system, reconstruction algorithm or SC technique [83], [86], [87]. It can be used to resolve the ground truth expected from an imaging event and therefore it can help to identify the corrections required for SPECT/CT imaging. Most MC simulation toolkits are developed for high energy physics and have been extrapolated for the use of medical applications, which therefore gives them some limitations [86].

GATE (Geant4 application for tomographic emission) is an open source collaboration built on the Geant4 toolkit (based on C++ language), which has been used for more than 15 years for MC simulations of nuclear-based imaging systems [83]–[85]. GATE uses libraries from Geant4 to provide a modular scripted MC simulation toolkit for nuclear medicine and it can be used to describe time-dependent variables such as detector heads moving, or source distribution, allowing it to simulate time-activity curves [83], [86], [88]. It contains a database of validated physics models, geometry descriptions and visualisation tools. The steps of setting up a MC simulation in GATE are; defining the scanner geometry, defining the phantom (or object being imaged) geometry, setting up the physics processes, initialising the simulation, setting up the digitiser, defining the radioactive source, specifying the data output format and finally starting the simulation [85], [86], [89]–[91].

The user can create a MC model of an imaging system by building the layers of the detector, such as the collimator, scintillation crystal and PMTs, or CZT detector, and the shielding surrounding the gamma camera detector. The detector must be defined as a sensitive detector using an “attachCrystalSD” command, so the physics interactions can be tracked within the crystal. Each object is defined by the user in size and space, through a translation tool, and which other objects it is associated with. An example of a visualisation of a gamma camera using GATE is given in Figure 19 [92]. The material of each component is defined using a materials database, which describes a material by its density, constituent elements and abundance [91]. To aid visualisation of the MC simulation a colour can be allocated to each component. The phantom needs to be defined, which can either be a simple shape such as a cylinder (as seen in Figure 19 [92]) or a more complex geometry. The phantom must be defined as a sensitive phantom by using a similar command as for the detector (“attachPhantomSD”).

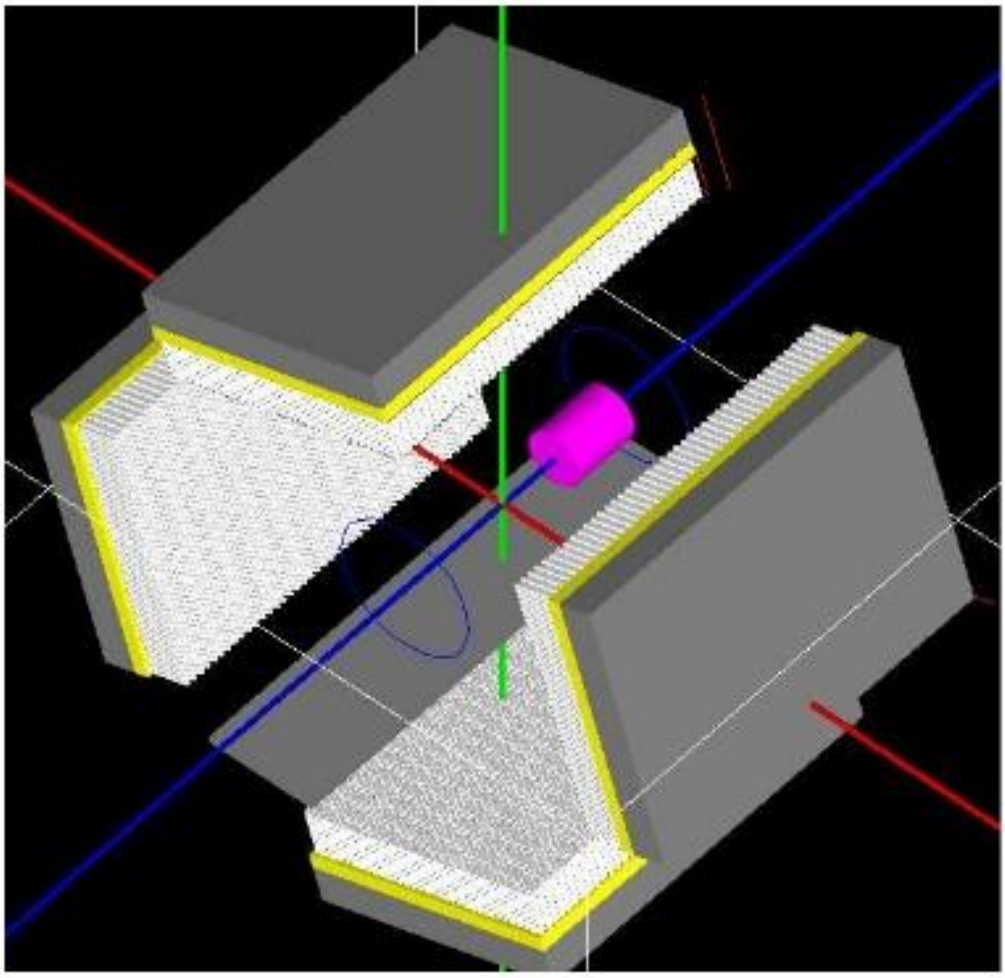

Figure 19: An example of a four-headed gamma camera system modelled in GATE, showing the crystal (yellow), collimator (white), phantom (pink) and coordinate axes (red, blue and green lines) (taken from Open GATE website) [92]

The physics processes are a key part of GATE and can be defined once the detector and phantom geometries are described. The physics models are from Geant4 and the specific physics model should be chosen based on the type of simulation being carried out and the radiation type being used [91]. There is a range of options in the GATE database that can be selected by the user. The physics processes can be chosen and updated by the user to include all physics processes required for the simulation. For example, a physics process is to model the electromagnetic interactions of particles with matter (as described in section 2.2), which describes the interaction length of a process [85], [91]. The next step is the initialisation, which triggers the calculation of the geometry and physics.

The next step in the MC simulation development is setting up the digitiser. In GATE there are specific vocabulary that are used to describe the output from the MC simulation. When an individual particle interacts within a detector element they are defined as *hits* and they contain

the information about the interaction process type, position, energy deposited, time, etc [84]. The *hits* within the same readout volume are called *singles*. The digitiser is set to build physical observables from the hits and to model the tracks of the radiation used [91]. This step also involves setting the energy resolution of the system by adding a blurring to a set energy level.

The source is set up by defining the type of radiation that it should contain, for example gamma and beta radiation [85]. A source is created as a volume where the radiation is emitted from. The user will define the volume geometry and the activity, type of radiation, half-life, direction of emission and energy [91]. The geometry can be a simple shape or more complex, and it is possible to create a phantom and source geometry from a CT scan, by converting it to a voxelised phantom and source.

The final steps involve setting the type of output that the MC simulation should produce, for example a ROOT file [93], and starting the acquisition. The MC simulation is defined by a length of total time and the length of time slices that will be created during the total acquisition [91]. The type of random generator is selected, and three different types are available in GATE. ROOT is an object-oriented data analysis framework which can analyse a large amount of data [83], [93]. The ROOT file stores the hits and singles within the simulation, which includes a range of information about each event, such as the energy, the processes its undergone and its location within the image. The digitiser can be customised to include all required information. The ROOT file can be analysed using macros (written in C++) to create an image and an energy spectrum, resembling a gamma camera, which can therefore be compared to what is produced by a gamma camera to help validate the MC simulation [83], [93], [94].

3 LITERATURE REVIEW

This chapter reviews the literature for quantitative imaging on a NaI gamma camera, including scatter correction (in section 3.1) and for ^{177}Lu (in section 3.2), and on a CZT gamma camera (in section 3.3). In addition, the literature for MC simulations is reviewed in section 3.4.

3.1 Scatter Correction Techniques

One particular area of focus for this literature review is on different SC techniques available, which has been summarised in a review by Hutton et al [71]. There are various different methods for SC, which vary in accuracy, complexity and computational time. Generally, only very basic SC methods are used routinely in a clinical environment, which may be due to the practical implementation of the techniques, or because there are limited clinical trials or evaluations to investigate how useful more complex SC techniques are in the clinical setting compared to the simple techniques [71], [95]. The main basic methods used clinically are discussed in section 2.6.1. Generally SC techniques include incorporating the direct measurement of scatter, multiple energy windows, spectral analysis and MC scatter estimation [71]. An example of another SC technique is called effective source scatter estimation (ESSE), which efficiently incorporates a non-stationary scatter distribution into the reconstruction, where the attenuation from each point of Compton interaction to the detector is included in the model [71], [96]. ESSE is based on the probability of a photon from one position being scattered and detected at another location, the photon will reach the detector without being absorbed and the scattered photon will reach the detector in the defined energy window [96].

For ^{177}Lu, SC is more challenging as there are spill over effects from the scattered photons from the higher energy gamma into the lower energy photopeak window, which can be difficult to estimate. For multiple-energy isotopes similar SC techniques can be used as for multiple-isotope imaging, however it is not possible to isolate one of the energy peaks to estimate the down scatter contribution [71]. It is possible to use multiple energy windows to estimate the scatter in each [97]–[99]. Simultaneous equations can be used to describe the different energy windows which can derive scatter corrected projections for the photopeak using artificial neural networks [100], spectral analysis [101] or maximum likelihood estimation [71], [102]. MC methods can be useful where the effects of down scatter, detector and collimator effects can be modelled [103]. It may also be necessary to model the septal penetration artefact for high energy photons [71], [104], [105], as visualised in Figure 7.

3.2 Quantitative Imaging of Lutetium-177 on a Scintillation Gamma Camera

Accuracy of quantitative SPECT imaging is critical if absorbed doses to organs or tumours need to be calculated following ^{177}Lu-labelled radiopharmaceuticals administration [1], [106], however it cannot be currently used reliably as a quantitative tool, due to technical challenges [4]. These technical challenges are described in chapter 2 and include attenuation, scatter and PVE, which all require corrections to compensate. However, there is no set standard of how to account for these technical challenges. There is guidance from EANM, International Atomic Energy Agency (IAEA) and MIRD [3], [65], [107] on quantitative SPECT, however they indicate different methods, therefore consistency between centres does not exist causing problems with reliable dosimetry [4], [108], [109]. Gamma camera calibration factors depend on the reference condition used [32], [108]. Current methods for quantitative SPECT include; TEW or DEW SC, iterative reconstruction, AC, RR, PVC and dead time [1], [4], [62], [65], [67].

The literature has been reviewed to investigate different methods of calculating calibration factors, their accuracy and gamma camera dead time, for phantoms and in patients. The methods used include the phantom or patient details, energy windows used, SC technique used (including no SC (NSC)), reconstruction techniques, use of AC, RR and a filter and the method for defining the ROI, which is summarised in Table 4 [1], [4], [117]–[126], [56], [127], [128], [110]–[116]. Not all details were included in each reference and therefore the summary includes what was available for review.

Table 4: Summary of methods used within literature to calculate calibration factors, accuracies and dead time for ^{177}Lu on NaI gamma cameras

Study	Phantom and/or Patient Details	Energy Windows	Scatter Correction Method(s)	Reconstruction Technique and Attenuation Correction	ROI Selection Method(s)
Arienzo et al 2016 [32]	Point source in air, 16 ml sphere in air and water and a 20 cm cylinder	113 keV ± 15% 208 keV ± 20% 98.8 keV ± 10% 127.1 keV ± 10% 176.8 keV ± 10% 239.2 keV ± 10%	TEW	MLEM (20 it) with Chang AC	Size of object plus 3 cm
Bailey et al 2015 [111]	In vivo: Patient whole body and SPECT imaging using calibration flask	208 keV ± 10%	SPECT: CT used for transmission-dependent scatter	Whole body: AC using Co-57 flood transmission	Generous ROI

				SPECT: OSEM, CTAC for SPECT	
Beauregard et al 2011 [112]	Ten sources of <1 ml ^{177}Lu in 1.5 ml Eppendorf tubes. 1 to 4 sources were placed in various combinations in the camera FOV in air and in scatter (e.g., polystyrene icebox with 8 one-litre saline bags)	208 keV ± 10% 176.8 keV ± 5% 110.9 keV ± 50% 37.0 keV ± 50%	DEW	OSEM (4 it 8 ss) with AC and RR	Percentage threshold of maximum on SPECT (1-40%)
Celler et al 2014 [113]	Water filled bottle (70 ml) and two point sources	113 keV ± 10% 60.5 keV ± 67% 139 keV ± 10% 322 keV ± 50%	TEW	OSEM with CTAC and RR	Various sizes
De Nijs et al 2014 [56]	NEMA 2007/IEC 2008 image quality phantom (radioactive spheres and background)	113 keV ± 10% 208 keV ± 10% 182.6 keV ± 2.5%	NSC, TEW, DEW, ESSE	OSEM (3 it 8 ss, 3 it 16 ss, 4 it 16 ss, 8 it 16 ss) with RR	Not specified, but appear generous

		234.2 keV ± 2% 185.6 keV ± 1% 231.2 keV ± 1% 96.7 keV ± 5% 129.3 keV ± 4% 99.7 keV ± 2% 126.3 keV ± 1.5% 166.8 keV ± 12% 90.4 keV ± 12.5% 229.2 keV ± 9% 135.6 keV ± 8% 198 keV ± 5%			

Desy et al 2022 [114]	NEMA 2012/IEC 2008 image quality phantom	208 keV ± 10% Lower scatter 10% width Upper scatter 10% width Three additional to cover 18 – 680 keV	TEW	OSEM (4 it 8 ss) with CTAC and RR	CT-based VOIs drawn manually and expanded by 0.5 cm or 1 cm
Frezza et al 2020 [115]	Capillary tubes (1.1 by 7.5 mm) in air or water and Jaszczak phantom.	208 keV ± 10% 176.5 keV ± 6% 239.5 keV ± 4% 465 keV ± 47% 111 keV ± 50% 37 keV ± 50%	DEW & TEW	OSEM (4 it 8 ss) with CTAC and RR	Geometry and threshold: For Jaszczak ROI was geometry plus 2 cm, for capillaries ROI was 3.8 cm circles and threshold using 1% maximum
He et al 2012 [116]	Torso phantom (lungs, liver, background, and two spherical	113 keV ± 10%	*Not specified*	Three different reconstructions	Manual ROI using CT

	compartments with inner diameters of 30 mm)	208 keV ± 10%			
Marin et al 2017 [117]	NEMA 2012/IEC 2008 image quality phantom	208 keV ± 10% 177 keV ± 6%	DEW	OSEM (16 it 16 ss) with CTAC, RR and 12 mm Gaussian filter	Spheres were defined by their dimensions. Background was defined by six 212 ml cylinders.
Mezzenga et al 2017 [118]	Cylindrical phantom, 16 ml sphere in a water-filled Jaszczak phantom and 4 ml, 8 ml and 16 ml spheres in a water-filled Jaszczak phantom	208 keV ± 10% Lower scatter (11.8% wide) Upper scatter (8.7% wide)	TEW	OSEM (1 to 50 it and 5, 10, 15, 20, 30 ss) with CTAC and RR	Cylinder VOI was minimum of 3 cm from the inner edge of the phantom boundaries. The sphere VOI was 6 cm diameter (~ double the diameter).
Peters et al 2020 [129]	Cylindrical Jaszczak phantom with 6 inserts (0.5 – 113 ml)	208 keV ± 10% Lower scatter (20% width)	DEW	Various: OSEM (9 it 10 ss, 6 it 8 ss, 4 it 8ss, 5 it 16 ss, 5 it 16 ss) with CTAC, RR and no filter, 4 mm or 5 mm Gaussian filter	VOIs for spheres were 50% threshold of the maximum voxel value corrected for background activity (where the background was the mean voxel voxel).

Raskin et al 2023 [120]	Various: PET cylindrical phantom, NEMA image quality phantom, anthropomorphic torso phantom and liver and kidney phantoms	208 keV ± 10% 166.4 keV ± 10%	DEW	OSEM (10 it 10 ss) with CTAC and RR	For PET cylindrical phantom a semi-automated delineation tool was used. There were 6 rectangular VOIs for the background drawn manually and sphere, kidney and liver VOIs were drawn manually using the CT images. No VOIs could be copied, therefore they were drawn manually by the same user each time.
Sanders et al 2015 [130]	Six spheres (0.5, 1, 2, 4, 8 and 16 ml) in cylinder phantom	113 keV ± 10% 208 keV ± 10% 92.1 keV ± 9% 131.6 keV ± 6%	TEW	OSEM (4 it 8 ss, 8 it 8 ss, 12 it 8 ss, 16 it 8 ss, 20 it 8 ss, 24 it 8 ss, 28 ss 8ss) with CTAC	Cylindrical VOIs for background. Sphere VOIs were the inner diameter of the sphere and placed using the CT image.

		166.4 keV ± 12.5% 249.6 keV ± 8%			
Shcherbinin et al 2012 [122]	Cylindrical container (70 ml) in a Jaszczak phantom	113 keV ± 10% 168 keV ± 10%	Various (none, down scatter and analytical photon distribution-interpolated)	OSEM (3 it 10 ss) with CTAC and RR	Two VOIs: true VOI was the dimensions of the object, according to CT, and a larger VOI was the true VOI plus 4 voxels in each direction.
Theisen et al 2022 [123]	3D printed phantoms: 3 gyroids (with thicknesses of 0.40, 1.29 and 2.65 mm), 3 cubes (64 cm^3), patient-specific kidney phantom	208 keV ± 10% Lower scatter window Upper scatter window	*Not specified*	xSPECT Quant (12 it 1 ss, 24 it 1 ss, 48 it 1 ss) with CTAC and post filters of 0, 10 and 20 mm	VOIs were based on the CT image plus 6 mm
Tran-Gia et al 2016 [124]	3D printed kidney shaped phantoms and a set of spheres with the same volumes as the kidney phantoms	208 keV ± 10% Lower scatter 10% width	TEW	OSEM (6 it 6 ss) with CTAC and RR	VOIs were based on the CT image expanded by an isotope-dependent enlargement factor (0.25 ± 0.01)

		Upper scatter 10% width			
Tran-Gia et al 2019 [125]	Jaszczak phantom (no inserts), NEMA image quality phantom with ^{177}Lu-filled spheres and smaller cylindrical (head) phantom with 2 ^{177}Lu-filled line source. (21.6 cm diameter and 18.6 cm height)	208 keV ± 10% Lower scatter 10% width Upper scatter 10% width	As per manufacturer setting (Flash 3D and xSPECT Quant)	Various: Flash 3D and xSPECT Quant (OSEM (various it and ss) with CTAC and RR), with and without a 16 mm Gaussian post-filter	Two VOIs: outside VOI contained the full phantom (23.6 cm diameter and 20.6 cm height, ~10% bigger than phantom) and inside VOI placed in the middle (14.5 cm diameter and 12.5 cm height, ~2/3 size of the phantom)
Tran-Gia et al 2021 [1]	Jaszczak phantom (6.9 l) for calibration. IEC NEMA PET body phantom for resolution and PVC. Two-organ phantom for validation.	208.4 keV ± 10% 181.3 keV ± 6% 235.5 keV ± 6%	Range (TEW, MC and ESSE)	OSEM (5, 10, 15, 20, 25, 30, 35, 40, 45, 50 it and 2 ss) with CTAC and no filter. With and without RR.	Defined using CT image. Calibrator factor used VOI corresponding to 130% of the radius and 120% of the height of the phantom.

Uribe et al 2017 [126]	Eight phantoms containing inserts of different sizes (0.5 to 199 ml) and shapes placed in air, water, and radioactive background	208 keV ± 10% 170 keV ± 10% 255 keV ± 10%	TEW and analytical photon distribution interpolated (APDI)	OSEM (6 it 10 ss) with CTAC and RR	Three methods: a fixed 40% threshold, VOI based on CT image and iterative adaptive dual thresholding.
Uribe et al 2018 [127]	295 ml bottle inside a large water cylinder	113 keV ± 10% 208 keV ± 10% 95 keV ± 7% 139 keV ± 10% 170 keV ± 10% 255 keV ± 10%	TEW	Planar only	Full FOV
Wevrett et al 2018 [4]	Radioactive inner and outer shells inside water filled phantom (Jaszczak) with lung and spine inserts	Range for the 7 different sites (always 208 keV ± 10% and 3/7 sites with 113 keV ± 7.5% or 10%, scatter windows at 98.7, 131,	Range (none, TEW, ESSE and MC)	OSEM (6 it 6 ss, 8 it 4 ss, 16 it 5 ss, 24 it 24 ss, 5 it 10 ss, 5 it 15 ss, 8 it 10 ss) with CTAC and 5/7 with RR	Various: CT VOI, CT VOI plus 10 mm, SPECT threshold and CT VOI plus SPECT auto-threshold

		176.8, 178, 214 and/or 239.2 keV ± 5%)			
Zhao et al 2018 [128]	9 phantom studies, 4 MC simulations. Planar scan of point source in air, SPECT of radioactive inserts in water, SPECT of radioactive inserts in radioactive water, and SPECT of radioactive cylinders	208 keV ± 10% 167 keV ± 12% 249 keV ± 8%	TEW	OSEM (6 it 10 ss) with CTAC and RR	Planar: full FOV, SPECT: the total number of counts summed across the 3D image

A range of phantoms were used, from simple geometries (such as point sources, lines sources, cylinders or spheres) to complex geometries (torso with bone and lung equivalent materials) [1], [4], [118], [120], [122]–[124], [126]–[130], [32], [131], [56], [112]–[117]. There were some studies that used patients for in vivo studies and compared their gamma camera images to blood or urine samples [111], [112], [130]. They counted the patients' blood samples in a gamma sample counter and compared to SPECT average blood activity (kilobecquerel/millilitre (kBq/ml)) [111]. Bailey et al imaged a calibration flask with the patient to estimate the activity in the patient, as seen in Figure 20 [111].

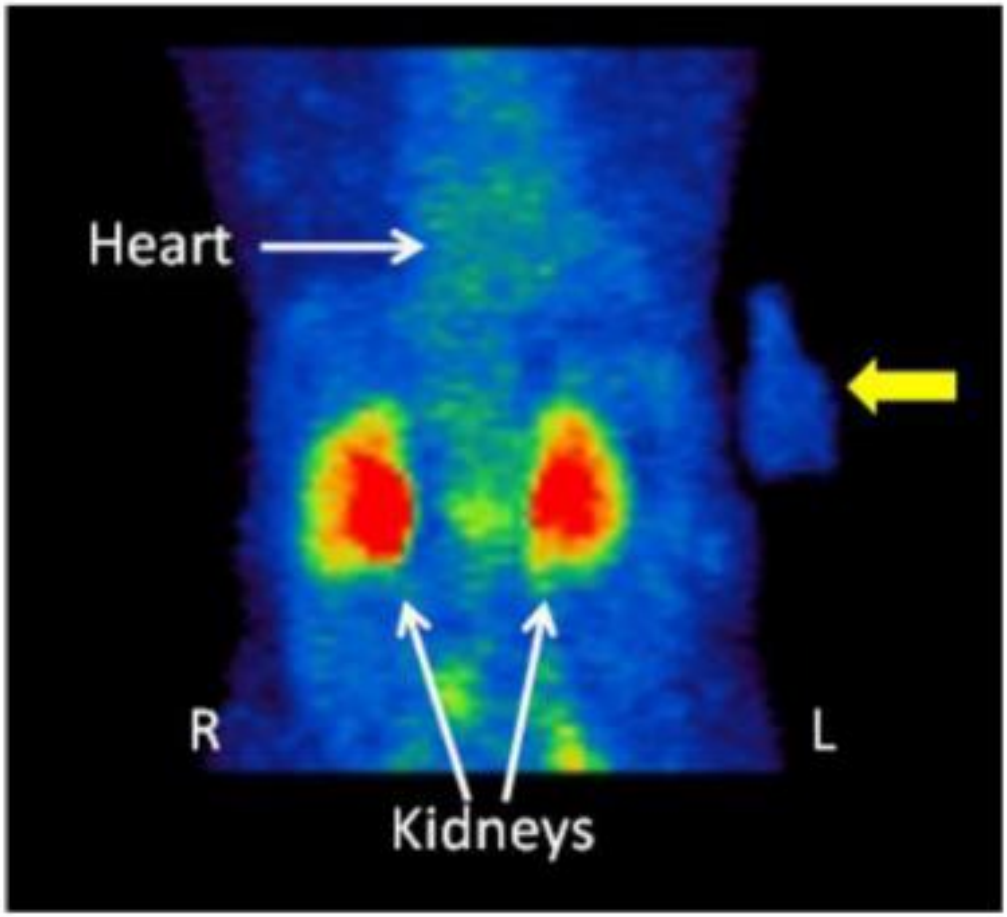

Figure 20: A maximum intensity projection image from the initial SPECT study for a subject (30 minutes after [^{177}Lu]Lu-DOTA-TATE administration), showing the location of the calibration flask (yellow arrow) relative to the subject, used by Bailey et al (taken from Bailey et al 2015) [111]

The energy window used was primarily 208 keV ± 10%, however 6 studies used 113 keV ± 10% and 208 keV ± 10% [4], [32], [56], [116], [127], [130]. There were 2 studies that used only the 113 keV photopeak, because they only had the low energy collimators available on their SPECT/CT systems [113], [122]. Some studies reported that they chose the 208 keV ± 10% due

to Bremsstrahlung contribution to the 113 keV window [112], [116]. For ^{177}Lu imaging it has been found that scatter and attenuation have a greater effect at 113 keV than 208 keV which will reduce quantitative accuracy [32]. A study by Nijs et al used phantom imaging to acquire counts in a range of energy windows using three different collimators (LEHR, low energy general purpose (LEGP) and medium energy general purpose (MEGP)) and SC was applied using a variety of methods (ESSE, TEW and DEW) [56]. They found the low energy collimators combined with 208 keV energy windows introduced septal penetration artefacts and the 113 keV gave large differences in sphere activity and background [56]. Their best method was using MEGP collimators with ESSE SC using both energy peaks, where a difference of less than 10% was seen [56].

Most studies used iterative reconstruction using OSEM and CTAC, however some studies used MLEM iterative reconstruction and a transmission AC technique for planar imaging [32], [111]. Most of the studies (15) used RR [4], [56], [124]–[126], [128], [129], [112]–[115], [117], [118], [120], [122] and there were four studies that used a post-processing Gaussian filter in at least part of their study [117], [123], [125], [129].

There was a range of methods used for defining the VOI, which included using; the dimensions of the object (defined in the CT) [109], [117], [120], [121], the dimensions of the object plus an extra border for count spill over [32], [111], [114], [118], [123], [124], a threshold technique based on the nuclear medicine (NM) image [112], [129] or a mixture of different methods for comparison within the results [4], [113], [115], [122], [126], [128], [131]. The results from the studies for the calculated calibration factors (converted to counts per second (cps) per megabecquerel (MBq) (cps/MBq) for comparison), accuracy and dead time are summarised in Table 5.

Table 5: Summary of the calibration factors, accuracies and dead time for a range of studies for ^{177}Lu on NaI gamma cameras

Study	Camera Manufacturer	Calibration Factor	Accuracy	Dead time
Arienzo et al 2016 [32]	Philips	Various for different phantoms, cameras and energy:	Various for different phantoms, cameras and energy: <5% for Camera 1 208 keV	2.30 µs for Camera 1 (IRIX) 1.46 µs for Camera 2 (AXIS)

		7.09 – 7.56 cps/MBq for Camera 1 208 keV 3.97 – 5.81 cps/MBq for Camera 1 113 keV 7.28 – 8.84 cps/MBq for Camera 2 208 keV 3.57 – 4.91 cps/MBq for Camera 2 113 keV	<24% for Camera 1 113 keV <12% for Camera 2 208 keV <29% for Camera 2 113 keV	
Bailey et al 2015 [111]	Siemens	*Not specified*	4.6 ± 5.9% for whole body patient scans -4.0 ± 7.8% for SPECT patient scans 2.0 ± 8.5% for phantoms	*Not investigated*
Beauregard et al 2011 [112]	Siemens	10.8 ± 0.02 cps/MBq	5.6 ± 1.9% for phantoms 2.6 ± 1.8% for patients	0.78 ± 0.03 μs wide spectrum 4.90 ± 0.10 μs photopeak with scatter material 3.20 ± 0.10 μs photopeak without scatter material
Celler et al 2014 [113]	GE Healthcare	*Not investigated*	*Not investigated*	13% in total spectrum

				16% in photopeak
De Nijs et al 2014 [56]	Philips	Range for scatter methods and collimators (3.1 - 13.5 kBq/cps, equivalent to 0.000074 – 0.0003 cps/MBq)	Range for scatter methods and collimators (3.7 – 285 %)	*Not investigated*
Desy et al 2022 [114]	Siemens	10.05 ± 0.04 cps/MBq	Range, mostly <5%, unless low activity or detector saturation	0.56 ± 0.14 µs
Frezza et al 2020 [115]	Siemens	9.36 ± 0.01 cps/MBq	Various, maximum was 0.71 ± 1.18%	0.550 ± 0.003 µs wide spectrum 2.13 ± 0.01 µs photopeak
He et al 2012 [116]	GE Healthcare	*Not investigated*	<3.2% for 208 keV <40% for 113 keV <14% with 113 & 208 keV	*Not investigated*
Marin et al 2017 [117]	Siemens	9.87 cps/MBq	Various, <30%. For activity concentration >20 kBq/ml the accuracy was <5%	*Not investigated*
Mezzenga et al 2017 [118]	GE Healthcare	~5.65 cps/MBq for cylinder ~6.27 cps/MBq for sphere in Jaszczak	16.4% for cylindrical phantom and 24.8% for the 16 ml sphere	*Not investigated*
Peters et al 2020 [129]	Siemens and GE Healthcare	6.2 cps/MBq for GE	*Not specified*	*Not investigated*

		10.1 – 10.3 cps/MBq for Siemens		
Raskin et al 2023 [120]	GE Healthcare	4.66 – 5.08 cps/MBq for the background PET phantom 3.49 – 4.64 cps/MBq for 26.52 cc sphere 2.67 – 3.86 cps/MBq for 11.49 cc sphere 1.78 – 3.08 cps/MBq for 5.71 cc sphere	Range: 0.16 – 30.28% 0.16 – 4.56% for 26.52 cc sphere 4.48 – 9.69% for 11.49 cc sphere 4.41 – 30.28% for 5.71 cc sphere	*Not investigated*
Sanders et al 2015 [130]	Siemens	20.83 ± 5 cps/MBq for 113 keV 18.83 ± 0.17 cps/MBq for 208 keV	10.1 ± 8.3% in vivo	*Not investigated*
Shcherbinin et al 2012 [122]	GE Healthcare	5 ± 1.4% cps/MBq	2.1 to 88.4%	*Not investigated*
Theisen et al 2022 [123]	Siemens	*Not specified*	<10%	*Not investigated*
Tran-Gia et al 2016 [124]	Siemens	26.94 ± 0.08 cps/MBq	<8%	*Not investigated*
Tran-Gia et al 2019 [125]	Siemens	18.62 – 20.44 cps/MBq for a range of reconstruction techniques	1.2 – 3.8 % for the outside VOI and 2.2 – 3.5 % for the inside VOI for a	*Not investigated*

			range of reconstruction techniques	
Tran-Gia et al 2021 [1]	Various	Range (approximately 10 to 50 cps/MBq)	Range (-25% to 160%)	*Not investigated*
Uribe et al 2017 [126]	Siemens	9.67 – 10.5 cps/MBq for SPECT 9.83 – 11.83 cps/MBq for planar	Various for phantoms, SC and VOI techniques. Phantoms in cold water: TEW SC <14%, ADPI SC <12%. Phantoms in warm water: TEW SC <60%, ADPI SC <60%, CT VOI was larger error and iterative adaptive dual thresholding was the smallest error.	*Not investigated*
Uribe et al 2018 [127]	Siemens	*Not investigated*	*Not investigated*	5.99 ± 0.02 µs for 113 keV 4.60 ± 0.052 µs for 208 keV 0.19 ± 0.18 µs for the full spectrum
Wevrett et al 2018 [4]	Various	*Not specified*	-2 to 20% for inner sphere -34 to 83% for outer sphere	*Not investigated*

Zhao et al 2018 [128]	Siemens	9.4 cps/MBq for point source 10.5 cps/MBq for spheres in water 9.5 cps/MBq for spheres in radioactive water 10.1 cps/MBq for cylinder	<6% overall <3% on same day experiments	*Not investigated*

The calibration factors varied depending on camera, energy windows, corrections applied and phantom or patient geometry. There were 2 studies which included Philips gamma cameras [32], [56], 15 studies which included Siemens gamma cameras [1], [4], [125]–[129], [111], [112], [114], [115], [117], [121], [123], [124] and 8 studies which include GE Healthcare gamma cameras [1], [4], [113], [116], [118], [120], [122], [129]. For the 113 keV energy window the calibration factors ranged from 3.57 – 5.81 cps/MBq [32], [122] and for the 208 keV energy window they ranged from 1.78 – 10.8 cps/MBq [32], [112], [114], [115], [117], [118], [120], [126], [128], [129], except for De Nijs et al which were equivalent to 0.000074 to 0.0003 cps/MBq [56], for Sanders et al which were 20.33 and 18.83 [121], respectively, and for Tran-Gia et al 2016, 2019 and 2021 which were approximately 10 to 50 cps/MBq [1], [124], [131]. De Nijs et al used a gamma counter to calculate the calibration factor for the gamma camera, which may account for some of the differences, however it is unlikely to explain the large difference in calibration factors to other studies, and the authors do not include a discussion about the differences, therefore these differences are unaccounted for [56]. The methods used by Sanders et al and Tran-Gia et al were consistent with other studies and therefore these differences are unaccounted for [1], [124], [125], [130]. Tran-Gia et al have concluded that the reconstruction software used, reconstruction technique and PVC will greatly affect the gamma camera calibration results [1].

The calculations for calibration factors varied across the studies. Marin et al calculated the gamma camera calibration factor using Equation 14:

$$\boldsymbol{CF} = \frac{\boldsymbol{C_{mes}}}{\boldsymbol{T_{acq}} \times \boldsymbol{C_{prep}} \times \boldsymbol{exp}\left(\frac{-\boldsymbol{ln2} \times \boldsymbol{\Delta t}}{\boldsymbol{T_{1/2}}}\right)} \qquad \textbf{Equation 14}$$

Where c_{mes} is the mean number of counts per voxel, T_{acq} is the acquisition duration, C_{prep} is the prepared activity, Δt is the time between the phantom preparation and the acquisition start and $T_{1/2}$ is the physical half-life [117]. A specific quality control test was implemented for this set of experiments by finding the calibration factor within a uniform bottle of ^{177}Lu to compare results overtime to another geometry and a calibration factor was used for the radionuclide calibrator to ensure consistency over time [117].

It has been shown that it is possible to resolve the activity within a phantom to approximately 2% within a standards laboratory (using a homogenous and stable solution), however it depends on the geometry of the activity and can be over 50% [1], [4], [118], [120]–[124], [126], [128], [129], [131], [32], [56], [111], [112], [114]–[117]. Accuracies were improved for the 208 keV photopeak compared to the 113 keV, where they were generally less than 10% for the 208 keV window [4], [32], [124], [125], [128], [111], [112], [114]–[117], [120], [123] (excluding Uribe et al 2017 [126]) and were between 17.2 and 88% for the 113 keV window [32], [116], [122]. Uribe et al 2017 found the accuracy improved for larger objects in water, <2%, compared to smaller objects in air, <11.5% [126]. Zhao et al compared 21 phantom experiments to 12 MC simulations and found TEW SC underestimated scatter and recommended using a planar scan for 5% accuracy [128]. A study by Peters et al found that an increased BMI will reduce the accuracy of quantification of small lesions (<10 ml) [108].

Peters et al used a cylindrical phantom with six spherical inserts (sphere to background activity concentration ratio of 10:1) to investigate four state-of-the-art SPECT/CT systems (GE Discovery NM/CT 670 Pro, Siemens Symbia Intevo and two Siemens Symbia T16 SPECT/CT systems) and reconstruction software to identify which had better ^{177}Lu SPECT/CT quantification accuracy [119]. The median recovery coefficient for the background compartment for the five different vendor-specific reconstructions was 0.97 (range of 0.92 – 1.06). They found that, for spheres less than 24.8 mm, there is an inter-system variation with vendor-specific reconstructions which resulted in a quantification difference of 118% for mean recovery coefficient and 139% for maximum recovery coefficient [119]. The RC range for the spheres for different vendors was up to 0.41 for mean recovery coefficient and 0.62 for maximum recovery coefficient. The full details are displayed in Figure 21.

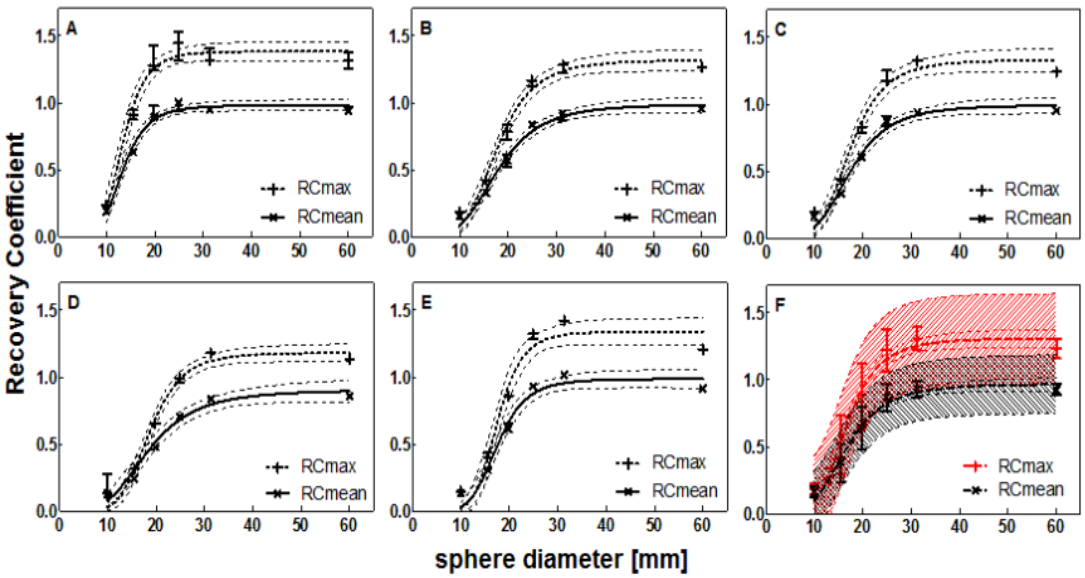

Figure 21: The recovery coefficient for a range of sphere diameters for different gamma cameras and reconstructions methods (A-E), and for all systems combined (F) using a vendor-specific algorithm. (A: GE Discovery NM/CT 670 Pro, B: Siemens Symbia Intevo Bold with xSPECT Quant, C: Siemens Symbia Intevo Bold with Broad Quantification, D and E: Siemens Symbia T16 systems). (Taken from Peters et al) [119]

Dead time effects have been investigated by Uribe et al, Arienzo et al, Beauregard et al, Desy et al, Frezza et al and Celler et al for ^{177}Lu quantification [32], [112]–[115], [127]. In the photopeak the dead time ranged from 1.46 to 5.99 μs and in the wider spectrum the dead time ranged from 0.19 to 0.78 μs [32], [112], [114], [115], [127]. Uribe et al found dead time correction factors of 23% were observed for the 113 keV photopeak and 20% for the 208 keV photopeak, which were three times higher than for the full spectrum [127]. However, Celler et al found the dead time factors for 2.85 GBq ^{177}Lu for the full spectrum and photopeak were 13% and 16%, respectively [113]. It is concluded that the dead time should be corrected for using the scatter-corrected photopeak energy window as opposed to the full spectrum [127]. Generally the dead time effects are seen at a much greater count rate (approximately 150 kcps in the full energy spectrum and 25 kcps in the 208 keV energy spectrum for dead time effects) than observed in patient studies (approximately 50 to 70 kcps in the full energy spectrum and 6 to 8 kcps in the 208 keV energy spectrum for patient count rate [127]) and therefore dead time is unlikely to have a significant effect of ^{177}Lu SPECT/CT clinical imaging [32], [112]–[115], [127].

As there are many variables investigated across these studies, there does not seem to be a clear correct method indicated, as concluded by Wevrett et al, however the accuracy of the calibration is improved for the 208 keV photopeak compared to the 113 keV [4], [32], [116]. It

can be concluded that quantitative gamma camera imaging of ^{177}Lu is possible, however a reliable method needs to be found for consistent results [1].

3.3 Quantitative Imaging on a CZT Gamma Camera

The CZT gamma camera was first developed for brain and cardiac imaging as the detectors were too small for a whole-body gamma camera imaging [132], [133]. A group from Israel first published using a CZT gamma camera for bone imaging in 2015 [134]. In 2016, GE launched their first general purpose CZT-SPECT system [135].

Most of the literature describes advantages for the CZT gamma camera over NaI in cardiology, neurology and mammography, however there is increasingly more literature in general nuclear medicine imaging [132], [133], [136]–[142]. Generally the CZT gamma camera has reduced imaging time and improved image quality when compared to the NaI gamma camera [29], [132], [133], [136]–[139]. Imbert et al compared the GE Discovery NM 530c, DSPECT and IQ SPECT CZT gamma cameras to a Siemens NaI gamma camera, and concluded that the performance of the CZT gamma cameras was superior to the NaI gamma camera [133]. For instance, measurements in the CZT gamma cameras resulted in greater sensitivity and improved spatial resolution which resulted in improved contrast to noise ratio and sharpness index for patient data (quantitative profile which is influenced by spatial resolution and can be measured on clinical images) than the same measurements on the NaI gamma camera [133]. Results of these metrics from cardiac phantom and clinical data (myocardial perfusion studies) are displayed in Figure 22. Overall, this work shows there is a difference in performance between NaI and CZT gamma cameras, and there is also a difference between various CZT gamma cameras.

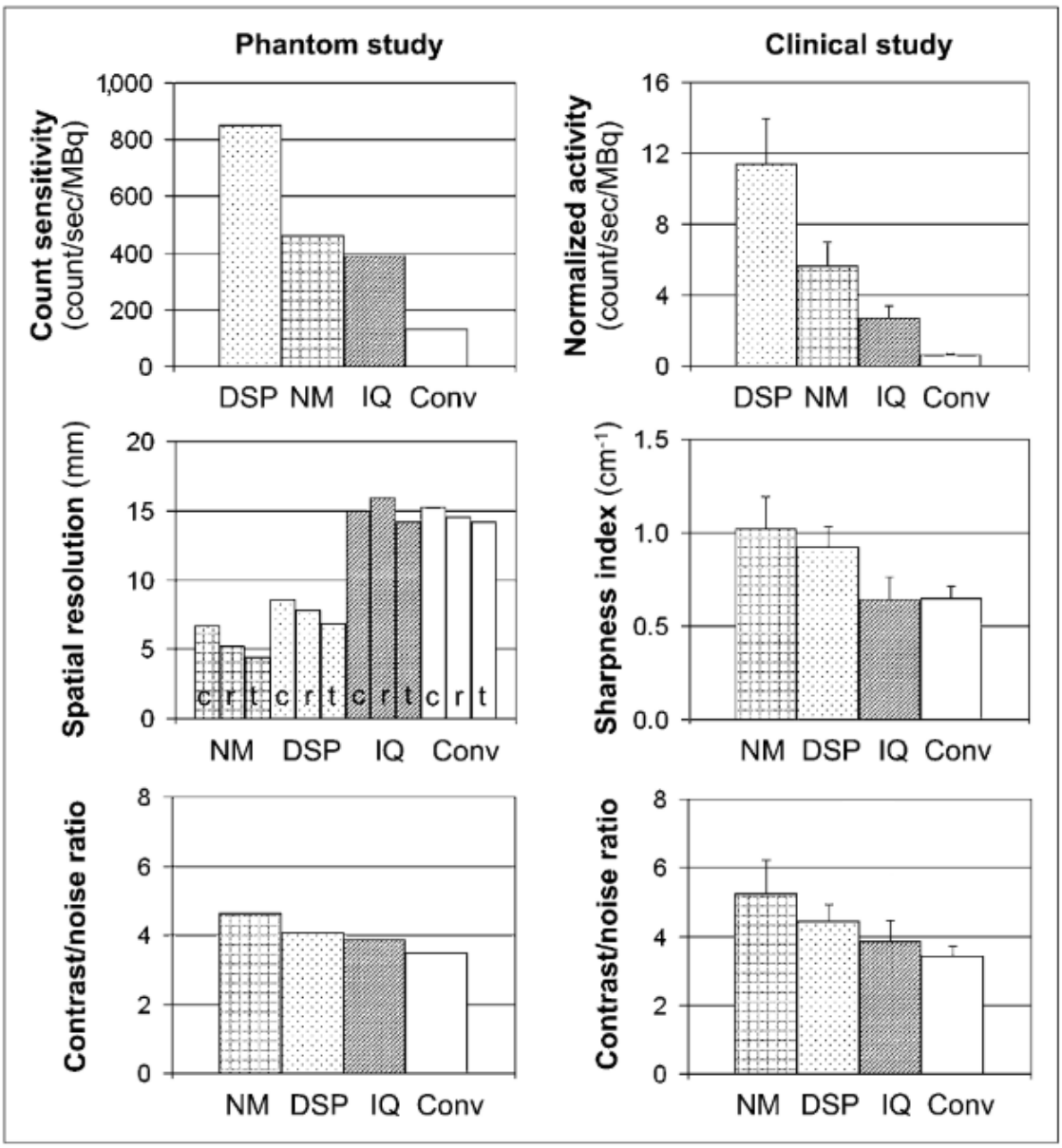

Figure 22: A comparison of four gamma cameras for sensitivity, spatial resolution, sharpness index and contrast to noise ratio for phantom and patient studies, carried out by Imbert et al. DSP = DSPECT, NM = GE Discovery NM 530c, IQ = IQ SPECT and Conv = conventional gamma camera (NaI), c = central resolution, r = radial resolution and t = tangential resolution (taken from Imbert et al 2012) [133]

These studies on cardiology and neurology used conventional SPECT imaging and reconstruction methods such as an energy peak at 140 keV (energy window widths were 15 to 20%) for ^{99m}Tc, OSEM or MLEM iterative reconstruction, with or without AC, with a post-processing filter (Gaussian or Butterworth), however generally no SC was used [136]–[139], [143]. However, when CZT technology was available for general purpose gamma cameras, there were some studies which used SC and investigated the best SC methods, however some studies assumed conventional SC methods would be feasible [144]–[147]. Songy et al used a conventional SC

technique for dual isotope cardiology imaging (for ^{99m}Tc and Thallium-201 (^{201}Tl)), and concluded that even though the CZT gamma camera has improved energy resolution, the downscatter from the higher energy isotope could lead to overestimation of a patient's cardiac defect, where without SC there would be an underestimation in the patient's cardiac defect, therefore the SC technique used was not sufficient [147].

As discussed in section 2.6.1, SC for a CZT gamma camera cannot be directly taken from SC techniques used for NaI gamma cameras, due to hole tailing effects [71]. Pourmoghaddas et al [145] have developed a SC method for ^{99m}Tc which involves a dual energy window approach, but with the additional consideration of the hole tailing contribution from the primary photopeak, which does not need correcting for, as described in Equation 15 and Equation 16:

$$\boldsymbol{Meas_{LW} = k \times Prim_{PW} + Scatter_{LW}} \qquad \textbf{Equation 15}$$

$$\boldsymbol{Meas_{PW} = Prim_{PW} + k' \times Scatter_{LW}} \qquad \textbf{Equation 16}$$

Where $Meas_{LW}$ and $Meas_{PW}$ are the measured photons in the lower energy window and photopeak energy window, k is the fraction of the primary photopeak measured in the lower energy scatter window, $Prim_{PW}$ is the primary photons in the photopeak, $Scatter_{LW}$ is the scattered photons measured in the lower energy window and k' represents the fraction of scattered photons detected in the photopeak energy window. Therefore, the primary photons can be expressed as seen in Equation 17:

$$\boldsymbol{Prim_{PW} = \frac{Meas_{PW} - k' \times Meas_{LW}}{1 - k \times k'}} \qquad \textbf{Equation 17}$$

This method is different to the standard DEW SC method as it includes a scaling factor that corrects for the photons from the primary photopeak which are detected in the lower scatter energy window due to hole-tailing effects [145]. It was assumed that the value of k is independent of the scattering media as it is a function of the detector alone. The factor k was calculated using a point source in air and k' was calculated using an anthropomorphic phantom with a cardiac insert imaged with and without a scatter material (water) present, however there are not full details about the phantom scans included in the literature. The value of k was calculated to be 0.17 ± 0.02 and the value of k' was calculated to be 1.0 ± 0.1. Pourmoghaddas concluded that this DEW CZT SC technique was sufficient for cardiology imaging on a GE Discovery NM 530c gamma camera and produced similar DEW SC images to a NaI gamma camera (GE Infinia Hawkeye) [145].

Fan et al devised a new CZT SC method for dual-isotope imaging of ^{99m}Tc and Iodine-123 (^{123}I), which provided more accurate self-scatter and down-scatter estimations for quantitative imaging than the conventional TEW SC method for a GE Discovery NM 530c/570c cardiology gamma camera [146]. The energy windows were defined for ^{99m}Tc and ^{123}I as shown in Figure 23, where the scattered photons were assumed to have undergone Compton scatter at various scatter angles.

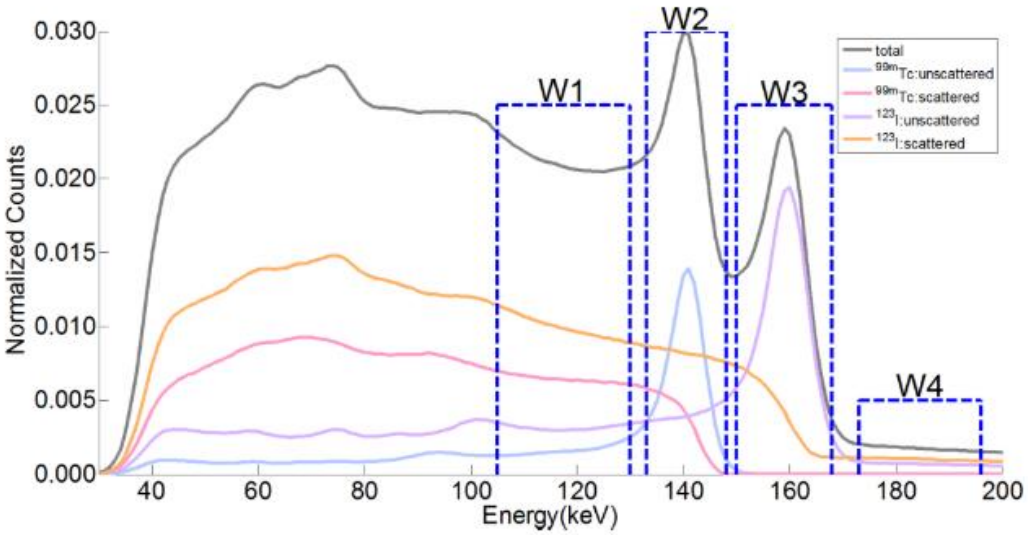

Figure 23: The total normalised energy spectra including the breakdown for ^{99m}Tc and ^{123}I, scattered and unscattered energy spectra, including the energy windows as described by Fan et al 2015 (taken from Fan et al) [146]

The total counts (*T*) within each energy window (*1, 2, 3* and *4*) were described by Equation 18, Equation 19 and Equation 20:

$$\boldsymbol{T_1 = \sum_{i=2}^{3} O_{i1} + \sum_{i=2}^{3} S_{i1} + H_1} \qquad \textbf{Equation 18}$$

$$\boldsymbol{T_2 = O_{32} + S_{32} + P_2 + S_2 + H_2} \qquad \textbf{Equation 19}$$

$$\boldsymbol{T_3 = P_3 + S_3 + H_3} \qquad \textbf{Equation 20}$$

Where O_ij and S_{ij} are the projections of hole tailing and down scattered photons in window *j* that originate from photopeak *i*, respectively (*i* = 2 for ^{99m}Tc and *i* = 3 for ^{123}I). P_j and S_j are the projections of primary and self-scattered photons in window *j*, respectively, and H_j is the contamination from the high energy components of the ^{123}I in window *j* [146]. The relationship between the hole tailing projections and down scatter was based on Hecht relationship (Equation 2) and defined by a relationship between the photons that are detected unscattered

and scattered through the pinhole collimator, with an associated attenuation coefficient and an incident photon angle, which provided an equation with several parameters to be determined. The parameters were detector attenuation coefficient, standard deviation of the Gaussian kernel and weighting factors, which were determined by imaging a point source in air [146]. The scatter model was defined by Equation 21:

$$S_{ij} = S_i \otimes \left[C_{ij} \left(\delta + \alpha_{ij} e^{-\lambda_{ij} r} \right) \right] \qquad \textbf{Equation 21}$$

Where $i = 2, 3$; $1 \leq j < i$, S_{ij} is the projection of the down-scatter photons in energy window j that originate from photopeak i, S_i is the projection of self-scatter photons in the photopeak, C_{ij}, α_{ij} and λ_{ij} are the scatter model parameters that need to be determined for each window pair i to j, and r is the radial distance [146]. Fan et al validated their model using MC simulations, phantom experiments and patient studies.

Kacperski et al proposed a CZT deconvolution SC technique, which they derived by analysing the energy spectra from point sources in air for ^{99m}Tc and ^{201}Tl using a D-SPECT dedicated cardiac CZT gamma camera [102]. They propose a complex set of equations which are defined for the photopeak and scatter energy windows separately, which require solving through an MLEM algorithm.

The SC methods described above are for the cardiac dedicated gamma cameras imaging ^{99m}Tc with or without ^{123}I or ^{201}Tl, which have different geometry and clinical applications to a general purpose CZT gamma camera, such as the GE Discovery 870 DR CZT gamma camera, which may affect the SC techniques required [102], [145], [146]. The proposed SC techniques for dual-energy imaging require a complex set of equations which require some MC simulations or experimental derivations of various parameters [102], [146].

3.3.1 Quantitative Lutetium-177 Imaging on a CZT Gamma Camera

The literature review identified six studies investigating ^{177}Lu on a CZT gamma camera by four research groups published to date [99], [148]–[152]. Kennedy et al investigated quantification of ^{177}Lu whole body SPECT for the CZT and NaI gamma cameras by determining the SUV for a set of spheres, using a NEMA IEC phantom with torso dimensions, a lung insert and six radioactive spheres [148], [150]. They used a 12:1 target-to-background ratio of [^{177}Lu]Lu-PSMA , where the background concentrations ranged from 15 to 110 kBq/ml [148], [150]. The phantom was imaged using a range of protocols for the photopeak and SC method used, as summarised in Table 6.

Table 6: The four methods of NEMA IEC phantom acquisitions used by Kennedy et al, where LE and HE are low and high energy, respectively [148], [150]

Method	Image energy window (keV)		Scatter energy window (keV)	
	Peak(s)	Range	Peak(s)	Range
LE 113 TEW	113	101.7 – 124.3	96.6	91.6 – 101.6
			129.4	124.4 – 134.4
HE 113 & 208 TEW	113	101.7 – 124.3	96.6	91.6 – 101.6
	208	187.2 – 228.8	129.4	124.4 – 134.4
			182	177.5 – 186.6
			234	229.3 – 238.7
HE 208 TEW	208	187.2 – 228.8	182	177.5 – 186.6
			234	229.3 – 238.7
HE 208 DEW	208	187.2 – 228.8	166	145.3 – 186.7

The images were reconstructed using OSEM (4 iterations and 10 subsets), no post processing filter, CTAC, RR and SC (TEW or DEW, as defined in Table 6). They calculated the sensitivity and recovery coefficients. The sensitivities were calculated to be 5.5, 10.8, 6.1 and 6.7 cps/MBq for the acquisition methods LE 113 TEW, HE 113 & 208 TEW, HE 208 TEW and HE 208 DEW, respectively and the recovery coefficients can be seen in Figure 24. They concluded the ^{177}Lu quantitation was equivalent on the CZT camera as for the NaI camera, however the CZT showed no measurable dead time loss [148], [150].

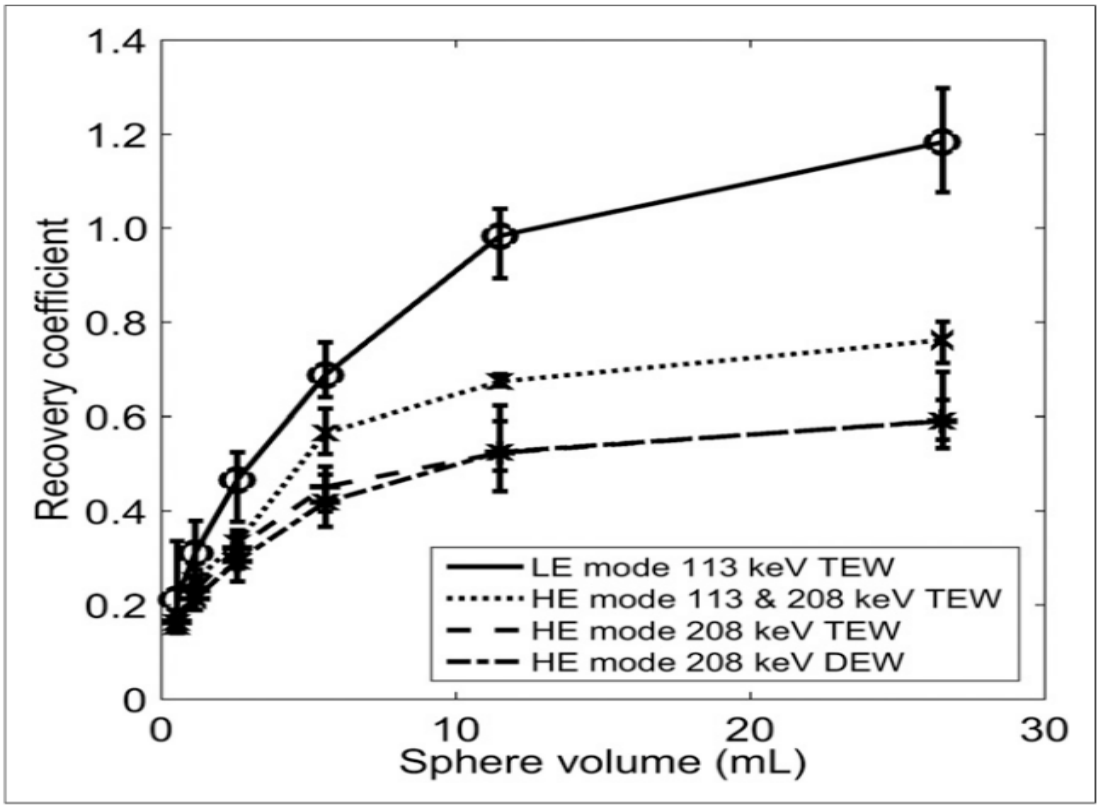

Figure 24: The recovery coefficients for a range of sphere volumes for the four different acquisition methods used by Kennedy et al 2020 (taken from Kennedy et al) [150]

Sandstorm et al compared ^{177}Lu quantitative imaging on the GE Discovery 670 CZT and the GE Discovery 670 Pro (a NaI gamma camera) [99], however the literature available does not include full details of the methods used for this work. They used the PET NEMA image quality phantom (NEMA NU 2-2001 [153]) with a target-to-background ratio of 8:1 and acquired the image using both photopeak peaks (113 keV ± 6% and 208 keV ± 6%). The percentage contrast was calculated for the 113 keV photopeak with and without TEW SC and the 208 keV without SC and compared to the contrast calculated for the GE Discovery 670 Pro (NaI) gamma camera, as shown in Table 7, however the exact methods were not specified. Septal penetration was observed for the 208 keV peak, and scatter was seen at the 113 keV peak, which both caused a detriment to quantitative imaging. The authors concluded there is good potential to use the CZT for quantitative imaging, once the septal penetration is resolved for the 208 keV images and the SC is resolved for the 113 keV images [99].

Table 7: The percentage contrast calculated by Sandstrom et al for a range of spheres for the GE Discovery 670 CZT for 113 and 208 keV photopeaks and the GE Discovery 870 Pro (NaI) for the 208 keV photopeak [99], [153]

Sphere diameter (mm)	Contrast (%)			
	113 keV		208 keV	
	CZT NSC	CZT TEW SC	CZT	NaI
1.0	7	7	7	4
1.3	13	16	13	9
1.7	20	23	17	15
2.2	26	32	22	20
2.8	36	47	30	26
3.7	48	63	38	37

In 2019 Sandstrom et al published a second study on comparing intrinsic and extrinsic uniformity maps on a CZT gamma camera to a NaI gamma camera [149]. SPECT imaging was carried out using 360s per view and the MEHR collimator on the CZT gamma camera with an energy window of 208 keV ± 6% and MEGP collimator on the NaI gamma camera with an energy window of 208 keV ± 10%. All images were attenuation corrected using a low dose CT and were reconstructed using OSEM (8 iterations and 8 subsets), and for the CZT gamma camera the images were reconstructed using the intrinsic and extrinsic uniformity maps. A 20 cm cylindrical phantom was filled with 500 MBq ^{177}Lu and the integral uniformity was calculated using a ROI at 80% of the phantom diameter averaged across five slices. The SPECT uniformity for the CZT gamma camera was 14% with severe ring artefacts when intrinsic uniformity correction was applied, however with extrinsic uniformity applied the uniformity was 5% with no visible artefacts, therefore indicating an extrinsic uniformity map should be used for the CZT gamma camera [149]. They also concluded that image contrast on the CZT gamma camera was improved compared to the NaI gamma camera.

Roth et al investigated system spatial resolution, energy resolution, sensitivity, uniformity, septal penetration and temperature dependence of a hand-held CZT gamma camera (CrystalCam) for ^{177}Lu using a range of collimators (LEHR, LEHS and MEGP) and energy windows (55, 113 and 208 keV) [151]. They found that the hand-held CZT gamma camera gave sensitivities of 99.8, 225.9 and 663.3 cps/MBq for the MEGP, LEHR and LEHS collimators, respectively. They concluded that the hand-held CZT gamma camera could be used for imaging ^{177}Lu, however there were some image-degrading effects for specific collimator and energy window

combinations, and the LEHR or MEGP collimator with the 113 keV energy window gave the best results [151].

Chevalier et al used a Veriton CZT SPECT system to carry out post [^{177}Lu]Lu-DOTA-TATE treatment imaging, using 20-minute whole-body SPECT (6 bed positions of 3 minutes each), using 113 keV photopeak, CTAC, SC and RR, which is shown in Figure 25 [111]. They state that they validated the system prior to the clinical imaging, using an IEC phantom, which produced <10% error in activity of the spheres ranging from 17 to 37 mm diameter, however they do not provide any specific details on their phantom validation methods. This image does show promising signs that clinical imaging of ^{177}Lu-labelled radiopharmaceuticals using a CZT gamma camera is possible, however the SC technique used is not described and there is no mention of using the 208 keV photopeak for imaging.

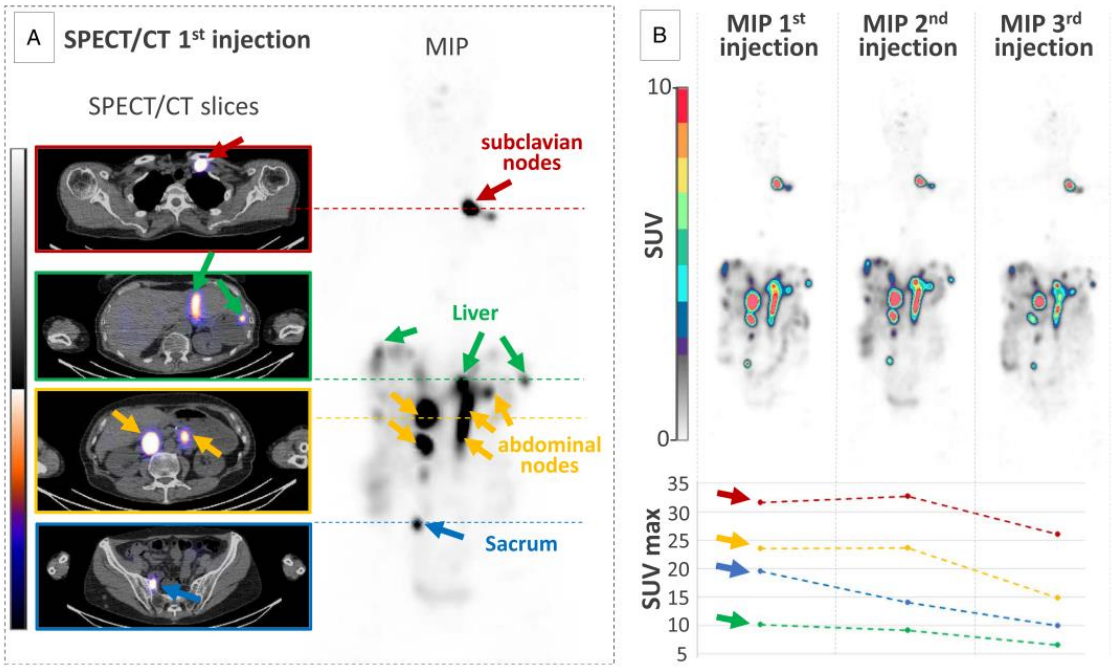

Figure 25: CZT SPECT/CT images using a Veriton system of a NET patient following 3 cycles of 7.4 GBq [^{177}Lu]Lu-DOTA-TATE, at two-month intervals, with corresponding maximum SUV values for each SPECT/CT slice (taken from Chevalier 2020) [152]

These studies do not have the full range of phantom geometries as used on NaI gamma cameras, and they do not have published accuracies and dead time factors. There should be work carried out on planar and SPECT CZT images for a full range of phantoms to compare to the current work published, as previous work on quantification on a NaI gamma camera showed that calibration factors can vary over different days, different systems and heavily depend on geometries and reconstruction of images.

3.4 Comparison to Monte Carlo Simulations

There are a range of published studies which involve creating MC simulations for NaI gamma cameras and CZT detectors [154], [155], [164]–[166], [156]–[163]. Examples of some of the literature available for MC simulations for NaI gamma cameras imaging ^{177}Lu have investigated the effects of calibration factors and recovery coefficients on quantification accuracy [161], SC on activity quantification [162], energy window and collimator optimisation [154] and energy-dependent spectral resolution [159].

Asmi et al used a MC simulation to assess the optimal collimator and energy window to use for ^{177}Lu imaging, using a simulated point source placed in a cylindrical water-filled phantom [154]. They concluded that the medium energy collimator with a 20% energy window gave the best results. Morphis et al used a MC simulation to model the energy spectra for a range of phantom geometries and they found that the model provided an improved accuracy in the FWHM compared to a theoretical energy resolution relationship, for energies above 160 keV [159].

Ramonaheng et al created a model for a Siemens Symbia T16 gamma camera which they validated by comparing experimental and simulated outputs for the 208 keV photopeak using the medium energy collimator [166]. The tests they used included intrinsic and extrinsic energy resolution, system spatial resolution, planar system sensitivity, SPECT calibration factor in air and in water. They found their results were within 5% of their experimental data. Once validated, they used their MC model to optimise OSEM reconstruction, investigate calibration factors and recovery coefficients using spheres in water and a cylindrical phantoms [161]. They used voxel-based phantoms for each simulation, produced from the CT images of the phantoms. They found that the calibration factor using a sphere-based phantom was more accurate than a cylinder-based phantom, without PVC and with PVC the calibration factors produced for each method were comparable. They concluded that when all corrections were applied (attenuation, scatter and PVC) the quantification errors were less than 4%, however they highlighted that patient-specific PVC would improve accuracy but would not be practical to use clinically.

Robinson et al investigated the influence of TEW SC on activity quantification for ^{177}Lu MRT using a combination of phantom experiments and MC simulations [162]. They found that the MC simulation was able to fully analyse the events within the reconstructed VOI and therefore providing the relative contributions from the PVE and inaccuracies in the TEW SC to the overestimation of activity recovery. They found that even with perfect PVC, the TEW SC cannot produce a patient-specific activity distribution without prior knowledge of the full activity distribution, which is not feasible in a clinical scenario.

There are several studies on MC simulations for CZT gamma cameras or detectors to investigate the design and performance [155], [157], [158], [160], [165], SC including hole tailing effects [156], [164] and a hand-held CZT gamma camera for ^{177}Lu imaging [163]. The MC simulations for the design were able to review the performance of the detectors and gamma cameras being reviewed, for example the energy resolution, spatial resolution, sensitivity and efficiency [155], [157], [158], [160], [165].

Holstensson et al and Suzuki et al used MC simulation to investigate scatter and hole tailing effects for dual isotope imaging of ^{99m}Tc and ^{123}I in cardiology and neurology applications, respectively [156], [164]. Both studies used a MC SC technique to account for the hole tailing effects to carry out SC effectively and provide similar results as for single isotope imaging, however the use of these methods within the clinical setting is not currently feasible.

Roth et al used MC simulations to model a hand-held CZT gamma camera for imaging ^{177}Lu, which links to the quantitative gamma camera experiments they carried out, described in section 3.3.1 [163]. They modelled the charge transport and signal induction in three dimensions to investigate the effects of the high energy photons to the counts within the lower energy windows, due to hole tailing effects. They compared their MC simulation outputs to the experimental outputs to validate their MC model and concluded that it was successful, and it would be useful for future optimisation of the gamma camera.

This literature review did not discover a published MC model of the GE Discovery 870 DR CZT gamma camera and there is limited research into using a CZT gamma camera for quantitative ^{177}Lu imaging. However, the studies included in this review show that MC simulations of ^{177}Lu on a CZT gamma are feasible and can play a useful role in optimisation of gamma camera performance for quantitative imaging.

3.5 Conclusion

Quantitative gamma camera imaging is important for ^{177}Lu dosimetry and individualising patient treatment plans. Several studies have calculated calibration factors for imaging ^{177}Lu on a NaI gamma camera, which conclude that there are a range of methods available, and their accuracy depends on the gamma camera, geometry of object imaged, energy window, SC, AC, RR and dead time correction. However, little research has currently been carried out on quantitative imaging for ^{177}Lu on a CZT solid-state gamma camera using experimental or MC simulation methods. There are bright prospects that the accuracy of ^{177}Lu quantitative CZT imaging could be improved over a NaI gamma camera, however further research is required.

The motivation for this work has stemmed from an interest in using the GE Discovery 870 DR CZT gamma camera based at the Royal Surrey County Hospital (RSCH) to image ^{177}Lu-labelled radiopharmaceuticals following MRT in oncology applications. The literature review has identified that the CZT gamma camera should provide images with improved image quality, compared to NaI gamma cameras, which could be beneficial for accurate quantitative measurements of tumour and organ uptake required for dosimetry. The literature review has summarised the methods that have been used for NaI quantitative imaging of ^{177}Lu-labelled compounds, which can be applied to the CZT gamma camera at RSCH. However, a gap in the literature has been identified for a clinically appropriate SC technique which will be suitable for imaging ^{177}Lu on a CZT gamma camera, and therefore one of the aims of this work is to derive a new SC technique. Another challenge identified is the limited availability of collimators for this CZT gamma camera, compared to the range available for NaI gamma cameras. The only collimator available for the GE Discovery 870 DR CZT at the time of this work was the WEHR which was recommended for use with ^{177}Lu [167]. This literature review has identified that there will need to be a range of phantom acquisitions to calibrate the gamma camera, which will include uniformity, SC, sensitivity, optimisation of reconstruction and PVC, which are further discussed in chapter 4.

In addition, the literature review has identified that MC simulations can assist with optimisation and validation of calibrations for CZT gamma cameras. The MC simulation will be useful to aid the validation process of the CZT gamma camera by modelling the ground truth which can be used as a comparison to the gamma camera measurements. MC simulations can provide an insight into the physics processes which are not directly experimentally observable, such as SC and AC, within the gamma camera acquisition. Therefore, this work will aim to create a MC model of the CZT gamma camera based at RSCH, which is further described in chapter 5.

4 ^{177}LU CADMIUM ZINC TELLURIDE GAMMA CAMERA CALIBRATIONS

4.1 Uniformity

4.1.1 Introduction

The GE Discovery 870 DR CZT gamma camera based at the RSCH was routinely used for ^{99m}Tc imaging only, and therefore a uniformity calibration and test were required for ^{177}Lu. The aim was to set up a ^{177}Lu energy window which could be used for TEW SC using both the 113 keV and 208 keV photopeaks, then carry out a uniformity calibration and finally calculate the uniformity of the final images. The uniformity calibration and test were carried out extrinsically as per manufacturer's guidance and literature [149]. As the WEHR collimator aligned with the individual detector elements of the CZT gamma camera, it was not advised to remove the collimator as this could affect the uniformity calibration and therefore clinical images if it were misaligned.

4.1.2 Methods

Prior to the uniformity calibration, a dual photopeak ^{177}Lu energy session was created with scatter windows. The energy windows included the 113 keV ± 10% and 208 keV ± 10% photopeaks, with scatter windows at 98.7 keV ± 3%, 130.9 keV ± 5%, 176.2 keV ± 5% and 240.9 keV ± 5%. The energy windows were taken from those clinically used on the NaI gamma cameras at RSCH. Approximately 77 MBq of [^{177}Lu]Lu-DOTA-TATE was drawn up from the residual from a patient vial. The ^{177}Lu was injected into a fillable flood phantom (FP67S Flächenphantom, IBS, Ingenieurbüro Schöppy, Stemwede) with an inbuilt mixer, which continued to mix during the acquisition. The phantom was filled with deionised water and topped up as required before use. The air bubbles within the phantom were moved to the edge of the phantom, by tilting the phantom, to ensure there was a uniform source. The gamma camera was moved into H-mode, so the detectors were parallel. The fillable flood phantom was positioned parallel to the detectors, on a positioning cart, between the detector heads, as shown in Figure 26. The uniformity calibration was completed using the ^{177}Lu energy windows with WEHR collimators and 300 million counts at the 113 keV photopeak. When the acquisition finished, the uniformity calibration was processed on the camera and the uniformity map was attached, which included all six energy windows for ^{177}Lu (as specified above).

Figure 26: Gamma camera set up for the uniformity calibration and test using the fillable flood phantom with inbuilt mixer placed on the positioning cart

To test the uniformity calibration, a uniformity test was carried out. The same set up was used as for the calibration, with 85 million counts and a pixel size of 2.46 mm. Two separate uniformity test acquisitions were carried out using the 113 keV and 208 keV photopeaks, independently, which included each of the scatter energy windows. The corrections for energy, uniformity, bad cells and noise were applied. The bad cells describe the individual pixels which are not functioning optimally, which could be due to various reasons, such as high or low level of noise, incorrect energy peak or out of tolerance for uniformity. The noise is associated with the background level of individual pixels. Bad cells and noise corrections are specific to a CZT gamma camera and are calibrated by the manufacturer engineers using energy peaking, a uniform source or other calibration, as required. All bad pixels were closed. The uniformity test images

were processed on Fiji ImageJ, using the planar uniformity tool within the NEMA NM quality control (QC) toolkit plug in. The uniformity test included the differential and integral uniformity for the UFOV and CFOV. The uniformity test images were processed for all six energy windows.

4.1.3 Results

The uniformity map creation was successful and passed based on the GE acquisition terminal criteria. The results of the uniformity tests for all energy windows on both detector heads are displayed in Table 8. The results include the differential and integral uniformity for both the UFOV and CFOV. The results are split between the emission energy windows (113 and 208 keV) and the scatter energy windows (98.7, 130.9, 176.2 and 240.9 keV).

Table 8: ^{177}Lu uniformity results processed on Fiji ImageJ using the NMQC NEMA planar uniformity plug in for 113 keV and 208 keV emission energy windows and 98.7 keV, 130.9 keV, 176.2 keV and 240.9 keV scatter energy windows. (Int: integral uniformity, dif: differential uniformity, UFOV: useful field of view, CFOV: central field of view).

Energy (keV)	Detector 1				Detector 2			
	UFOV		CFOV		UFOV		CFOV	
	Int (%)	Dif (%)	Int (%)	Dif (%)	Int (%)	Dif (%)	Int (%)	Dif (%)
113	3.63	2.25	2.80	2.25	3.38	2.15	2.67	1.93
208	5.27	2.73	4.16	2.73	5.47	2.30	3.23	2.06
98.7	7.00	4.81	5.30	4.81	6.93	4.10	6.38	4.10
130.9	5.49	3.17	4.00	3.17	5.22	3.22	4.25	3.12
176.2	6.18	3.51	4.90	3.18	6.08	4.27	5.03	3.60
240.9	100	100	100	100	100	100	100	100

The uniformity images were reviewed for defects and generally looked acceptable. There was one non-uniform section on detector 1 for the 208 keV emission energy window, which appears at the bottom left-hand quadrant of the image. Examples of the ^{177}Lu uniformity test images can be seen in Figure 27, which show the 113 and 208 keV emission energy windows for detector 1 with different window widths and levels.

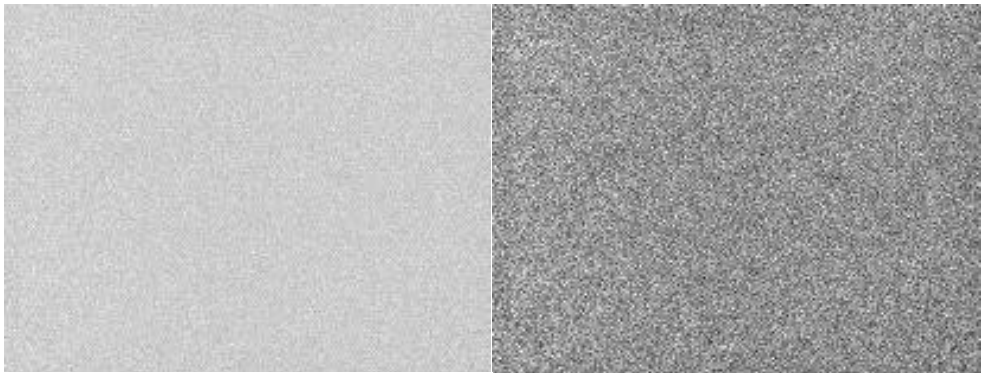

A: 113 keV, default windowing **B: 113 keV, adjusted windowing**

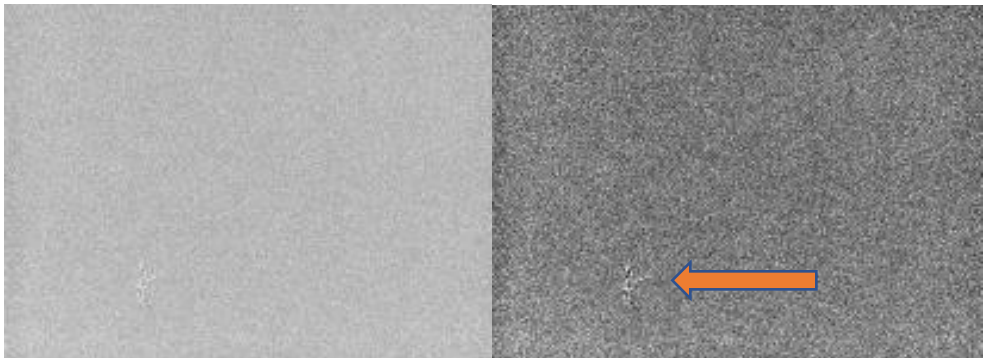

C: 208 keV, default windowing **D: 208 keV, adjusted windowing**

Figure 27: ^{177}Lu uniformity images for detector 1 on a GE 870 DR CZT gamma camera for 113 keV ± 10% (A and B) and for 208 keV ± 10% (C and D), displayed with different window levels and widths (orange arrow indicates a non-uniformity in the 208 keV images)

4.1.4 Discussion

The uniformity results (shown in Table 8) indicate that the uniformity is better for the 113 keV photopeak compared to the 208 keV photopeak overall. The differential uniformity results are comparable for both photopeaks, but the integral uniformity is poorer for the 208 keV photopeak compared to the 113 keV photopeak. The same ^{177}Lu fillable flood phantom was used for each of the uniformity calibration and both uniformity tests. However, the longer the phantom is used for the more air bubbles are introduced into the phantom. The 113 keV uniformity test was carried out two days before the 208 keV uniformity test, which may have resulted in the relatively poor uniformity results for the 208 keV uniformity test, compared to the 113 keV uniformity test. The other factor is that the later uniformity test would have been carried out with less activity in the phantom, which would have increased the amount of time taken to complete the test. There is a slight non-uniformity visible on the 208 keV images (seen in Figure 27), which could also be caused by the bubbles being introduced into the phantom, and therefore effecting the quantitative uniformity results.

The scatter energy windows generally showed poorer uniformity results compared to the photopeak energy windows, which is expected as there would be less counts acquired in each of the scatter energy windows compared to the photopeak energy windows. The results for the 240.9 keV scatter energy window are the poorest (100%) as there are very few counts in that energy window, which is expected. This would suggest that the SC for the 208 keV photopeak will not be greatly affected by the upper energy window if TEW SC is used. The results indicate there is sufficient uniformity (approximately 3% for integral uniformity and 2% for differential uniformity [15]) for the 113 keV photopeak, however the uniformity test results should be further investigated for 208 keV photopeak.

To investigate these test results further the uniformity test should be repeated, and if this were to be used clinically the uniformity test should be completed regularly as part of routine gamma camera quality control testing. However, there is a practical and cost implication for carrying out regular uniformity testing for ^{177}Lu using this method. The test acquired 85 million counts using residual ^{177}Lu from a patient vial and therefore there was not sufficient activity to complete the test quickly, and it took a total of 26.3 hours for the 113 keV uniformity test acquisition and 13.2 hours for the 208 keV uniformity test acquisition. Therefore, these acquisitions were set to run over the weekend or overnight. To complete these tests within a manageable timescale it would require significantly more ^{177}Lu activity (approximately 2 GBq), which would cost the department, give staff a greater radiation dose when handling the phantom and potentially cause storage issues in a radioactive waste store. To implement this clinically there would need to be radiation and manual handling risk assessments to assess the health and safety issues to ensure compliance with the relevant legislation (such as the Ionising Radiation Regulations 2017 (IRR) [168] and the Environmental Permitting Regulations 2016 (EPR) [169]).

These results are comparable to the SPECT extrinsic uniformity results reported by Sandstrom et al for a GE Discovery 870 CZT gamma camera with medium energy collimators [149]. They concluded that extrinsic uniformity maps produced better results than intrinsic uniformity maps, which were less than 5% and approximately 14%, respectively [149]. Their methods differed as they used more activity in a smaller volume (500 MBq of ^{177}Lu in a cylindrical phantom) for SPECT uniformity only and calculated the uniformity results using a 208 keV ± 6% energy window only.

4.2 Scatter Correction

4.2.1 Introduction

As discussed in sections 2.6.1 and 3, a new method of SC was required for the CZT gamma camera due to hole tailing, which would affect the SC required for the low energy window.

Therefore, the aim was to derive a method of TEW SC suitable for imaging ^{177}Lu on a CZT gamma camera. The scatter and hole tailing effects were assessed by imaging a small sphere in air and imaging the same sphere in scatter, then analysing the energy spectra to create an estimate for the hole tailing and scatter, which could be used for SC.

4.2.2 Methods

4.2.2.1 Scatter Correction Method Derivation

A derivation of an appropriate SC technique was carried out using the assumptions summarised in Equation 22, Equation 23 and Equation 24, using inspiration from Pourmoghaddas et al, Kacperski et al and Fan et al [102], [145], [146] (described in section 3.3).

$$\boldsymbol{C_L = P_L + S_L} \qquad \textbf{Equation 22}$$

$$\boldsymbol{C_P = P_P + S_P} \qquad \textbf{Equation 23}$$

$$\boldsymbol{C_U = S_U} \qquad \textbf{Equation 24}$$

Where $C_{L,P,U}$ are the measured counts in the lower, primary and upper energy windows, respectively, $P_{L,P}$ are the counts from the primary photopeak window measured in the lower and primary energy windows, respectively, and $S_{L,P,U}$ are the counts from Compton scattered photons in the lower, primary and upper energy windows, respectively, which is displayed in Figure 28.

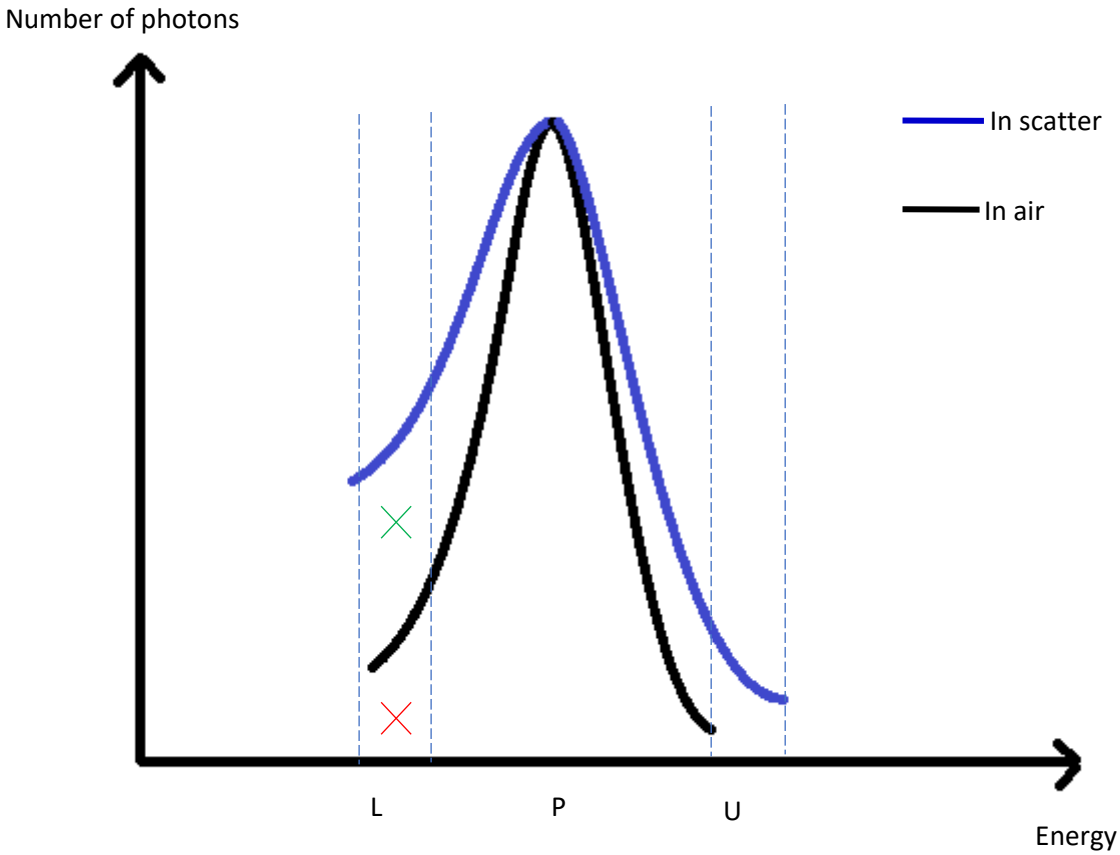

Figure 28: A schematic of the energy spectrum for an object imaged in air (black line) and in scatter (blue line), with energy windows for lower (L), photopeak (P) and upper (U) highlighted. The red cross marks the primary photons (from hole tailing) which are detected in the lower energy window. The green cross marks the scattered photons which are detected in the lower energy window.

The variable to calculate was the primary photons in the photopeak (P_P) by removing the scattered photons detected in the photopeak (S_P), using TEW SC. However, the counts measured in the lower energy window include the photons from the primary photopeak which have been trapped due to hole tailing and photons that have been scattered due to Compton scatter. Therefore, only the scattered photons need to be used as part of the TEW SC technique. Therefore, the CZT SC technique was derived as described below.

From Equation 23:

$$\boldsymbol{P_P = C_P - S_P} \qquad \textbf{Equation 25}$$

Using the method for TEW SC (Equation 4), from Ogawa et al [72], substitute the scattered counts in the lower energy window with Equation 22, which gives:

$$S_P = \left(\left(\frac{C_l - P_L}{W_l} + \frac{C_U}{W_U}\right) \times \frac{W_P}{2}\right) \quad \textbf{Equation 26}$$

Assuming that the hole tailing ratio is constant and independent of energy peak height and scatter conditions [145], gives:

$$\frac{P_L}{P_P} = h \quad \textbf{Equation 27}$$

If there is no scatter present, then *h* can be calculated using:

$$h = \frac{C_{L,air}}{C_{P,air}} \quad \textbf{Equation 28}$$

Where $C_{L,air}$ *and* $C_{P,air}$ are the counts measured for an object in air in the lower and primary energy windows, respectively. It can be assumed that for a point source imaged in air, the energy spectrum will not include Compton scatter. Therefore, the counts measured in the upper energy window can be assumed to be zero, the counts measured in the photopeak energy window is assumed to be the photons from the primary photopeak only and the counts measured in the lower energy window is assumed to be the photons from the photopeak which are trapped due to hole tailing. Therefore, using Equation 26 and Equation 27:

$$S_P = \left(\left(\frac{C_l - hP_P}{W_l} + \frac{C_U}{W_U}\right) \times \frac{W_P}{2}\right) \quad \textbf{Equation 29}$$

Where *h* can be calculated by imaging a small sphere in air. By substituting Equation 29 into Equation 25:

$$P_P = C_P - \left(\left(\frac{C_l - hP_P}{W_l} + \frac{C_U}{W_U}\right) \times \frac{W_P}{2}\right) \quad \textbf{Equation 30}$$

Which can be rearranged to give Equation 31:

$$P_P = \frac{2C_P - w_P(C_L/w_L + C_U/w_U)}{2 - hw_P/w_L} \quad \textbf{Equation 31}$$

All parameters in Equation 31 are variables and are obtained from each imaging event, except *h* which can be calculated by imaging a small sphere in air and analysing the counts in the energy spectrum.

A 0.5ml Jaszczak sphere was filled with 4.88 MBq [^{177}Lu]Lu-DOTA-TATE and was imaged in air and in a water-filled Jaszczak phantom using six separate planar images taken in different

positions across the detector heads, as shown in Figure 29. The activity in the sphere was drawn up from a vial of [^{177}Lu]Lu-DOTA-TATE using a syringe and then injected into the 0.5 ml sphere. The activity in the vial was measured in a radionuclide calibrator before and after the syringe removed an amount of activity. The activity residual of the syringe was also measured. The planar images were acquired with a 256x256 matrix, a 2.21 mm pixel size and were imaged for 300s. The images were acquired in list mode.

A: Sphere in air **B: Sphere in scatter**

Figure 29: Phantom set up for 0.5 ml sphere in air (A) and sphere in scatter (B) planar images acquired for six positions across the detector

The energy spectrum of each planar image was reviewed through the GE Lister application and the energy spectrum was exported to a .txt file for further analysis.

The energy spectrum analysis was completed using Microsoft Excel. The mean, standard deviation, maximum and minimum counts in each energy bin were calculated for both the sphere imaged in air and in scatter across all positions imaged. The mean counts across the different positions imaged were plotted against energy (keV). The energy spectrum data was separated for the 113 keV and 208 keV photopeaks and normalised for each for visual assessment. The normalised counts (C_N) were calculated using Equation 32. Where C_{mean} are the mean counts for the different positions imaged and C_{min} and C_{max} were the minimum and maximum counts in the range being normalised to, respectively.

$$C_N = \frac{C_{mean} - C_{min}}{C_{max} - C_{min}} \qquad \textbf{Equation 32}$$

To assess the effect of scatter on the energy spectrum the energy spectra were normalised to the 208 keV peak. The energy spectra were binned into different energy windows as displayed in Table 9. The averaged normalised counts for each keV were summed across each energy bin.

Table 9: Energy ranges used for the sphere in air and sphere in scatter energy bins

Energy Bin	Lower Energy (keV)	Upper Energy (keV)
113 keV lower	96	101
113 keV peak	102	124
113 keV upper	125	137
208 keV lower	167	185
208 keV peak	187	228
208 keV upper	229	252

The quantity of photons from the primary energy window, which were detected in the lower scatter energy window was calculated by dividing the normalised counts in the lower energy window measured in the sphere in air by the normalised counts in the primary energy window (as described in Equation 28), for both the 113 keV peak and the 208 keV separately. This variable, defined as *h*, is the hole tailing contribution to the lower energy scatter window and was used in the SC equation derived.

4.2.2.2 Practical Implementation of Scatter Correction Technique

GE Xeleris was used to create an Aladdin script for this CZT SC method, by adapting a local Aladdin script for TEW SC using the Ogawa method [72]. The isotope list and energy windows were updated (as described in section 4.1). The SC method was updated to: "PValues_scatter(zz,yy,xx) = (2*Pvalues1(zz,yy,xx) – e_width1*0.5*(Pvalues2(zz,yy,xx)/e_width2*0.5 + Pvalues3(zz,yy,xx)/e_width3*0.5)) / (2 - h * e_width1*0.5/ e_width2*0.5)", based on Equation 31. Therefore, the script was updated for the *h* values calculated from sections 4.2.2.1 and 4.2.3.1.

4.2.3 Results

4.2.3.1 Scatter Correction Method Derivation

The mean of the counts per energy bin over the full energy spectra for the sphere imaged in air and in scatter across the six different detector positions is shown in Figure 30. The effect of scatter on the energy spectra can be seen as the two photopeaks are significantly decreased for the sphere in scatter compared to the sphere in air images.

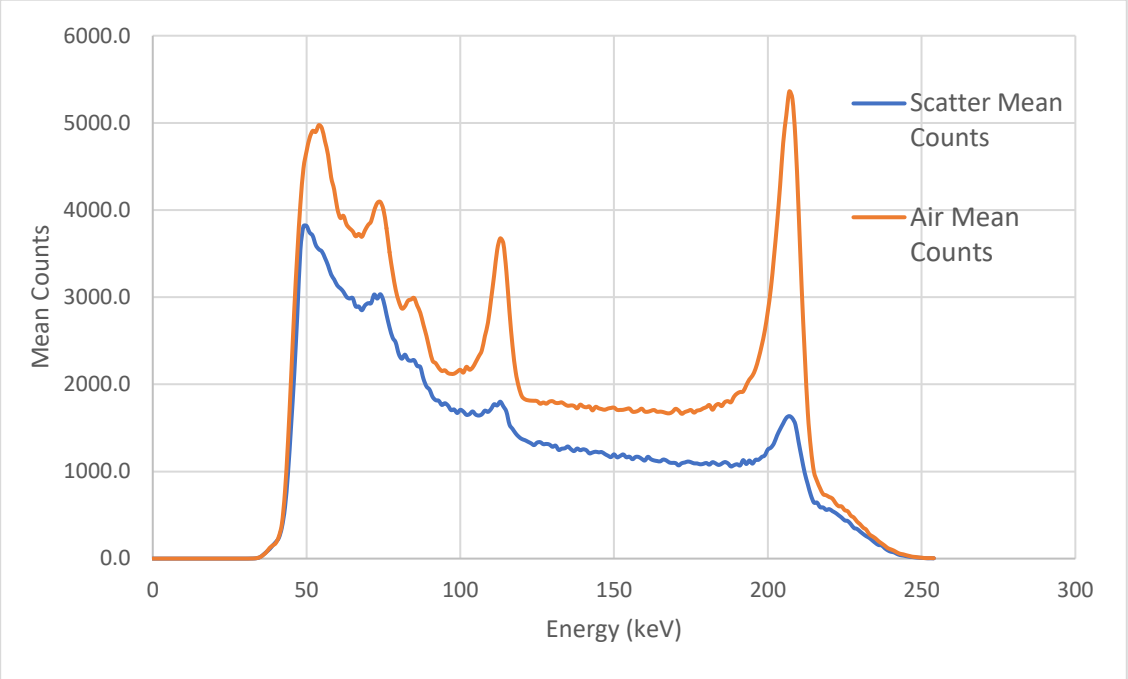

Figure 30: The mean counts per energy bin for the six sphere in air and sphere in scatter planar images

The normalised counts for the two photopeaks are shown separately in Figure 31 (for 113 keV and 208 keV). The 113 keV photopeak is affected by scatter more than the 208 keV photopeak. Both photopeaks show that there is a different shape to the energy peak for the lower energy compared to the higher energy, which is more clearly seen in the 208 keV photopeak than the 113 keV photopeak.

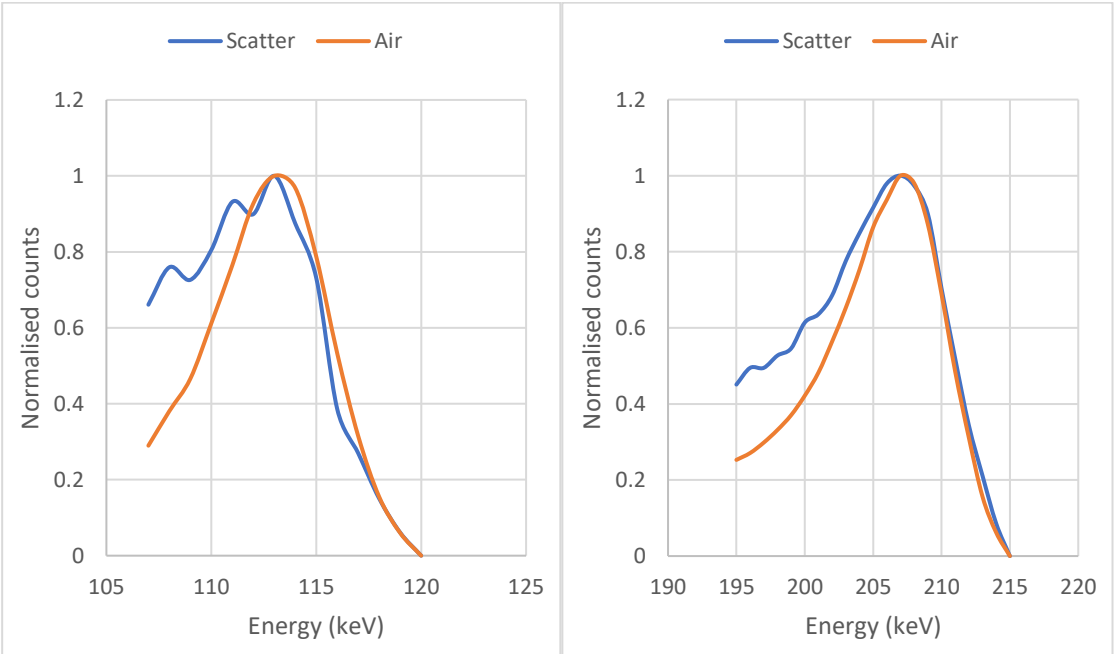

A: 113 keV photopeak | **B: 208 keV photopeak**

Figure 31: The mean normalised counts per energy bin for the 113 keV photopeak (107 - 120 keV) for the sphere in air and sphere in scatter (A) across all positions imaged over gamma camera detector and the mean normalised counts per energy bin for the 208 keV photopeak (195 - 215 keV) for the sphere in air and sphere in scatter (B) across all positions imaged over gamma camera detector

The results for the values of *h* calculated using the normalised energy spectra for sphere in air, where the data was normalised to the 208 keV peak, are shown in Table 10. The value for *h* therefore changes depending on the energy spectra and photopeak being imaged, and therefore the SC method will need to be updated for the optimal value for *h*.

Table 10: The summed normalised counts for each energy window and the calculated value for *h* for each photopeak for the sphere in air

Energy Window (keV)	Normalised counts summed for sphere in air	Calculated value for h
113 lower scatter (96 – 101)	2.39	
113 photopeak (102 – 124)	10.74	0.22
113 upper scatter (125 – 137)	4.31	
208 lower scatter (167 – 185)	6.04	
208 photopeak (187 – 228)	17.05	0.35
208 upper scatter (229 – 252)	0.62	

4.2.3.2 Practical Implementation of Scatter Correction Technique

The Xeleris Aladdin script for the CZT TEW SC technique was implemented successfully and was used throughout the following sections, where the value of *h* was adjusted as required.

4.2.4 Discussion

A new method of SC for a CZT gamma camera has been developed, which can be implemented easily for clinical imaging. The method was based on validated techniques used in the literature and was based on the concept that TEW SC would be required for ^{177}Lu imaging, but the hole tailing effects of the CZT gamma camera required an additional factor to account for them and avoid over correcting [72], [102], [145], [146]. The proposed CZT TEW SC method was successfully incorporated into an Xeleris Aladdin script for ease of use and was applied to a range of phantom images.

There are several underlying assumptions used in this method, which include the hole tailing effects are constant, a sphere in air image includes no scattered photons, and the TEW SC presented by Ogawa et al [72] is accurate. However, none of these assumptions are completely true. There are differences in the values of *h* for the 113 keV and 208 keV photopeaks (0.22 and 0.35, respectively), and therefore *h* is not constant. It is unlikely that the sphere in air energy spectrum is fully free from scatter as there will be other objects that will cause photons to scatter, which will be detected by the gamma camera. The Ogawa TEW SC technique is widely used and accepted as a simple method for SC, however it does assume an average scatter contribution across the photopeak energy window, which can be calculated as an average of the upper and lower energy windows. These points are discussed further below and in section 4.6.

A value for *h* was determined using a sphere in air to reduce the effect of scatter within the image and isolate the hole tailing effects. The value of *h* was calculated as different values for each of the photopeaks, where value of *h* for the 208 keV photopeak was greater than for the 113 keV photopeak (shown in Table 10), which suggests that there was a greater hole tailing effect in the 208 keV photopeak compared to the 113 keV photopeak. The value of *h* would therefore need to be determined for each energy being imaged and therefore a range of values of *h* would need to be determined for clinical use and therefore would require optimisation. This CZT TEW SC method is a simple method and therefore there are some assumptions used, which will make the method less accurate than those SC methods developed by Fan et al [146] and Kacperski et al [102], however this may make it easier to implement in a clinical setting. This method includes TEW SC which is a benefit compared to Pourmoghaddas et al [145], as their method was DEW SC, which would not be suitable for dual photopeak imaging. Therefore, this method provides a practical solution for CZT TEW SC. The method for calculating the hole tailing effects were similar to the methods used by Pourmoghaddas et al [145] and their calculated *k* (equivalent to *h*) to be 0.17 ± 0.02 for ^{99m}Tc, which is close to the values calculated in Table 10 for ^{177}Lu. These values cannot be directly compared as they are for different radionuclides, however the methods used to calculate them are similar. However, to fully validate the value of *h* used it would need to be applied to various phantoms and the images and energy spectra will need to be compared to other SC techniques and no SC, which is discussed further in section 4.6. It would also be helpful to calculate a value for *h* for ^{99m}Tc so the results could be directly compare to Pourmoghaddas et al [145].

The sphere was also imaged in scatter and the energy spectra were compared for both the scatter mediums (shown in Figure 30 and Figure 31). There is a clear reduction in counts when the sphere was imaged in water compared to air, which is to be expected. The most significant

reduction in counts were for the two photopeaks (113 and 208 keV), but less significant reduction at other energies. These energy spectra are from planar images and therefore attenuation is going to have a significant reduction in the counts for the air in scatter energy spectrum. There will be more scattered photons in the sphere in scatter phantom than the sphere in air, therefore increasing the relative counts below 208 keV which are not at the photopeaks. The next sections in this work will cover SPECT acquisitions, where the images are attenuation and scatter corrected, which will reduce the effects seen in the planar images in this section.

The normalised counts energy spectra for the sphere in air and sphere in scatter for each photopeak (shown in Figure 31) indicate that the lower energy counts are much greater for the sphere in scatter than for sphere in air, which is due to the scattered photons. However, it is also possible that the hole tailing effect is different for different scatter conditions. As both the Compton scattered photons and the hole tailing photons would appear in the lower energy side of the energy spectra it is not possible to distinguish the split of the contributions are using this method alone, and therefore requires further investigation.

4.3 Sensitivity

4.3.1 Introduction

The sensitivity of the CZT gamma camera for imaging ^{177}Lu was established using a cylindrical phantom, which could be used as a calibration factor for the gamma camera counts to activity measured. The sensitivity was measured for a range of reconstructions to assess the variation.

4.3.2 Methods

A cylindrical phantom was used for the sensitivity measurement. The phantom was filled with approximately 80% water and then 39 MBq [^{177}Lu]Lu-DOTA-TATE was injected into the phantom and mixed. Water was added until it was at the total volume of the phantom and mixed again. The times of the activity measurement and scan time were recorded so the activity could be decay-corrected to the scan time.

The phantom was imaged using a SPECT/CT and six energy windows (as described in section 4.1) so that both photopeaks could be imaged with scatter windows. The WEHR collimator was used, 40 seconds per view, 120 views, 128x128 matrix and a voxel size of 4.42 mm as shown is Figure 32. The CT used a 512x512 matrix, 5mm slices, helical, 120 kV (kilovolts) and 20 mA (milliamps). The centre of rotation (COR) correction was on.

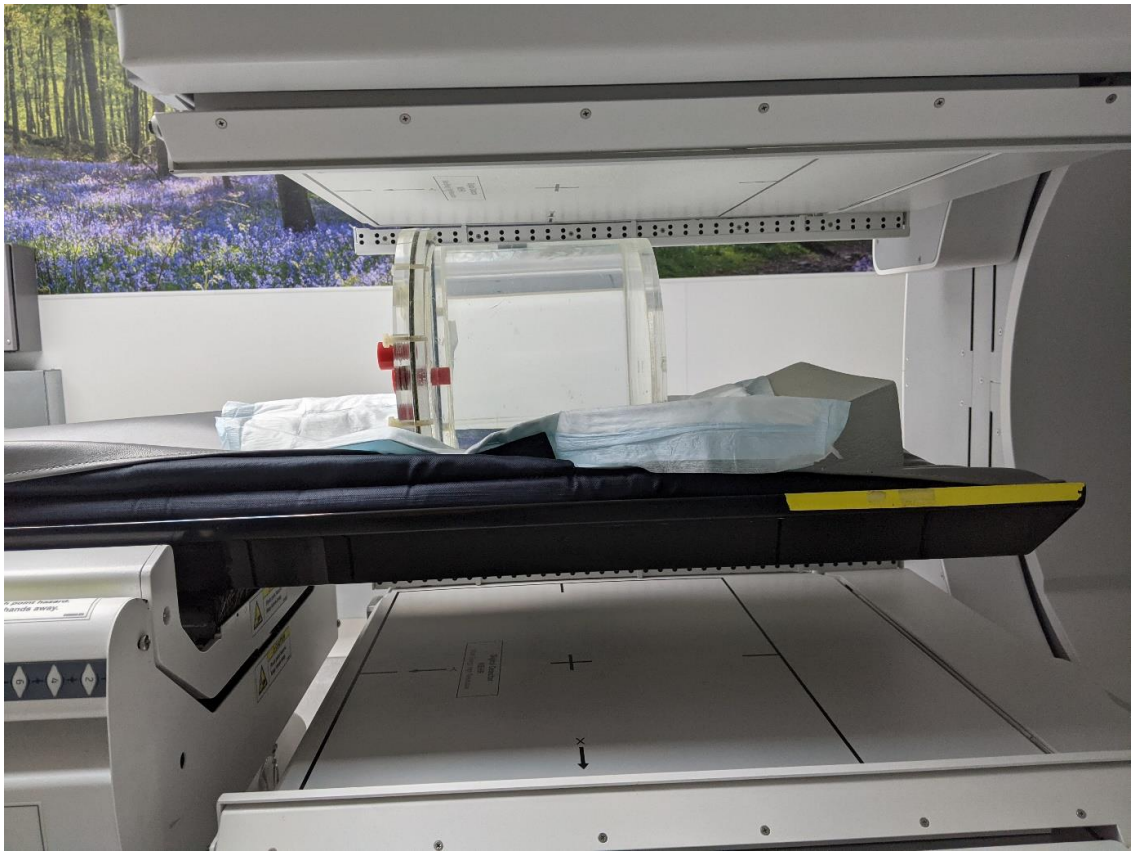

Figure 32: The set up for the SPECT/CT of the sensitivity phantom

Xeleris Volumetrix software (version 4.12, GE Healthcare) was used to reconstruct the images using a range of parameters to assess how the sensitivity changed with SC method, OSEM reconstruction with a number of updates, photopeak selection and RR setting. The SC methods included the CZT TEW SC (as derived in section 4.2.2.1 and shown in Equation 31) with a range of values for *h*, the Ogawa TEW SC (as discussed in section 2.6.1 and shown in Equation 4) and NSC. The number of updates ranged from 10 to 200. All reconstructions included CTAC as part of the reconstruction.

The images were processed using Amide [170] and two different sizes of VOIs, based on EANM ^{131}I-MIBG dosimetry guidelines [171] and MRTDosimetry [172]. EANM suggest using a VOI 75% of the volume of the phantom and MRTDosimetry suggest using a VOI with 130% of the phantom radius and 120% of the phantom length. Amide allows multiple images to be imported and results from the VOI analysis can be exported in a table for the same set of VOIs across multiple images.

Amide exports the VOI results as the mean value of each voxel and the size of the VOI. Therefore, total counts was calculated using Equation 33:

$$C_T = C_m \times \frac{V_T}{V_V} \quad \textbf{Equation 33}$$

Where is C_T and C_m are the counts in the total VOI and mean counts per voxel and V_T and V_V are the volume total volume and the volume of each voxel, respectively. Sensitivity was calculated using Equation 34:

$$S = \frac{{}^{C_T}/_t}{A} \quad \textbf{Equation 34}$$

Where *S* is the sensitivity factor (in cps/MBq), *t* is the scan time in seconds and *A* is the activity at scan time in MBq. For the larger VOI the total activity injected into the phantom was used. For the 75% VOI the fraction of activity within the VOI was calculated by calculating the volume of the 75% VOI of the phantom and then dividing by the total volume of the phantom. The activity with the 75% VOI was then the fraction of the VOI to the total phantom volume, multiplied by the total activity. The uncertainty for the sensitivity was calculated using Equation 13, as per the EANM guidance [81], in Microsoft Excel.

4.3.3 Results

The sensitivity results for a range of reconstruction methods, including uncertainties, are summarised into two categories; with RR and without RR, are shown in Figure 33 and Figure 34, respectively. The smaller VOI results in a lower sensitivity than the larger VOI, which is more significant for the 208 keV photopeak, compared to the 113 keV photopeak. There is septal penetration in the 208 keV images and therefore that could cause the sensitivity to be overestimated, which is likely to be more significant in the larger VOI than the smaller VOI.

The CZT TEW SC with *h* equal to 0.35 results in a greater sensitivity than for *h* equal to 0.22. The sensitivity is greater for the lowest number of updates (1 iteration and 10 subsets) and then reduces until it plateaus at approximately 50 updates (5 iterations and 10 subsets) for all VOI sizes, SC method and energy photopeak. RR significantly increases the sensitivity results compared to the reconstructions without RR. RR affects the sensitivity calculated with the smaller VOI more than the sensitivity calculated with the larger VOI for the lowest number of updates.

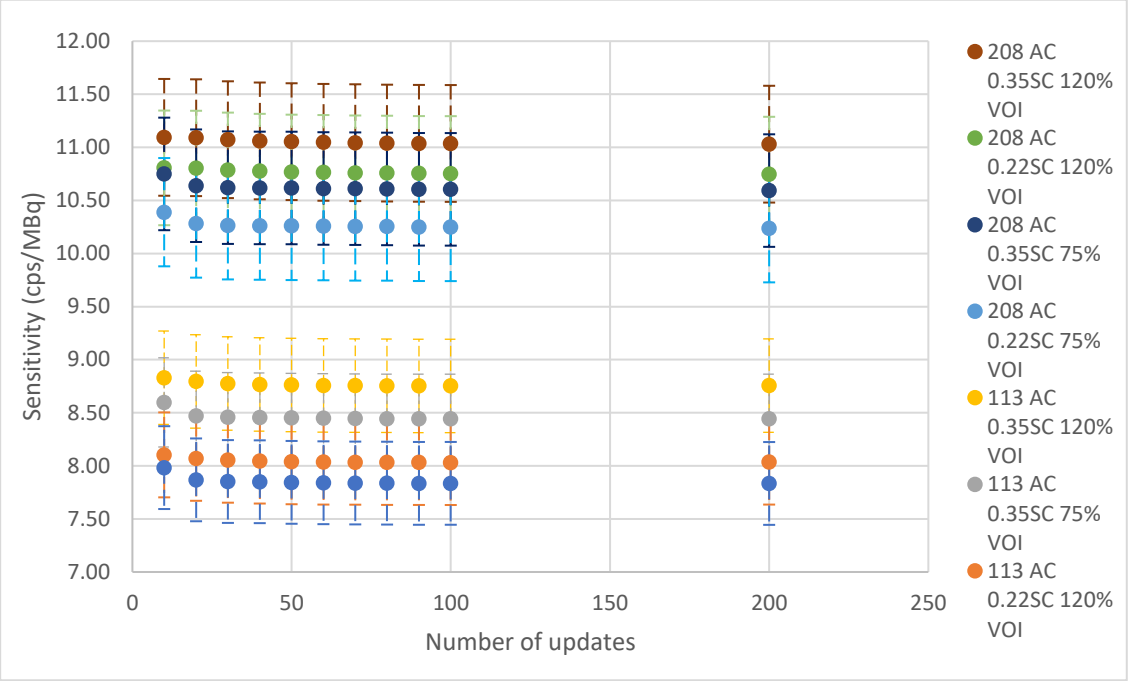

Figure 33: Calculated sensitivity plotted against number of updated for the 75% VOI and the 120% VOI for the 113 keV and 208 keV AC without RR reconstruction with *h* equals 0.22 and 0.35, where the uncertainties are displayed for each point in colour coded bars

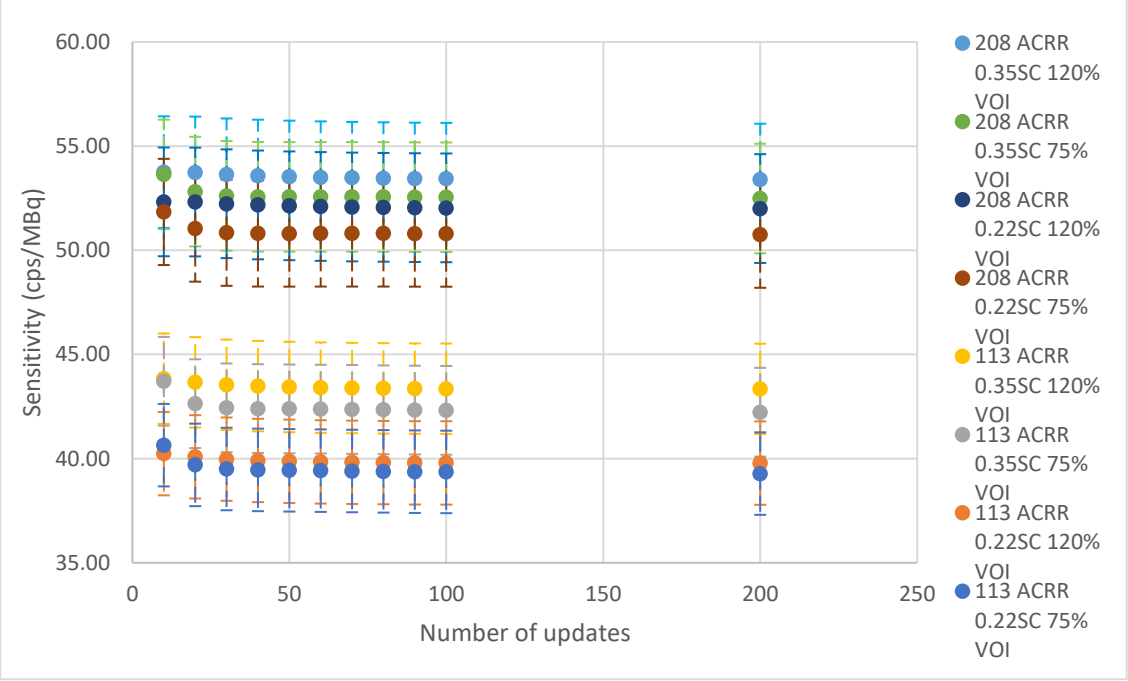

Figure 34: Calculated sensitivity plotted against number of updated for the 75% VOI and the 120% VOI for the 113 keV and 208 keV AC with RR reconstruction with *h* equals 0.22 and 0.35, where the uncertainties are displayed for each point in colour coded bars

The sensitivity was compared for a set number of updates (5 iteration and 10 subsets) using only the 75% VOI, to avoid the potential overestimate of sensitivity, shown in Table 11. The maximum

calculated sensitivity was for the CZT TEW SC with *h* equals 1 and the minimum calculated sensitivity was for Ogawa TEW SC method. The sensitivity for the 208 keV peak was generally greater than for the 113 keV peak.

Table 11: Sensitivity values calculated in cps/MBq with associated uncertainty for a range of reconstruction parameters and SC techniques (NSC, CZT TEW SC for a range of *h* values and Ogawa TEW SC) for 5 iterations and 10 subsets with and without RR and for both the photopeaks

Sensitivity (cps/MBq)				
Scatter Correction	**113 keV**		**208 keV**	
	AC	**ACRR**	**AC**	**ACRR**
NSC	10.87 ± 0.54	55.11 ± 2.76	10.65 ± 0.53	52.77 ± 2.64
0.1SC	7.19 ± 0.36	36.03 ± 1.80	9.98 ± 0.50	49.39 ± 2.47
0.22SC	7.84 ± 0.39	39.42 ± 1.97	10.25 ± 0.51	50.81 ± 2.54
0.35SC	8.45 ± 0.42	42.35 ± 2.12	10.61 ± 0.53	52.56 ± 2.63
1SC	13.31 ± 0.67	66.87 ± 3.34	13.70 ± 0.69	67.88 ± 3.39
TEW Ogawa	4.17 ± 0.21	20.48 ± 1.02	6.91 ± 0.35	33.99 ± 1.70

The images for the sensitivity phantom, viewed in Mirada DBx (Mirada Medical, Oxford) for 5 iterations, 10 subsets and, CZT TEW SC with *h* equals 0.22, for 113 keV and 208 keV without RR are displayed in Figure 35, where minor septal penetration artefact was observed, however this is more clearly identified in section 4.4. There is less counts and more noise seen in the 113 keV images, compared to the 208 keV images. There was no evidence of the ^{177}Lu-labelled compounds sticking to the walls of the phantom (or plating out [173]) within the phantom images.

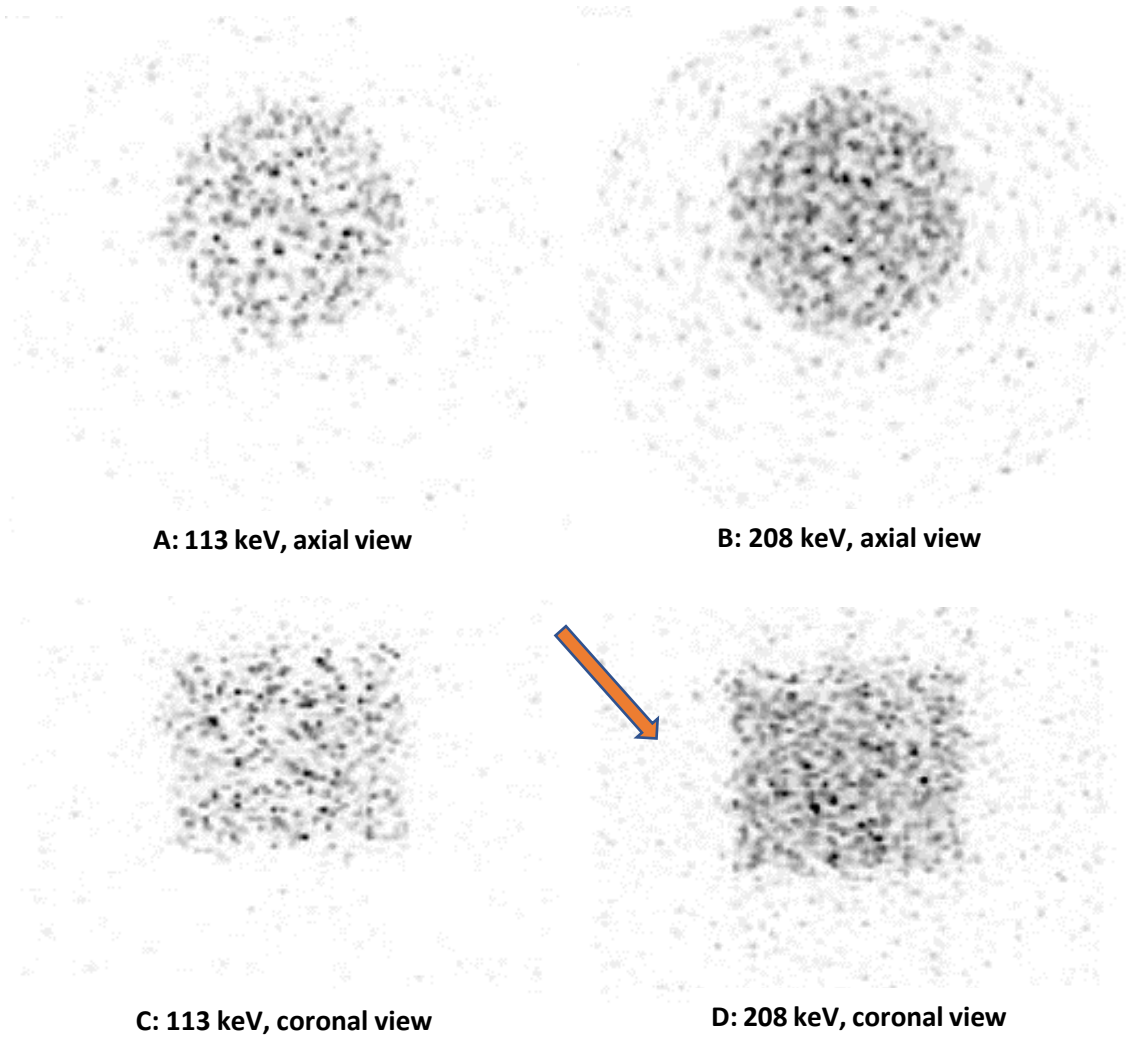

A: 113 keV, axial view

B: 208 keV, axial view

C: 113 keV, coronal view

D: 208 keV, coronal view

Figure 35: The sensitivity phantom images, displayed in Mirada, for 5 iterations, 10 subsets, CTAC, no RR and CZT TEW SC with *h* equals 0.22 for; 113 keV (A and C) and 208 keV (B and D) for the axial (A and B) and coronal (C and D) planes. Minor septal penetration artefact is observed in the 208 keV coronal image (D), as indicate by the orange arrow.

4.3.4 Discussion

There are a range of sensitivity values calculated for the different reconstruction and SC techniques used (seen in Figure 33, Figure 34, and Table 11). When RR was applied the sensitivity value was increased by approximately a factor of 5, which is mostly due to the RR algorithm used by Xeleris (GE Healthcare), which includes a default multiplication factor of 4 [174]. For any VOI size, energy window, SC technique and with or without RR, the sensitivity values decreased with increasing number of updates from 10 updates to approximately 50 updates, where the sensitivity value was generally consistent. This can help identify an optimised number of updates for the optimised reconstruction technique, which is further discussed in section 4.4.

The smaller VOI gave lower sensitivity values compared to the larger VOI, which is due to the spill over counts that would be included in the larger VOI, which are not included in the smaller VOI. There was a larger difference between different VOI methods for the 208 keV photopeak than for the 113 keV photopeak, which is likely due to the septal penetration artefact (also observed by Kennedy et al [150]) that can be seen in some of the 208 keV images (for example in Figure 35, image D), and therefore is likely to be the less accurate method, which is further discussed in section 4.6. When reviewing the literature for methods of calculating sensitivity, seen in Table 4, most studies used a VOI that was either the same size as the object, or larger, however as there are septal penetration artefacts for the WEHR collimators used this is unlikely to be the most accurate method, unless another correction can be included for the septal penetration artefact.

The sensitivity for the 208 keV photopeak is greater than for the 113 keV photopeak, which is because the height of the 208 keV photopeak is greater than the 113 keV photopeak and therefore there will be more counts for the same about of activity in the 208 keV energy window compared to the 113 keV energy window. The CZT TEW SC value of *h* effected the sensitivity values. The greater the value of *h* the great the sensitivity value, which indicates that the greater the number of photons that are released due to hole tailing effects the greater the sensitivity.

When comparing the NSC and Ogawa TEW SC to the CZT TEW SC technique, the sensitivity is least for the Ogawa TEW SC and second most for the NSC images. However, when the value of *h* is increased to 1, the CZT TEW SC provides a larger sensitivity than for the NSC technique. This could suggest that the Ogawa TEW SC technique is overcorrecting the images, which could be because the hole tailing effects are not considered in this SC technique. The value of *h* for the CZT TEW technique is further discussed in section 4.6. The uncertainties calculated for each sensitivity value are generally around 5%, as seen in Table 11.

The images produced (shown in Figure 35) for a fixed number of updates, but with different photopeaks, show a slight difference between the two photopeaks. The activity concentration used was relatively low and therefore the images are noisy. There is a very slight indication that there is septal penetration seen in the 208 keV photopeak in the coronal plane, however this will be more clearly seen in section 4.4.

When comparing the sensitivity calculated here to the literature, the Ogawa TEW SC for the 113 keV and 208 keV can be directly compared to Kennedy et al [150]. The sensitivity value for 113 keV for Ogawa TEW SC for Kennedy et al was 5.5 cps/MBq and therefore greater than the 113 keV sensitivity without RR for Ogawa TEW SC (4.17 cps/MBq), but less than the 113 keV

sensitivity with RR for Ogawa TEW SC (20.48 cps/MBq). However, if Kennedy et al removed the factor of 4 applied during the RR algorithm then their sensitivity value would be approximately 22 cps/MBq, which is comparable to the value calculated in this work. Kennedy et al did not specify how they calculated their value of sensitivity and therefore if they choose a larger VOI than 75% then the sensitivity will be greater, which could therefore account for the difference. For the 208 keV photopeak the sensitivity for Kennedy et al (6.1 cps/MBq) was less than calculated in this work for both the values without RR (6.91 cps/MBq) and with RR (33.99 cps/MBq). This could be explained by inconsistent VOI methods or by the difference in scatter energy windows selected. Kennedy et al used narrower energy windows for the scatter energy windows, which were placed closer to the photopeak than this work, which would therefore lead to a greater average scatter contribution being subtracted from the 208 keV photopeak than in this work.

The results from the CZT gamma camera sensitivity calculated in this work were comparative to the sensitivities calculated for NaI gamma cameras, summarised in Table 5. The range of sensitivity values for the 113 keV photopeak using the CZT TEW SC in this work were 7.19 – 13.31 cps/MBq and for the NaI literature review were 3.57 – 5.81 cps/MBq. The range of sensitivity values for the 208 keV photopeak using the CZT TEW SC in this work were 9.98 – 13.70 cps/MBq and for the NaI literature review were 1.78 – 10.8 cps/MBq. This indicates that the CZT gamma camera is more sensitive than the NaI gamma camera, when an appropriate SC technique is used, which agrees with Imbert et al [133].

4.4 Optimisation of Reconstruction

4.4.1 Introduction

A range of reconstruction parameters, including number of updates, SC technique and use of RR were used to establish the optimal reconstruction parameters. These reconstruction parameters were applied to a selection of different size spheres to assess variations in counts and activity recovery.

4.4.2 Methods

Nine spheres with different volumes were imaged in scatter to optimise the reconstruction parameters. Six spheres were used from a Jaszczak phantom which were 0.5 ml, 1 ml, 2 ml, 4 ml, 8 ml and 16 ml. Three spheres were 3D printed spheres by National Physics Laboratory (NPL) which were 100 ml, 150 ml and 200 ml. The ^{177}Lu was dispensed from the residual from the patient vials into a schott vial and diluted as appropriate. The activity dispensed for each sphere was calculated by subtraction method from a schott vial. For the three largest spheres a bottle

was used to dilute the activity into the correct volume. The bottle was weighed before and after adding and removing the activity so the activity concentration could be calculated for the bottle. The spheres were weighed before and after the activity was added so the total activity could be calculated for the spheres. For the six smallest spheres an activity check was possible by adding the spheres individually into the radionuclide calibrator. The time of activity measurement was recorded. The activity for each sphere is recorded in Table 12.

Table 12: Volume, weight and ^{177}Lu activity of each sphere for optimisation of reconstruction and PVC

Nominal Sphere volume (ml)	Sphere Radius (mm)	Empty weight (g)	Full weight (g)	Measured Volume (ml)	Activity from vial subtraction method (MBq)	Time	Activity check from sphere (MBq)	Time
0.5	4.92	4.5680	5.1047	0.54	1.36	17:44	1.33	18:41
1	6.20	4.8250	5.8799	1.05	2.68	17:44	2.71	18:40
2	7.82	5.1566	7.2374	2.08	5.28	17:44	5.13	18:39
4	9.85	6.3439	10.4531	4.11	10.42	17:44	10.3	18:38
8	12.41	7.2969	15.4658	8.17	30.88	18:33	31.4	18:38
16	15.63	8.9512	25.1497	16.20	42.16	18:02	42.7	18:18
100	28.79	32.5	132.5	100	8.61	17:50		
150	32.96	41.5	193.5	152	13.09	17:50		
200	36.28	50	249.5	199.5	17.18	17:50		

The spheres were imaged in an elliptical Jaszczak phantom with a cold background of water, as shown in Figure 36. They were imaged using five individual SPECT/CTs. The three largest spheres were imaged individually. The three smallest spheres (0.5 – 2 ml) were imaged together and the three medium spheres (4 – 16 ml) were imaged together, as shown in Figure 36. The spheres were split into groups to avoid spill out from the larger spheres effecting the larger spheres. Line profiles were drawn on the SPECT images, using Xeleris, to ensure the counts were at background levels between the spheres. The SPECT images were acquired using the ^{177}Lu energy session set up in section 4.1, the WEHR collimator, 40s per view, 60 views per detector, 128x128 matrix, a voxel size of 4.42 mm and with the COR correction switched on. The CT images were acquired using a 512x512 matrix, 5mm slices, helical, 120 kV and 20 mA.

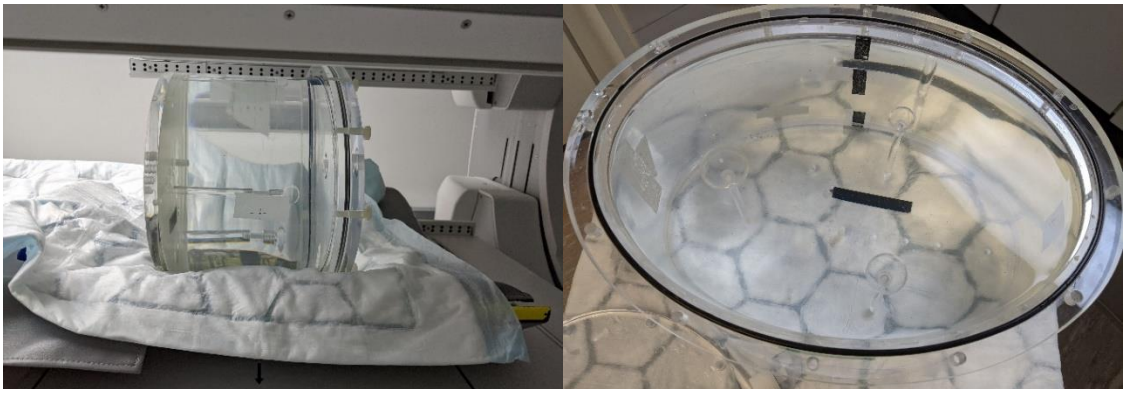

A: 0.5 – 2ml spheres on the gamma camera

B: 4 – 16 ml spheres in the Jaszczak phantom

Figure 36: Phantom set up for optimisation imaging using the smallest spheres (0.5 - 2 ml) positioned in the elliptical Jaszczak phantom on the gamma camera (A) and the medium spheres (4 - 16 ml) positioned in the elliptical Jaszczak phantom (B).

The 5 SPECT/CT images were reconstructed using Xeleris for a range of updates, SC techniques, energy windows and with and without RR. All reconstructions used CTAC. The updates ranged from 10 to 200. The SC techniques included the CZT TEW SC method, described in section 4.2.2.1 and Equation 31, with a range of values for *h*, the Ogawa TEW SC method and no SC (NSC).

The images were processed using Amide where the VOIs were drawn at 100% of the volume of each sphere. The counts within each sphere were calculated using Equation 33. The activity recovery was calculated and compared for each different sphere size. The calculated activity in each sphere was assessed by converting the measured counts into activity using the sensitivity factor, by using Equation 34 to find activity. The activity recovery was calculated by dividing the calculated activity by the known activity in each sphere (from Table 12). The activity recovery was plotted against the number of updates to assess where the plateau occurs to identify the optimal number of updates and the convergence was at least 90% of the maximum [62]. To confirm the optimal number of updates, the counts for each sphere were normalised to the counts at the start of the plateau identified for each reconstruction where the number of updates could be compared across different spheres, for the different SC methods, energy peaks and RR setting. The level of noise in each image was assessed qualitatively.

4.4.3 Results

The recovery coefficient plotted against number of updates for the 113 keV photopeak and 208 keV photopeak without RR show the recovery coefficient varies from the lowest number of updates until approximately 30 to 50 updates, where it plateaus, as shown in Figure 37 and Figure 38. Therefore, the optimised number of updates chosen was 50. The graphs appeared

very similar for the CZT TEW SC with *h* equals 0.35 and therefore examples of those graphs are not included.

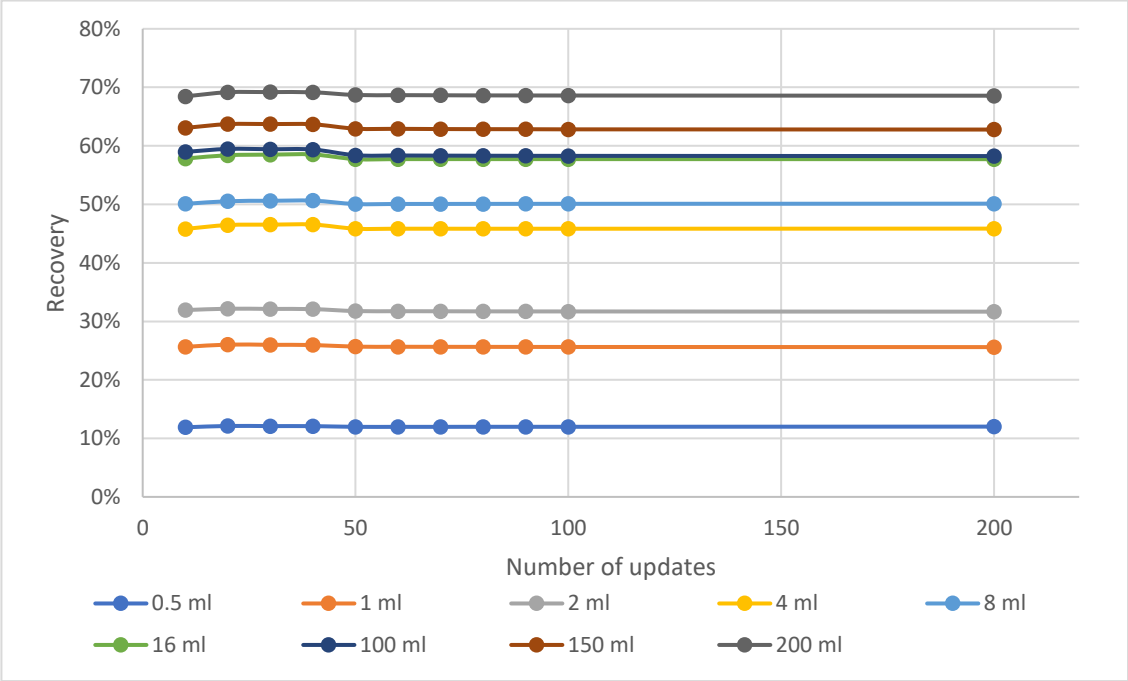

Figure 37: The recovery coefficient (%) against number of updates for a range of different size spheres for the 113 keV photopeak with AC and CZT TEW SC with *h* equals 0.22 (the lines are a visual aid)

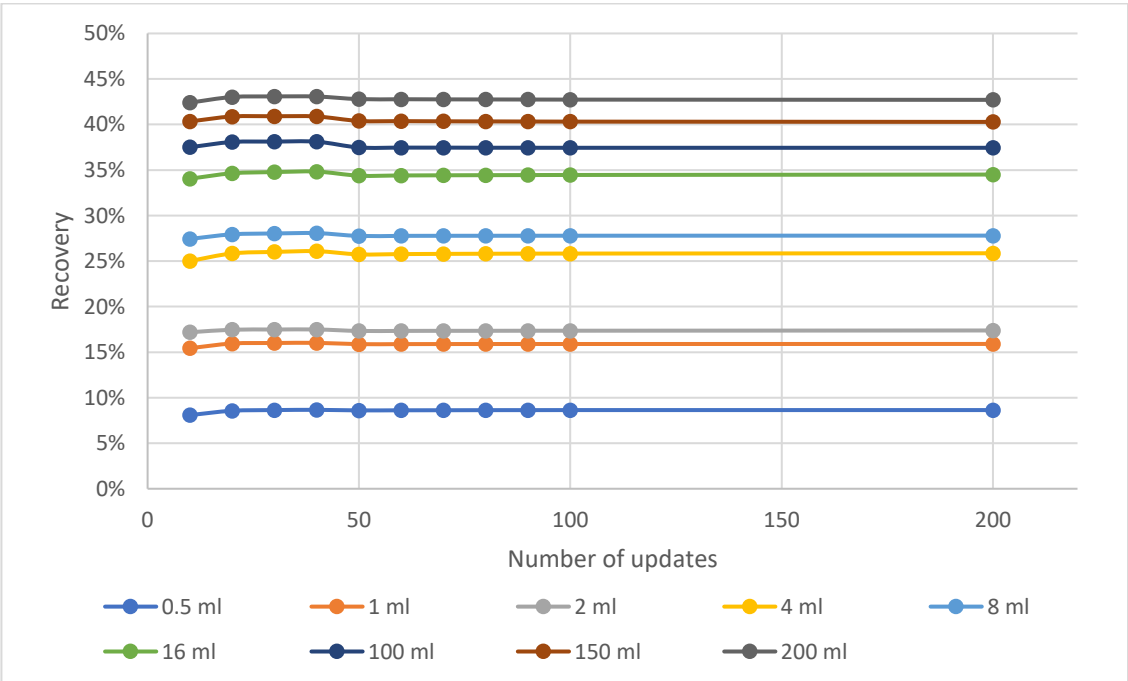

Figure 38: The recovery coefficient (%) against number of updates for a range of different size spheres for the 208 keV photopeak with AC and CZT TEW SC with *h* equals 0.22 (the lines are a visual aid)

The counts were normalised to the counts at 50 updates. The normalised counts plotted against number updates for the 113 keV photopeak and 208 keV photopeak without RR showed the counts increased from the lowest number of updates until approximately 30 to 50 updates, where it either decreased or plateaued, as shown in Figure 39 and Figure 40. The normalised counts were between 98% and 101% for 20 to 200 updates and therefore there is only a small variation in normalised counts from the optimal number of updates chosen.

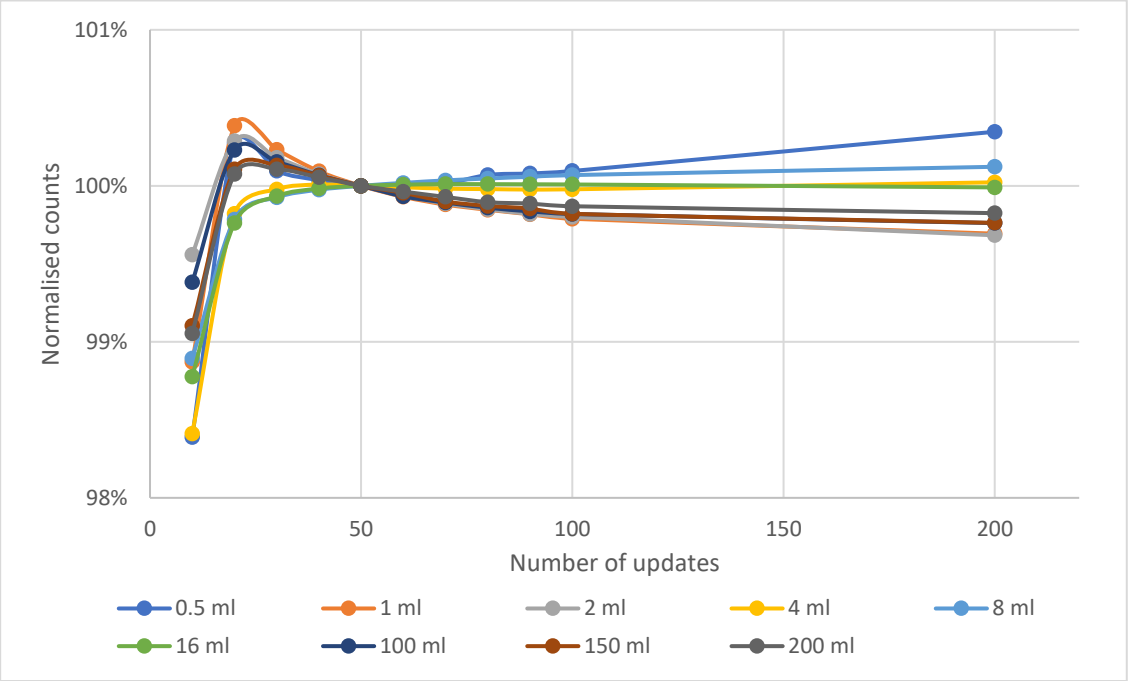

Figure 39: Normalised counts to counts at 50 updates for a range of updates and sphere volume to assess the convergence of counts for 113 keV photopeak with AC and CZT TEW SC with *h* equals 0.22 (the lines are a visual aid)

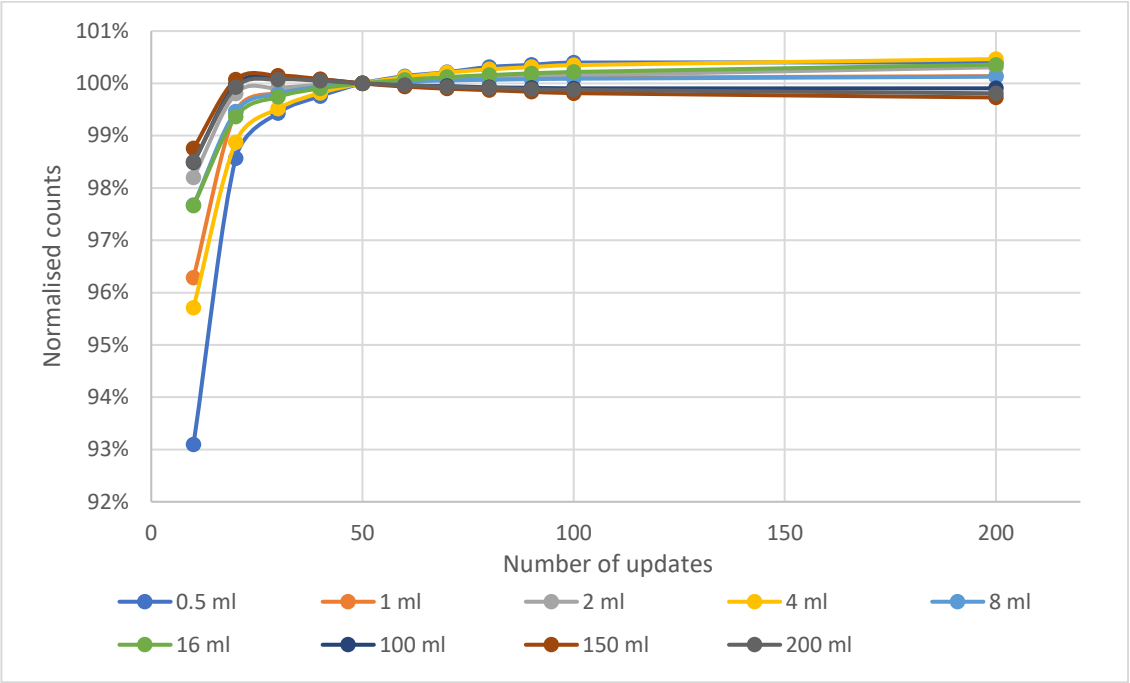

Figure 40: Normalised counts to counts at 50 updates for a range of updates and sphere volume to assess the convergence of counts for 208 keV photopeak with AC and CZT TEW SC with *h* equals 0.22 (the lines are a visual aid)

When RR was applied the recovery coefficient had a much greater range for the smaller spheres than when RR was not applied, as seen by comparing Figure 41 and Figure 42 to Figure 37 and Figure 38. With RR, the three largest spheres did appear to plateau at approximately 50 updates, however there was not a clear plateau for the smaller spheres, therefore the proposed number of updates was 50.

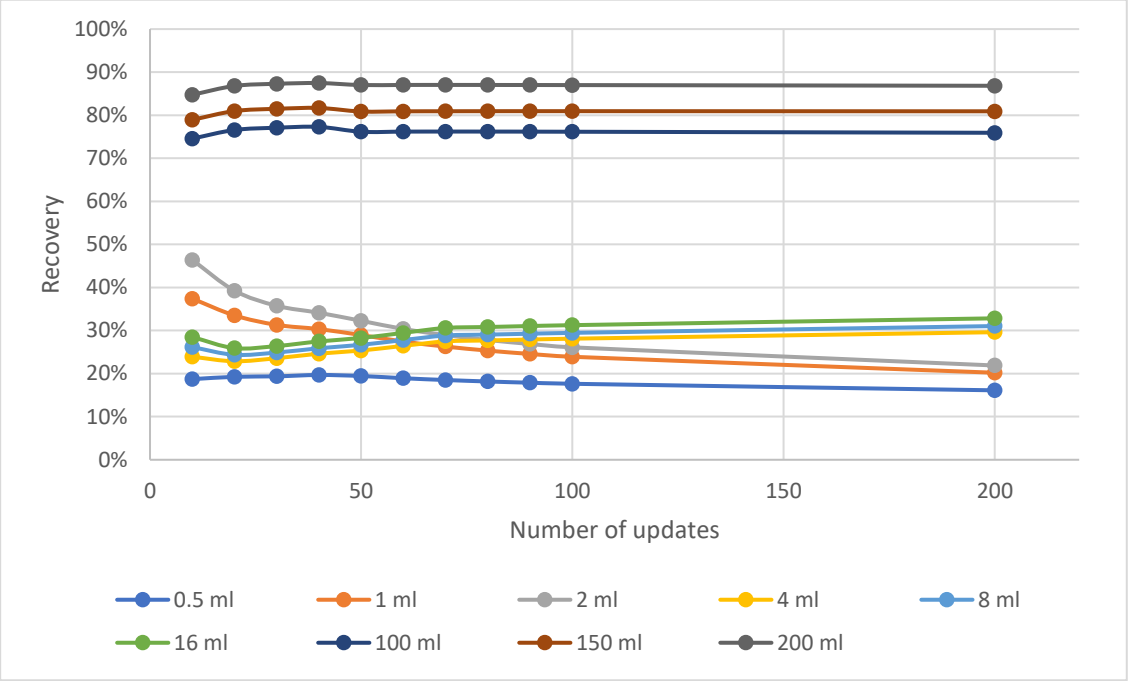

Figure 41: The recovery coefficient (%) against number of updates for a range of different size spheres for the 113 keV photopeak with AC, RR and CZT TEW SC with *h* equals 0.22 (the lines are a visual aid)

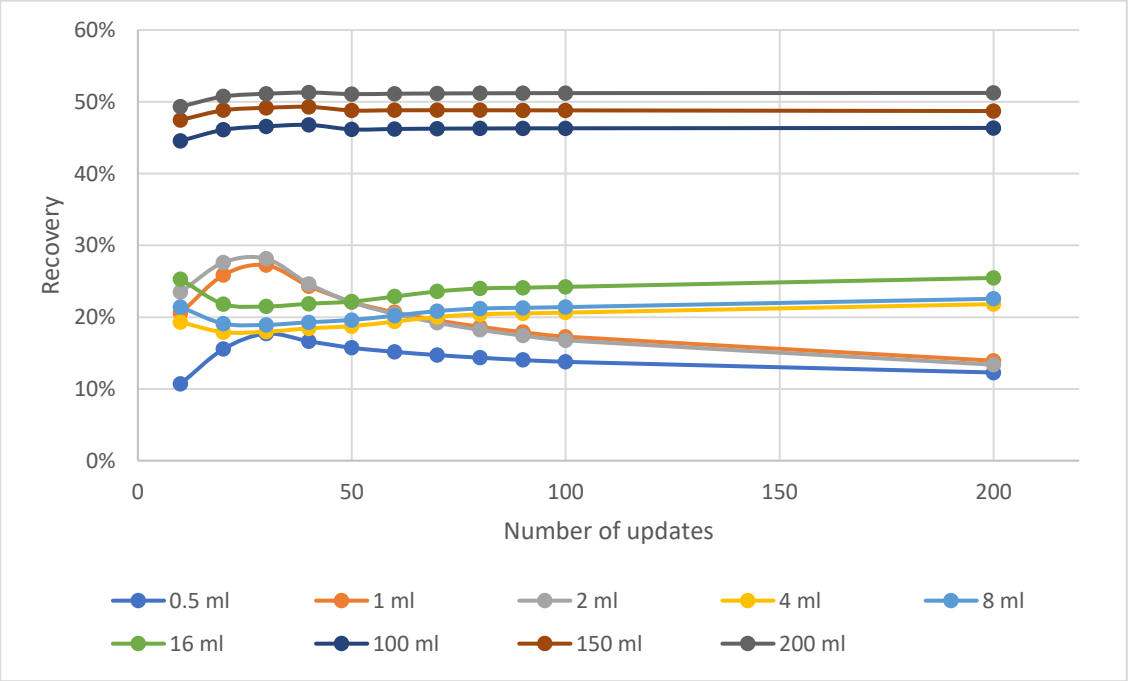

Figure 42: The recovery coefficient (%) against number of updates for a range of different size spheres for the 208 keV photopeak with AC, RR and CZT TEW SC with *h* equals 0.22 (the lines are a visual aid)

The counts were normalised to the counts at 50 updates. When RR was applied the normalised counts had a much greater range than when RR was not applied, as seen by comparing Figure

43 and Figure 44 to Figure 39 and Figure 40. With RR, in the range of 10 to 100 updates the normalised counts ranged from 81% to 142% for the 113 keV photopeak and from 67% to 126% for the 208 keV photopeak.

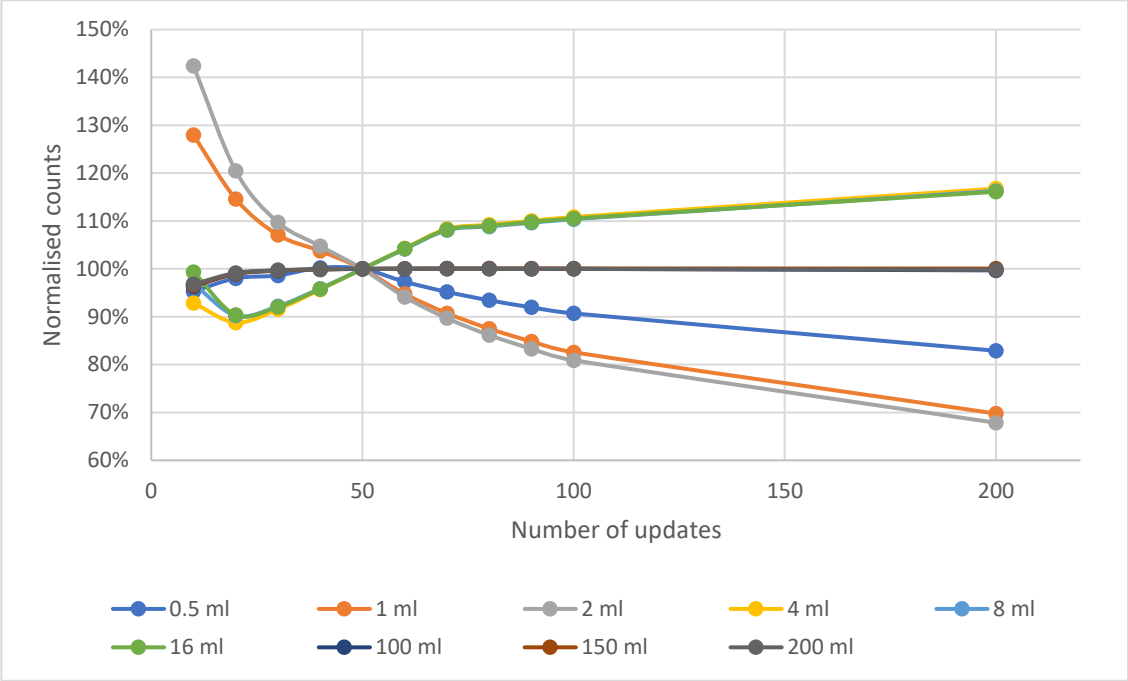

Figure 43: Normalised counts to the counts at 50 updates for a range of updates and sphere volume to assess the convergence of counts for 113 keV photopeak with AC, RR and CZT TEW SC with *h* equals 0.22 (the lines are a visual aid)

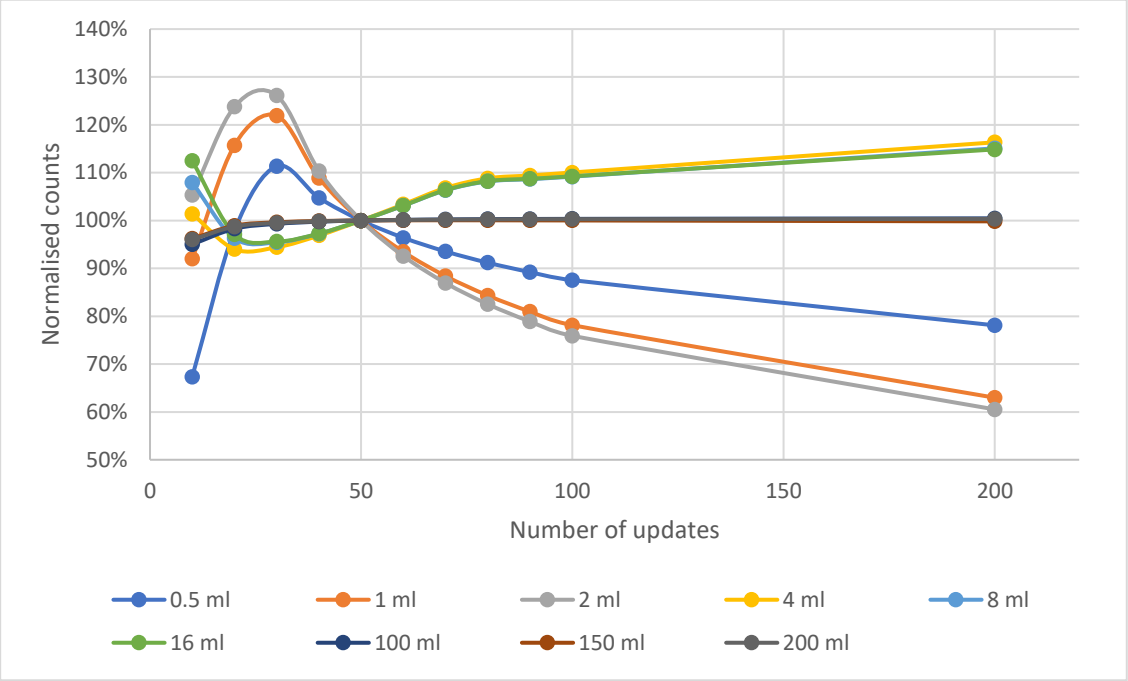

Figure 44: Normalised counts to the counts at 50 updates for a range of updates and sphere volume to assess the convergence of counts for 208 keV photopeak with AC, RR and CZT TEW SC with h equals 0.22 (the lines are a visual aid)

The images for the smallest spheres in the Jaszczak phantom, viewed in Mirada, for 5 iterations, 10 subsets and CZT TEW SC with *h* equals 0.22, for 113 keV and 208 keV without RR are displayed in Figure 45. There is a line artefact seen in the 208 keV coronal image, due to septal penetration.

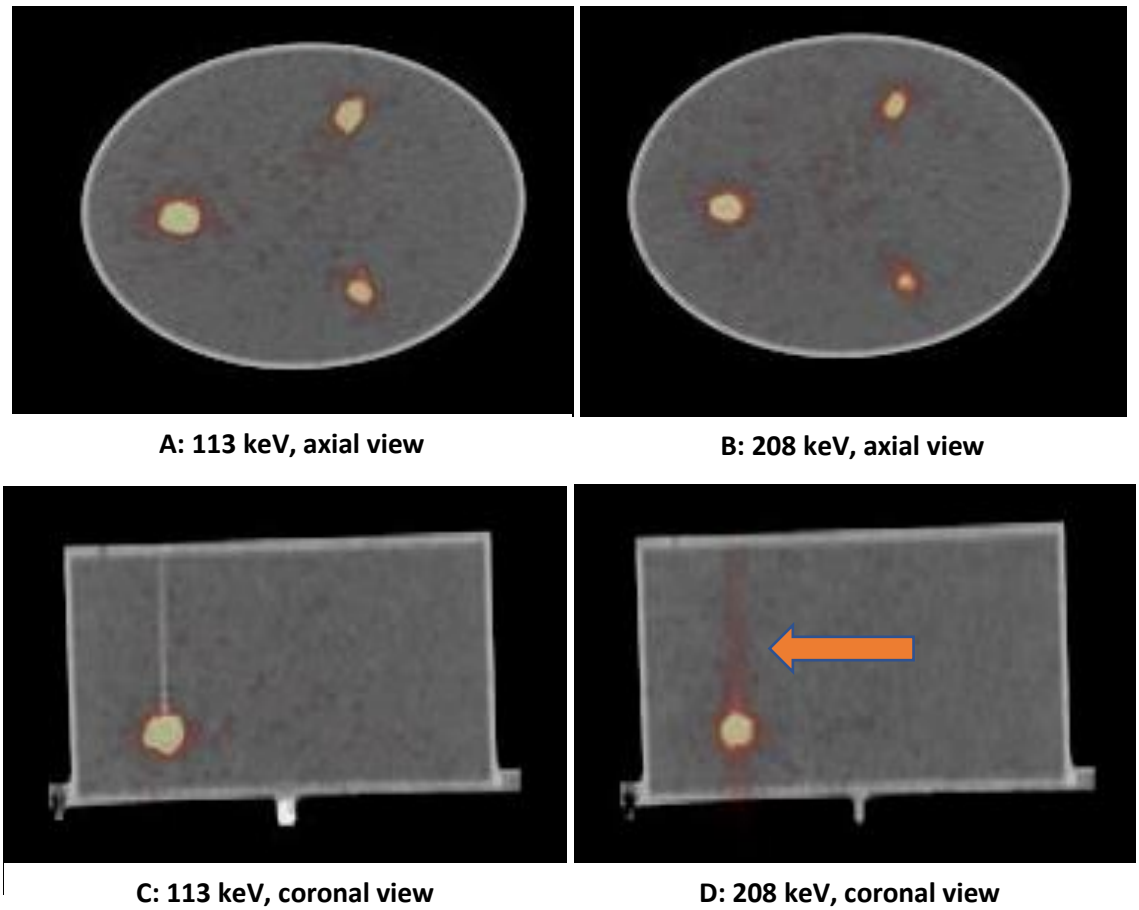

A: 113 keV, axial view **B: 208 keV, axial view**

C: 113 keV, coronal view **D: 208 keV, coronal view**

Figure 45: The 0.5 ml, 1 ml and 2 ml spheres in the water-filled Jaszczak phantom images, displayed in Mirada, for 5 iterations, 10 subsets, no RR and CZT TEW SC with *h* equals 0.22 for 113 keV RR (A and C), and 208 keV (B and D) for the axial (A and B) and coronal (C and D) planes. The orange arrow shown is pointing at an image artefact suspected to be caused by septal penetration.

The images for the medium size spheres (4 ml, 8 ml and 16 ml) in the Jaszczak phantom, viewed in Mirada, for a range of iterations, 10 subsets, CZT TEW SC with *h* equals 0.22, for 113 keV, with and without RR are displayed in Figure 46.

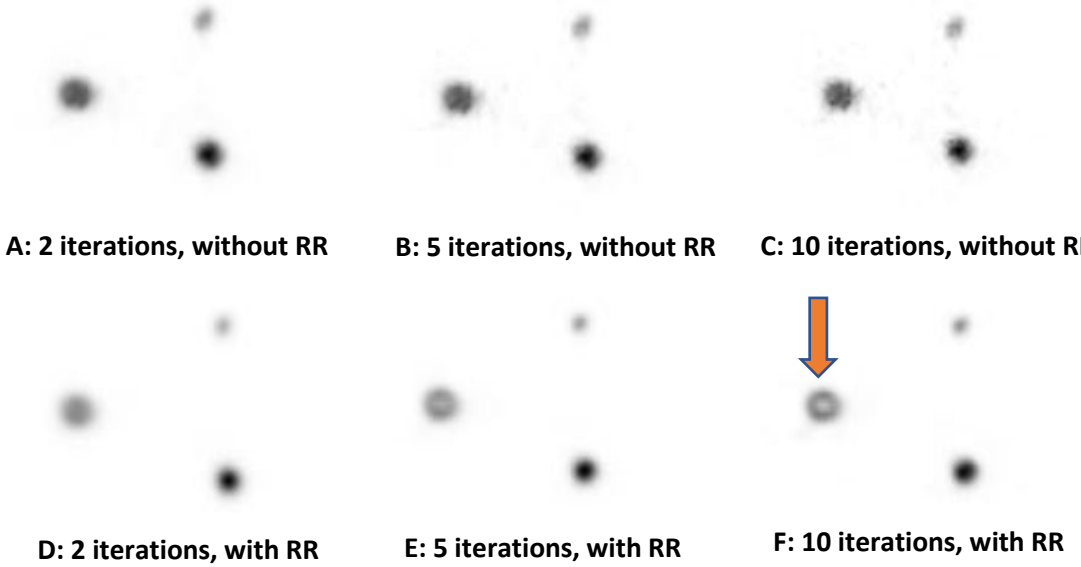

Figure 46: The 4 ml, 8 ml and 16 ml spheres in a water-filled Jaszczak phantom SPECT images, displayed in Mirada, for 10 subsets, 113 keV, CTAC and a range of iterations and with and without RR. The top row is without RR (A, B and C) and the bottom row is with RR (D, E and F). The iterations were 2 (A and D), 5 (B and E) and 10 (C and F). The orange arrow indicates an example of Gibb's artefact (F).

4.4.4 Discussion

The activity recovery was calculated for each sphere size and number of updates for a range of reconstruction parameters, which indicated the minimum number of updates where the recovery plateaued was 50, as displayed in Figure 37, Figure 38, Figure 41 and Figure 42. This was clearer for the non-RR reconstructions, than the RR reconstructions. As increasing the number of updates increases the amount of noise introduced into the image it is therefore optimal to select the minimum number of updates when the activity recovery or counts plateau, which is at approximately 50 updates. However, the level of noise was qualitatively assessed and not quantitatively assessed. The activity recovery was different for different sphere sizes, which is due to the partial volume effect, as discussed in section 2.6.4. However, the activity recovery for the 16 ml and 100 ml spheres was similar, which is likely due to the different activity concentrations used for imaging each sphere. If PVE was the only factor effecting the activity recovery across the different size spheres, then there should be a relationship between the sphere size and activity recovery. This was further investigated in section 4.5

The recovery coefficients were lower for each sphere and number of updates for the 208 keV photopeak compared to the 113 keV photopeak, seen by comparing Figure 37 to Figure 38. The 208 keV photopeak has a larger sensitivity compared to the 113 keV, as discussed in section 4.3, which accounts for the relatively higher abundance of 208 keV to 113 keV. However, the 208

keV images display a septal penetration artefact (as seen in Figure 45), which will cause some of the gamma photons to be detected outside the VOI used and will have a greater effect for smaller objects compared to larger objects. Kennedy et al also found there was reduced recovery coefficients for the 208 keV photopeak compared to the 113 keV photopeak, as displayed in Figure 24 [150].

The variation in the recovery was fairly minimal and therefore this was further investigated by investigating the normalised counts against number of updates, as seen in Figure 39, Figure 40, Figure 43 and Figure 44. The variation was less for the 113 keV photopeak compared to the 208 keV photopeak for the non-RR.

The optimal number of updates determined that there should be 5 iterations and 10 subsets, which is similar to the OSEM reconstruction used by Kennedy et al [150] and Sandstrom et al [149], who used 4 iterations and 10 subsets and 8 iterations and 8 subsets, respectively. Neither study specified how they optimised their iterations and subsets used and therefore the methods cannot be compared to this work.

The use of a post-processing filter was not investigated as the use of a post-processing filter can degrade the spatial resolution and therefore make the PVE worse, however they can be useful for suppressing noise within the image [62], [65]. The noise in an image can also be suppressed using RR, however in this work the RR appears to cause issues with the smaller spheres. The RR algorithm compensates for collimator-detector response and therefore is likely to be optimised by GE Healthcare for a standard hexagon hole collimator used by many NaI gamma cameras. When the images were reviewed, they displayed a ring artefact, called a Gibb's artefact [25], [77], [175], [176], as shown in Figure 46 for the largest (left-hand) sphere on images E and F. Gibb's artefact is an overshoot in the reconstructed counts at a high count level and it appears truncated [25], [77], [175], [176]. There is discussion in the literature about the collimator selection and RR for reasons why this artefact can occur. Therefore, RR will not be further investigated within this work as the counts will be inaccurate when a Gibb's artefact is seen.

4.5 Partial Volume Correction

4.5.1 Introduction

PVC was assessed using the range of different sized spheres imaged in section 4.4 and by calculating the recovery coefficients. The PVC recovery curve was determined by finding a best fit line for the experimental data.

4.5.2 Methods

The SPECT/CT images of the nine spheres acquired in section 4.4 were used for the partial volume correction evaluation. The recovery coefficient was calculated as described in section 4.4. The PVC curve was created by plotting the activity recovery coefficient against the sphere volume for the optimised reconstruction (derived in section 4.4) and a range of SC techniques. The PVC curve was modelled using the curve fitting tool in Matlab (R2020b, Mathworks, Massachusetts, USA) and a custom equation as shown in Equation 35 [177]:

$$f_{RC}(V) = \frac{\alpha}{1+(\gamma/V)^{\beta}} \qquad \textbf{Equation 35}$$

Where α, β, and γ are fitting parameters, RC is the recovery coefficient and V is the volume of the sphere (ml). The uncertainty was calculated using Equation 12 in section 2.6.6.

4.5.3 Results

The recovery coefficient was plotted against the sphere volume (including uncertainties) for 113 keV, 208 keV for no SC, CZT TEW SC and Ogawa TEW SC, as shown in Figure 47 and Figure 48. The CZT TEW SC with a range of values for *h* only displayed small, insignificant differences and therefore *h* equals 0.22 will be used as a representation for the CZT TEW SC technique. Generally, the 113 keV photopeak had a greater activity recovery compared to the 208 keV photopeak across the different sphere sizes. For the 113 keV photopeak the Ogawa TEW SC method showed a decrease in recovery coefficient for 100 to 150 ml spheres compared to the 16 ml and 200 ml spheres. The Ogawa TEW SC method resulted in the greatest recovery coefficient and the lowest recovery coefficients was with no SC. There was less variation in the recovery coefficients for the different SC techniques for the 208 keV photopeak than the 113 keV photopeak.

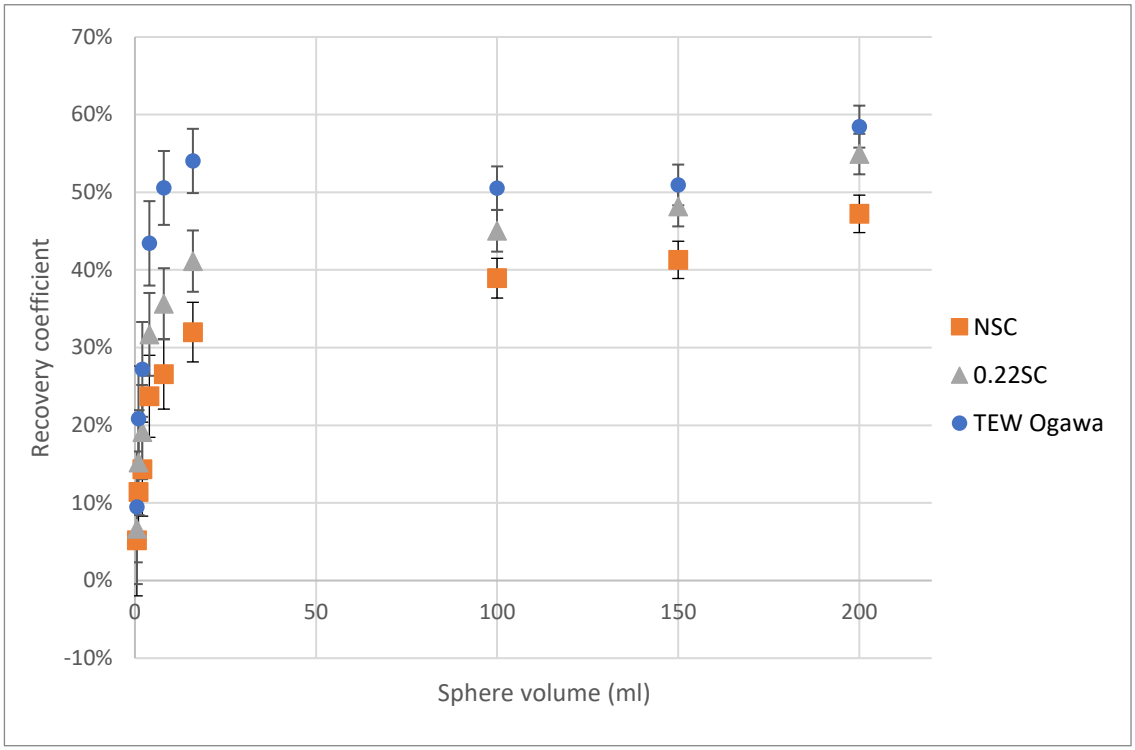

Figure 47: Recovery coefficient (%) against sphere volume (ml) for 113 keV attenuation corrected reconstruction with 5 iterations and 10 subsets with NSC (orange), CZT SC with *h* equals 0.22 (0.22SC, grey) and Ogawa TEW SC (blue), including uncertainties

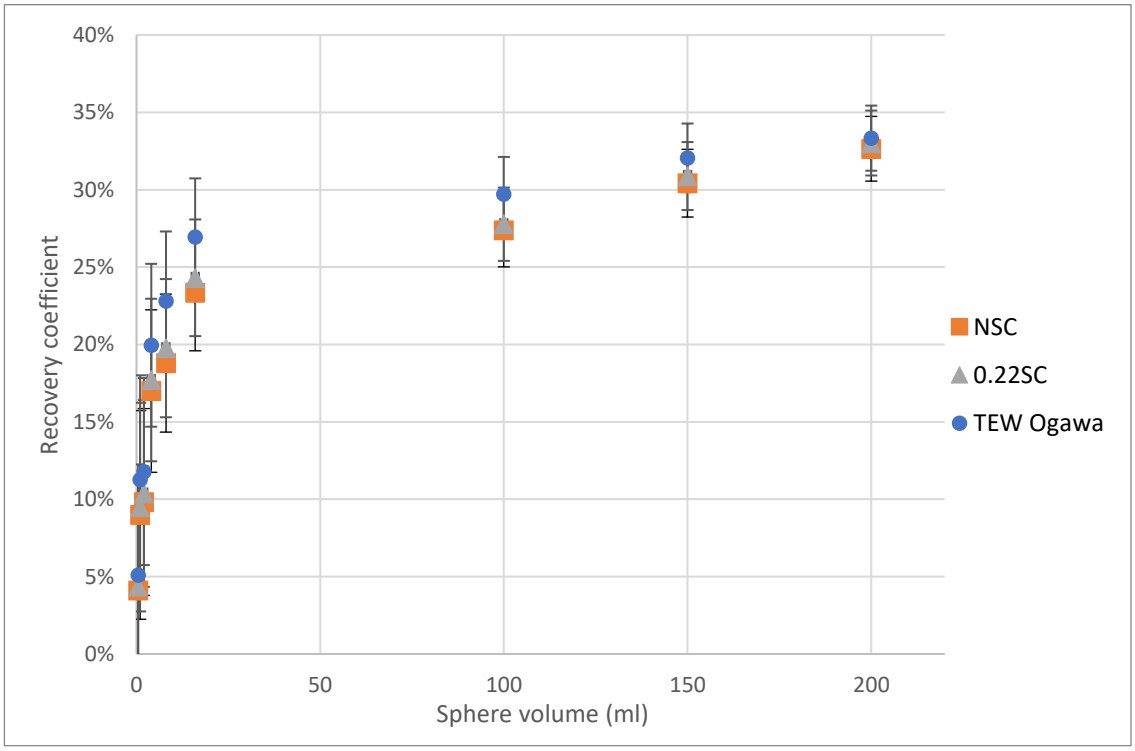

Figure 48: Recovery coefficient (%) against sphere volume (ml) for 208 keV attenuation corrected reconstruction with 5 iterations and 10 subsets with NSC (orange), CZT SC with *h* equals 0.22 (0.22SC, grey) and Ogawa TEW SC (blue), including uncertainties

For reference, when RR was applied there was a clear separation between the six smallest spheres and the three largest spheres for both photopeaks, as seen in Figure 49 and Figure 50. For the 113 keV photopeak the recovery coefficients for the smallest spheres were approximately 15%, whereas for the three largest spheres the recovery coefficients were approximately 60%. For the 208 keV photopeak the recovery coefficients for the smallest spheres were approximately 15%, whereas for the three largest spheres the recovery coefficients were approximately 40%.

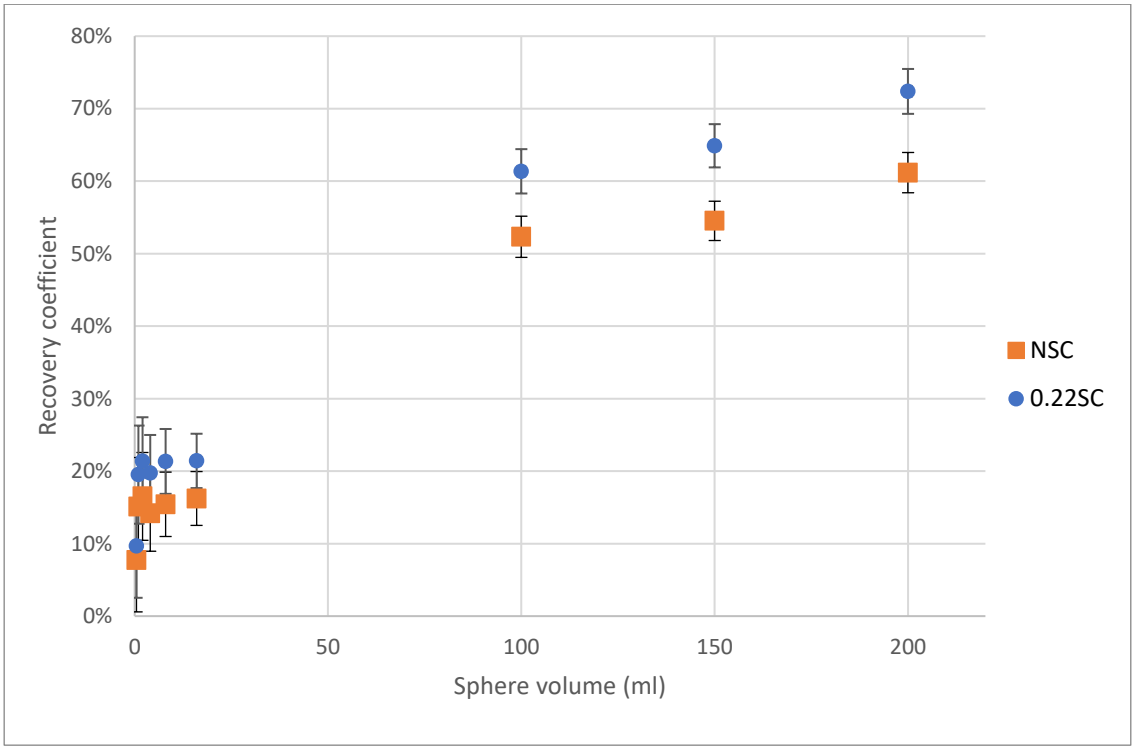

Figure 49: Recovery coefficient (%) against sphere volume (ml) for 113 keV attenuation corrected reconstruction with RR, 5 iterations and 10 subsets with no SC (NSC, orange) and CZT TEW SC with *h* equals 0.22 (0.22SC, blue) including uncertainties

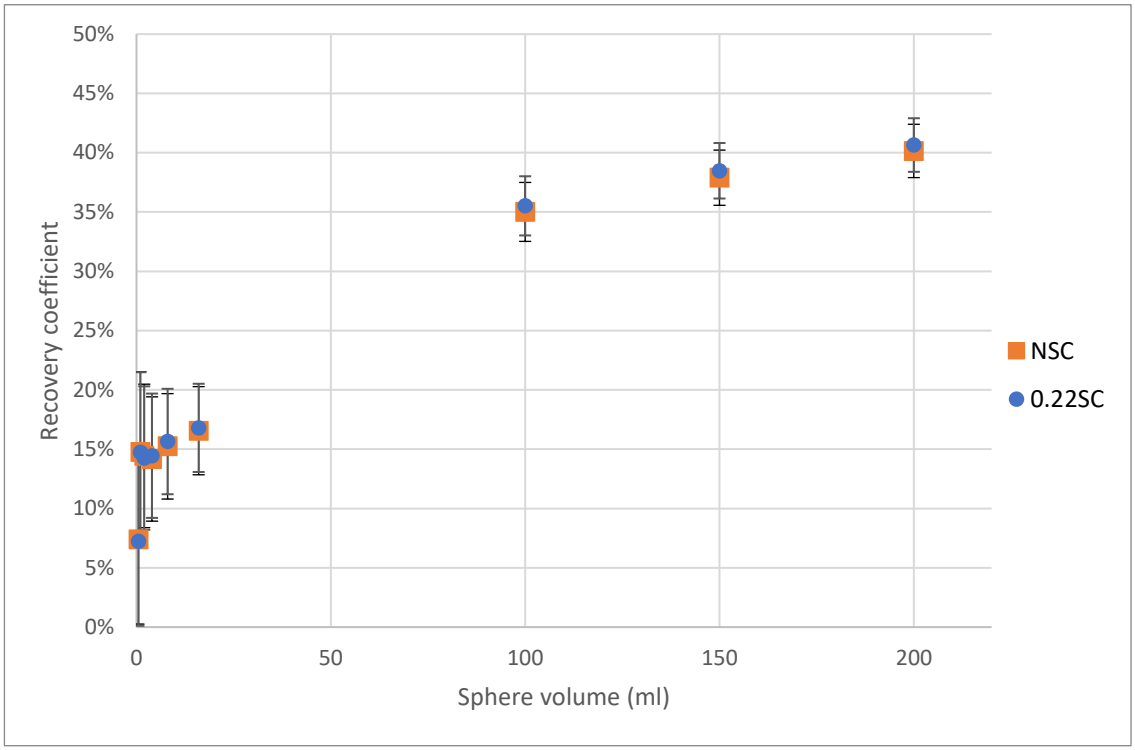

Figure 50: Recovery coefficient (%) against sphere volume (ml) for 208 keV attenuation corrected reconstruction with RR, 5 iterations and 10 subsets with no SC (NSC, orange) and CZT TEW SC with *h* equals 0.22 (0.22SC, blue), including uncertainties

The PVC fitting parameters, using Equation 35, for a range of SC techniques, and both 113 keV and 208 keV photopeaks, can be seen in Table 13. The PVC curve model for the 113 keV and 208 keV photopeaks with the CZT TEW SC without RR are shown in Figure 51 and Figure 52, respectively. The PVC curve falls within the uncertainty of the measured data for the 208 keV photopeak. The uncertainty for each sphere size is a similar value for the 113 keV and 208 keV, however as the recovery coefficients are lower for 208 keV than 113 keV the uncertainties are a greater proportion of the calculated recovery coefficients.

Table 13: Partial volume correction fitting parameters values for 113 keV and 208 keV photopeaks and a range of scatter correction techniques, calculated in Matlab, with 95% confidence bounds and R-squared

SC	Energy (keV)	α		β		γ		R-square
		Coefficient	95% confidence	Coefficient	95% confidence	Coefficient	95% confidence	
CZT TEW	113	0.5085	0.4481, 0.569	0.9119	0.5203, 1.303	2.962	1.521, 4.403	0.972
	208	0.3284	0.2827, 0.3742	0.7579	0.451, 1.065	4.239	1.734, 6.744	0.979
NSC	113	0.4619	0.3872, 0.5366	0.7438	0.4181, 1.07	5.054	1.575, 8.532	0.978
	208	0.3288	0.2781, 0.3795	0.7301	0.4273, 1.033	4.898	1.664, 8.132	0.98
Ogawa TEW	113	0.5434	0.4976, 0.5893	1.377	0.8035, 1.951	1.611	1.093, 2.128	0.970
	208	0.3297	0.2976, 0.3619	0.8528	0.5621, 1.144	2.928	1.741, 4.116	0.982

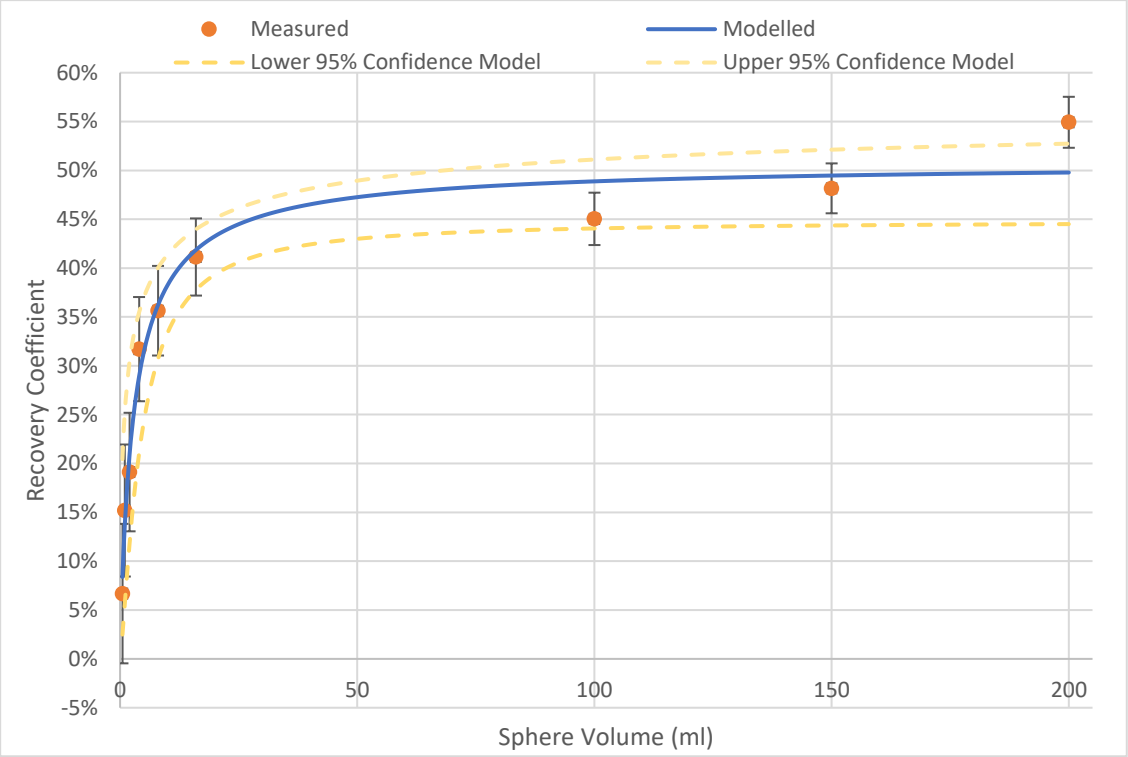

Figure 51: Comparison of modelled (blue line) partial volume correction curve (including model with 95% confidence bounds (yellow dashed line)) and measured recovery coefficients (orange markers) with uncertainties (black bars) for 113 keV AC with *h* equals 0.22

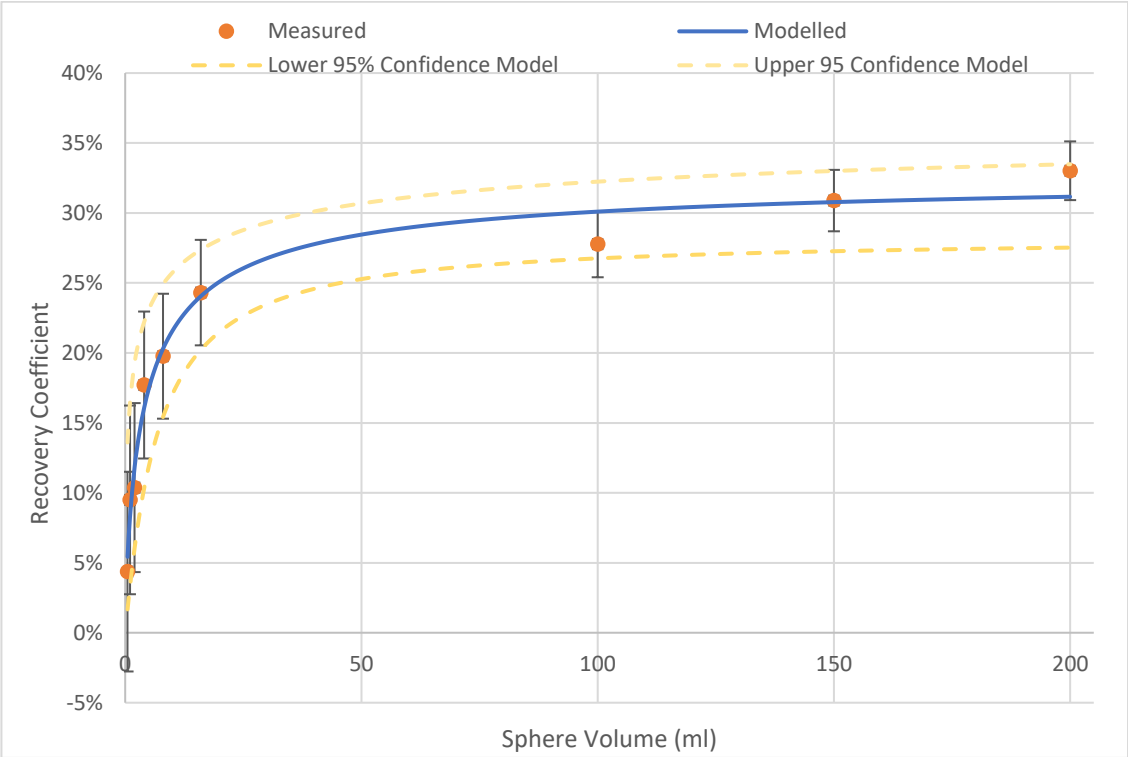

Figure 52: Comparison of modelled (blue line) partial volume correction curve (including model with 95% confidence bounds (yellow dashed line)) and measured recovery coefficients (orange markers) with uncertainties (black bars) for 208 keV AC with *h* equals 0.22

4.5.4 Discussion

The recovery coefficients were plotted against the sphere volume to create PVC curves for 113 keV and 208 keV photopeaks for CZT TEW SC, Ogawa TEW SC, no SC, with and without RR, as seen in Figure 47, Figure 48, Figure 49 and Figure 50. As discussed in section 4.4, the recovery curves have a greater recovery for the 113 keV photopeak compared to the 208 keV, due to septal penetration artefact. The PVC curves for no SC have the lowest recovery coefficients for each sphere volume, compared to the CZT TEW SC and Ogawa TEW SC, and the greatest recovery coefficient for each sphere is the Ogawa TEW SC method.

As discussed in section 4.4, the RR images display Gibb's artefacts and therefore are not going to be further investigated in this work. However, they are included here as a comparison to the PVC without RR. The recovery coefficients for the largest and smallest volume spheres with RR are greater than without RR, however the recovery coefficients for the medium spheres are less with RR than without. This could be due to the Gibb's artefact as there was a greater activity concentration (seen in Table 12) in the medium three spheres (4 ml – 16 ml) compared to the smallest and largest spheres (0.5 ml – 2 ml and 100 ml – 200 ml) and therefore the Gibb's artefact

is likely to have a greater effect on the smallest six spheres, due to the higher activity concentration. The recovery coefficients for the larger spheres with RR are greater than those without RR, therefore, if the Gibb's artefact can be resolved, RR may be a promising option, however, further work is required.

The modelled PVC curves were compared to the measured recovery coefficients for 113 and 208 keV photopeaks for the CZT TEW SC technique and are displayed in Figure 51 and Figure 52, respectively, including the 95% confidence bounds for the modelled PVC and uncertainty bars for the measured data. The measured data is generally within the 95% confidence bounds of the modelled PVC curve, except for the 200 ml recovery coefficient for the 113 keV photopeak. However, when the uncertainty for the 200 ml sphere imaged using the 113 keV photopeak is considered, the measured data does fall within the 95% confidence bounds of the modelled data. Therefore, the PVC curve model is a good representation of the measured data. The percentage difference between the PVC model and the measured data is greatest for the 0.5 ml sphere and is approximately 25% for both photopeaks, this is due to the relatively large uncertainty associated with the small volume measurements. The percentage differences between the PVC model and the measured data for the other spheres are between 1.6% and 9.4% for the 113 keV photopeak and are between 0.4% and 14.4% for the 208 keV photopeak. This could be investigated by repeating the PVC method using the phantom in different orientations, as described by the EANM guideline for quantitative SPECT/CT [65] and it may be helpful to investigate the PVE on different sized phantoms for a range of different shapes, which closely relate to those found in patient anatomy. There was limited access to ^{177}Lu during this work, which may have led to the similar activity recovery for the 16 ml and 100 ml spheres, due to the differences in activity concentration between different spheres. Therefore, it would be beneficial to repeat the imaging of the spheres with a consistent activity concentration for all sphere sizes, which would reduce the number of variables in the methods.

One study, by Hippelainen et al, investigated the PVC required for ^{177}Lu SPECT imaging using a NaI gamma camera and the effect PVC has on clinical ^{177}Lu imaging [94]. They showed the PVC curve for the 208 keV photopeak using medium energy collimators was greatest for the RR and SC reconstruction, compared to RR alone. They reported that the recovery at 100 ml was approximately 80%. Kennedy et al [150] investigated the recovery coefficients for a CZT gamma camera using ^{177}Lu and reported that the recovery coefficients for the 113 keV photopeak were greater than the 208 keV photopeak, which agrees with the results shown in Figure 51 and Figure 52. They reported that for the 113 keV photopeak the recovery coefficient at approximately 28 ml was approximately 120%, and for 208 keV photopeak the recovery coefficient at

approximately 28 ml was approximately 55%, which is significantly more than the results reported in Figure 51 and Figure 52, which could be due to the use of RR used by Kennedy et al [150]. In addition, Kennedy et al [150] and Hippelainen et al [94] calculated the PVC using a ^{177}Lu-filled phantom background, as opposed to the non-active background used in this work, which will affect the results. In this work, the phantom measurements were performed without background radiation, which is a standard in nuclear medicine harmonisation trials [1], however it does not necessarily represent clinical situations, where background radioactivity might be present. It is expected that the recovery coefficient might change by different quantities depending on a range of factors, for example, different background activity concentrations due to PVE (spill in and spill out), image reconstruction parameters, level of noise and post-filtering of the images. An assessment of recovery coefficients with more realistic background to sphere ratios, matching clinical situations encountered in ^{177}Lu-radiopharmaceutical post-therapy clinical imaging, could be investigated in the future work.

4.6 Validation of Gamma Camera Calibrations

4.6.1 Introduction

The SC method was assessed by imaging a sphere in air and in scatter to assess the validity of the SC method against no SC and a commonly used method for SC. The gamma camera calibrations derived and calculated in the previous sections were applied to a separate phantom to assess how accurate they were.

4.6.2 Methods

4.6.2.1 Comparison of Sphere in Scatter with Scatter Correction to Sphere in Air

To assess the effect of the different SC techniques, a SPECT/CT of the sphere in scatter (described in section 4.2, with 1.3 MBq ^{177}Lu) was acquired using the ^{177}Lu energy session set up in section 4.1, the WEHR collimator, 40s per view, 60 views per detector, 128x128 matrix, a voxel size of 4.42 mm and with the COR correction switched on. The CT images were acquired using a 512x512 matrix, 5mm slices, helical, 120 kV and 20 mA. The images were reconstructed using the CZT TEW SC (derived in section 4.2.2.1) with a range of values for *h*, the Ogawa TEW SC technique and no SC. The images were reconstructed for the 113 keV and 208 keV photopeaks independently. The sphere in air SPECT images (described in section 4.2) were assumed to be the ideal solution and therefore no SC was applied. All images were reconstructed with 5 iterations and 10 subsets and CTAC.

ImageJ was used to plot line profiles through the transverse plane of all the reconstructed sphere in scatter images and the sphere in air images. A fixed rectangular ROI was used to ensure

there was consistency, which was the width of two pixels and centred at the middle of the sphere. The position data was centred to the position of maximum counts so there could be comparison between the sphere in scatter and sphere in air data. The raw counts were plotted against the centred position and compared for all SC methods for the sphere in scatter and to the sphere in air.

4.6.2.2 Assessment of the Accuracy of Gamma Camera Calibrations in a Simple Phantom

The gamma camera corrections derived and calculated from sections 4.2, 4.3, 4.4 and 4.5 were applied to the sphere in scatter SPECT/CT images (described in section 4.2, with 1.3 MBq ^{177}Lu) to assess how accurate the calibrations were. The sphere in scatter SPECT/CT was reconstructed using the optimum number of updates (5 iterations and 10 subsets), with CTAC and a range of SC techniques, including the CZT TEW SC, with a range of values for *h*, Ogawa TEW SC and no SC. A VOI at 100% of the size of the sphere was drawn. The reconstructed images were processed using Amide and the appropriate sensitivity factor was applied to calculate the activity in the phantom. The appropriate PVC model was then used to recover the activity from the appropriate size sphere. The results were compared to the known activity measured in the phantom.

4.6.3 Results

4.6.3.1 Comparison of Sphere in Scatter with Scatter Correction to Sphere in Air

The centred line profiles for the sphere in air and sphere in scatter images for the transverse plane are displayed for a range of SC methods for 113 keV photopeak and 208 keV photopeak in Figure 53 and Figure 54, respectively. The pixel size was 4.42 mm and therefore the line profiles interpolate between the counts at each pixel.

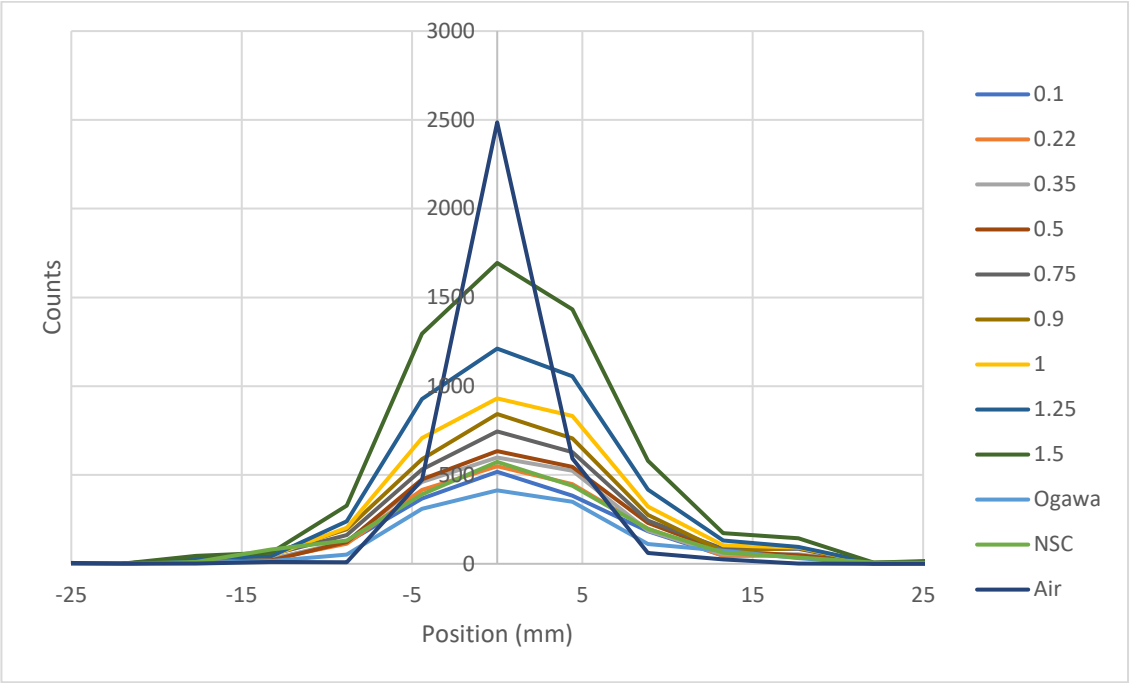

Figure 53: The measured counts against the centred position for the CZT TEW SC for a range of values for *h* (0.1 to 1.5), Ogawa TEW SC and NSC for the sphere in scatter and the non-scatter corrected sphere in air for the 113 keV photopeak reconstructed with CTAC, 5 iterations and 10 subsets, displayed with a straight-line scatter plot

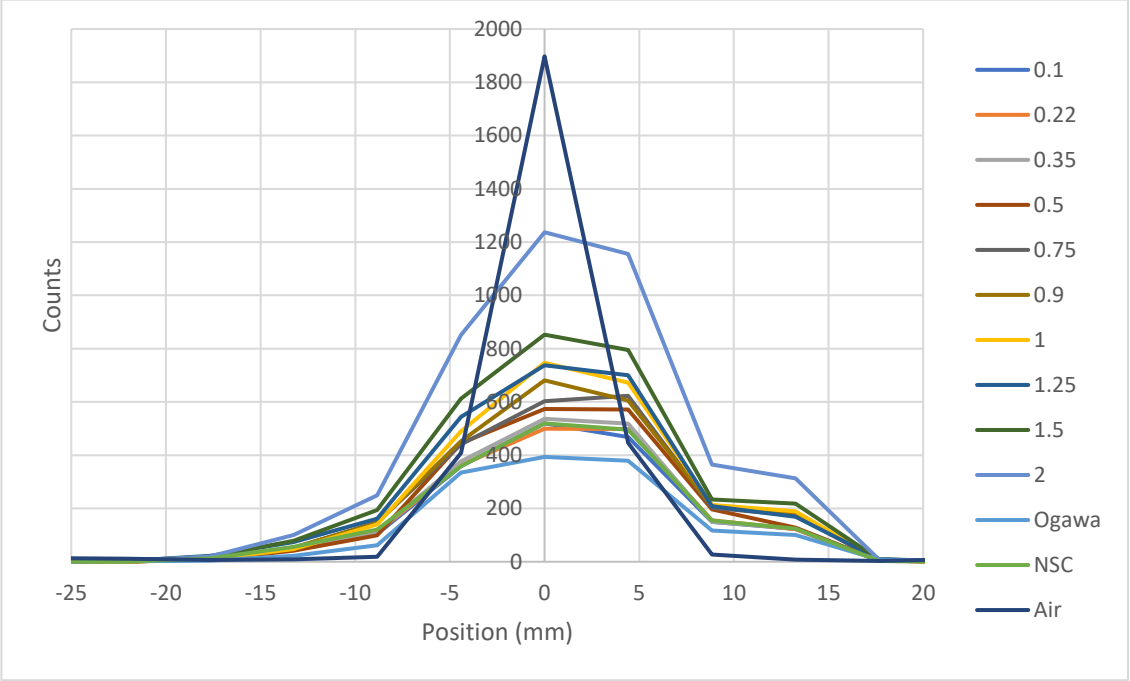

Figure 54: The measured counts against the centred position for the CZT TEW SC for a range of values for h, Ogawa TEW SC and NSC for the sphere in scatter and the non-scatter corrected sphere in air for the 208 keV photopeak reconstructed with CTAC, 5 iterations and 10 subsets, displayed with a straight-line scatter plot

For both the 113 keV and 208 keV line profiles, the sphere in air line profiles have the largest peak counts compared to all the sphere in scatter line profiles. The sphere in air line profile is narrower than the sphere in scatter profiles. The sphere in air line profile has greater peak counts for the 113 keV photopeak than the 208 keV.

For both photopeaks the sphere in scatter line profile with the lowest peak counts is for the Ogawa TEW SC line profiles. For both photopeaks the non-scatter corrected line profiles reach similar peak counts to the CZT TEW SC with *h* equals 0.22.

For the CZT TEW SC sphere in scatter line profiles, the increase in value of *h* increases the peak counts. For the 113 keV photopeak, the peak for CZT TEW SC with *h* equals 1.5 is approximately 68% of the peak counts for the sphere in air line profile. For the 208 keV photopeak, the peak for the CZT TEW SC with *h* equals 1.5 is approximately 45% of the peak counts for the sphere in air, which is therefore less than for the 113 keV photopeak. The 208 keV line profile graph includes the CZT TEW SC for *h* equals 2, however when this was included for the 113 keV line profile graph the peak counts reached over four times the sphere in air peak counts.

The spread or FWHM for all the sphere in scatter line profiles are greater than for the sphere in air. The FWHM for the sphere in air line profiles is approximately 6% and for the sphere in scatter line profiles is approximately 14%. They are similar for both photopeaks and for all SC techniques.

4.6.3.2 Assessment of the Accuracy of Gamma Camera Calibrations in a Simple Phantom

The sensitivity factors from Table 11 and the partial volume correction from Table 13 for the 0.5 ml sphere were applied to the sphere in scatter SPECT/CT reconstructed with CTAC, 5 iterations, 10 subsets and a range of SC techniques. The 95% confidence bounds for the PVC model were used to calculate a range of activities for each SC method. The decay corrected activity in the sphere was calculated to be 1.268 MBq at the middle point of the SPECT/CT. The results for the calculated activity and difference to the known activity are shown in Table 14.

Table 14: The calculated activity and the percentage difference (% dif) to the true activity for the sphere in scatter SPECT/CT using the derived calibration factors and PVC for a range of SC methods and both the 113 and 208 keV photopeaks reconstructed with CTAC, 5 iterations and 10 subsets. The 95% confidence range is taken from the PVC model summarised in Table 13.

Energy	113 keV				208 keV			
PVC Value	Modelled		95% Confidence Range		Modelled		95% Confidence Range	
Scatter correction	Activity	% dif	Activity	% dif	Activity	% dif	Activity	% dif
NSC	0.662	-48%	0.226 – 2.616	-82% - 106%	0.835	-34%	0.307 – 2.955	-76% - 133%
0.1SC	0.753	-41%	0.309 - 2.541	-76% - 100%	0.826	-35%	0.219 – 1.803	-83% - 42%
0.22SC	0.759	-40%	0.311 - 2.559	-75% - 102%	0.813	-36%	0.216 – 1.773	-83% - 40%
0.35SC	0.744	-41%	0.305 - 2.509	-76% - 98%	0.813	-36%	0.216 – 1.773	-83% - 40%
1SC	0.763	-40%	0.313 - 2.572	-75% - 103%	0.845	-33%	0.224 – 1.843	-82% - 45%
TEW Ogawa	0.973	-23%	0.429 - 3.161	-66% - 149%	0.836	-34%	0.417 – 2.042	-67% - 61%

Overall, the calculated activity for the PVC model was underestimated for all energy windows and SC techniques. The CZT TEW SC technique was more accurate than no SC for the 113 keV photopeak. The Ogawa TEW SC technique was most accurate for the 113 keV photopeak. For the 208 keV photopeak all SC techniques produced similar activities. Overall, the 208 keV photopeak resulted in the more accurate activity calculations.

However, when considering the 95% confidence bounds for the PVC curve fitting parameters, there are large inaccuracies ranges, from approximately -82% to 149% overall. For the CZT TEW SC the range was -76% to 103% and for the Ogawa TEW SC the range was -67% to 149%.

4.6.4 Discussion

4.6.4.1 Comparison of Sphere in Scatter with Scatter Correction to Sphere in Air

The line profiles for the sphere in scatter using a range of SC techniques were compared to the line profiles for the sphere in air for the 113 keV and 208 keV photopeaks, displayed in Figure 53 and Figure 54. The line profiles show that the greater the value for the *h* for the CZT TEW SC, the higher the counts in the line profile are, which is due to the SC technique, displayed in Equation 31. The greater the value for the *h* indicates that there is a greater ratio of primary counts detected in the lower energy window compared to the photopeak energy window, due to hole tailing (as shown in Equation 27). When reviewing the energy spectra from Figure 30, it is unlikely that the value of *h* would be greater than 1 as the counts in the lower energy window

are less than the counts photopeak energy window, for both photopeaks, however there is a smaller difference in the counts in the two energy windows for the 113 keV photopeak than the 208 keV photopeak. At the 113 keV photopeak there is greater Compton scatter, which is likely to affect the total counts in the energy spectrum at the 113 keV photopeak and therefore supress the effect of hole tailing.

The pixel size used was 4.42 mm, and therefore the line profiles have displayed the interpolated counts for each pixel, and therefore it has not captured a fully accurate picture of the line profiles. The line profiles for the 208 keV photopeak are asymmetrical, which is due to the maximum counts being between the centred pixel and the adjacent pixel. To improve the line profiles the images would need to be acquired with a smaller pixel size, which should be carried out as further work.

It is clear than none of the SC techniques fully correct the images to a similar line profile as the sphere in air, therefore these techniques are not perfect solutions. However, when comparing the CZT TEW SC to a routinely used SC technique (Ogawa TEW SC) and no SC it can recover more of the counts, however this depends on the value of *h* used. The Ogawa TEW SC results in the lowest counts compared to the CZT TEW SC and no SC, which suggests that there is an overcorrection present, which is likely due to the hole tailing in the lower energy window for the CZT gamma camera, as suggested by Songy et al [147]. Therefore, it can be argued that the proposed CZT TEW SC method is an improvement on the Ogawa TEW SC for the CZT gamma camera and it is easy to implement in a clinical setting.

The sphere in scatter peak line profiles for no SC and the CZT TEW SC technique with *h* is less than or equal to 0.5 for both photopeaks are approximately 25% of the value of the sphere in air peak line profile, therefore there are a significant proportion of counts that are not being recovered in the CZT TEW SC technique. At *h* equals 1 the peak counts in the centre of the sphere in scatter line profile is approximately 40% of the peak counts in the centre of the sphere in air line profile. When *h* is greater than 1 the sphere in scatter line profiles approach the peak height of the sphere in air peak. The sphere in air peak counts were exceeded for *h* equals 2 for the 113 keV photopeak sphere in scatter and therefore was not included in these results. It is therefore likely that the sphere in air peak counts for the 208 keV photopeak would be exceeded for *h* is greater than 2. However, the FWHM is less for the sphere in air compared to the sphere in scatter (approximately 6% and 14%, respectively). There is not a significant difference between the shape of the line profiles across the different photopeaks, nor across the different SC techniques. Therefore, this indicates that none of the SC techniques investigated are completely suitable for recovering the reduction in spatial resolution when the scatter material is

introduced and therefore a more suitable SC technique is required. However, the CZT TEW SC may be a more appropriate option than the Ogawa TEW SC technique for imaging ^{177}Lu on a CZT gamma camera.

4.6.4.2 Assessment of the Accuracy of Gamma Camera Calibrations in a Simple Phantom

The accuracies of the calculated activity for the different reconstruction techniques were analysed and displayed in Table 14, where all calculated activities were underestimated from the true activity. The most accurate results were generally for the 208 keV photopeak, except for the Ogawa TEW SC for the 113 keV photopeak (-23%). All the accuracies for the 208 keV photopeak were similar (-33% to -36%). However, when the accuracies for the 95% confidence bounds for the PVC fitting parameters are considered, the accuracy of the calculated activity displays a large overall range (-82% to 149%), which suggests that there are no differences between any of the SC techniques and energy windows used. The main limitation with this validation method is the small sphere (0.5 ml) used resulted in the greatest range of results as small volumes and activities are associated with larger uncertainties. For example, the range of uncertainties for the PVC across all SC techniques and photopeaks for the 0.5 ml sphere is from 60% to 200%, whereas for the 16 ml the uncertainty range is from 6% to 22%. The 0.5 ml sphere was used in this work as the images were already available (from a phantom acquisition in section 4.2, which was not required for calibration) and there was limited time and resources to fill and image an additional phantom. Therefore, there should be further work carried out to repeat this validation using a range of different size spheres to fully validate the gamma camera calibrations. As there is little difference in the accuracies for the values of *h* investigated, it can be assumed that the value of *h* should be 0.22 for the 113 keV photopeak and 0.35 for the 208 keV photopeak, as calculated in section 4.2.

The methods used in this work for the accuracy calculation used a smaller object volume than used in the literature, which therefore provided a worse case result. The details of the validation process within the literature is not always clearly stated, but generally the methods used an object of at least 16 ml [110], [112]. The literature reported a wide range of accuracies for a NaI gamma camera, as described in section 3.2 [4], [32], [120]–[124], [126], [128], [129], [131], [56], [111], [112], [114]–[118]. One study quoted the accuracies based on a 37 mm sphere and their accuracies ranged from 4% to 285%, excluding their uncertainties [56]. Not all the results in the literature included uncertainties and therefore it is not possible to fully compare all the results reported. Uribe et al concluded that the accuracies were improved with larger objects, compared to smaller object [126] and therefore the validation should be completed with a larger object. The main comparison that can be made for a CZT gamma camera was for the Veriton CZT

SPECT, which concluded that the errors in activity were less than 10%, however the authors did not give a description of their methods and it was for a different design of CZT gamma camera to the GE Discovery 870 DR CZT used in this work [152].

Generally, the literature concluded that the accuracy was improved using the 208 keV photopeak for NaI gamma cameras, however this work cannot draw a full conclusion for CZT gamma cameras, due to the range of uncertainty. A limitation is that this work was carried out on a WEHR, which is not optimised for imaging the 208 keV photopeak and resulted in a septal penetration artefact. GE Healthcare has recently created a MEHRS collimator for the GE Discovery 870 DR CZT gamma [29], which would therefore be more appropriate for imaging the 208 keV photopeak. Therefore, the calibration methods carried out in this work should be fully repeated using the MEHRS collimator. Ito et al investigated the different collimators for a CZT gamma camera and a NaI gamma camera using ^{99m}Tc and ^{123}I [29]. They have summarised the differences between the WEHR and MEHRS collimators, which is shown in Table 3, which shows the septal thickness is greater for the MEHRS compared to the WEHR, which would reduce the septal penetration artefacts seen at the 208 keV photopeak. The septal penetration for the MEHRS collimator for imaging ^{177}Lu should be similar to the septal penetration for the WEHR collimator for imaging ^{99m}Tc, which appears to be insignificant.

4.6.4.3 Summary

These results summarise a step towards the validation process of the gamma camera calibrations, however, to strengthen this validation process the accuracy of the calibrations should be applied to a range of phantoms, including anthropomorphic-shaped phantoms and a range of different sizes. Applying the calibrations to a range of different size and shaped phantoms would assess the accuracy of the calibrations in clinically relevant situations and it would assess how consistent the calibrations were. It would also be beneficial to carry out a direct comparison to a NaI gamma camera using the same methods for gamma camera calibrations as this work, as there is more literature available for NaI gamma cameras and therefore it would be easier to compare the results directly. This comparison is also important as the NaI gamma camera is currently the “gold-standard” for nuclear medicine imaging and therefore the accuracies reported here should be directly compared to a local NaI gamma camera to minimise the number of variables in the two investigations. In an ideal scenario the same phantoms would be imaged on the CZT gamma camera and the NaI gamma camera on the same day, so the variables and uncertainties associated with phantom filling would be consistent across the two investigations.

The validation methods used in this work were similar to the literature, however this work has not been fully validated using a range of phantoms, patient studies or MC simulations, as described by Fan et al [146] and Pourmoghaddas et al [145]. To fully validate the proposed calibration methods described in this work the calibration methods should be applied to a range of different size and shape phantoms, including an anthropomorphic phantom, and using a MC simulation. A MC simulation is created and discussed further in chapter 5. Once those validation steps are complete the final step would be to image a set of patients and make a direct comparison to the accuracy of quantitative imaging on a NaI gamma camera. However, to complete the final step an ethics application would need to be considered and patient consent would be required, which falls outside the scope of this work.

5 MONTE CARLO MODEL OF THE CZT GAMMA CAMERA

5.1 Initial CZT Gamma Camera Monte Carlo Model

5.1.1 Introduction

A MC simulation of the CZT gamma camera was required to model the energy spectrum and image that the GE Discovery 870 DR CZT gamma camera would produce. It would be used to compare the gamma camera output to the "ground truth" and with the aim to aid the validation process for the gamma camera calibrations calculated in chapter 4. A model needed to be developed using simple geometry and a radioisotope with one photopeak, which is commonly used in nuclear medicine imaging. The aim of this work was to learn how to use GATE and to create a MC model of the GE Discovery 870 DR CZT.

The MC model developed was initially tested using a simple cylindrical phantom filled with ^{99m}Tc. The aim of the section was to carry out the initial testing of the MC model using an easily available isotope and a simple phantom geometry.

5.1.2 Methods

The MC model was created on the University of Manchester Nuclear Physics Department network using linux and run using GATE version 8. A range of resources were used to create the MC model for the GE Discovery 870 DR CZT gamma camera [91]. A model of a NaI gamma camera from the University of Manchester and the National Physical Laboratory (NPL) was used initially and adapted for the differences in the CZT gamma camera [162].

The geometry of the CZT gamma camera was obtained from measurements and literature [15], [29]. The MC model was created by defining one CZT detector, including the collimator and detector, and then multiplying it to have the correct number to create a full CZT gamma camera. The CZT material was defined in a "Gate Materials" database, with density equal to 5.68 g/cm^3, solid and included Cadmium (n=9), Zinc (n=1) and Tellurium (n=10), which is available with the GATE package [91].

A CZT macro was created to simulate the components of the gamma camera. A SPECT head was created as a box, with dimensions of 25 by 69 by 88 cm, to contain the full gamma camera head. A second gamma camera detector was created by using the repeaters function and copying the first SPECT head. A detector was set up to include the CZT "crystal" and collimator and defined as a box. The dimensions of the detector were defined as 5.5 by 0.246 by 0.246 cm. The CZT "crystal" was defined as a box within the detector with dimensions of 1 by 0.246 by 0.246 cm,

positioned at the top of the detector, with the CZT material. The collimator was defined as another box within the detector, positioned below the “crystal”, with dimensions of 4.5 by 0.246 by 0.246 cm, with lead material. The collimator hole was inserted into the collimator as a box with dimensions 4.5 by 0.226 by 0.226 cm and air as the material. The detector module was repeated in an array of 160 by 208 to create a full GE CZT gamma camera. A pressure plate was added as an aluminium box to the bottom of the SPECT head, with dimensions of 0.1 by 40 by 52 cm. A back compartment was created to include the electronics, with dimensions of 5 by 40 by 52 cm. This macro linked to the shielding and table macros.

The shielding macro contained sheets of lead to surround the SPECT head. There were five individual shields defined as the top, front, back, left and right shields. The dimensions of the shielding were 3 cm thick and a total of 10.6 by 46 by 58 cm, depending on the orientation of the shielding plate defined.

The table macro included the table and the mattress. The table was defined as a box with dimensions 1.9 by 35 by 200 cm, made of carbon fibre. The mattress was defined as a box, with dimensions 2.2 by 35 by 200 cm, made of PVC – fabric. A foam core to the mattress was defined as a box with dimensions 1.6 by 34.6 by 200 cm.

A simple phantom was created to test the CZT MC model with ^{99m}Tc. The phantom was defined as a cylinder, with a radius of 7.5 cm and a height of 1 cm and made of water. The source macro defined the source as a cylinder, with the dimensions to match the phantom, the activity was 10 MBq, the half-life was defined as 21636.0 seconds and both x-rays and gamma radiation were defined and modelled.

The simulation was run using a “runSim.mac” macro, which linked to the CZT, phantom and source macros and material databases. The macros were made sensitive by attaching the crystalSD to the detector and attaching the phantomSD to all other volumes. The physics was defined as “emstandard_opt3”. The energy resolution was added using blurring with 6.36% at 140 keV (based on routine gamma camera QC carried out at Royal Surrey County Hospital) and the spatial resolution was added using spblurring with a resolution of 1.7 mm. The output file was defined as a ROOT file [93]. The random engine used was “JamesRandom”, which is an algorithm originating from the universal random number generator proposed by Marsaglia and Zaman in 1987 [178], [179]. The simulation was run for 10 seconds, with time slices at 1 second intervals.

The initial test simulations were run on an individual PC within the University network. The MC simulated geometry visualisation, energy spectrum and image produced were assessed. The simulation was compared with an image and energy spectrum produced using the CZT gamma camera, with ^{99m}Tc. The energy spectrum from the gamma camera was exported using the list mode data and transferred to the University of Manchester network as a .txt file. The gamma camera energy spectrum was converted to a ROOT file so it could be directly compared with the MC simulation outputs, using a macro (written in C++).

5.1.3 Results

The initial GE Discovery 870 DR CZT MC model was created successfully, after a few iterations and improvements. The visualisation for the MC model with the ^{99m}Tc cylindrical phantom is shown in Figure 55, where the CZT detector is displayed as yellow, the collimator is displayed as red, the back compartment is displayed as grey, the table is displayed as blue, the shielding is displayed as blue (for the right and back sections) and grey (for the top, front and left sections) and the phantom is light blue.

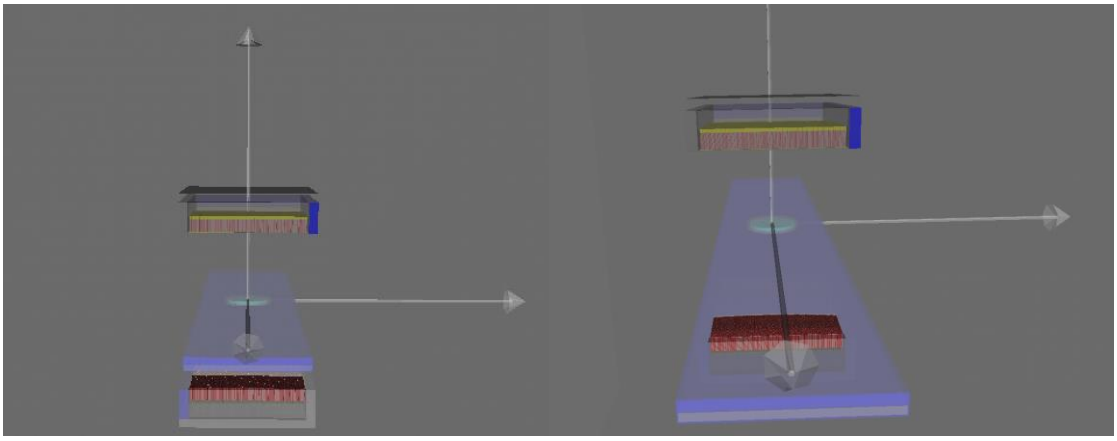

Figure 55: Visualisations of the MC simulation set up in GATE for the GE Discovery 870 DR CZT with a flat cylinder phantom positioned on the table, viewed from two different angles.

The ^{99m}Tc cylindrical phantom MC simulation was modelled with 10 MBq for 10 seconds, which produced the image in Figure 56 and the energy spectrum in Figure 57.

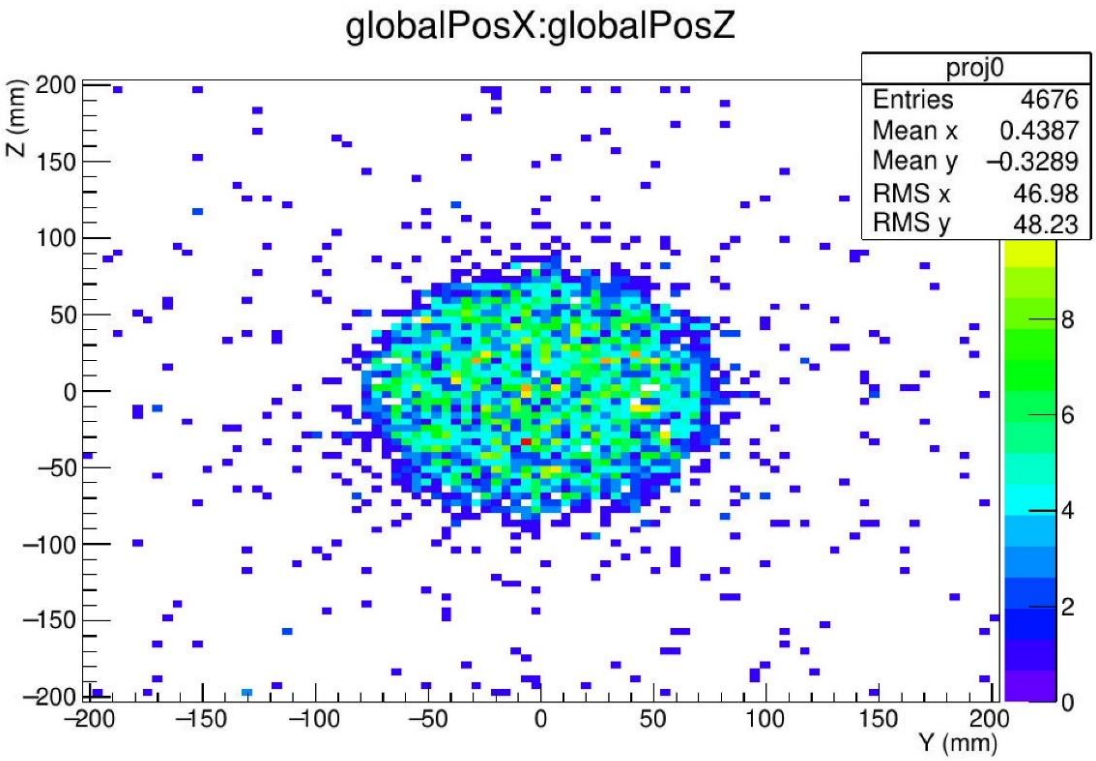

Figure 56: An image produced for the ^{99m}Tc flat cylindrical source using the MC simulation for the GE Discovery 870 DR CZT

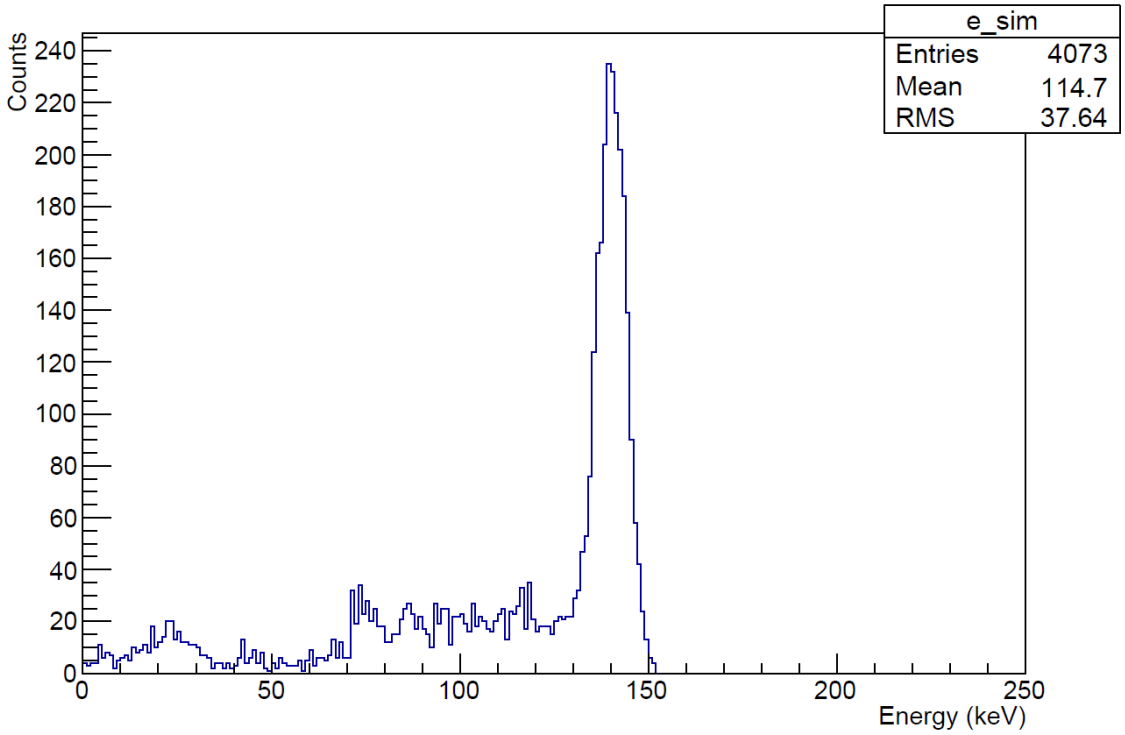

Figure 57: The energy spectrum produced for the ^{99m}Tc flat cylindrical source using the MC simulation for the GE Discovery 870 DR CZT

The ^{99m}Tc cylindrical phantom MC simulation energy spectrum (from Figure 57), was compared to a gamma camera energy spectrum taken of a cylindrical phantom containing approximately 150 MBq ^{99m}Tc, which is displayed in Figure 58. The energy spectra are scaled to display the same orders of magnitude of counts. The energy spectra are similar shapes, however there is less noise in the gamma camera energy spectrum compared to the MC simulation as there was significantly more activity in the gamma camera image than the MC simulation. The counts for the SPECT camera energy spectrum are zero below approximately 40 keV, whereas the MC simulation does not include a section of zero counts. The general shape of the two energy spectra are similar and therefore show that the MC model for the GE Discovery 870 DR CZT is usable and further work can be completed using ^{177}Lu.

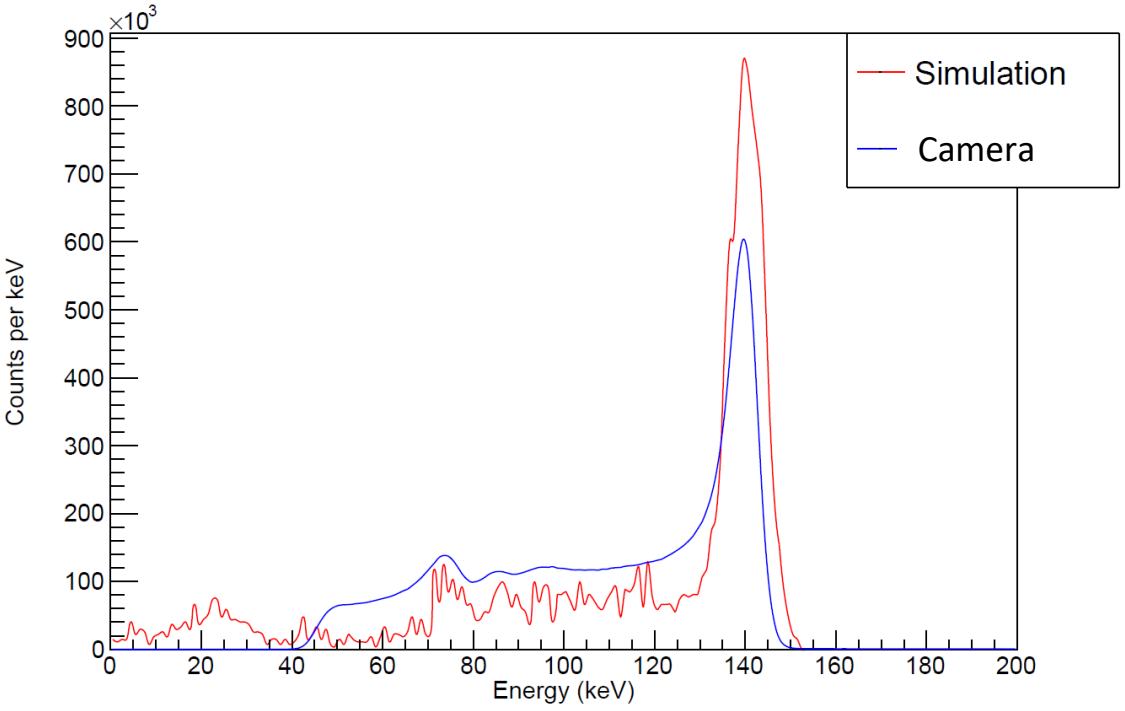

Figure 58: The energy spectrum produced for the ^{99m}Tc flat cylindrical source using the MC simulation for the GE Discovery 870 DR CZT (red line) compared with the SPECT camera energy spectrum (blue line), scaled to the same order of magnitude

5.1.4 Discussion

A MC model of the GE Discovery 870 DR CZT gamma camera was successfully created, based on a previously validated MC model of a NaI gamma camera created by the University of Manchester and the NPL. The MC model was split into different macros to enable easy updates, including a change in the phantom and source. There were several iterations of the MC model created and tested before the results were produced as displayed in section 5.1.3. Each iteration

of the MC model aimed to make an improvement in the previous model. The main issues were the geometry of each element, which is where the visualisation of the MC model was key to assessing where the issues were.

The image and energy spectrum produced in Figure 56 and Figure 57 represent the phantom and radionuclide that was used in the MC simulation, and therefore the simulation needed to be compared to a gamma camera energy spectrum, which is displayed in Figure 58. The energy spectrum from the gamma camera used in this comparison was much greater than the activity used in the simulation and therefore there were some differences expected. The aim of this comparison was to assess any major issues as opposed to fine details. As the overall shape of the two energy spectra was similar, the MC model was ready to be used for the ^{177}Lu phantoms used within chapter 4, which will be discussed in sections 5.2 and 5.3 for cylindrical sensitivity phantom (from section 4.3) and for the sphere in scatter (from section 4.2), respectively.

5.2 MC Simulation for the ^{177}Lu Sensitivity Phantom

5.2.1 Introduction

A voxel-based phantom of the ^{177}Lu sensitivity phantom, used in section 4.3, was created and the MC model of the CZT gamma camera was updated to use ^{177}Lu. The aim was to compare the energy spectrum from the gamma camera images produced in section 4.3 against the MC model outputs.

5.2.2 Methods

A voxel-based phantom was created for the ^{177}Lu sensitivity phantom based on the CT data from the SPECT/CT described in section 5.2. ImageJ was used to convert the CT images into a voxel-based phantom and source, which could be used in GATE for the MC simulation. The CT was imported into ImageJ and a macro was used to save the image as an interfile. A rectangular ROI was selected for the full phantom. A macro was used to process the image by cropping, scaling and flipping it, as shown in Figure 59 (A). Two files were created, a header file and an image file. The file extensions for the phantom macros were updated to .h33 for the header file and .i33 for the image file. To create the source macro a circular ROI was drawn to include all active volume within the phantom, as shown in Figure 59 (B).

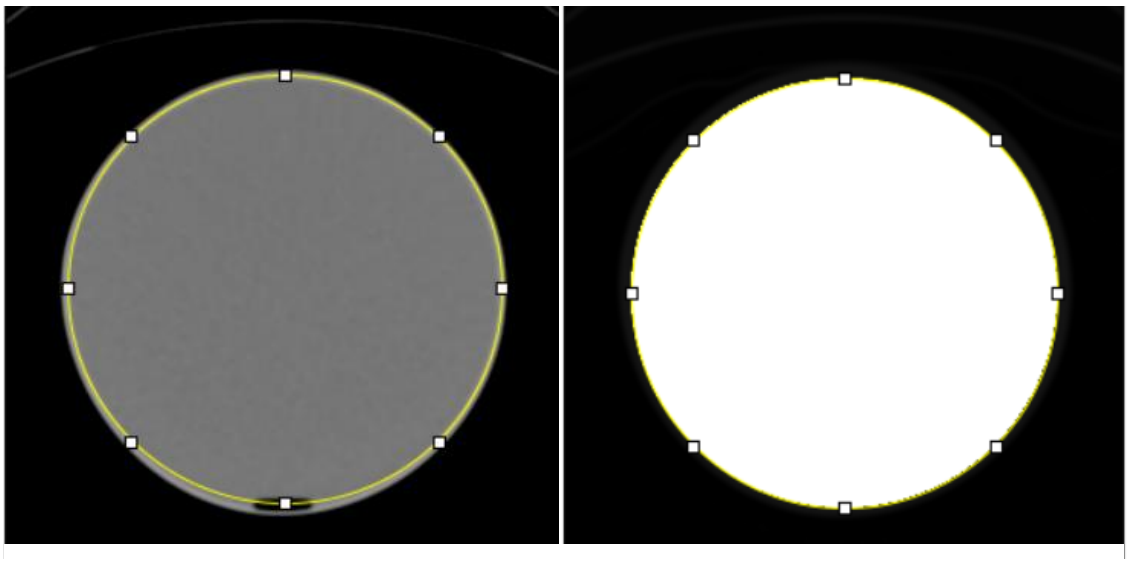

A: The sensitivity phantom macro **B: The sensitivity source macro**

Figure 59: The sensitivity phantom macro produced using ImageJ with the ROI created for the source macro (A). The sensitivity source macro produced using ImageJ (B).

A macro was used to create the source macro for GATE using the phantom macro from ImageJ and the ROI set selected. The source macro sets all the Hounsfield units within the ROI to be 15000, so that they can be easily differentiated from any other value within the CT image as shown in Figure 59 (B). Another set of header and image files were created for the source macro and the file extensions were updated to .h33 and .i33 as for the phantom macro.

To use the voxel-based phantoms a new macro for the source and phantom were required for GATE. The voxel phantom macro created an insert using the "ImageNestedParametrisedVolume" function and the geometry was set to the .h33 phantom header file, created in ImageJ, which linked to the .i33 phantom image file. The Hounsfield units within the phantom image were converted to different materials using a text file which listed the materials with links to the appropriate Hounsfield unit range. The voxel source macro was used to include a source which linked to the .h33 source header source file, created in ImageJ, which linked to the .i33 source image file. The activity ranges were linked to data files which were updated for the appropriate activity levels per voxel and the Hounsfield unit defined in ImageJ, which was 15000. The physics including the half-life of ^{177}Lu (581817.6 seconds), gamma, beta and x-ray emissions were defined. The energy resolution was set to 5.9% at the 208 keV photopeak using the blurring insert. The energy resolution was selected based on gamma camera acquisitions.

The MC simulation was run using the University of Manchester Nuclear Physics Department's cluster. The simulation was split into a number of jobs to allow it to run across the cluster efficiently. The simulation was initially tested with 1 MBq, 10 seconds over 100 jobs to ensure it

would run successfully. After the results were reviewed the sensitivity MC simulation was updated for 70 MBq, 300 seconds and 300 jobs. The activity value was split between two data files, one for beta emissions and one for gamma emissions. The activity per voxel was calculated using Equation 36:

$$A_{vox} = \frac{A}{N} \times B \qquad \text{Equation 36}$$

Where A_{vox} is the activity per voxel, A is the total activity in the phantom, N is the number of voxels in the ROIs drawn in ImageJ to create the source macro and B is the branching ratio. Therefore the activity per voxel for the beta data file was 48.43 Bq/voxel and for the gamma data file it was 11.43 Bq/voxel.

The MC simulation output was saved as a ROOT file. The ROOT file was analysed using a range of marcros to create an image for the 113 keV and 208 keV photopeaks and an energy spectrum. The energy spectrum was further analysed by plotting the Compton scattered events and the events that had not undergone Compton scattering. In addition, the name of the component where the scattering occurs was analysed for the full energy spectrum and for a low energy section, from 50 to 70 keV.

The image energy spectrum from the simulation was compared to the image and energy spectrum from the gamma camera image described in section 4.3.

5.2.3 Results

The voxel-based phantom for the ^{177}Lu cylindrical sensitivity phantom, with 70 MBq, was created successfully using ImageJ and the MC simulation for the planar image output for 113 keV and 208 keV photopeaks are displayed in Figure 60. The images are visually similar for the 113 keV and 208 keV photopeaks, however there are more events within the 208 keV photopeak image, which is due to the higher relative abundance for the 208 keV photopeak compared to the 113 keV photopeak. Both images are not completely uniform, which will be discussed in section 5.2.4.

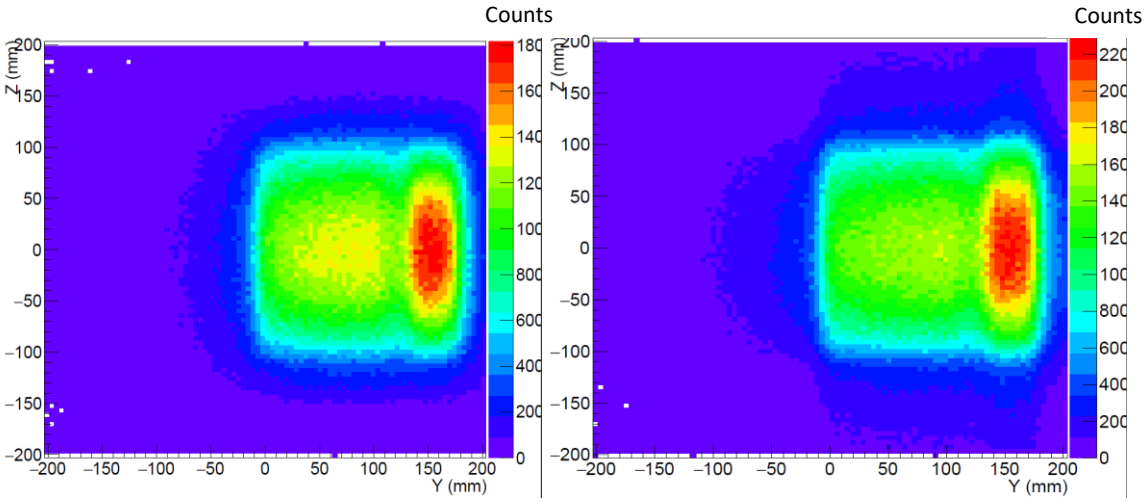

A: 113 keV **B: 208 keV**

Figure 60: The MC simulation image produced for the ^{177}Lu sensitivity phantom for the 113 keV (A) and 208 keV (B) photopeaks using 70 MBq for 300 seconds

The energy spectrum for the MC simulation is displayed in Figure 61 and it is compared to the gamma camera energy spectrum (produced in section 4.3) in Figure 62. The MC simulation energy spectrum is scaled to match the camera energy spectrum, due to the difference in activity for each phantom, so they can be directly compared.

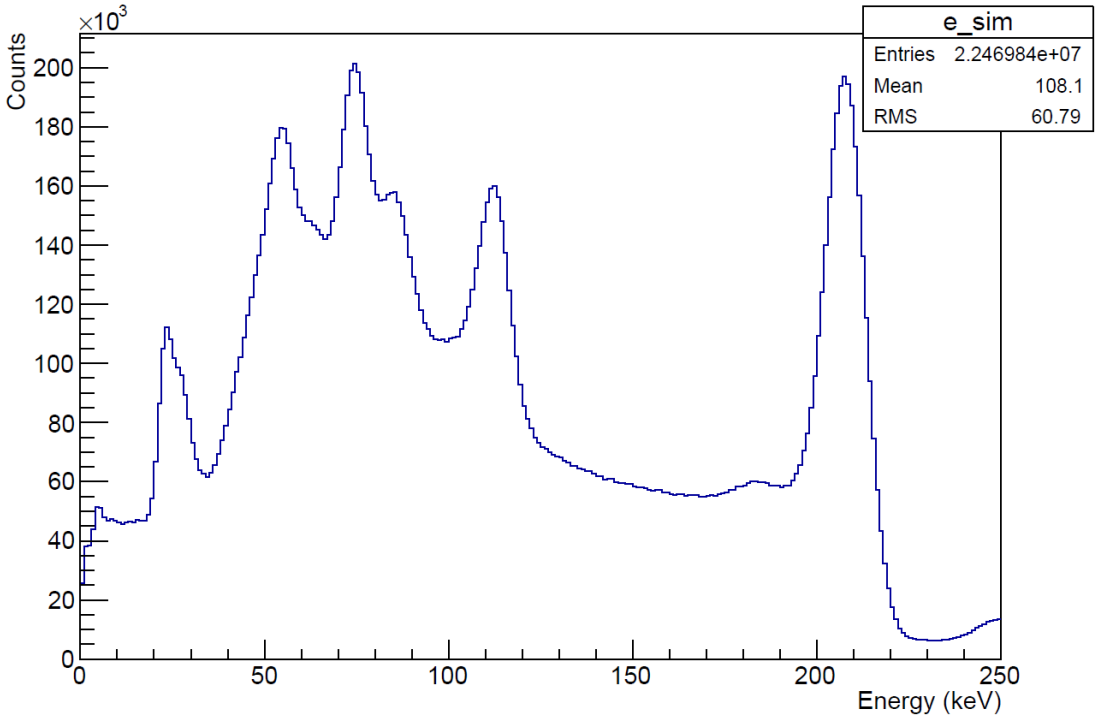

Figure 61: The energy spectrum produced for the ^{177}Lu sensitivity phantom using the MC simulation for the GE Discovery 870 DR CZT using 70 MBq for 300 seconds

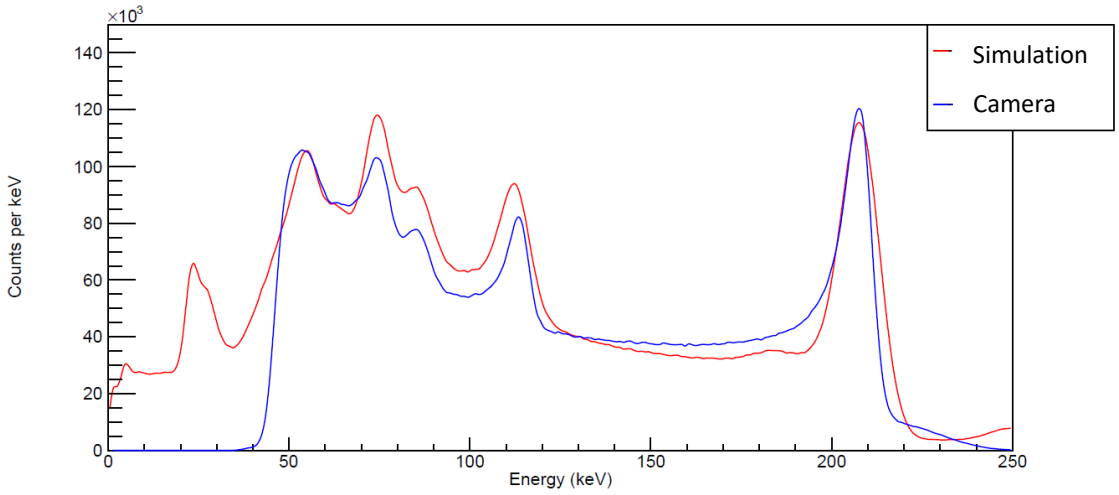

Figure 62: The energy spectra for the simulation (red line) and planar camera image (blue line) for the ^{177}Lu sensitivity phantom, scaled to the 208 keV photopeak

The energy spectra for the MC simulation and the gamma camera are similar in shape. The photopeaks at 113 keV and 208 keV are slightly different heights between the MC simulation and the gamma camera. The 208 keV photopeak for the camera energy spectrum has a longer tail to the lower energy side than the MC simulation low energy tail. The counts fall to zero for below 40 keV for the gamma camera energy spectrum. The MC simulation energy spectrum was further analysed by separating out the events that did and did not undergo Compton scattering, as displayed in Figure 63. The components where the scattering events occurred were assessed for the full energy spectrum and for a low energy range (50 to 70 keV) only, displayed in Figure 64 and Figure 65, respectively. Where no Compton scattering has taken place, the output is given as “null”.

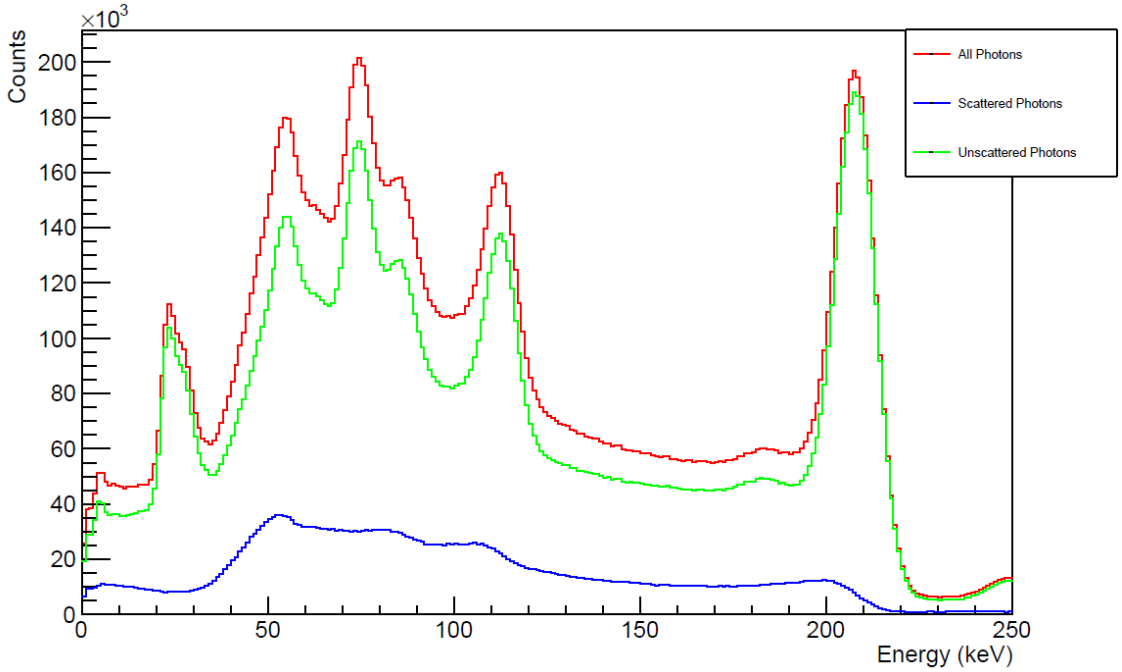

Figure 63: The energy spectrum for the ^{177}Lu sensitivity phantom simulation (red line), with the Compton scattered energy spectrum (blue line) and the energy spectrum for events that have not undergone Compton scattering (green line)

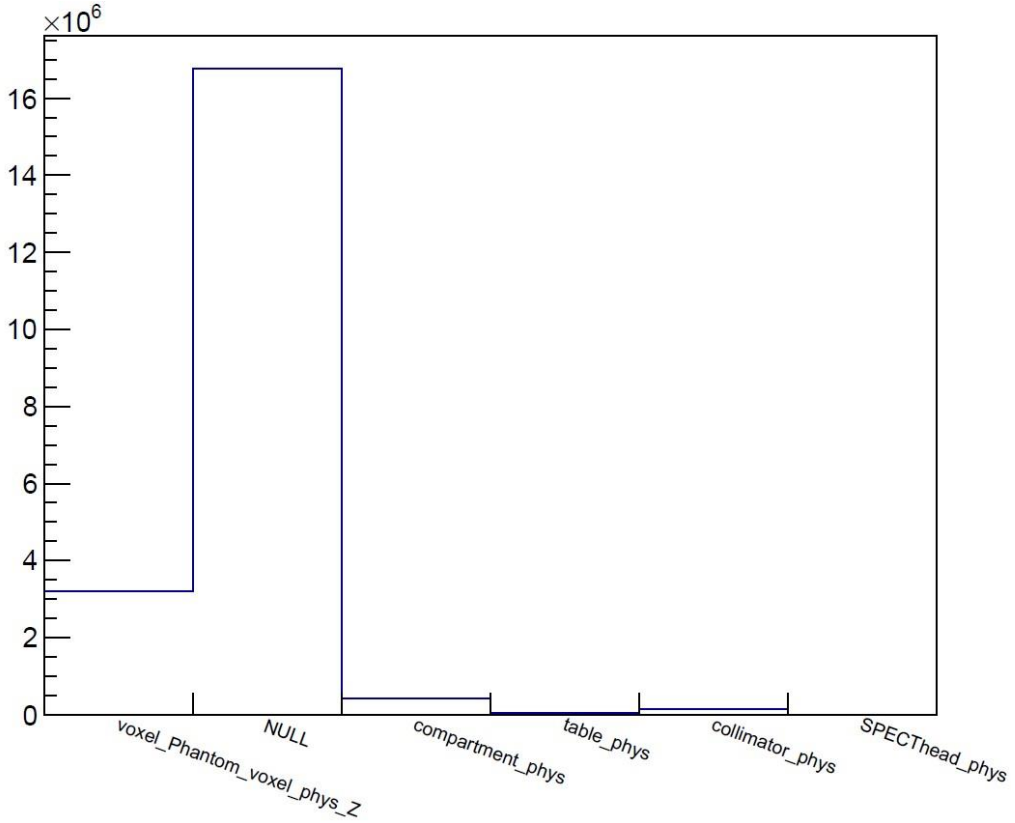

Figure 64: The events for the ^{177}Lu sensitivity phantom simulation which have been scattered in an object, where null is there has not been any scattering for those events, across all energy events

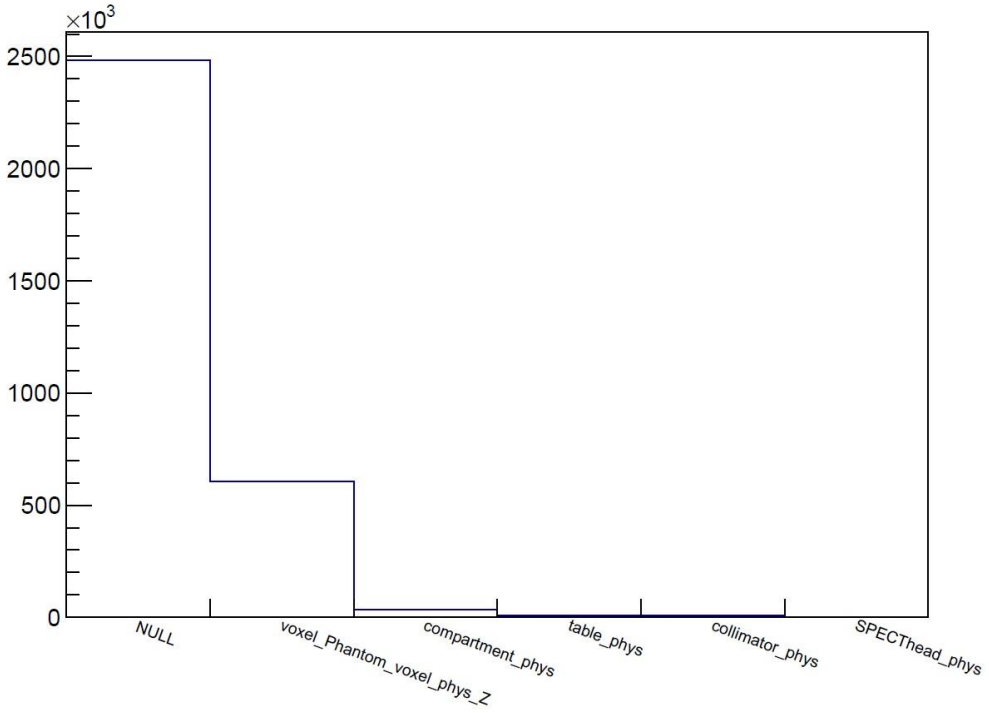

Figure 65: The events for the ^{177}Lu sensitivity phantom simulation which have been scattered in an object, where null is there has not been any scattering for those events, across the energy range of 50 to 70 keV

The Compton scattered events are greatest at approximately 50 keV, and they are generally increased at lower energies compared to higher energies, which results in the low energy photopeak to have a larger contribution of Compton scattered events than the higher energy photopeak at 208 keV. The breakdown of where the Compton scattering takes place shows that most events are not scattered, which is consistent with the energy spectrum output. The Compton scattered events occur in the cylindrical voxel-based phantom, back compartment, table, collimator and the gamma camera head. The SPECT head contains the crystal, collimator, plate and compartment. There are relatively more events scattered overall and particularly in the collimator for the full energy spectrum than at the low energy spectrum.

5.2.4 Discussion

A MC model for the sensitivity phantom used in section 4.3 was created. The images, energy spectra and Compton scattered events were analysed and compared to the gamma camera results. The images created for the 113 keV and 208 keV photopeaks (displayed in Figure 60) showed the correct outline of the cylindrical phantom, however more counts are observed at one end of the phantom, in an oval shape, compared to the other side of the phantom. The scale used is not optimal for assessing the exact level of the number of events detected, however it appears that there are approximately 30% more events detected on the right-side middle

compared to the left-side middle. It also appears that this effect is slightly worse for the 208 keV photopeak image compared to the 113 keV photopeak image. As the phantom used in this simulation was created as a voxel-based phantom the visualisation displayed it as a large grey box, and therefore it was not helpful to identify the exact location of the phantom and source. The simulation took almost a month to acquire and therefore was not simple to repeat it. It is possible that the issue is related to a storage issue as some of the simulation runs in the 70 MBq for 300 seconds simulation were smaller in file size than most of the other runs. When the phantom was run with a lower activity, as a test simulation, the image appeared relatively uniform, as displayed in Figure 66. Therefore, the full simulation should be repeated, as further work, to assess why there is a non-uniformity in the images produced.

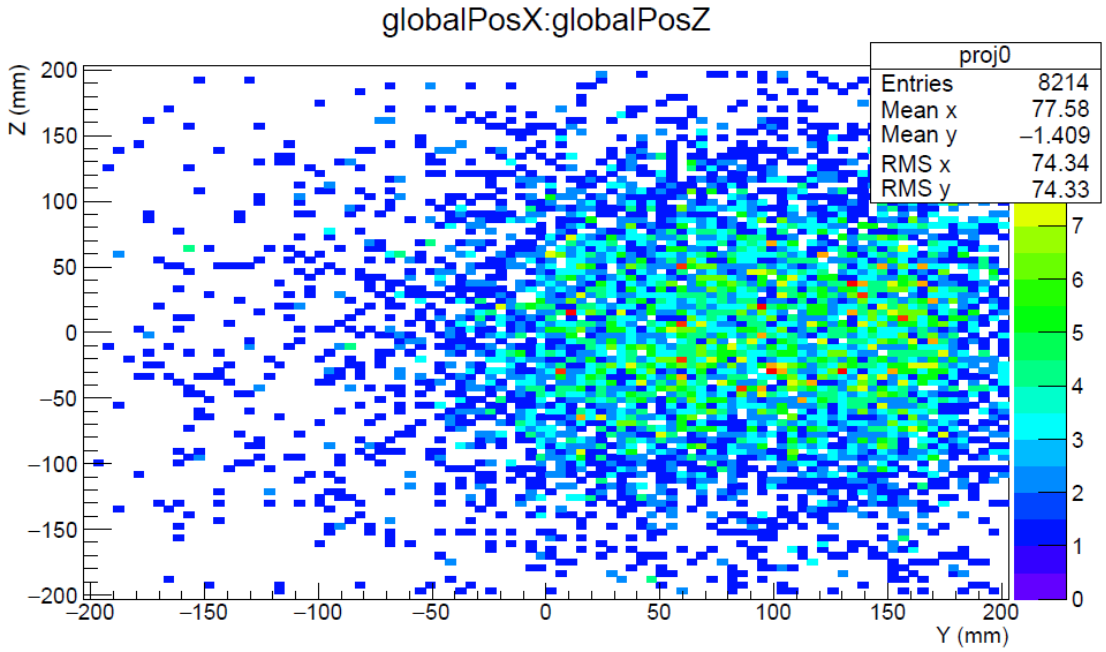

Figure 66: The MC simulation image produced for the ^{177}Lu sensitivity phantom for 10 seconds and 1 MBq

The energy spectrum produced for the 70 MBq ^{177}Lu sensitivity phantom over 300 seconds (displayed in Figure 61) is a similar shape to the gamma camera energy spectrum (as compared in Figure 62). The MC simulation energy spectrum is shifted to match the 208 keV photopeak of the gamma camera energy spectrum, so that can be directly compared. The 208 keV photopeak for the simulation does not fully match the low energy tail in the gamma camera spectrum. The low energy tail in the 208 keV photopeak is due to hole-tailing within the CZT detector (as described in sections 2.3, 2.6.1 and 3.3), therefore this difference suggests that the hole tailing is not accurately modelled in GATE. It may therefore be necessary to apply another correction to the MC simulation data to ensure the hole tailing is modelled accurately or the depth of

interaction could be investigated within a MC simulation to assess the hole-tailing effects. The correction for the hole tailing requires further investigation.

The energy spectrum at the low energy for a gamma camera is removed and therefore there is also a difference between the MC simulation and gamma camera energy spectrum below 50 keV. The lower energy MC simulation spectrum is further investigated by assessing the amount of Compton scattering that occurs (displayed in Figure 63). This shows that the largest quantity of Compton scattered events occurs between approximately 50 and 110 keV, which therefore increases the total counts in the energy spectrum at this energy range. There was further analysis to identify the location of where the Compton scattering occurs (displayed in Figure 64 and Figure 65), which identified that the Compton scattering occurred mostly in the phantom and there was also Compton scattering in the back compartment, table, collimator and gamma camera head. The gamma camera head contains the back compartment and collimator and therefore it is likely that these sub-components are causing most of the Compton scattering within the gamma camera head component. The collimator is placed between the phantom and the crystal and therefore some events will scatter within the collimator. The compartment is placed behind the crystal so will represent any back scatter that my occur from the electronics of the gamma camera. The phantom contains water which is surrounded by plastic and therefore any events initiated from the centre of the phantom will penetrate through a volume of water and plastic, before reaching the gamma camera, where Compton can take place. The events detected from the phantom will be a combination of non-scattered and scattered events as described in section 2.6.1.

As described in section 3.4, there is limited literature for a MC simulation for a CZT gamma camera imaging ^{177}Lu, therefore a direct comparison between the results from this work and the literature cannot be made. However, Robinson et al produced a MC simulation using ^{177}Lu for a NaI gamma camera which resulted in a similar energy spectrum to the gamma camera energy spectrum, displayed in Figure 67, where the difference between the MC simulation and gamma camera simulation are similar to the results produced in this work. The main difference is the contribution of the scatter within the energy spectra, where Robinson et al indicate there is a significant proportion related to the scattered events, whereas the results in this work have a much lower proportion of scattered events. However, the energy spectrum cannot be directly compared as Robinson et al used a different gamma camera technology, collimator and phantom.

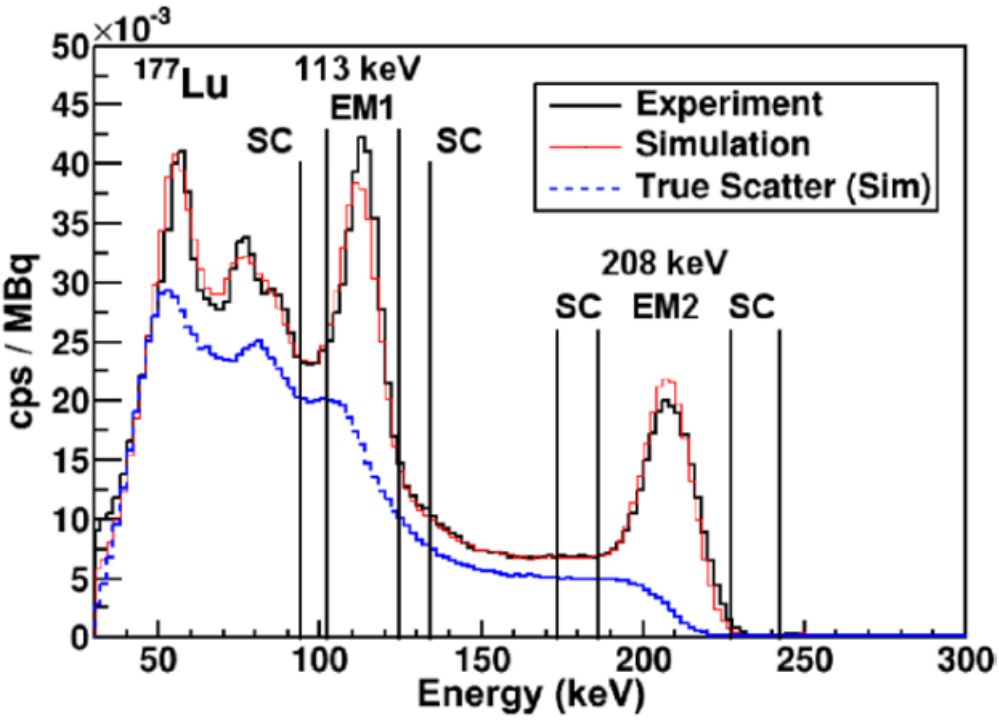

Figure 67: The emission spectrum for a water filled phantom measured using a GE Infinia Hawkeye gamma camera (black) and from a MC simulation (red) for ^{177}Lu with a MEGP collimator. The true scatter is visualised from the MC simulation (blue). The energy window ranges are highlighted (black vertical lines). (Taken from Robinson et al) [162]

5.3 MC Simulation for the ^{177}Lu Sphere in Scatter Phantom

5.3.1 Introduction

The same approach used in section 5.2 was used to create a MC model for the sphere in scatter phantom, used in section 4.2, to compare to the results from the gamma camera calibrations, described in section 4.2.

5.3.2 Methods

A voxel-based phantom for the sphere in scatter, described in section 4.2, was created using ImageJ using the same method as described in section 5.2.2. The sphere in scatter phantom image created with the ROI for the source macro can be seen in Figure 68 (A) and the sphere in scatter source image can be seen in Figure 68 (B).

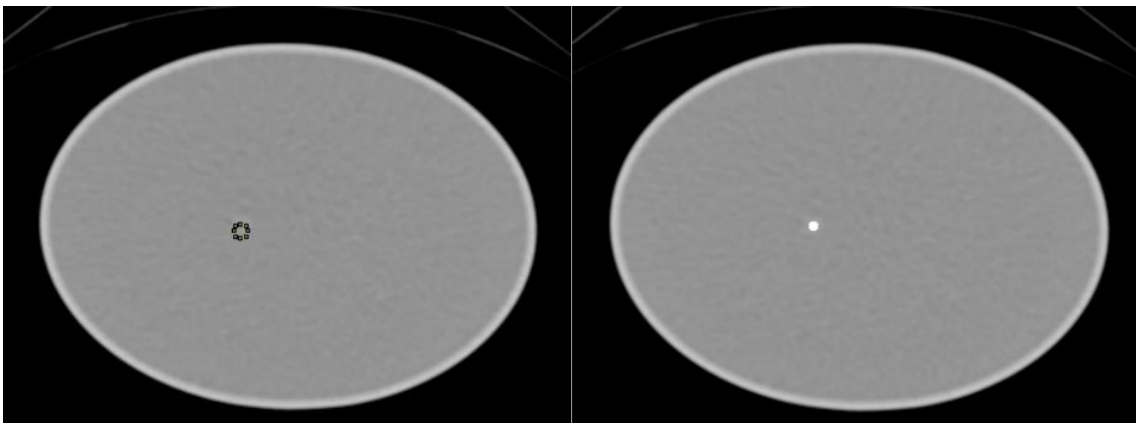

A: Sphere in scatter phantom macro **B: Sphere in scatter source macro**

Figure 68**: The sphere in scatter phantom macro produced using ImageJ with the ROI created for the source macro (A). The sphere in scatter source macro produced using ImageJ displayed as the white circle (B).**

The simulation was run using 4.88 MBq where the activity per voxel for the beta data file was 67330 Bq/voxel and for the gamma data file was 15890 Bq/voxel, calculated using Equation 36. The time was set to 300 seconds, over 300 jobs.

The MC simulation outputs were saved as ROOT files. The ROOT file for the MC simulated planar image was analysed using a range of macros to create an image for the 113 keV and 208 keV photopeaks and an energy spectrum, as described in section 5.2.2. In addition, the energy was analysed for whether the event penetrated the septa or hole of the collimator.

5.3.3 Results

The voxel-based phantom for the ^{177}Lu sphere in scatter phantom, with 4.9 MBq, was created successfully using ImageJ and the MC simulation for the planar image output for the 113 keV and 208 keV photopeaks are displayed in Figure 69. There are less events displayed in the 113 keV photopeak image compared to the 208 keV photopeak image and the spatial resolution appears to be less in the 113 keV photopeak image compared to the 208 keV photopeak image. The 208 keV photopeak displayed a cross artefact through vertical and horizontal lines in the image.

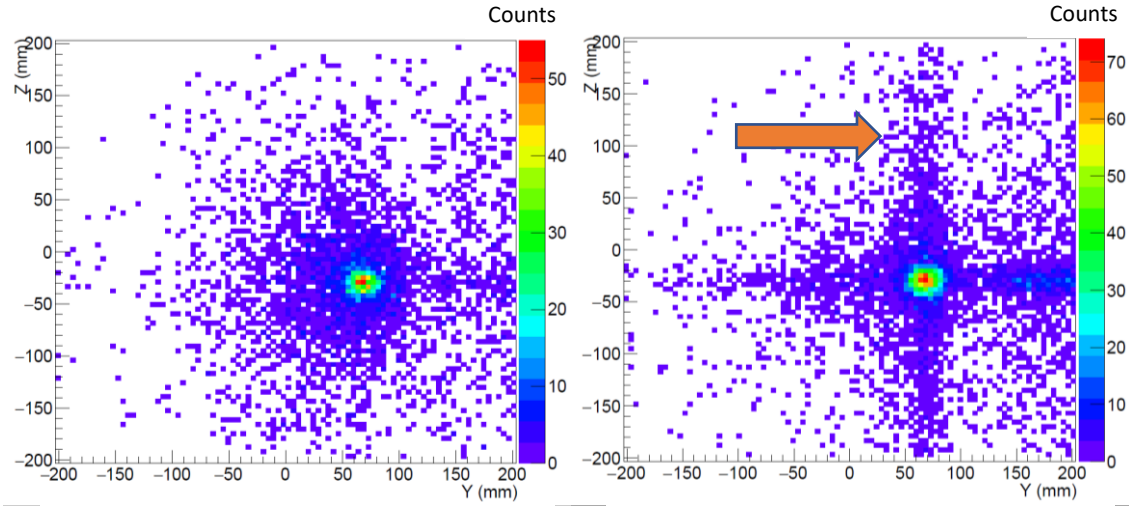

A: 113 keV **B: 208 keV**

Figure 69: The MC simulation image produced for the ^{177}Lu sphere in scatter phantom planar image for the 113 keV (A) and 208 keV (B) photopeak energy windows. The orange arrow indicates the cross artefact.

The energy spectrum for the 4.9 MBq ^{177}Lu sphere in scatter phantom for the MC simulation is displayed in Figure 70 and is compared to the gamma camera planar image energy spectrum in Figure 71. The energy spectrum appears to have relatively smaller peaks for the sphere in scatter phantom than for the sensitivity phantom (displayed in Figure 61). When comparing the energy spectrum for the sphere in scatter MC simulation to the gamma camera energy spectrum they are similar shapes, however, there appears to be a shift in the relative heights of the full spectrum, particularly at low energy (50 – 70 keV).

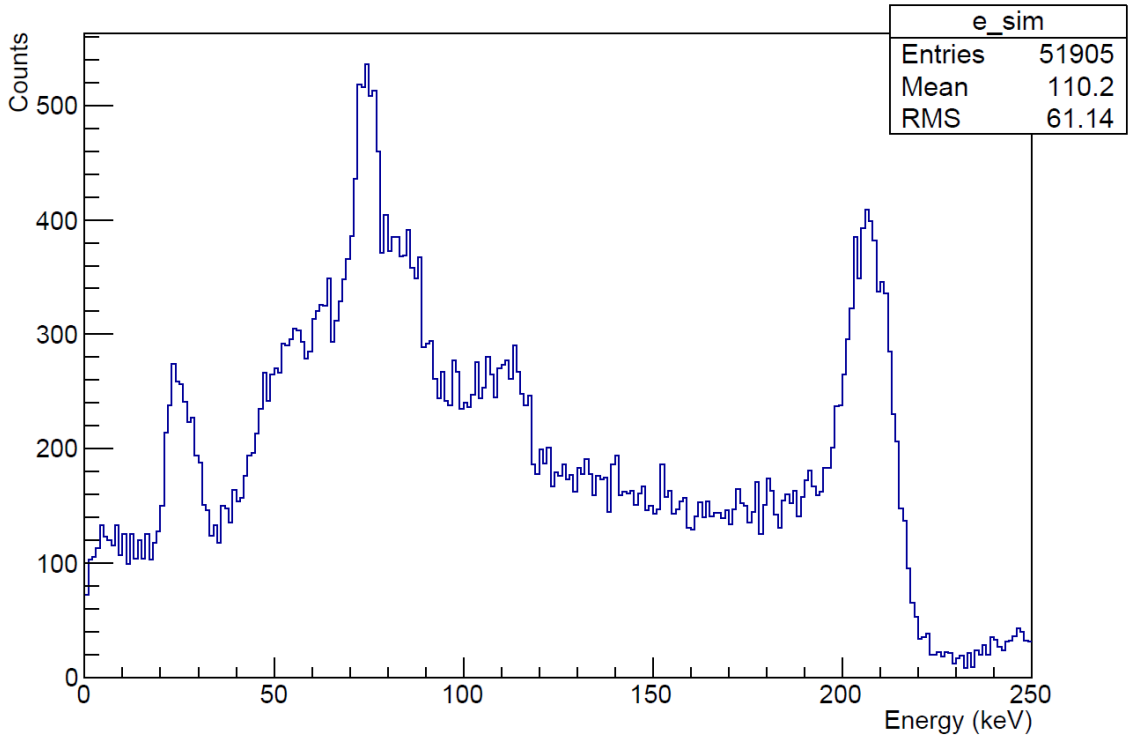

Figure 70: The energy spectrum produced for the ^{177}Lu sphere in scatter phantom planar image using the MC simulation for the GE Discovery 870 DR CZT

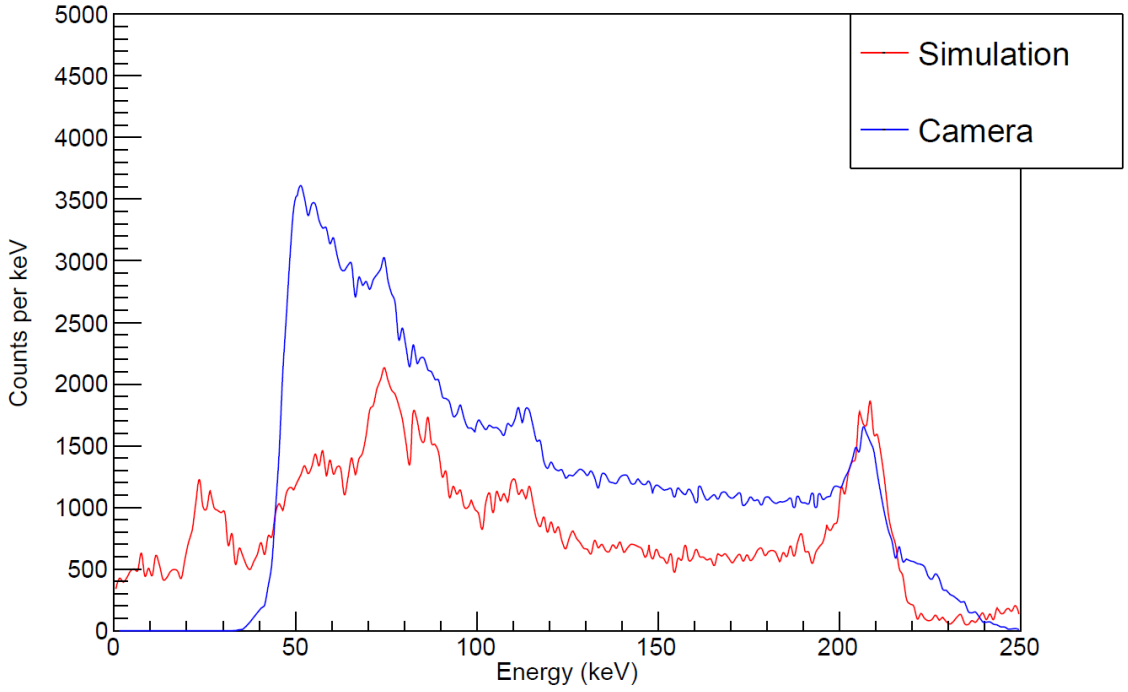

Figure 71: The energy spectra for the simulation (red line) and planar camera image (blue line) for the ^{177}Lu sphere in scatter phantom, normalised to the 208 keV photopeak

The MC simulation energy spectrum was further analysed by separating out the events that did and did not undergo Compton scattering, as displayed in Figure 72. The components where the

scattering events occurred were assessed for the full energy spectrum and for a low energy range (50 to 70 keV) only, displayed in Figure 73 and Figure 74, respectively. The energy spectrum was also divided into those events that penetrated the collimator septa and those events that did not penetrate the septa, as displayed in Figure 75. The Compton scattered events contribution was generally relatively small compared to the overall energy spectrum. The overall shape of the Compton scattered events was similar to the shape of the Compton scattered events analysed for the sensitivity phantom (displayed in Figure 63). As for the sensitivity phantom MC simulation, the breakdown of where the Compton scattering takes place shows that most events are not scattered, and the location they are scattered include the phantom, compartment, collimator and table. The septal penetration analysis shows that there is a large contribution of events at approximately 208 keV which do penetrate the septa and relatively few at lower energies. There is also a peak of events that undergo septal penetration at approximately 75 keV.

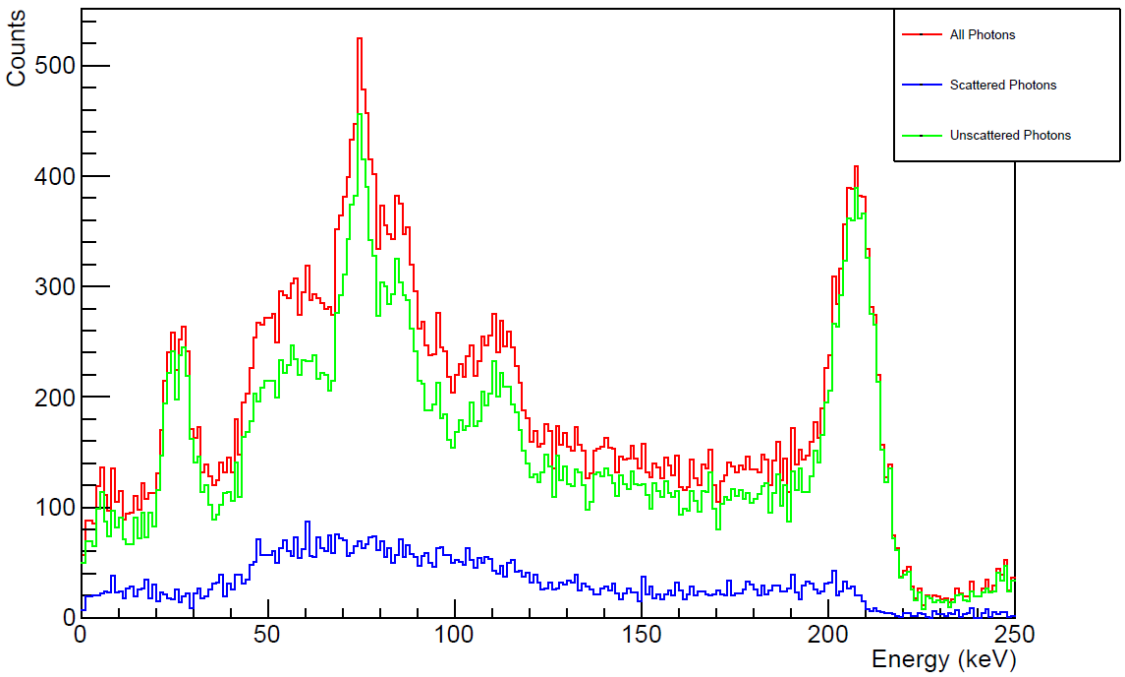

Figure 72: The energy spectrum produced for the ^{177}Lu sphere in scatter phantom planar image using the MC simulation for the GE Discovery 870 DR CZT, including all events (red line), Compton scattered events (blue line) and events that have not undergone Compton scattering (green line)

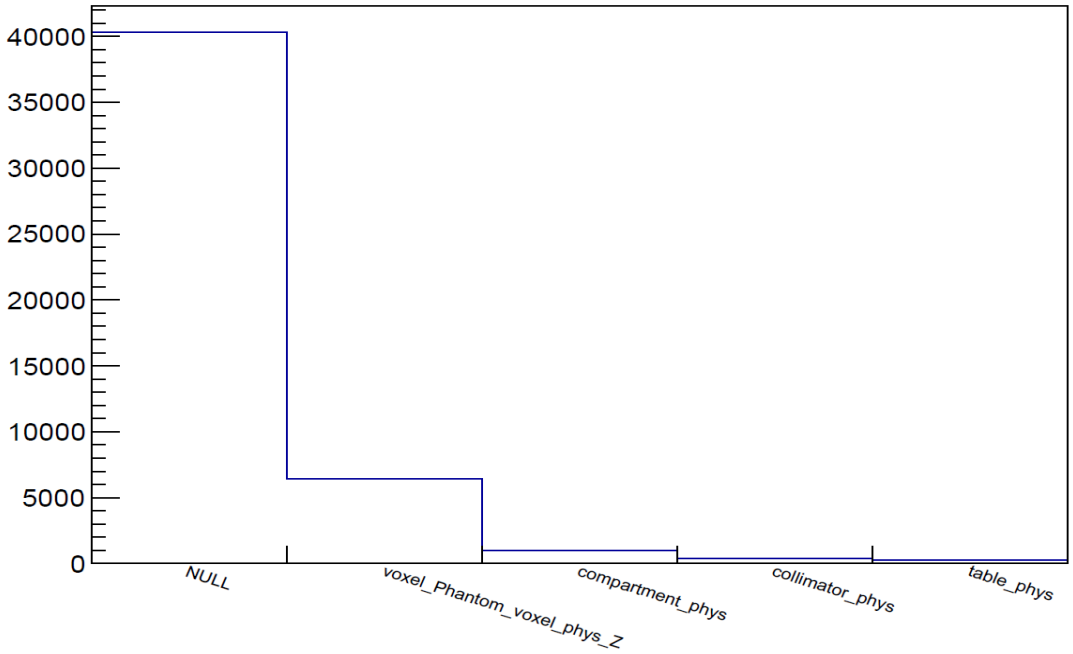

Figure 73: The events for the ^{177}Lu sphere in scatter phantom simulation which have been scattered in an object, where null is there has not been any scattering for those events, across all energy events

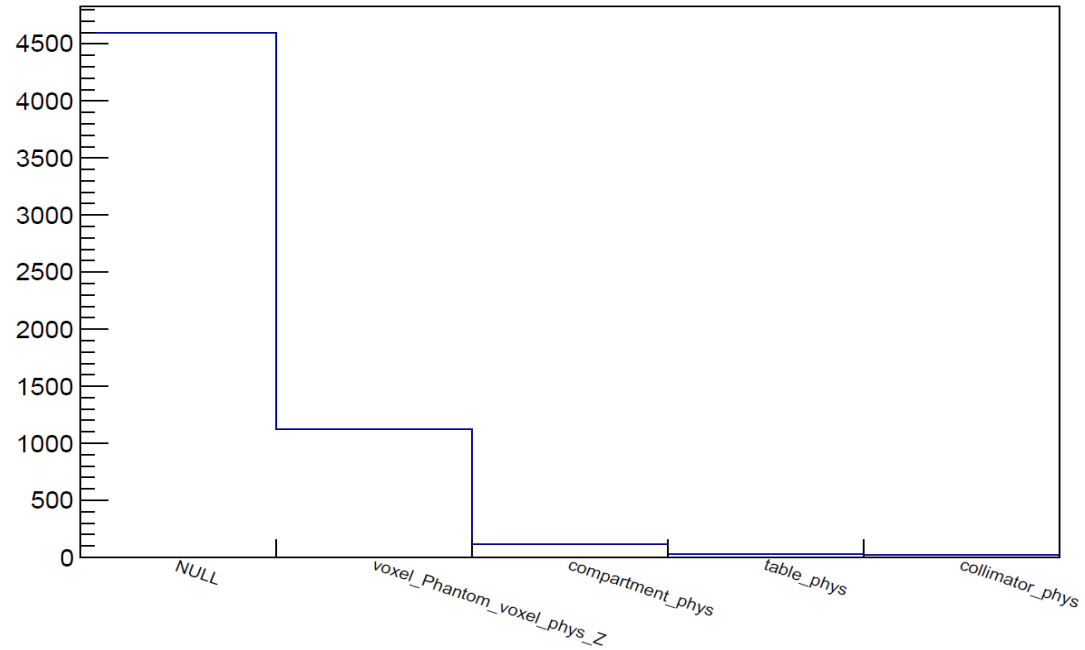

Figure 74: The events for the ^{177}Lu sphere in scatter phantom simulation which have been scattered in an object, where null is there has not been any scattering for those events, across the energy range between 50 to 70 keV

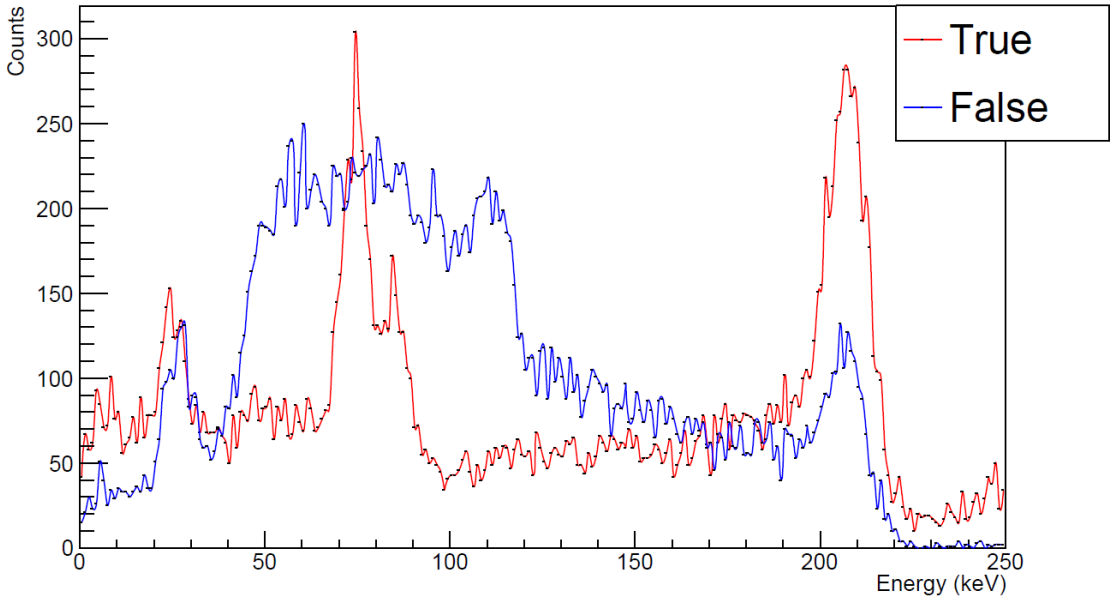

Figure 75: The energy spectrum produced for the ^{177}Lu sphere in scatter phantom planar image using the MC simulation for the GE Discovery 870 DR CZT, including the events that have penetrated the septa (red line) and the events that have not penetrated the septa (blue line)

5.3.4 Discussion

The sphere in scatter phantom was successfully modelled using a MC simulation, by creating a voxel-based phantom for the MC simulation, using the CT image. The images produced from the MC simulation for the 113 keV and 208 keV photopeaks display a sphere as expected (shown in Figure 69). There are more events recorded for the 208 keV photopeak than the 113 keV photopeak, which is consistent with the difference in relative abundance of the two photopeaks. The 113 keV photopeak image displays visually more scattered events than the 208 keV photopeak image. The scattered events are consistent with the water-filled phantom that surrounds the sphere, the phantom is displayed in Figure 29. The 208 keV image displays a septal penetration artefact (displayed as a cross), which is consistent with the gamma camera images produced in chapter 4 and with work presented by Roth et al and Sandstrom et al [99], [151].

The energy spectrum produced for the sphere in scatter MC simulation (displayed in Figure 70) is similar to the energy spectrum produced for the sensitivity phantom MC simulation (displayed in Figure 61), however the photopeaks from the gamma emissions and characteristic x-rays are relatively reduced for the sphere in scatter, due to the increase in scatter material and lower level of activity used. When the MC simulation energy spectrum for the sphere in scatter is compared to the gamma camera energy spectrum (displayed in Figure 71), there is a difference

in the shape of the energy spectra, particularly between 50 and 70 keV. This is likely due to the MC simulation not fully representing the Compton scatter, bremsstrahlung and characteristic x-rays as observed in the gamma camera energy spectrum. The contribution of the various components to the MC simulation energy spectrum were investigated by reviewing the Compton scatter and septal penetration within the simulation.

The Compton scatter contribution was investigated by reviewing the events that underwent Compton scatter and their contribution to the energy spectrum, displayed in Figure 72, and the location of where the Compton scattering occurred, displayed in Figure 73 and Figure 74. The Compton scattered energy spectrum for the sphere in scatter MC simulation is a similar shape to the sensitivity phantom energy spectrum (Figure 63), however the spectrum appears to contain more noise for the sphere in scatter than for the sensitivity phantom, which is likely to be due to the difference in activity used. It appears that Compton scattering does not have a large contribution to the energy spectrum and therefore it may be that there are more Compton scattered photons detected by the gamma camera than the MC simulation has predicted. This should be further investigated by assessing the use of different materials within the phantom. As the energy spectra for the sensitivity phantom had a better similarity, it is unlikely that the cause is due to the CZT gamma camera MC model, but is due to the phantom defined, or the set up used in the gamma camera experiment. If there was a lead carry case or equivalent close to the gamma camera when imaging was carried out then that may cause a larger number of photons detected at lower energies, which have not been included in the MC simulation. To further investigate this, the sphere in scatter gamma camera imaging should be repeated. The breakdown of location of the Compton scattered events (displayed in Figure 73 and Figure 74) shows that the biggest contribution is the phantom, and therefore the phantom should be reviewed to assess if the contribution is modelled accurately.

The septal penetration analysis (displayed in Figure 75) shows that there are a large number of events that have undergone septal penetration and are detected in the gamma camera simulation for an energy between 190 and 220 keV, which is consistent with the septal penetration artefact displayed in Figure 69. The septal penetration analysis also shows a high level of septal penetration for 70 to 90 keV, which is likely to be due to characteristic x-rays produced in the lead collimator at 72 keV and 84 keV, which is consistent with the literature [3], [74], [166]. The larger number of events at low energies for the gamma camera energy spectrum is likely to be due to either bremsstrahlung radiation [123], [127] or characteristic x-rays, however further investigation is required to confirm this.

6 CONCLUSIONS

As stated in section 1.2, the aims of this work were:

- Perform a literature review to identify the methods used for quantitative NaI gamma camera imaging and analyse whether these techniques could be used for quantitative CZT gamma camera imaging.
- Develop a SC technique that can be used for imaging ^{177}Lu on a CZT gamma camera which is appropriate for routine clinical use.
- Calculate ^{177}Lu CZT gamma camera calibrations for uniformity, sensitivity and PVC and determine the optimal parameters for SPECT reconstruction.
- Carry out a validation for the ^{177}Lu gamma camera calibrations calculated.
- Develop a MC model of a CZT gamma camera which could be used to aid the validation of the gamma camera calibrations calculated.

This chapter reviews the methods, results and discussions within this work and summarises how the research aims were met, what limitations there were and suggestions for further work within this area of research.

6.1 Summary and Conclusions

In summary, a literature review was carried out for methods used for quantitative NaI gamma camera imaging of ^{177}Lu and the status of quantitative CZT gamma camera imaging for all isotopes, including SC techniques. This work used the GE Discovery 870 DR CZT gamma camera to successfully create a ^{177}Lu uniformity calibration, create a TEW SC technique that could be used for the CZT gamma camera, calculate a range of sensitivity values, propose the optimal reconstruction parameters that should be used (5 iterations, 10 subsets, CTAC, CZT TEW SC and no RR), create a PVC and carry out a basic validation of the calibrations. In addition, a MC model of the GE Discovery 870 DR CZT gamma camera was created, and some validation steps were carried out to test the MC simulation against two gamma camera phantom images and energy spectra produced within this work. This work shows that using a CZT gamma camera for quantitative imaging of ^{177}Lu is feasible, however some further work is required to improve the proposed calibrations and fully validate the results within this work.

6.1.1 ^{177}Lu CZT Gamma Camera Calibrations

The uniformity test concluded that the uniformity was generally acceptable for both detectors using the 113 keV photopeak, however the 208 keV photopeak uniformity results require further

investigation. The SC technique created was based on the Ogawa TEW SC technique with an additional term to account for the hole tailing effects of the CZT detector, defined as *h.* The CZT TEW SC technique was simple to implement for routine clinical SC through creating a processing script in GE Xeleris, using Aladdin. This work indicated that the optimal reconstruction parameters are 5 iterations, 10 subsets, CTAC, CZT TEW SC and no RR. The value of *h* used would depend on the photopeak being imaged and should be 0.22 for the 113 keV photopeak and 0.35 for the 208 keV photopeak (displayed in Table 10). The calibration factors are 7.84 ± 0.39 cps/MBq for the 113 keV photopeak (*h* equals 0.22) and 10.61 ± 0.53 cps/MBq for the 208 keV photopeak (*h* equals 0.35). The PVC should be applied to correct for the PVE using the values in Table 13 and Equation 35, where a different PVC is required for the 113 keV and 208 keV images. The validation process showed that the accuracy was -40% (95% confidence interval -75% to 102%) for a 113 keV photopeak and was -36% (95% confidence interval -83% to 40%) for a 208 keV photopeak. The gamma camera imaging and MC simulation highlighted a septal penetration artefact when using the 208 keV photopeak and therefore it is likely that the 113 keV photopeak would be most suitable for qualitative and quantitative imaging for the WEHR collimators on the GE Discovery 870 DR CZT gamma camera.

6.1.2 Monte Carlo Model of the CZT Gamma Camera

The MC model produced was adapted from a validated MC model for a NaI gamma camera to create a model of the GE Discovery 870 DR CZT gamma camera. It was initially tested using a simple phantom using ^{99m}Tc to assess its basic suitability. The MC simulation was then adapted for voxel-based phantoms using the CT from two phantoms imaged on the gamma camera during the gamma camera calibration work, a uniformly filled water cylindrical phantom and a small sphere placed within a water-filled non-active background. The images produced for all simulations generally looked acceptable, however the cylindrical phantom was not completely uniform, which therefore requires further investigation. The energy spectra produced for the MC simulations were compared to the gamma camera energy spectra and they were generally similar shapes, however the low energy events did not fully match the gamma camera energy spectrum, particularly for the sphere imaged in scatter. There was some analysis carried out into the components of the energy spectra for the MC simulation to identify the Compton scattered events and the events that had penetrated the septa, however further work is required to fully investigate the differences between the energy spectra.

6.2 Future work

6.2.1 Limitations

There are some limitations in this work, including the number of phantom images acquired, the artefacts seen for RR and the 208 keV photopeak, the use of the WEHR collimator and the validation process used. Some of the main limitations of this work are that the phantom investigations were only carried out once, which resulted in a range of uncertainties. These phantom investigations link to the optimisation, sensitivity, calculation for the value of *h*, the PVC calibration and the validation process. The uncertainties could be reduced by more accurately measuring the activity of ^{177}Lu using a radionuclide calibrator with a direct calibration to the NPL primary standard calibrator, the phantom measurements could be repeated to ensure all measurements are repeatable and the phantoms could be imaged in multiple positions on the gamma camera.

The uniformity test should be repeated to assess the defect in the 208 keV photopeak image and to identify a requirement for the routine quality control testing schedule. It is possible that the uniformity calibration will need regular updates, however this frequency is currently unknown as the uniformity test has not been repeated. As the gamma camera images were carried out over a period of approximately six months it is possible the ^{177}Lu uniformity calibration would need repeating. The gamma camera is routinely tested for ^{99m}Tc uniformity using a fillable flood phantom for clinical use, and therefore this would have identified any major issues in uniformity (for example, if a detector block needed replacing), however it would not identify any gradual drift in uniformity performance for ^{177}Lu.

In addition, the RR applied in this work produced Gibb's artefacts and therefore was not further investigated, however RR is widely used in the literature and therefore the RR should be further investigated to assess if the Gibb's artefact can be avoided and how the results with RR compare to the accuracy reported in the literature and to the accuracy of the results without RR in this work.

Another limitation is that the validation process was only carried out on one small sphere, which covered a basic validation. To carry out a full validation there would need to be a range of different size and shape phantoms used, including anthropomorphic phantoms. There should also be a fully validated MC simulation to aid validation of the gamma camera calibrations, a comparison to a NaI gamma camera and then there should be a phase of clinical validation. The line profiles used in the validation process used 4.42 mm pixels, which did not provide accurate analysis, therefore the line profiles should be repeated for smaller pixels to provide improved

spatial resolution. The MC model created should be fully validated and tested against a wide range of phantoms, including the anthropomorphic phantoms. The validated MC simulation would then be able to help fully validate the gamma camera calibrations produced in this work.

Finally, the CZT TEW SC method proposed did display some improvements on the Ogawa TEW SC method, however it was not the ideal solution for CZT SC. There are a few other methods of CZT SC described in the literature, as identified in section 3.3, and therefore there should be a direct comparison of the CZT TEW SC method derived in this work and some of the CZT SC methods described in the literature (for example by Fan et al [146], Pourmoghaddas et al [145] and Kacperski et al [102]).

6.2.2 Further Research

This work raised multiple research questions, which should be investigated as further work. The first questions are; what is an appropriate tolerance for the ^{177}Lu uniformity test and how often should the ^{177}Lu uniformity test be carried out for routine use. This could be investigated by repeating the uniformity test on multiple occasions and analysing the results to assess the tolerances and the required frequency.

Another set of questions are about the components that make up the energy spectra for the CZT gamma camera and how this links to the SC method required for the clinical environment. Therefore, a fully validated MC simulation could be used to analyse the energy spectra. Part of this work has been investigated in chapter 5, however the MC model requires further validation.

In addition, the validation process has not been applied to a range of phantoms or any clinical data, and therefore the next research question is how accurate are these calibrations in a range of phantoms and in clinical cases. The phantoms should include anthropomorphic phantoms, as these can be directly applied to clinical cases. These additional phantom investigations should be filled with a known activity and the gamma camera images should be processed to calculate the activity within the phantom, which can then be compared to the known activity in the phantom. The phantoms should include more than one volume of activity so the effects of septal penetration can be assessed in a more clinically relevant scenario. When the full range of phantoms have been analysed and are within an acceptable accuracy, the final stage is to complete some clinical validation. This could involve imaging some patients on a NaI gamma camera and a CZT gamma camera for a direct comparison, however ethics will need to be considered for this stage of the process.

As there were artefacts seen for the RR and 208 keV photopeak, there are questions related to how could RR improve the accuracy of the quantification, how does the septal penetration artefact effect quantification of more than one volume and could the medium energy collimators result in a more accurate quantification for the 208 keV photopeak. These should be investigated by adjusting the scaling factor used in Xeleris for the RR processing to assess if that reduces the Gibb's artefact. It may also be beneficial to use a lower activity in the phantoms that displayed a Gibb's artefact. The effect of the septal penetration artefact on multiple volumes of interest can be investigated by using an anthropomorphic phantom (as suggested above). Once this work has been completed, results should then be directly compared to a NaI gamma camera to see if there could be an improvement on the current routine practice. The gamma camera calibrations and MC simulation should also be repeated with medium energy collimators and compared to the accuracy of quantification for the WEHR collimators.

Finally, there are questions about how accurate the MC model created is and whether it can be used to validate the gamma camera calibrations. To investigate this the simulations should be repeated for the cylindrical phantom with the septal penetration tracking switched on and to assess whether there are any associated errors. It may also be beneficial to repeat some of the phantom imaging whilst ensuring there are no additional scatter materials close to the field of view. There also needs to be an additional component included for the hole tailing effect seen for the CZT detector, which may need to be applied to the data in an additional step, outside the MC simulation software. Or the MC simulation could be run for two different techniques for energy blurring, one for the higher energy side and another for the lower energy side. The required blurring could be assessed by using a curve fitting tool (for example, in Matlab) to calculate the curve associated with the higher and lower energy parts of a photopeak from a gamma camera acquired energy spectrum. Alternatively, the MC simulation could be used to analyse the depth of interaction of the photons with the CZT detector, which would lead to an estimation of the hole tailing effect.

7 APPENDIX A: DCLINSCI APPENDIX – LIST OF AMBS A UNITS AND MEDICAL PHYSICS B UNITS TOGETHER WITH ASSIGNMENTS – ANNA CHILCOTT

AMBS – A Units		
Unit title	**Credits**	**Assignment wordcount**
A1: Professionalism and professional development in the healthcare environment	30	A1 – assignment 1 – 2500 words Group work/presentation – 10 minutes (10%) A1 – assignment 2 – 3000 words
A2: Theoretical foundations of leadership	20	A2 – assignment 1 – 3000 words A2 – assignment 2 – 3000 words
A3: Personal and professional development to enhance performance	30	A3 – assignment 1 – 1500 words A3 – assignment 2 – 4000 words
A4: Leadership and quality improvement in the clinical and scientific environment	20	A4 – assignment 1 – 3000 words A4 – assignment 2 – 3000 words
A5: Research and innovation in health and social care	20	A5 – Group work/presentation – 15 minutes (25%) A5 – assignment – 4000 words
Medical Physics – B Units		
B1: Medical Equipment Management	10	Group presentation 1500 word assignment
B2: Clinical and Scientific Computing	10	Group presentation 1500 word assignment
B3: Dosimetry	10	Group presentation 1500 word assignment
B4: Optimisation in Radiotherapy and Imaging	10	Group presentation

		1500 word assignment
B6: Medical statistics in medical physics	10	3000 word assignment
B8: Health technology assessment	10	3000 word assignment
B9: Clinical applications of medical imaging technologies in radiotherapy physics	20	Group presentation 2000 word assignment
B10b: Assessment of Image Quality	10	Group presentation 1500 word assignment
B10f: Radiation Protection Advice	10	1500 word portfolio item
B10g: Radiation Waste Advice	10	1500 word portfolio item
Generic B Units		
B5: Contemporary issues in healthcare science	20	1500 word assignment + creative project
B7: Teaching Learning Assessment	20	20 minute group presentation

8 APPENDIX B: INNOVATION PROPOSAL

Executive Summary

This innovation proposal assesses the accuracy of quantification of Lutetium-177 (^{177}Lu) imaging on a solid-state gamma camera against a scintillation gamma camera, by identifying the optimal methods for calibration. Nuclear medicine imaging is generally assessed visually and qualitatively, which can lead to observer dependent interpretation. ^{177}Lu is a type of molecular radiotherapy used for cancer treatment and imaging is carried out following therapy to assess the distribution of the ^{177}Lu within the patient. If accurate quantitative ^{177}Lu imaging is possible then the radiation dose given to the patient can be calculated, which will open the door for personalised therapies using a technique called dosimetry, as required by the Ionising Radiation (Medical Exposures) Regulations 2017 (IRMER17) [54].

This can be achieved by calibrating the solid-state cadmium zinc telluride (CZT) gamma camera using a range of measurements with a known radioactivity within simple geometry objects. The reconstruction of images can be optimised, and a calibration factor can be calculated to recover the activity within the image from the counts detected by the camera. This experimental work will be supported by computer simulations of the imaging system to assess any differences between the gamma camera image and the ideal image, and therefore whether corrections are suitably applied. The CZT gamma camera is more efficient than a conventional scintillation gamma camera, which may lead to more accurate quantification and therefore improvement in patient dosimetry and treatment outcomes.

The potential barriers for this proposal include securing funding to buy the required equipment for calibrations and testing, the additional staff time to make the measurements and the possible need to routinely repeat the calibrations. The equipment and staff time can be funded through the higher specialist scientist training programme, which includes a budget for project work and protected time for staff to undertake the project.

Background

Nuclear medicine is the diagnosis or treatment of disease using a radioactive tracer, which is administered to the patient. Gamma cameras are used to acquire an image of the radioactive tracer distribution within the patient. Conventional scintillation sodium iodide (NaI) gamma cameras are often used to produce the image. A new digital technology (called cadmium zinc telluride (CZT)) has recently been introduced which improves the efficiency in image production. The CZT detector has a narrower energy peak indicating it has improved energy resolution than

the NaI detector. Solid-state gamma cameras with CZT detectors provide improved energy resolution and enhanced count-rate performance compared to conventional scintillation cameras. Increased detector performance can improve patient images, which can help clinicians make a better diagnosis and therefore improve the patient's outcome.

This proposal will focus on imaging ^{177}Lu, which is used to treat cancer (either neuroendocrine tumours or metastatic prostate cancer), and a gamma camera image is acquired following the therapy to assess treatment success. If multiple images are taken following a therapy, the radiation dose to the patient can be calculated, which can used to personalise treatments, however this is dependent on accurate quantification of ^{177}Lu imaging.

The problems with the current methods are images for ^{177}Lu are assessed visually, which depends on a trained reporting doctor, and therefore image interpretation is observer dependent. It is also not possible to calculate the radiation dose received by the patient as there are technology limitations, and image corrections are required. These corrections include scatter (radiation being detected that has not travelled perpendicular to the detector, or has changed direction before being detected), reconstruction (how the image is produced in the computer), attenuation (radiation that travels further through the patient will have less intensity than if it is at the edge of the patient) and dead time (high radiation levels can saturate the detector). Some of these technology limitations can be corrected for, but a perfect image is not possible.

Innovation Proposal

The innovation proposed is to determine the optimal imaging parameters and calibration methodology for quantitative ^{177}Lu post therapy imaging on a solid-state gamma camera and compare the quantification accuracy to scintillation gamma cameras. There is currently very little research on ^{177}Lu imaging on a CZT gamma camera and therefore multiple gamma camera measurements and computer simulations will be made to assess the accuracy of quantification of ^{177}Lu imaging.

Computer simulations will be used to predict how the CZT gamma camera will react to the ^{177}Lu and what kind of images it may produce. These predictions will then be compared to real gamma camera images. Initially, simple objects (such as rectangles or cylinders) will be used to assess the best imaging settings for the digital gamma camera and calculate the relationship between the known quantity of radiation and the calculated radiation from the images produced. The same methods will be carried out on the conventional gamma camera to assess the differences

and whether there is an improvement. Finally, more complex geometry will be imaged, which is similar to a patient's anatomy, so the accuracy of methods for a patient image can be assessed.

Options Appraisal

Optional One – No change

This will involve no additional staff time or costs, however there will be no improvements to the patient's pathway and the radiation dose to patients following therapies will not be calculated. This is not suitable as the department will be non-compliant with IRMER17 [54].

Optional Two – Quantification of ^{177}Lu on a NaI gamma camera

It is possible to calculate the radiation dose to a patient following a ^{177}Lu therapy using a scintillation gamma camera, however it cannot reliably be used as a quantitative tool as there are many technical challenges [4]. Scintillation gamma cameras are less efficient than solid-state gamma cameras and therefore it is likely that the accuracy of the quantification will be reduced. There is no consensus on the methods used for gamma camera calibrations and there is a range of published literature on different methods and equipment used [4], [32], [127]–[130], [56], [112], [113], [115]–[118], [126], and therefore more work will be required to determine the best approach and therefore this is not a suitable option.

Option Three – Quantification of ^{177}Lu on a CZT gamma camera

A fillable flood tank is required for weekly testing and calibration of the CZT gamma camera used to acquire clinical images. It is essential that the gamma camera is tested and calibrated weekly to ensure the quality of the clinical images is suitable to make diagnoses and to reduce the risk of patients receiving a radiation dose without images being acquired. The nuclear medicine department owns one fillable flood tank which is used for the most common isotope used for gamma camera imaging.

To implement quantification of ^{177}Lu on the CZT gamma camera, an additional fillable flood tank with shielding and a positioning cart will be purchased. This will be required so routine testing will not be interrupted, and there will be opportunities for a range of service developments and improve staff health and safety. The additional shielding and positioning cart will reduce manual handling from the current methods used and radiation doses to staff should be as low as reasonable practicable [168].

Calibration of the CZT gamma camera with ^{177}Lu will provide valuable opportunities to broaden its use for calculations of patient radiation dose, which may be more accurate than for NaI gamma cameras. If the radiation dose to the patient can be calculated accurately then it is possible to personalise the patient's treatment, resulting in improved patient outcomes and compliance with legislation. The Ionising Radiation (Medical Exposures) Regulations 2017 recommends that "the absorbed dose to the tumour, and to non-target volumes and tissues, following each administration should be measured and recorded, to permit subsequent optimisation of total doses" [180].

The cost of the fillable flood tank, shielding and positioning cart is £8734.31. This equipment will be used for a range of isotopes, which will lead to a number of service development projects in the department. There will be additional staff time required to acquire the calibration and test images, which is primarily funded by the higher specialist scientist training programme budget.

The barriers to this option are that there may be regular calibrations required for ^{177}Lu (in addition to ^{99m}Tc which is used daily), there may be a problem in creating a uniformity calibration for the scatter energy windows (required for scatter correction) and there may be issues with dead pixels appearing in the ^{177}Lu image (which are calibrated using other isotopes). ^{177}Lu is routinely imaged on scintillation gamma cameras using dual-energy scatter-corrected windows, however this may not be possible on the CZT gamma camera as it is currently only designed to image low energy gamma emissions and the scatter energy windows will need a separate uniformity calibration to the peak energy calibration. This is the first calibration that will be acquired and therefore these potential barriers can be assessed at the start of the project. The uniformity calibration will be repeated for the energy peak and scatter windows and testing will be carried out to test whether this is successful. Computer simulations will support the practical work and identify the differences between the CZT gamma camera images and what the ideal image and energy spectrum should look like. To complete the computer simulations a new skill will be learnt, which will require additional staff time, but once learnt it can be used for other service development work.

Stakeholder Engagement

The main team that this work will initially affect is the nuclear medicine physics team. A small group of the team were approached to provide verbal feedback on this innovation proposal. There was generally good feedback about the overall outcome of the project and the benefit to patient pathways, however there were some barriers discussed. There will be additional staff time to carry out the experimental work and computer simulations which is partly funded by the

higher specialist scientist training scheme, but there will need to be additional time and resources from a range of staff members. There will be a significant amount of gamma camera time required, which will primarily be out of hours. There is a cost of purchasing a fillable flood tank to carry out the calibrations, however this is also be used in a range of service development projects. There was a concern that the calibrations will require regular repeats due to the nature of the equipment, however this will be possible with the purchase of the additional fillable flood tank.

The CZT gamma camera is primarily used for low energy gamma emitting isotopes and ^{177}Lu is generally considered to be medium energy. It is possible to have a specific medium energy collimator for the CZT gamma camera, but this may require extra costs or discussion with the manufacturer. If a medium energy collimator is acquired, then the calibrations and testing will need to be repeated.

Conclusion

This innovation proposal provides potential improvement to cancer patient pathways by allowing improved accuracy in calculations of the radiation dose received by the patient from ^{177}Lu molecular radiotherapy. This project will involve additional staff time and funding, however this is primarily funded by the higher specialist scientist training scheme. The new equipment and skills required for this project will aid future service development projects which will benefit the department further.

9 REFERENCES

[1] J. Tran-Gia *et al.*, "A multicentre and multi-national evaluation of the accuracy of quantitative Lu-177 SPECT/CT imaging performed within the MRTDosimetry project," *EJNMMI Phys.*, vol. 8, no. 1, 2021, doi: 10.1186/s40658-021-00397-0.

[2] P. Jackson, M. Hofman, L. McIntosh, J. P. Buteau, and A. Ravi Kumar, "Radiation Dosimetry in 177Lu-PSMA-617 Therapy," *Semin. Nucl. Med.*, vol. 52, no. 2, pp. 243–254, 2022, doi: 10.1053/j.semnuclmed.2021.11.003.

[3] M. Ljungberg, A. Celler, M. W. Konijnenberg, K. F. Eckerman, Y. K. Dewaraja, and K. Sjögreen-Gleisner, "MIRD pamphlet no. 26: Joint EANM/MIRD guidelines for quantitative 177Lu SPECT applied for dosimetry of radiopharmaceutical therapy," *J. Nucl. Med.*, vol. 57, no. 1, pp. 151–162, 2016, doi: 10.2967/jnumed.115.159012.

[4] J. Wevrett *et al.*, "Inter-comparison of quantitative imaging of lutetium-177 (177Lu) in European hospitals," *EJNMMI Phys.*, vol. 5, no. 1, 2018, doi: 10.1186/s40658-018-0213-z.

[5] S. Brown, D. L. Bailey, K. Willowson, and C. Baldock, "Investigation of the relationship between linear attenuation coefficients and CT Hounsfield units using radionuclides for SPECT," *Appl. Radiat. Isot.*, vol. 66, no. 9, pp. 1206–1212, 2008, doi: 10.1016/j.apradiso.2008.01.002.

[6] S. R. Cherry, J. Sorenson, and M. E. Phelps, *Physics in Nuclear Medicine*, 4th ed. Philadelphia: Elsevier Saunders, 2012.

[7] H. Young and R. Freedman, *University Physics*, 11th ed. San Francisco, 2004.

[8] a M. Syme, C. Kirkby, T. a Riauka, B. G. Fallone, and S. a McQuarrie, "Monte Carlo investigation of single cell beta dosimetry for intraperitoneal radionuclide therapy.," *Phys. Med. Biol.*, vol. 49, no. 10, pp. 1959–1972, 2004, doi: 10.1088/0031-9155/49/10/009.

[9] T. Peterson and L. Furenlid, "SPECT detectors: the Anger Camera and beyond," *Phys Med Biol*, vol. 56, no. 17, pp. R145–R182, 2011, doi: 10.1088/0031-9155/56/17/R01.SPECT.

[10] General Electric Healthcare, "CZT Technology: Fundamentals and Applications - White

Paper," Waukesha, WI, 2009.

[11] M. Ljungberg and P. H. Pretorius, "Nuclear medicine: Physics and instrumentation special feature review article: SPECT/CT: An update on technological developments and clinical applications," *Br. J. Radiol.*, vol. 91, no. 1081, 2018, doi: 10.1259/bjr.20160402.

[12] M. Dondi, S. Palm, E. Busemann Sokole, R. Z. Stodilka, a. V. Wegst, and R. E. Zimmerman, *Quality Assurance for SPECT Systems*. Vienna, Austria: IAEA, 2009.

[13] NEMA, "NEMA NU 1-2007. Performance Measurements of Gamma Cameras." National Electrical Manufacturers Association, 2007.

[14] G. Muehllehner, "Effect of resolution improvement on required count density in ECT imaging: A computer simulation," *Phys. Med. Biol.*, vol. 30, no. 2, pp. 163–173, 1985, doi: 10.1088/0031-9155/30/2/005.

[15] GE Healthcare, "NM/CT 870 CZT - A Digital SPECT/CT Data Sheet." 2021. [Online]. Available: https://www.gehealthcare.com/products/molecular-imaging/nuclear-medicine/nm-ct-870-czt

[16] W. Akutagawa and K. Zanio, "Gamma response of semi-insulating material in the presence of trapping and detrapping," *J. Appl. Phys.*, vol. 40, no. 9, pp. 3838–3854, 1969, doi: 10.1063/1.1658281.

[17] P. N. Luke, "Unipolar Charge Sensing with Coplanar Electrodes—Application to Semiconductor Detectors," *IEEE Trans. Nucl. Sci.*, vol. 42, no. 4, pp. 207–213, 1995, doi: 10.1109/23.467848.

[18] E. Goshen, L. Beilin, E. Stern, T. Kenig, R. Goldkorn, and S. Ben-haim, "Feasibility study of a novel general purpose CZT-based digital SPECT camera : initial clinical results," *EJNMMI Phys.*, vol. 5, no. 6, pp. 1–12, 2018.

[19] W. W. Moses, "Current trends in scintillator detectors and materials," *Nucl. Instruments Methods Phys. Res. Sect. A Accel. Spectrometers, Detect. Assoc. Equip.*, vol. 487, no. 1–2, pp. 123–128, 2002, doi: 10.1016/S0168-9002(02)00955-5.

[20] A. Bousselham, H. H. Barrett, V. Bora, and K. Shah, "Photoelectron anticorrelations and sub-Poisson statistics in scintillation detectors," *Nucl. Instruments Methods Phys. Res. Sect. A Accel. Spectrometers, Detect. Assoc. Equip.*, vol. 620, no. 2–3, pp. 359–362, 2010,

doi: 10.1016/j.nima.2010.03.152.Photoelectron.

[21] P. Dorenbos, J. T. D. de Haas, and C. W. V. van Eijk, “Non-Proportionality in the Scintillation Response and the Energy Resolution Obtainable with Scintillation Crystals,” *IEEE Trans. Nucl. Sci.*, vol. 42, no. 6, pp. 2190–2202, 1995, doi: 10.1109/23.489415.

[22] GE Healthcare, “NM/CT 870 CZT,” 2023. https://www.gehealthcare.co.uk/products/molecular-imaging/nuclear-medicine/nm-ct-870-czt (accessed Mar. 19, 2023).

[23] GE Healthcare, “NM830 Data Sheet.” 2021.

[24] Y. Takahashi, M. Miyagawa, Y. Nishiyama, H. Ishimura, and T. Mochizuki, “Performance of a semiconductor SPECT system: Comparison with a conventional Anger-type SPECT instrument,” *Ann. Nucl. Med.*, vol. 27, no. 1, pp. 11–16, 2013, doi: 10.1007/s12149-012-0653-9.

[25] Y. H. Lau, B. F. Hutton, and F. J. Beekman, “Choice of collimator for cardiac SPET when resolution compensation is included in iterative reconstruction,” *Eur. J. Nucl. Med.*, vol. 28, no. 1, pp. 39–47, 2001, doi: 10.1007/s002590000387.

[26] C. B. Hruska, M. K. O. Connor, and D. A. Collins, “Comparison of small field of view gamma camera systems for scintimammography,” *Nucl. Med. Commun.*, vol. 26, no. 5, pp. 441–445, 2005.

[27] A. K. Pandey, P. D. Sharma, J. P. Kumar, K. Saroha, and C. Sekhar, “Calculating Gamma Camera Uniformity Parameters : Beyond the Vendor - specific Protocol,” *Indian J. Nucl. Med.*, vol. 32, pp. 279–282, 2017, doi: 10.4103/ijnm.IJNM.

[28] D. Delacroix, J. P. Guerre, P. Leblanc, and C. Hickman, “Radionuclide and radiation protection data handbook 2002,” *Radiat. Prot. Dosimetry*, vol. 98, no. 1, pp. 9–168, 2002, doi: 10.1118/1.1538616.

[29] T. Ito *et al.*, “Experimental evaluation of the GE NM/CT 870 CZT clinical SPECT system equipped with WEHR and MEHRS collimator,” *J. Appl. Clin. Med. Phys.*, vol. 22, no. 2, pp. 165–177, 2021, doi: 10.1002/acm2.13158.

[30] F. Barrack, J. Scuffham, and S. McQuaid, “Septal penetration correction in I-131 imaging following thyroid cancer treatment,” *Phys. Med. Biol.*, vol. 63, no. 7, 2018, doi:

10.1088/1361-6560/aab13a.

[31] A. Stenvall *et al.*, “Relationships between uptake of [68Ga]Ga-DOTA-TATE and absorbed dose in [177Lu]Lu-DOTA-TATE therapy,” *EJNMMI Res.*, vol. 12, no. 1, 2022, doi: 10.1186/s13550-022-00947-2.

[32] M. D. Arienzo *et al.*, “Gamma camera calibration and validation for quantitative SPECT imaging with 177 Lu,” *Appl. Radiat. Isot.*, vol. 112, pp. 156–164, 2016, doi: 10.1016/j.apradiso.2016.03.007.

[33] M. H. Maqsood, A. Tameez, U. Din, and A. H. Khan, “Neuroendocrine Tumor Therapy with Lutetium-177 : A Literature Review Mechanism of action and use,” *Cureus*, vol. 11, no. 1, pp. 1–7, 2019, doi: 10.7759/cureus.3986.

[34] J. Strosberg *et al.*, “Phase 3 Trial of ^{177} Lu-Dotatate for Midgut Neuroendocrine Tumors,” *N. Engl. J. Med.*, vol. 376, no. 2, pp. 125–135, 2017, doi: 10.1056/NEJMoa1607427.

[35] J. J. Zaknun *et al.*, “The joint IAEA, EANM, and SNMMI practical guidance on peptide receptor radionuclide therapy (PRRNT) in neuroendocrine tumours,” *Eur. J. Nucl. Med. Mol. Imaging*, vol. 40, no. 5, pp. 800–816, 2013, doi: 10.1007/s00259-012-2330-6.

[36] W. A. Van Der Zwan, L. Bodei, J. Mueller-Brand, W. W. De Herder, L. K. Kvols, and D. J. Kwekkeboom, “Radionuclide therapy in neuroendocrine tumors,” *Eur. J. Endocrinol.*, vol. 172, no. 1, pp. R1–R8, 2015, doi: 10.1530/EJE-14-0488.

[37] A. Dash, M. R. A. Pillai, and F. F. Knapp, “Production of 177Lu for Targeted Radionuclide Therapy: Available Options,” *Nucl. Med. Mol. Imaging (2010).*, vol. 49, no. 2, pp. 85–107, 2015, doi: 10.1007/s13139-014-0315-z.

[38] T. Talme, J. Ivanoff, M. Hägglund, R. J. J. Van Neerven, A. Ivanoff, and K. G. Sundqvist, “Somatostatin receptor (SSTR) expression and function in normal and leukaemic T-cells. Evidence for selective effects on adhesion to extracellular matrix components via SSTR2 and/or 3,” *Clin. Exp. Immunol.*, vol. 125, no. 1, pp. 71–79, 2001, doi: 10.1046/j.1365-2249.2001.01577.x.

[39] I. Shimon, X. Yan, J. E. Taylor, M. H. Weiss, M. D. Culler, and S. Melmed, “Somatostatin receptor (SSTR) subtype-selective analogues differentially suppress in vitro growth hormone and prolactin in human pituitary adenomas: Novel potential therapy for

functional pituitary tumors," *J. Clin. Invest.*, vol. 100, no. 9, pp. 2386–2392, 1997, doi: 10.1172/JCI119779.

[40] J. Strosberg *et al.*, "Health-Related Quality of Life in Patients With Progressive Midgut Neuroendocrine Tumors Treated With Lu-Dotatate in the Phase III NETTER-1 Trial," *J. Clin. Oncol.*, vol. 36, no. 25, 2018, doi: 10.1200/JCO.2018.78.5865.

[41] M. Cives and J. R. Strosberg, "Gastroenteropancreatic Neuroendocrine Tumors," *CA. Cancer J. Clin.*, vol. 68, no. 6, pp. 471–487, 2018, doi: 10.3322/caac.21493.

[42] D. Taïeb *et al.*, "European Association of Nuclear Medicine Practice Guideline/Society of Nuclear Medicine and Molecular Imaging Procedure Standard 2019 for radionuclide imaging of phaeochromocytoma and paraganglioma," *Eur. J. Nucl. Med. Mol. Imaging*, vol. 46, no. 10, pp. 2112–2137, 2019, doi: 10.1007/s00259-019-04398-1.

[43] E. S. Mittra, "Neuroendocrine Tumor Therapy: 177Lu-DOTATATE," *Am. J. Roentgenol.*, vol. 211, no. August, pp. 278–285, 2018.

[44] I. Hervas *et al.*, "Tratamiento con 177LU-DOTATATE en tumores neuroendocrinos. Estudio preliminar. Rev," *Rev. Esp. Med. Nucl. Imagen Mol.*, vol. 36, no. 2, pp. 91–98, 2017.

[45] National Institute for Health and Care Excellence, "Lutetium (177Lu) oxodotreotide for treating unresectable or metastatic neuroendocrine tumours," 2018. [Online]. Available: https://www.nice.org.uk/guidance/ta539

[46] A. Löser, S. M. Schwarzenböck, M. Heuschkel, H. S. Willenberg, B. J. Krause, and J. Kurth, "Peptide receptor radionuclide therapy with effect of hematological toxicity on survival," *Nucl. Med. Commun.*, vol. 39, pp. 236–246, 2018, doi: 10.1097/MNM.0000000000000795.

[47] A. Delker *et al.*, "Dosimetry for 177Lu-DKFZ-PSMA-617: a new radiopharmaceutical for the treatment of metastatic prostate cancer," *Eur. J. Nucl. Med. Mol. Imaging*, vol. 43, no. 1, pp. 42–51, 2016, doi: 10.1007/s00259-015-3174-7.

[48] M. S. Hofman *et al.*, "[177 Lu]-PSMA-617 radionuclide treatment in patients with metastatic castration-resistant prostate cancer (LuPSMA trial): a single-centre, single-arm, phase 2 study," *Lancet Oncol.*, vol. 19, no. 6, pp. 825–833, 2018, doi:

10.1016/S1470-2045(18)30198-0.

[49] National Institute for Health and Care Excellence, “Prostate cancer diagnosis and management,” 2019. doi: 10.1016/S0140-6736(96)07393-X.

[50] O. Sartor *et al.*, “Lutetium-177–PSMA-617 for Metastatic Castration-Resistant Prostate Cancer,” *N. Engl. J. Med.*, vol. 385, no. 12, pp. 1091–1103, 2021, doi: 10.1056/nejmoa2107322.

[51] C. Kratochwil *et al.*, “EANM procedure guidelines for radionuclide therapy with 177Lu-labelled PSMA-ligands (177Lu-PSMA-RLT),” *Eur. J. Nucl. Med. Mol. Imaging*, vol. 46, no. 12, pp. 2536–2544, 2019, doi: 10.1007/s00259-019-04485-3.

[52] National Institute for Health and Care Excellence, “177Lu-PSMA-617 for treating PSMA-positive hormone-relapsed metastatic prostate cancer after 2 or more therapies,” 2021.

[53] M. Konijnenberg *et al.*, “EANM position paper on article 56 of the Council Directive 2013/59/Euratom (basic safety standards) for nuclear medicine therapy,” *Eur. J. Nucl. Med. Mol. Imaging*, vol. 48, no. 1, pp. 67–72, 2021, doi: 10.1007/s00259-020-05038-9.

[54] The Stationary Office, *The Ionising Radiation (Medical Exposure) Regulations 2017*. UK, 2018.

[55] Care Quality Commission, “IR(ME)R annual report 2020/21,” 2022.

[56] R. De Nijs, V. Lagerburg, T. L. Klausen, and S. Holm, “Improving quantitative dosimetry in 177Lu-DOTATATE SPECT by energy window-based scatter corrections,” *Nucl. Med. Commun.*, vol. 35, no. 5, pp. 522–533, 2014, doi: 10.1097/MNM.0000000000000079.

[57] M. Lassmann, C. Chiesa, G. Flux, and M. Bardiès, “EANM Dosimetry Committee guidance document: Good practice of clinical dosimetry reporting,” *Eur. J. Nucl. Med. Mol. Imaging*, vol. 38, no. 1, pp. 192–200, 2011, doi: 10.1007/s00259-010-1549-3.

[58] A. Chicheportiche *et al.*, “Dosimetry after peptide receptor radionuclide therapy: impact of reduced number of post-treatment studies on absorbed dose calculation and on patient management,” *EJNMMI Phys.*, vol. 7, no. 1, pp. 1–15, 2020, doi: 10.1186/s40658-020-0273-8.

[59] M. Del Prete *et al.*, “Accuracy and reproducibility of simplified QSPECT dosimetry for

personalized 177Lu-octreotate PRRT," *EJNMMI Phys.*, vol. 5, no. 25, pp. 1–20, 2018, doi: 10.1186/s40658-018-0224-9.

[60] H. Hänscheid, C. Lapa, A. K. Buck, M. Lassmann, and R. A. Werner, "Dose mapping after endoradiotherapy with 177 Lu-DOTATATE/DOTATOC by a single measurement after 4 days," *J. Nucl. Med.*, vol. 59, no. 1, pp. 75–81, 2018, doi: 10.2967/jnumed.117.193706.

[61] W. Snyder, M. R. Ford, G. G. . Warner, and S. B. Watson, "MIRD pamphlet No. 11: 'S' absorbed dose per unit cumulated activity for selected radionuclides and organs," Oak Ridge, Tennassee, 1975.

[62] Y. K. Dewaraja *et al.*, "MIRD Pamphlet No. 23: Quantitative SPECT for patient-Specific 3-dimensional dosimetry in internal radionuclide therapy," *J. Nucl. Med.*, vol. 53, no. 8, pp. 1310–1325, 2012, doi: 10.2967/jnumed.111.100123.

[63] J. A. Siegel *et al.*, "MIRD pamphlet no. 16: Techniques for quantitative radiopharmaceutical biodistribution data acquisition and analysis for use in human radiation dose estimates.," *J. Nucl. Med.*, vol. 40, pp. 37S-61S, 1999, doi: 10025848.

[64] W. E. Bolch, K. F. Eckerman, G. Sgouros, and S. R. Thomas, "MIRD pamphlet No. 21: a generalized schema for radiopharmaceutical dosimetry--standardization of nomenclature.," *J. Nucl. Med.*, vol. 50, no. 21, pp. 477–484, 2009, doi: 10.2967/jnumed.108.056036.

[65] J. C. Dickson *et al.*, "EANM practice guideline for quantitative SPECT-CT," *Eur. J. Nucl. Med. Mol. Imaging*, 2022, doi: 10.1007/s00259-022-06028-9.

[66] P. Ritt, H. Vija, J. Hornegger, and T. Kuwert, "Absolute quantification in SPECT," *Eur. J. Nucl. Med. Mol. Imaging*, vol. 38, no. SUPPL. 1, pp. 69–77, 2011, doi: 10.1007/s00259-011-1770-8.

[67] J. Kennedy, A. Chicheportiche, and Z. Keidar, "Quantitative SPECT/CT for Dosimetry of Peptide Receptor Radionuclide Therapy," *Semin. Nucl. Med.*, vol. 52, no. 2, pp. 229–242, 2022, doi: 10.1053/j.semnuclmed.2021.11.004.

[68] A. H. Compton, "A Quantum Theory of the Scattering of X-rays by Light Elements," *Phys. Rev.*, vol. 21, no. 5, pp. 483–502, 1923, doi: 10.1103/PhysRev.21.483.

[69] B. H. Arthur Compton, "The Spectrum of Scattered X-Rays," *Phys. Rev.*, vol. 22, no. 5, pp.

409–413, 1923.

[70] C. K. Qiao, J. W. Wei, and L. Chen, “An overview of the compton scattering calculation,” *Crystals*, vol. 11, no. 5, pp. 1–21, 2021, doi: 10.3390/cryst11050525.

[71] B. F. Hutton, I. Ene Buvat, and F. J. Beekman, “Review and current status of SPECT scatter correction,” *Phys. Med. Biol. Phys. Med. Biol*, vol. 56, no. 56, pp. 85–112, 2011, doi: 10.1088/0031-9155/56/14/R01.

[72] K. Ogawa, Y. Harata, T. Ichihara, A. Kubo, and S. Hashimoto, “A Practical Method for Position-Dependent Compton-Scatter Correction in Single Photon Emission CT,” *IEEE Trans. Med. Imaging*, vol. 10, no. 3, pp. 408–412, 1991, doi: 10.1109/42.97591.

[73] D. Kupitz *et al.*, “Optimization of SPECT/CT imaging protocols for quantitative and qualitative 99mTc SPECT,” *EJNMMI Phys.*, vol. 8, no. 1, 2021, doi: 10.1186/s40658-021-00405-3.

[74] C. B. Hruska and M. K. O’Connor, “A Monte Carlo model for energy spectra analysis in dedicated nuclear breast imaging,” *IEEE Trans. Nucl. Sci.*, vol. 55, no. 1, pp. 491–500, 2008, doi: 10.1109/TNS.2007.910882.

[75] P. P. Bruyant, “Analytic and iterative reconstruction algorithms in SPECT,” *J. Nucl. Med.*, vol. 43, no. 10, pp. 1343–1358, 2002.

[76] H. M. Hudson and R. S. Larkin, “Ordered Subsets of Projection Data,” *IEEE Trans. Med. Imaging*, vol. 13, no. 4, pp. 601–609, 1994.

[77] S. Liu and T. H. Farncombe, “Collimator-detector response compensation in quantitative SPECT reconstruction,” *IEEE Nucl. Sci. Symp. Conf. Rec.*, vol. 5, pp. 3955–3960, 2007, doi: 10.1109/NSSMIC.2007.4436983.

[78] S. H. Manglos, R. J. Jaszczak, C. E. Floyd, L. J. Hahn, K. L. Greer, and R. E. Coleman, “Nonisotropic attenuation in SPECT: Phantom tests of quantitative effects and compensation techniques,” *J. Nucl. Med.*, vol. 28, no. 10, pp. 1584–1591, 1987.

[79] J. S. Fleming, “A technique for using CT images in attenuation correction and quantification in SPECT,” *Nucl. Med. Commun.*, vol. 10, no. 2, pp. 83–97, 1989, [Online]. Available: http://journal.um-surabaya.ac.id/index.php/JKM/article/view/2203

[80] O. G. Rousset, Y. Ma, and A. C. Evans, “Correction for Partial Volume Effects in PET: Principle and Validation,” *J. Nucl. Med.*, vol. 39, no. 5, pp. 904–911, 1998.

[81] J. I. Gear *et al.*, “EANM practical guidance on uncertainty analysis for molecular radiotherapy absorbed dose calculations,” *Eur. J. Nucl. Med. Mol. Imaging*, vol. 45, no. 13, pp. 2456–2474, 2018, doi: 10.1007/s00259-018-4136-7.

[82] The European Parliament and the Council of the European Union, *REGULATION (EU) 2017/745 OF THE EUROPEAN PARLIAMENT AND OF THE COUNCIL of 5 April 2017 on medical devices, amending Directive 2001/83/EC, Regulation (EC) No 178/2002 and Regulation (EC) No 1223/2009 and repealing Council Directives 90/385/EEC and 93/42/EE*. 2017. doi: 10.1177/2165079915576935.

[83] S. Staelens *et al.*, “Monte Carlo simulations of a scintillation camera using GATE: Validation and application modelling,” *Phys. Med. Biol.*, vol. 48, no. 18, pp. 3021–3042, 2003, doi: 10.1088/0031-9155/48/18/305.

[84] D. Sarrut *et al.*, “Advanced Monte Carlo simulations of emission tomography imaging systems with GATE,” *Phys. Med. Biol.*, vol. 66, no. 10, 2021, doi: 10.1088/1361-6560/abf276.

[85] S. Jan *et al.*, “GATE: A simulation toolkit for PET and SPECT,” *Phys. Med. Biol.*, vol. 49, pp. 4543–4561, 2004.

[86] K. Assié *et al.*, “Monte Carlo simulation in PET and SPECT instrumentation using GATE,” *Nucl. Instruments Methods Phys. Res. Sect. A Accel. Spectrometers, Detect. Assoc. Equip.*, vol. 527, no. 1–2, pp. 180–189, 2004, doi: 10.1016/j.nima.2004.03.117.

[87] S. Stute *et al.*, “Monte Carlo simulations of clinical PET and SPECT scans: Impact of the input data on the simulated images,” *Phys. Med. Biol.*, vol. 56, no. 19, pp. 6441–6457, 2011, doi: 10.1088/0031-9155/56/19/017.

[88] D. Strul, G. Santin, D. Lazaro, V. Breton, and C. Morel, “GATE (Geant4 Application for Tomographic Emission): A PET/SPECT general-purpose simulation platform,” *Nucl. Phys. B - Proc. Suppl.*, vol. 125, pp. 75–79, 2003, doi: 10.1016/S0920-5632(03)90969-8.

[89] Open GATE Collaboration, “General Concept - Getting Started,” *Open GATE*, 2023. https://opengate.readthedocs.io/en/latest/getting_started.html (accessed Mar. 26,

2023).

[90] L. Imbert *et al.*, “Assessment of a Monte-Carlo simulation of SPECT recordings from a new-generation heart-centric semiconductor camera: from point sources to human images,” *Phys. Med. Biol.*, vol. 60, no. 3, pp. 1007–1018, 2015, doi: 10.1088/0031-9155/60/3/1007.

[91] Open GATE Collaboration, “Users Guide V8.0,” *Open GATE*. Marseille, 2017. [Online]. Available: http://www.opengatecollaboration.org/sites/default/files/GATE-UsersGuideV8.0.pdf

[92] Open GATE Collaboration, “Imaging Application - Defining a system,” *Open GATE*, 2023. https://opengate.readthedocs.io/en/latest/defining_a_system_scanner_ct_pet_spect_optical.html (accessed Mar. 26, 2023).

[93] R. Brun and F. Rademakers, “ROOT - An object oriented data analysis framework,” *Nucl. Instruments Methods Phys. Res. Sect. A Accel. Spectrometers, Detect. Assoc. Equip.*, vol. 389, no. 1–2, pp. 81–86, 1997, doi: 10.1016/S0168-9002(97)00048-X.

[94] K. Assié, A. Dieudonné, I. Gardin, P. Véra, and I. Buvat, “A preliminary study of quantitative protocols in indium 111 SPECT using computational simulations and phantoms,” *IEEE Trans. Nucl. Sci.*, vol. 57, no. 3 PART 1, pp. 1096–1104, 2010, doi: 10.1109/TNS.2010.2041252.

[95] I. Buvat, H. Benali, A. Todd-Pokropek, and R. Di Paola, “Scatter correction in scintigraphy: the state of the art,” *Eur. J. Nucl. Med.*, vol. 21, no. 7, pp. 675–694, 1994, doi: 10.1007/BF00285592.

[96] E. C. Frey and B. M. W. Tsui, “A new method for modeling the spatially-variant, object-dependent scatter response function in SPECT,” *1996 IEEE Nucl. Sci. Symp. Conf. Rec.*, vol. 2, pp. 1082–1086, 1996, doi: 10.1109/NSSMIC.1996.591559.

[97] S. C. Moore *et al.*, “Simultaneous Tc-99m/Tl-201 Imaging Using Energy-Based Estimation of the Spatial Distributions of Contaminant Photons,” *IEEE Trans. Nucl. Sci.*, vol. 42, no. 4, pp. 1189–1195, 1995, doi: 10.1109/23.467879.

[98] K. Knesaurek and J. Machac, “Comparison of correction techniques for simultaneous 201Tl/99mTc myocardial perfusion SPECT imaging: A dog study,” *Phys. Med. Biol.*, vol.

45, no. 11, 2000, doi: 10.1088/0031-9155/45/11/405.

[99] M. Sandström, E. Ilan, A. Sundin, and M. Lubberink, “Image quality measurements with Lu-177 on a GE Discovery 670 CZT,” *J. Nucl. Med.*, vol. 58, no. supplement 1, p. 763, 2017, [Online]. Available: http://jnm.snmjournals.org/content/58/supplement_1/763.abstract?sid=1f441c14-b5ab-44cd-a452-c848e604ab7a&utm_source=TrendMD&utm_medium=cpc&utm_campaign=J_Nucl_Med_TrendMD_0

[100] G. El Fakhri, S. C. Moore, P. Maksud, A. Aurengo, and M. F. Kijewski, “Absolute activity quantitation in simultaneous 123I/99mTc brain SPECT,” *J. Nucl. Med.*, vol. 42, no. 2, pp. 300–308, 2001.

[101] S. Hapdey, M. Soret, and I. Buvat, “Quantification in simultaneous 99mTc/123I brain SPECT using generalized spectral factor analysis: A Monte Carlo study,” *Phys. Med. Biol.*, vol. 51, no. 23, pp. 6157–6171, 2006, doi: 10.1088/0031-9155/51/23/015.

[102] K. Kacperski, K. Erlandsson, S. Ben-Haim, and B. F. Hutton, “Iterative deconvolution of simultaneous 99mTc and 201Tl projection data measured on a CdZnTe-based cardiac SPECT scanner,” *Phys. Med. Biol.*, vol. 56, no. 5, pp. 1397–1414, 2011, doi: 10.1088/0031-9155/56/5/012.

[103] H. W. A. M. De Jong, W. T. Wang, E. C. Frey, M. A. Viergever, and F. J. Beekman, “Efficient simulation of SPECT down-scatter including photon interactions with crystal and lead,” *Med. Phys.*, vol. 29, no. 4, pp. 550–560, 2002, doi: 10.1118/1.1462638.

[104] B. He and E. C. Frey, “Comparison of conventional, model-based quantitative planar, and quantitative SPECT image processing methods for organ activity estimation using In-111 agents,” *Phys. Med. Biol.*, vol. 51, no. 16, pp. 3967–3981, 2006, doi: 10.1088/0031-9155/51/16/006.

[105] G. El Fakhri, S. C. Moore, and M. F. Kijewski, “Optimization of Ga-67 imaging for detection and estimation tasks: Dependence of imaging performance on spectral acquisition parameters,” *Med. Phys.*, vol. 29, no. 8, pp. 1859–1866, 2002, doi: 10.1118/1.1493214.

[106] P. Thuillier *et al.*, “Clinical Assessment of 177Lu-DOTATATE Quantification by Comparison of SUV-Based Parameters Measured on Both Post-PRRT SPECT/CT and 68Ga-DOTATOC

PET/CT in Patients with Neuroendocrine Tumors: A Feasibility Study," *Clin. Nucl. Med.*, vol. 46, no. 2, pp. 111–118, 2021, doi: 10.1097/RLU.0000000000003412.

[107] B. E. Zimmerman *et al.*, "Multi-centre evaluation of accuracy and reproducibility of planar and SPECT image quantification: An IAEA phantom study," *Med. Phys.*, vol. 27, no. 2, pp. 98–112, 2017, doi: 10.1016/j.physbeh.2017.03.040.

[108] S. M. B. Peters *et al.*, "Towards standardization of absolute SPECT/CT quantification: a multi-center and multi-vendor phantom study," *EJNMMI Phys.*, vol. 6, no. 29, pp. 1–14, 2019, doi: 10.1186/s40658-019-0268-5.

[109] M. Lassmann, U. Eberlein, and J. Tran-Gia, "Multicentre Trials on Standardised Quantitative Imaging and Dosimetry for Radionuclide Therapies," *Clin. Oncol.*, vol. 33, no. 2, pp. 125–130, 2021, doi: 10.1016/j.clon.2020.11.008.

[110] M. D. Arienzo *et al.*, "Quantitative 177 Lu SPECT imaging using advanced correction algorithms in non-reference geometry," *Phys. Medica*, vol. 32, no. 12, pp. 1745–1752, 2016, doi: 10.1016/j.ejmp.2016.09.014.

[111] D. L. Bailey *et al.*, "In vivo quantification of 177Lu with planar whole-body and SPECT/CT gamma camera imaging," *EJNMMI Phys.*, vol. 2, no. 1, pp. 1–17, 2015, doi: 10.1186/s40658-015-0123-2.

[112] J. M. Beauregard, M. S. Hofman, J. M. Pereira, P. Eu, and R. J. Hicks, "Quantitative 177Lu SPECT (QSPECT) imaging using a commercially available SPECT/CT system," *Cancer Imaging*, vol. 11, no. 1, pp. 56–66, 2011, doi: 10.1102/1470-7330.2011.0012.

[113] A. Celler, H. Piwowarska-Bilska, S. Shcherbinin, C. Uribe, R. Mikolajczak, and B. Birkenfeld, "Evaluation of dead-time corrections for post-radionuclide-therapy (177)Lu quantitative imaging with low-energy high-resolution collimators.," *Nucl. Med. Commun.*, vol. 35, no. 1, pp. 73–87, 2014, doi: 10.1097/MNM.0000000000000011.

[114] A. Desy, G. F. Bouvet, N. Lafrenière, A. Zamanian, P. Després, and J. M. Beauregard, "Impact of the dead-time correction method on quantitative 177Lu-SPECT (QSPECT) and dosimetry during radiopharmaceutical therapy," *EJNMMI Phys.*, vol. 9, no. 1, 2022, doi: 10.1186/s40658-022-00484-w.

[115] A. Frezza *et al.*, "Comprehensive SPECT / CT system characterization and calibration for

177 Lu quantitative SPECT (QSPECT) with dead- time correction," *EJNMMI Phys.*, vol. 7, no. 10, pp. 1–22, 2020.

[116] B. He, A. Nikolopoulou, J. Osborne, S. Vallabhajosula, and S. Goldsmith, "Quantitative SPECT imaging with Lu-177: A physical phantom evaluation," *J. Nucl. Med.*, vol. 53, p. np. supplement 1 2407, 2012, [Online]. Available: http://jnm.snmjournals.org/content/53/supplement_1/2407.short

[117] G. Marin *et al.*, "Accuracy and precision assessment for activity quantification in individualized dosimetry of 177Lu-DOTATATE therapy," *EJNMMI Phys.*, vol. 4, no. 7, pp. 1–15, 2017, doi: 10.1186/s40658-017-0174-7.

[118] E. Mezzenga *et al.*, "Quantitative accuracy of 177Lu SPECT imaging for molecular radiotherapy," *PLoS One*, vol. 12, no. 8, pp. 1–18, 2017, doi: 10.1371/journal.pone.0182888.

[119] S. M. B. Peters *et al.*, "Variability in lutetium-177 SPECT quantification between different state-of-the-art SPECT/CT systems," *EJNMMI Phys.*, vol. 7, no. 1, 2020, doi: 10.1186/s40658-020-0278-3.

[120] S. Raskin, D. Gamliel, D. Abookasis, S. Ben-Haim, and A. Chicheportiche, "Towards accurate 177Lu SPECT activity quantification and standardization using lesion-to-background voxel ratio," *EJNMMI Phys.*, vol. 10, no. 5, 2023, doi: 10.1186/s40658-023-00526-x.

[121] J. C. Sanders, T. Kuwert, J. Hornegger, and P. Ritt, "Quantitative SPECT/CT Imaging of 177Lu with In Vivo Validation in Patients Undergoing Peptide Receptor Radionuclide Therapy," *Mol. Imaging Biol.*, vol. 17, no. 4, pp. 585–593, 2015, doi: 10.1007/s11307-014-0806-4.

[122] S. Shcherbinin, H. Piwowarska-Bilska, a Celler, and B. Birkenfeld, "Quantitative SPECT/CT reconstruction for ^{177}Lu and ^{177}Lu/^{90}Y targeted radionuclide therapies.," *Phys. Med. Biol.*, vol. 57, no. 18, pp. 5733–47, 2012, doi: 10.1088/0031-9155/57/18/5733.

[123] A. L. Theisen, M. Lassmann, and J. Tran-Gi, "Towards a patient-specific traceable quantification of SPECT/CT-based radiopharmaceutical distributions.," *J. Nucl. Med.*, vol. 63, no. 7, pp. 1108–1116, 2022, doi: 10.2967/jnumed.121.262925.

[124] J. Tran-Gia, S. Schlögl, and M. Lassmann, “Design and fabrication of kidney phantoms for internal radiation dosimetry using 3D printing technology,” *J. Nucl. Med.*, vol. 57, no. 12, pp. 1998–2005, 2016, doi: 10.2967/jnumed.116.178046.

[125] J. Tran-Gia and M. Lassmann, “Characterization of noise and resolution for quantitative 177 Lu SPECT/CT with XSPECT quant,” *J. Nucl. Med.*, vol. 60, no. 1, pp. 50–59, 2019, doi: 10.2967/jnumed.118.211094.

[126] C. F. Uribe *et al.*, “Accuracy of 177Lu activity quantification in SPECT imaging: a phantom study,” *EJNMMI Phys.*, vol. 4, no. 1, 2017, doi: 10.1186/s40658-016-0170-3.

[127] C. F. Uribe, P. L. Esquinas, M. Gonzalez, W. Zhao, J. Tanguay, and A. Celler, “Deadtime effects in quantification of 177 Lu activity for radionuclide therapy,” *EJNMMI Phys.*, vol. 5, no. 2, pp. 1–16, 2018, doi: 10.1186/s40658-017-0202-7.

[128] W. Zhao *et al.*, “Determination of gamma camera calibration factors for quantitation of therapeutic radioisotopes,” *EJNMMI Phys.*, vol. 5, no. 8, pp. 1–16, 2018, doi: 10.1186/s40658-018-0208-9.

[129] S. M. B. Peters *et al.*, “Variability in lutetium-177 SPECT quantification between different state-of-the-art SPECT/CT systems,” *EJNMMI Phys.*, vol. 7, no. 9, pp. 1–13, 2020, doi: 10.1186/s40658-020-0278-3.

[130] J. C. Sanders, T. Kuwert, J. Hornegger, and P. Ritt, “Quantitative SPECT/CT Imaging of 177Lu with In Vivo Validation in Patients Undergoing Peptide Receptor Radionuclide Therapy,” *Mol. Imaging Biol.*, vol. 17, no. 4, pp. 585–593, 2015, doi: 10.1007/s11307-014-0806-4.

[131] J. Tran-Gia and M. Lassmann, “Calibration and Verification of Quantitative Imaging using SPECT / CT: MRTDosimetry Workshop Teddington 20th & 21st May 2019,” 2019. http://mrtdosimetry-empir.eu/wp-content/uploads/2019/06/07_M_Lassmann_and_J_Tran-Gia_Calibration_and_Verification_of_QI.pdf (accessed May 15, 2021).

[132] K. Farid *et al.*, “First Experience DaTSCAN Imaging Using Cadmium-Zinc-Telluride Gamma Camera SPECT,” *Clin. Nucl. Med.*, vol. 37, no. 8, pp. 211–212, 2012.

[133] L. Imbert *et al.*, “Compared Performance of High-Sensitivity Cameras Dedicated to

Myocardial Perfusion SPECT: A Comprehensive Analysis of Phantom and Human Images," *J. Nucl. Med.*, vol. 53, pp. 1897–1903, 2012, doi: 10.2967/jnumed.112.107417.

[134] V. Koulikov, H. Lerman, M. Kesler, and E. Even-sapir, "Tc-MDP bone scintigraphy of the hand : comparing the use of novel cadmium zinc telluride (CZT) and routine NaI (Tl) detectors," *EJNMMI Res.*, vol. 5, no. 63, 2015, doi: 10.1186/s13550-015-0139-6.

[135] GE Healthcare, "Going Beyond Analog: GE Healthcare Launches Digital, Next-Generation Molecular Imaging Systems That Can Help Clinicians Advance Quantitative Care and Research," *GE Newsroom*, 2016. https://www.genewsroom.com/press-releases/going-beyond-analog-ge-healthcare-launches-digital-next-generation-molecular-imaging# (accessed Jun. 06, 2019).

[136] A. Verger *et al.*, "Comparison between stress myocardial perfusion SPECT recorded with cadmium-zinc-telluride and Anger cameras in various study protocols," *Eur. J. Nucl. Med. Mol. Imaging*, vol. 40, pp. 331–340, 2013, doi: 10.1007/s00259-012-2292-8.

[137] M. Fiechter *et al.*, "Nuclear myocardial perfusion imaging with a novel cadmium-zinc-telluride detector SPECT / CT device : first validation versus invasive coronary angiography," *Eur. J. Nucl. Med. Mol. Imaging*, vol. 38, pp. 2025–2030, 2011, doi: 10.1007/s00259-011-1877-y.

[138] I. M. Blevis, M. K. O. C, Z. Keidar, A. Pansky, H. Altman, and W. H, "CZT Gamma Camera for Scintimammography," *Phys. Medica*, vol. XXI, pp. 56–59, 2006.

[139] J. Oddstig, F. Hedeer, and J. Jo, "Reduced administered activity , reduced acquisition time, and preserved image quality for the new CZT camera," *J. Nucl. Cardiol.*, vol. 20, no. 1, pp. 38–44, 2012, doi: 10.1007/s12350-012-9634-6.

[140] S. Ben-Haim, J. Kennedy, and Z. Keidar, "Novel cadmium zinc telluride devices for myocardial perfusion imaging - Technological aspects and clinical applications," *Semin. Nucl. Med.*, vol. 46, no. 4, pp. 273–285, 2016, doi: 10.1053/j.semnuclmed.2016.01.002.

[141] D. Agostini, P. Marie, S. Ben-haim, and F. Rouzet, "Performance of cardiac cadmium-zinc-telluride gamma camera imaging in coronary artery disease : a review from the cardiovascular committee of the European Association of Nuclear Medicine (EANM) Left ventricular," *Eur. J. Nucl. Med. Mol. Imaging*, pp. 2423–2432, 2016, doi: 10.1007/s00259-016-3467-5.

[142] P. Ritt, “Recent Developments in SPECT/CT,” *Semin. Nucl. Med.*, vol. 00, pp. 1–10, 2022, doi: 10.1053/j.semnuclmed.2022.01.004.

[143] J. Oddstig, E. Martinsson, J. Jo, H. Engblom, and C. Hindorf, “Differences in attenuation pattern in myocardial SPECT between CZT and conventional gamma cameras,” 2018, doi: 10.1007/s12350-018-1296-6.

[144] R. Zhang *et al.*, “Impacts of acquisition and reconstruction parameters on the absolute technetium quantification of the cadmium–zinc–telluride-based SPECT/CT system: a phantom study,” *EJNMMI Phys.*, vol. 8, no. 1, 2021, doi: 10.1186/s40658-021-00412-4.

[145] A. Pourmoghaddas, K. Vanderwerf, T. D. Ruddy, and R. Glenn Wells, “Scatter correction improves concordance in SPECT MPI with a dedicated cardiac SPECT solid-state camera,” *J. Nucl. Cardiol.*, vol. 22, no. 2, pp. 334–343, 2015, doi: 10.1007/s12350-014-0008-0.

[146] P. Fan *et al.*, “Scatter and crosstalk corrections for 99mTc 123I dual-radionuclide imaging using a CZT SPECT system with pinhole collimators,” *Med. Phys.*, vol. 42, no. 12, pp. 6895–6911, 2015.

[147] B. Songy *et al.*, “Feasibility of simultaneous dual isotope acquisition for myocardial perfusion imaging with a cadmium zinc telluride camera,” *J. Nucl. Cardiol.*, vol. 27, no. 3, pp. 737–747, 2020, doi: 10.1007/s12350-018-1452-z.

[148] J. Kennedy, R. Lugassi, I. Reizberg, and Z. Keidar, “Quantitation of Lu-177 using General Purpose Whole-body Solid State CZT and Standard SPECT/CT Camera,” *J. Nucl. Med.*, vol. 58, no. supplement 1, p. 398, 2017, [Online]. Available: http://jnm.snmjournals.org/content/58/supplement_1/398.short

[149] M. Sandström, A. Sundin, and M. Lubberink, “Intrinsic or extrinsic uniformity maps using Lu-177 on a GE Discovery 870 CZT gamma camera,” *J. Nucl. Med.*, vol. 60, no. supplement 1, p. 1363, 2019, [Online]. Available: http://jnm.snmjournals.org/content/60/supplement_1/1363.abstract?sid=71f8f94e-bdc1-4470-9a4e-d097c0639008&utm_source=TrendMD&utm_medium=cpc&utm_campaign=J_Nucl_Med_TrendMD_0

[150] J. A. Kennedy, R. Lugassi, R. Gill, and Z. Keidar, “Digital solid-state spect/ct quantitation of absolute 177lu radiotracer concentration: In vivo and in vitro validation,” *J. Nucl. Med.*,

vol. 61, no. 9, pp. 1381–1387, 2020, doi: 10.2967/jnumed.119.239277.

[151] D. Roth, E. Larsson, A. Sundlöv, and K. Sjögreen Gleisner, “Characterisation of a hand-held CZT-based gamma camera for 177Lu imaging,” *EJNMMI Phys.*, vol. 7, no. 1, 2020, doi: 10.1186/s40658-020-00313-y.

[152] E. Chevalier, C. Boursier, M. Claudin, P. Y. Marie, and L. Imbert, “Feasibility of 177Lu Therapy Monitoring Using Fast Whole-Body SPECT Recordings Provided by a High-Speed 360° CZT Camera,” *Clin. Nucl. Med.*, vol. 45, no. 11, pp. e493–e494, 2020, doi: 10.1097/RLU.0000000000003169.

[153] M. E. Daube-Witherspoon *et al.*, “PET Performance Measurements Using the NEMA NU 2-2001 Standard,” *J. Nucl. Med.*, vol. 43, pp. 1398–1409, 2002.

[154] H. Asmi, F. Bentayeb, Y. Bouzekraoui, F. Bonutti, and S. Douama, “Energy Window and Collimator Optimization in Lutetium-177 Single-photon Emission Computed Tomography Imaging using Monte Carlo Simulation,” *Indian J. Nucl. Med.*, vol. 177, no. 4, pp. 359–362, 2019, doi: 10.4103/ijnm.IJNM.

[155] N. Boutaghane, M. Hesse, B. Bouzid, H. Zaidi, F. Jamar, and S. Walrand, “Dual-layer collimator for improved spatial resolution in SPECT with CZT camera: An analytical and Monte Carlo study,” *Phys. Med. Biol.*, vol. 67, no. 6, 2022, doi: 10.1088/1361-6560/ac5671.

[156] M. Holstensson, K. Erlandsson, G. Poludniowski, S. Ben-Haim, and B. F. Hutton, “Model-based correction for scatter and tailing effects in simultaneous 99mTc and 123I imaging for a CdZnTe cardiac SPECT camera,” *Phys. Med. Biol.*, vol. 60, no. 8, pp. 3045–3063, 2015, doi: 10.1088/0031-9155/60/8/3045.

[157] K. A. L. Koch-Mehrin, J. E. Lees, and S. L. Bugby, “A spectroscopic Monte-Carlo model to simulate the response of pixelated CdTe based detectors,” *Nucl. Instruments Methods Phys. Res. Sect. A Accel. Spectrometers, Detect. Assoc. Equip.*, vol. 976, no. April, p. 164241, 2020, doi: 10.1016/j.nima.2020.164241.

[158] B. P. Lopez, F. Guan, G. M. Rauch, and S. C. Kappadath, “Monte Carlo simulation of pixelated CZT detector with Geant4: Validation of clinical molecular breast imaging system,” *Phys. Med. Biol.*, vol. 66, no. 12, 2021, doi: 10.1088/1361-6560/ac0588.

[159] M. Morphis, J. A. van Staden, H. du Raan, and M. Ljungberg, “Modelling of energy-dependent spectral resolution for SPECT Monte Carlo simulations using SIMIND,” *Heliyon*, vol. 7, no. 2, p. e06097, 2021, doi: 10.1016/j.heliyon.2021.e06097.

[160] M. E. Myronakis and D. G. Darambara, “Monte Carlo investigation of charge-transport effects on energy resolution and detection efficiency of pixelated CZT detectors for SPECT/PET applications,” *Med. Phys.*, vol. 38, no. 1, pp. 455–467, 2011, doi: 10.1118/1.3532825.

[161] K. Ramonaheng, J. A. van Staden, and H. du Raan, “The effect of calibration factors and recovery coefficients on 177Lu SPECT activity quantification accuracy: a Monte Carlo study,” *EJNMMI Phys.*, vol. 8, no. 1, 2021, doi: 10.1186/s40658-021-00365-8.

[162] A. P. Robinson, J. Tipping, D. M. Cullen, and D. Hamilton, “The influence of triple energy window scatter correction on activity quantification for 177Lu molecular radiotherapy,” *Phys. Med. Biol.*, vol. 61, no. 14, pp. 5107–5127, 2016, doi: 10.1088/0031-9155/61/14/5107.

[163] D. Roth, E. Larsson, M. Ljungberg, and K. Sjögreen Gleisner, “Monte Carlo modelling of a compact CZT-based gamma camera with application to 177Lu imaging,” *EJNMMI Phys.*, vol. 9, no. 1, pp. 1–21, 2022, doi: 10.1186/s40658-022-00463-1.

[164] A. Suzuki *et al.*, “Monte Carlo-based scatter correction considering the tailing effect of a CdTe detector for dual-isotope brain SPECT imaging,” *Biomed. Phys. Eng. Express*, vol. 2, no. 4, 2016, doi: 10.1088/2057-1976/2/4/045010.

[165] F. Weng, S. Bagchi, Q. Huang, and Y. Seo, “Design Studies of a CZT-based Detector Combined with a Pixel-Geometry-Matching Collimator for SPECT Imaging,” *IEEE Nucl Sci Symp Conf Rec*, 2013, doi: 10.1109/NSSMIC.2013.6829458.Design.

[166] K. Ramonaheng, J. A. van Staden, and H. du Raan, “Validation of a Monte Carlo modelled gamma camera for Lutetium-177 imaging,” *Appl. Radiat. Isot.*, vol. 163, no. April, p. 109200, 2020, doi: 10.1016/j.apradiso.2020.109200.

[167] General Electric Healthcare, “GE Discovery NM/CT 870 CZT Performance Specifications.” 2019.

[168] The Stationary Office, *The Ionising Radiations Regulations 2017*. UK, 2017.

[169] Environment Agency, *The Environmental Permitting (England and Wales) Regulations 2016*. UK, 2016.

[170] A. M. Loening and S. S. Gambhir, "AMIDE: A Free Software Tool for Multimodality Medical Image Analysis," *Mol. Imaging*, vol. 2, no. 3, pp. 131–137, 2003, doi: 10.1162/153535003322556877.

[171] J. Gear *et al.*, "EANM Dosimetry Committee series on standard operational procedures for internal dosimetry for 131I mIBG treatment of neuroendocrine tumours," *EJNMMI Phys.*, vol. 7, no. 1, 2020, doi: 10.1186/s40658-020-0282-7.

[172] N. Calvert *et al.*, "Standard Operating Procedure for MRTDosimetry Comparison Exercise – Part 5: Liquid I-131 Sources."

[173] K. Ferreira, M. Lassmann, V. Smyth, J. Tran-gia, and J. Wevrett, "Protocol for Calibration of a Spect Camera for Traceable Quantitative Imaging. July 2019," 2019.

[174] G. Healthcare, "Xeleris Help Guide." 2023.

[175] D. L. Snyder, M. I. Miller, L. J. Thomas, and D. G. Politte, "Noise and Edge Artifacts in Maximum-Likelihood Reconstructions for Emission Tomography," *IEEE Trans. Med. Imaging*, vol. 6, no. 3, pp. 228–238, 1987, doi: 10.1109/TMI.1987.4307831.

[176] T. Kangasmaa, A. Sohlberg, and J. T. Kuikka, "Reduction of Collimator Correction Artefacts with Bayesian Reconstruction in Spect," *Int. J. Mol. Imaging*, vol. 2011, pp. 1–6, 2011, doi: 10.1155/2011/630813.

[177] R. A. Gregory *et al.*, "Standardised quantitative radioiodine SPECT/CT Imaging for multicentre dosimetry trials in molecular radiotherapy," *Phys. Med. Biol.*, vol. 64, no. 24, 2019, doi: 10.1088/1361-6560/ab5b6c.

[178] F. Sepehri, M. Hajivaliei, and H. Rajabi, "Selection of random number generators in GATE Monte Carlo toolkit," *Nucl. Instruments Methods Phys. Res. Sect. A Accel. Spectrometers, Detect. Assoc. Equip.*, vol. 973, no. May, p. 164172, 2020, doi: 10.1016/j.nima.2020.164172.

[179] G. Marsaglia, A. Zaman, and W. Wan Tsang, "Toward a universal random number generator," *Stat. Probab. Lett.*, vol. 9, no. 1, pp. 35–39, 1990, doi: 10.1016/0167-7152(90)90092-L.

[180] ARSAC, “Notes for guidance on the clinical administration of radiopharmaceuticals and use of sealed radioactive sources. Administration of Radioactive Substances Advisory Committee.,” 2021.